Effect of macromolecular mass transport in microgravity vs 1G protein crystallization

Dissertation

zur Erlangung des Doktorgrades der Naturwissenschaften (Dr. rer. nat.)
am Fachbereich Chemie der Fakultät für Mathematik,
Informatik und Naturwissenschaften
Universität Hamburg

vorgelegt von

Arayik Martirosyan

Hamburg, August 2019

Die vorliegende Arbeit wurde im Zeitraum von September 2015 bis August 2019 in der Arbeitsgruppe von Prof. Ch. Betzel im Laboratorium für Strukturbiologie von Infektion und Entzündung am Institut für Biochemie und Molekularbiologie, des Fachbereichs Chemie der Universität Hamburg, durchgeführt.

1. Gutachter: **Prof. Dr. Dr. Christian Betzel**

2. Gutachter: **Prof. Dr. Andrew Torda**

Datum der Disputation: 11.10.2019

Table of Contents

List of abbreviations

<	Less than
>	Greater than
≥	Greater than or equal to
≤	Less than or equal to
±	Both plus and minus operations
1G	Earth gravity
Å	Angstrom
°C	Grad Celsius
µg	Microgravity
µl	Microliter
µm	Micrometer
µM	Micromolar
Amp	Ampicillin
$AmSO_4$	Ammonium sulfate
APS	Ammoniumpersulfat
As	Aminosäure
ASU	Asymmetric unit
a.u.	Arbitrary unit
BLAST	Basic Local Alignment Search Tool
BSA	Bovine Serum Albumin
ca.	Circa
CEWL	Chicken egg white lysozyme
CCD	Charge-coupled device
cm	Centimeter
CV	Column volumes
d	Day
Da	Dalton
DESY	Deutsches Elektronen Synchrotron
dH2O	Distilled water
DLR	Deutsche Luft und Raumfahrt Agentur
DLS	Dynamic light scattering
Dmax	Maximal diameter
DMSO	Dimethyl sulfoxide
DNA	Deoxyribonucleic acid
DOL	Degree of labeling
E. coli	*Escherichia coli*
EDTA	Ethylenediamine tetra-acetic acid
ESI	Electrospray ionization
EtOH	Ethanol
et al.	*lat.: „et alteri)*
FPLC	Fast protein liquid chromatography
g	Gramm
g	Relative centrifugal force
GFP	Green fluorescent protein
GSH	Glutathione
GST	Glutathione-S-transferase
h	Hour
HEWL	Han egg white lysozyme
IPTG	Isopropyl β-D-1-thiogalactopyranosid
ISS	International Space Station
kDa	Kilodalton
l	Liter

LB	Luria broth (Luria-Bertani)
LMM	Light microscope module
M	Molar
MALDI	Matrix assisted laser desorption/ionization
mA	Milliampere
mg	Milligram
min	Minute
ml	Milliliter
mM	millimolar
MS	Mass spectrometry
MW	Molecular weight
ms	Millisecond
NASA	National Aeronautics and Space Administration
ng	Nanogram
nM	Nanomolar
Ni-NTA	Nitrilotriacetic acid
OD	Optical Density
ON	Over night
ORF	Open reading frame
PAGE	Polyacrylamid-Gelelectrophorese
PBS	Phosphate buffered saline
***Pf*GST**	*Plasmodiun falciparum* glutathione-S-transferase
pI	Isoelectric point
pM	Picomolar
pmol	Picomole
R_h	Hydrodynamic Radius
rpm	Revolutions per minute
RT	Room temperature
s	Second
SD	Standard Deviation
SDS	Sodium dodecyl sulfate
SpaceX	Space Exploration Technologies Corp
TEMED	N,N,N',N'-Tetramethylethylendiamin
TfB	Transformation buffer
TOF	Time-of-flight
UV	Ultraviolet
V	Volt
v/v	Volume per volume
w/v	Weight per volume

I Introduction

1 Biological macromolecules, proteins

Biological macromolecules are vital building units of life. They are large molecules that consist of many, up to several hundred thousand identical or different atoms or atomic groups and thus can reach from small to a relatively large molecular weights. The nucleic acids (DNA, RNA), proteins (enzymes, antibodies, and collagen), polysaccharide (cellulose, starch) and lignin are among of the biological macromolecules. Proteins are highly complex biomolecules that are present in all living organisms and are directly involved in the bio-chemical processes essential for life, so they form the structures of living cells, transport metabolites, pump ions, play key role in signal transduction and catalyze chemical reactions. The term protein, emanated by the 18th-century Swedish chemist Jons Jacob Berzelius, has its origin from the Greek word *proteios,* meaning of the first rank and was first used in 1839 in a publication by Gerardus Johannes Mulder (Linderstrom-Lang, 1953; Mulder, 1839). The Human proteome contain more than 100000 proteins that are involved in essential functions of cells, tissues and organs (Adkins et al., 2002; Smith et al., 2013). Proteins are built of amino acids. Since 21 amino acids are known to occur regularly in proteins (Böck et al., 1991; Stadtman, 1996). Proteins consist of more than 100 amino acids, up to several thousand amino acids, wherein amino acid chains with a length of less than about 100 amino acids attributed to the peptides. The largest known human protein is Titin with approximately 3600 kDa, consists of more than 30,000 amino acids and contains 320 protein domains (Labeit et al., 1992; Wang et al., 1979). There are Proteins with diverse forms and functions, with different molecular sizes, shape compositions and properties. The proteins can be classified to four different structure levels. The primary structure of a protein represents the sequence of the individual amino acids of a polypeptide chain and describes the amino acid sequence, but not the spatial structure of the protein. The secondary structure of a protein determined by the composition of the protein from particularly common motifs for the spatial arrangement of the amino acids without any regard for the conformation of side chains or other segments of the main chain. The tertiary structure determined by the parent structure of the polypeptide chain superordinate to the secondary structure and is the result of the interaction between the side chains of the amino acids composing the protein. The quaternary structure is demonstrated by the formation of a protein complex. This may be either a clustering of different proteins or a unit of two or more polypeptide chains derived from the same polypeptide chain (Branden and Tooze, 1999; Gromiha et al., 2010).

For example, life without enzymes is not possible. All enzymes identified thus far are proteins. Enzymes catalyze biochemical and metabolic reactions that take place in animals, plants, and microorganisms. They enable an organism to build up or degrade the proteins, carbohydrates, nucleic acids and lipids.

Another example for proteins with important regulatory functions is hemoglobin. Hemoglobin transports oxygen from the lung to organism, organs and tissues, acting as oxygen carrier in the blood (Brunori et al., 1974; Fronticelli et al., 1995).

2 X-ray protein crystallography

X-ray crystallography is the predominate technique used to determine the three- dimensional structure of biological macromolecules. High-resolution three-dimensional structures provide information that is used to determine the function of proteins and other biomolecules, how they undergo conformational changes, how they perform catalysis in the case of enzymes and for drug discovery in cases where proteins play a role in different disorders or diseases. Growing high quality crystals of these biomolecules enhances the ability to obtain X-ray data at high resolution, thereby enabling more accurate three-dimensional structure determinations. Data and information obtained from crystallographic investigations are important for macromolecular engineering to optimize and biomolecules for various applications in biomedical research. The diffraction of X-rays by crystals was first discovered by Max von Laue in 1914 (Eckert, 2012; von Laue, 1915). William Henry Bragg and William Lawrence Bragg in 1915 analyzed crystal structures at the atomic level using the process of X-ray diffraction (Bragg, 1915; Bragg and Bragg, 1918). John Bernal and his student Dorothy Hodgkin in 1934 produced the first X-ray diffraction photograph of a digestive enzyme, pepsin, marking the beginning of protein crystallography (Bernal and Crowfoot, 1934). In addition, Hodgkin discovered the structure of penicillin using X -ray protein crystallography, which allowed pharmaceutical companies to mass-produce the antibiotic. (Hodkin, 1949; Kademani et al., 1999).
Since beginning of crystallographic studies for biomolecules, the structures of more than 154.939 (recent status: 18.08.2019) biomolecules, including proteins, nucleic acids and their complexes have been determined and are deposited in the Protein Data Bank (www.rcsb.org; Berman et al., 2000).

3 Protein crystallization and techniques

Protein crystallization is the process by which protein molecules are formed into 3D crystals. Since high quality, crystals can be hard to produce; thousands of samples are often created for just a single protein. Whereas the key to accurate 3D protein modeling is high-quality protein crystals, protein crystallization is argued to be the most difficult part of the crystallography process. Protein crystals are very fragile and can be affected by minor changes in heat, chemical conditions or pressure. After growing a protein crystal, X-ray diffraction experiments can be performed in synchrotron or using other commercial sources. Given data on diffraction patterns, proteins can be accurately modeled in three dimensions. With the resulting three-dimensional protein model, novel drugs can be designed that target a particular protein or toxin.

Crystallization can be illustrated by a phase diagram (Figure 1). The phase diagram is acquired by varying two parameters, protein concentration and precipitant concentration, at a time. In a protein crystallization phase diagram between four areas can be distinguished: precipitation zone, an area of very high supersaturation, the protein will precipitate; nucleation zone, an area of moderate supersaturation, the nucleation will occur; metastable zone, an area of lower supersaturation, protein crystals will grow; and undersaturation zone, the protein if dissolved and will not crystallize (Chayen 2005; Chayen and Saridakis 2008; Ducruix and Giegé 1999).

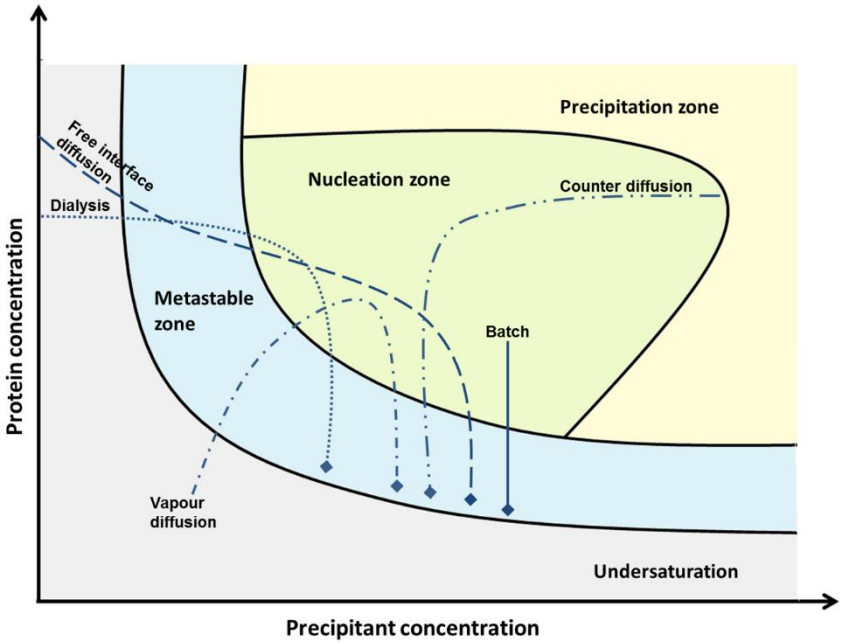

Figure 1. Schematic illustration of a protein crystallization phase diagram. Routes of the crystallization methods are represented: Batch, counter diffusion, dialysis, free interface diffusion and vapour diffusion. Each method runs a different routes to enter the nucleation and metastable zones.

Protein crystallization usually takes place in two successive phases: nucleation and crystal growth. In the nucleation phase a critical nucleus will be formed and crystal growth will follow (Ataka, 1993; Chayen and Saridakis, 2008; Stura and Wilson, 1991).

The most commonly crystallization techniques are: Vapour diffusion (hanging and sitting drops), dialysis, free interface diffusion, batch and counter diffusion (Chayen, 1998; Thomas et al., 1989). The vapour diffusion (sitting and hanging drop)-, dialysis- and counter diffusion methods are schematically represented in figure 2. Vapour diffusion is the most widely used technique. Vapour diffusion techniques are dynamic systems in which the crystallization conditions are changing during the crystallization process. The protein sample is either sitting (Figure 2B) or hanging (Figure 2A) drop that equilibrates against a reservoir containing crystalizing agents at either lower or higher

concentrations than in the protein drop (Chayen, 1998; Chayen, 2008). In the batch method the protein sample and the crystallizing agents are mixed at their final concentrations. The supersaturation in batch method is achieved upon mixing and the conditions are stable over the time (Chayen, 1998). In the dialysis method the slow diffusion of the higher precipitant concentration from the outer compartment into the inner compartment gradually raises the precipitant concentration in the protein solution (Figure C). The protein sample is gradually moved to a point of supersaturation by imposing a gradient of ionic strength or organic solvent concentration across the wall of the membrane (Thomas et al., 1989). Counter diffusion is a nonequilibrium crystallization techniques and can be used to obtain higher quality crystals. For counter diffusion thin capillaries will used (Figure 2).

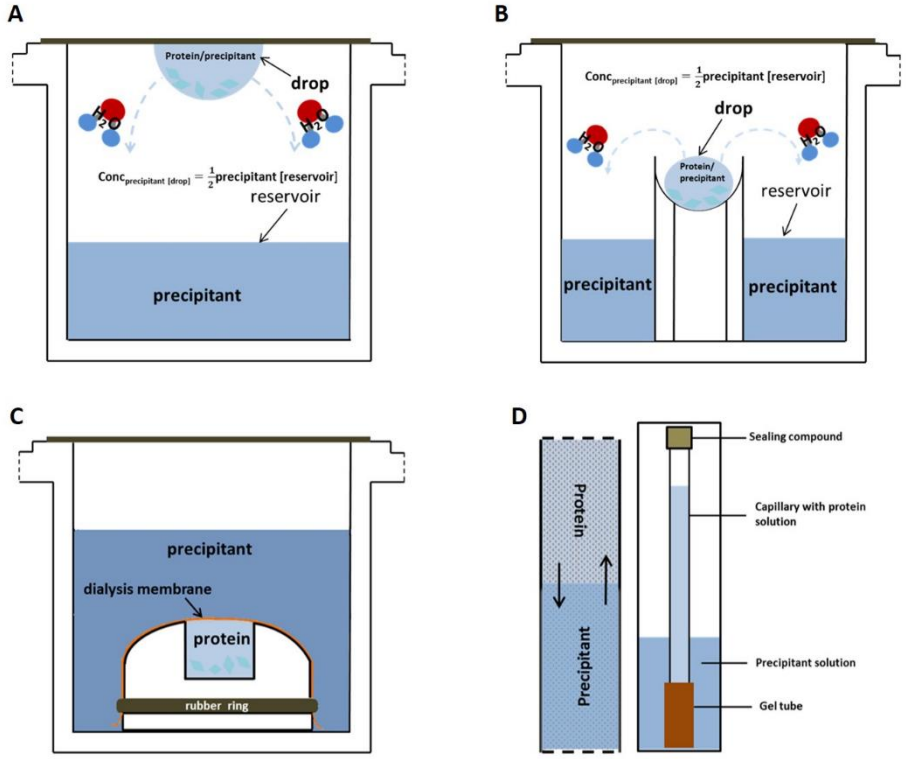

Figure 2. Schematic representation of the most commonly used crystallization methods. (A) Vapour diffusion, hanging drop. (B) Vapour diffusion, sitting drop. (C) Dialysis. (D) Counter diffusion.

In counter diffusion techniques, the interacting precipitating agent and protein solutions either contact one another directly or are separated by an intermediate chamber working as a physical buffer (Garcia-Ruiz, 2003; Otalora et al., 2009). The protein and precipitant solutions are placed to diffuse against each other, resulting in a spatial–temporal gradient of supersaturation along the capillary. The varying supersaturation conditions leading to protein precipitation, nucleation, and crystal growth can be obtained simultaneously in the capillary (Garcia-Ruiz, 2003; Ng and Garcia-Ruiz, 2003).

4 Macromolecular mass transport in impact of protein crystallization

Macromolecular transport in crystallization processes has been shown to directly affect crystal quality (García-Ruiz et al., 2016; McPherson et al., 1999; Vekilov, 1999). Gravity dependent flow effects, including convection and sedimentation, affect the crystal growth processes on earth (Lee and Chernov, 2002; Otálora et al., 2001; Wilcox, 1983). Density-driven solution convection (Figure 3) might be expected to force molecules to rapidly flow past the growing crystal, thus bringing impurities such as inorganic and organic particles and macromolecular aggregates to growing crystal surfaces (Lee and Chernov, 2002). Different concentrations at different parts of a crystal created with the flow patterns may lead to non-uniform growth conditions (DeLucas et al., 1986; Wilcox, 1983). Sedimentation is another gravity dependent effect that significantly alters the crystal growth process on earth (Figure 3).

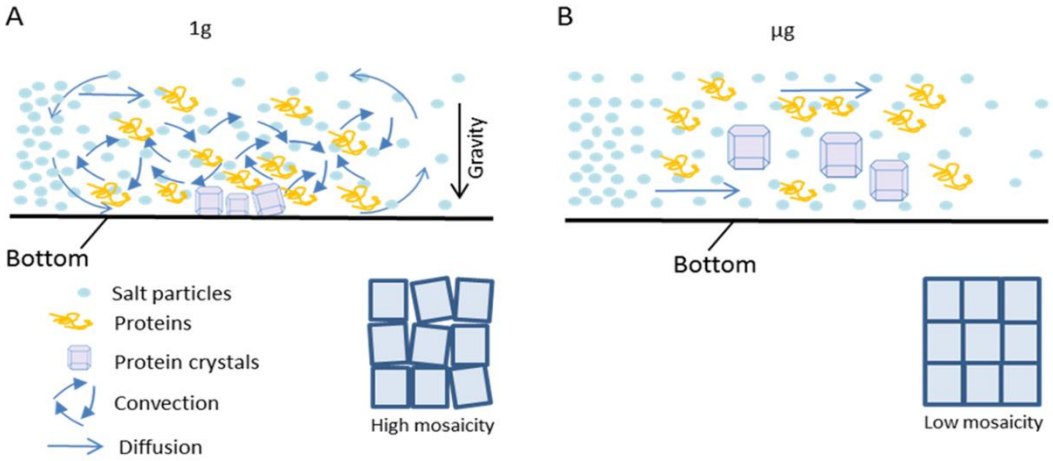

Figure 3. Comparative mass transport on earth and microgravity conditions. Resulting effect of crystal quality illustrated by size, sedimentation and mosaicity. (A) On Earth. (B) In microgravity.

Depending on the density of the growing crystals versus the solution density, crystals growing in a 1G environment migrate to the top, bottom or wall of a crystallization container (Carotenuto et al., 2002; DeLucas et al., 1986). Thus, sedimentation creates crystal accumulation on the surface, bottom or wall of a crystallization container (DeLucas et al., 1986; García-Ruiz et al., 2001a), which may interrupt further crystal growth (DeLucas et al., 1986; García-Ruiz et al., 2001a; Wilcox, 1983). Diffusion-controlled crystal growth processes in the absence of convection (and the elimination of the sedimentation effect) may be beneficial for crystal quality. Therefore, the microgravity environment appears to be ideally suited for growing crystals with improved quality (Kuranova et al., 2011; McPherson et al., 1999; Snell et al., 1997). In this context, it is important to investigate the effect of crystal growth rates versus crystal quality and size.

5 Impurity effect on protein crystallization

Macromolecule purity is a major parameter in the crystal growth process, such that removal of impurities and elimination of macromolecular heterogeneity improves the probability of growing higher quality crystals (Giege et al., 1986; McPherson et al., 1999; Vekilov and Rosenberger 1996). Crystal defects often originate from incorporation of molecular aggregates and other impurities into the lattice of a growing crystal (Adawy et al., 2015; Giege et al., 1986; McPherson et al., 1999; Vekilov and Rosenberger 1996). Hen egg-white lysozyme (HEWL) has been crystallized in presence of HEWL dimers on earth and under microgravity conditions to investigate the effect of impurity incorporation into a growing crystal. It was observed that the HEWL crystals grown under microgravity conditions contain 4.5 times less HEWL dimers than control experiments performed on earth (Carter et al., 1999). Another experiment demonstrated that the presence of chicken egg white lysozyme (CEWL) dimers in the crystallization solutions in microgravity reduced crystal size, increased mosaicity and reduced the signal-to-noise ratio of the X-ray data (Snell et al., 2001). Yet in another investigation, no significant difference in impurity incorporation between microgravity and ground crystals was observed (Snell et al., 2001).

6 Protein crystallization in microgravity

The first reported protein crystallization experiments in microgravity, performed in 1984, described the growth of lysozyme and β-galactosidase crystals on Spacelab 1 (Littke and John, 1984). Since then in subsequent space shuttle missions, unmanned satellite missions, on the Russian space station and on the ISS, more than one hundred different proteins (Table 1;2) have been crystallized under microgravity conditions (DeLucas et al., 1986; Krauspenhaar et al., 2002; Snell et al., 1997; Timofeev et al., 2012a; Vallaza et al., 2002). In 1989 Asano et al. performed a series of crystal growth experiments for bovine pancreatic ribonuclease-S under microgravity conditions using the COSIMA 2 system (Asano et al., 1992; Plaas-Link and Cornier, 1988). The microgravity-grown ribonuclease S single crystals revealed improved diffraction resolution compared to ground-grown crystals of equal size (Asano et al., 1992). In another experiment, crystals of uridine phosphorylase from Shewanella oneidensis MR-1 revealed improved quality for microgravity grown crystals compared to 1G controls (Safonova et al., 2012). However, some crystallization experiments performed under microgravity conditions showed no significant improvement in crystal quality (Hilgenfeld et al., 1992; Strong et al., 1999). It is argued that the microgravity environment on the ISS would be ideal for growing better quality protein crystals.

Table 1. Biomolecules crystallized in microgravity, 1984-2019.

Biomolecules	**Crystallization method/ techniques**	**Apparatus**	**Year/ time period**	**Mission**	**Reference**
β-galactosidase	Free interface diffusion/liquid-liquid diffusion	Protein crystallization facility	1984	European TEXUS rocket	Lottke and John 1984, 1986
Lysozyme	Vapor diffusion	VDA (Vapor diffusion apparatus)	1985 in July	STS-51F	DeLucas et al. 1986
Concanavalin B, C-reactive protein, Canavalin, Purine nucleoside phosphorylase, Human serum albumin	Vapour diffusion	VDA (Vapor diffusion apparatus)	1986 in January, 3-7 days	STS-61C	DeLucas et al. 1986
Gamma-interferon D, Porcine elastase, Isocitrate lyase	Vapour diffusion		1988 in September, 3 days	STS-26	DeLucas et al. 1989
Vanadate peroxidase, TET repressor, EF-Tu xGDP, Adenylate kinase (wild type), Adenylate kinase (mutante), *Streptomyces* Lysozyme, Thermolysin	Liquid-liquid diffusion		1988, August, 8 days	COSIMA 1, Long March CZ-2C rocket carried the Chinese re-entry capsule FWS-1	Erdmann et al. 1989
***Streptomyces* lysozyme, Thermolysin**	Vapor diffusion		1989, September, 10 days	COSIMA 2	Hilgenfeld et al. 1992
Hen egg white lysozyme	Vapor diffusion		1989, December - 1990 February, 56 days	Soviet space Station MIR	Strong et al. 1992
Ribonuclease S	Vapor diffusion		1989, September,	COSIMA 2	Asano et al. 1992
Aspartate ammonia lyase , Anti- Brucella Fab (monoclonal), Isocitrate dehydrogenase (*E.coli*), Betta-lactamase (*Enterobacter cloacae*), Betta-	Vapor diffusion		1989-1990	MIR space station	Stoddard et al. 1992

lactamase (*Bacillus lichenoformis*), D-Ala-D-Ala ligase (*E.coli*)					
Bovine ribonuclease A	Macro seeding		1991	Swedish Space Corporation (SSC), MASER rocket	Sjölin et al. 1991
Recombinant human Interferon gamma	Vapor diffusion		1991	STS-28	Ealick et al. 1991
Lysozyme , Bovine pancreatic trypisin inhibitor mutant	Vapor diffusion, microdialysis		1991, October, 16 days	Russian unmanned re-entry photon capsule, COSIMA- IV	Henning et al. 1994
Carbohydrate-Binding Fab	Liquid-liquid diffusion		1991, September, 1992 January	US space shuttle Discovery, Russian MIR	Borisova et al. 1996
Satellite tobacco mosaic virus (STMV), Canavalin from jack beans	Vapor dissusion, liquid-liquid diffusion	CRYOSTAT	1992, January 22–29	US Space Shuttle mission, IML-1, STS-42	Day and McPherson 1992
Malic Enzyme (NAD-dependent enzyme), Bovine brain prolyl-isomerase, HIV-1 reverse transcriptase complexed to a monoclonal antibody fragment and to a 19/18 base-paired double stranded DNA helical fragment	Vapor diffusion		1992, June, 5 days	USML-1 STS-50	DeLucas et al. 1994
Human serum albumin	Vapor diffusion		1992, January	STS-42, IML-1	DeLucas et al. 1994
Satellite tobacco mosaic virus	Liquid-liquid diffusion	CRYOSTAT	1992, January, 12 days	US Space shuttle STS-42, IML-1	Larson et al. 1998
Henn-egg-white lysozyme, Pyruvate aminotransferase	Vapor diffusion		1992-1997	STS-42, STS-47, STS-84	Aibara et al. 1997

from *Pseudomonas sp.*					
HEW lysozyme	Diffusion techniques		1992; 1994	Chinese experiment	Dong et al. 1998
HEW lysozyme	Vapor diffusion, liquid-liquid diffusion	APCF (Advanced protein crystallization facility)	1993, June	Space Hab-01 mission, STS-57	Vaney et al. 1996
Lysozyme	Dialysis		1993, June, 7.5 days	STS-57, Spacehab-1	Helliwell et al. 1996
Lysozyme, Collagenase	Liquid-liquid diffusion	APCF	1993, June	STS-57, Spacehab-1	Broutin et al. 1997
Lysozyme	Dialysis, free interface diffusion, vapor diffusion	APCF	1993, June, 10 days	STS-57, Spacehab-1	Riès-Kautt et al. 1997
Lysozyme	Dialysis		1994, July, 12.5 days	IML-2, STS-65	Helliwell et al. 1996
Lysozyme	Dialysis liquid diffusion		1994	STS-65, IML-2	Snell et al. 1995
Canavalin (rhombohedral crystal form), Canavalin (hexagonal crystal form), SatelliteTobacco Mosaic Virus, Satellite Panicum Mosaic Virus	Liquid-liquid diffusion	APCF	1994, July, 12.5 days	European space agency, IML-2, STS-65	Koszelak et al. 1995
Rhombohedral canavalin	Liquid-liquid diffusion	APCF (Advanced protein crystallization facility)	1994, July, 12.5 days	European space agency, IML-2, STS-65	Ko et al. 2001
Human insulin	Vapor diffusion	PCF (protein crystallization facility)	1993-94	US Space Shuttle, STS-57, STS-60	Smith et al. 1996; Moore et al. 1999; Lorber 2002

Serine protease collagenase from *Hypoderma lineatum*	Liquid-liquid diffusion		1994, July, 14.5 days	IML-2, STS-65	Broutin-L'Hermite et al. 2000
Human estrogenic 17β-hydroxysteroid dehydrogenase	Vapor diffusion		1993-1994, January, 88 days	Russian MIR station	Zhu et al. 1995
Acidic phospholipase A 2 from venom of *Agkistrodon halys* Pallas	Diffusion techniques		1994, July	Chinese space mission	Pan et al. 1996
Human Recombinant Insulin	Vapor diffusion		1994, February, 8 days	STS-60	Long et al. 1997; DeLucas 2001
Antithrombin	Vapor diffusion		1995	US Space Shuttle Flight STS-67	Wardell et al. 1997
Lysozyme from bacteriophage lambda	Vapor diffusion		1995	US Space Shuttle Flight STS-67	Evrard et al. 1998; Lorber 2002
Nucleosome core particle	Liquid-liquid diffusion	DCAM (Diffusion controlled apparatus for micogravity)	1995	US Shuttle mission USML-2, STS-73	Harp et al. 2000
Monoclinic HEWL	Vapor diffusion	APCF	1995, October	US Shuttle mission USML-2, STS-73	Vaney et al. 2001
Thaumatin	Dialysis, liquid-liquid diffusion		1995, October 1996, June	US Shuttle mission USML-2, LMS, STS-73	Ng et al. 1997
Apocrustacyanin C1	Vapor diffusion		1995	US Shuttle mission USML-2, STS-78	Snell et al. 1997
α-crustacyanin, the lobster capapace astaxanthin-protein	Liquid-liquid diffusion		Until 1995	EURECA, STS-46	Zagalsky et al. 1995
Apocrustacyanin C1	Vapor diffusion		1994, 8 July	STS-65, IML-2	Chayen et al. 1996; Chayen et al. 1997

HEWL	Dialysis, vapor diffusion		1994-1997	STS-62, STS-63, STS-76, STS-79, STS-81 STS-76, STS-79, STS-81, STS-67,	Carter et al. 1999a
Bacteriophage lambda lysozyme	Vapor diffusion		February 1995; March 1995	STS-63, STS-67	Evrard et al. 1997
Antithrombin	Vapor diffusion	PCAM (Protein crystallization apparatus for microgravity)	March 1995, 14 days	STS-67	Skinner et al. 1997
Hen egg-white lysozyme	liquid-liquid dialysis		1996, June	US Space Shuttle Flight STS-78	Dong et al. 1999
Aminoacyl-tRNA synthetase	Dialysis	APCF	1996, June	US Space Shuttle Flight STS-78	Ng et al. 2002
Lysozyme	Liquid-liquid diffusion		1996, June, 17 days	US Space Shuttle Flight STS-78	Otálora et al. 1999
Respiratory syncytial virus (RSV) antibody, HIV protease complex with cyclic area based inhibitor, Eco RI endonuclease–DNA complex	Vapor diffusion		1997, June-October	US Space Shuttle Flight STS-85	Carter et al. 1999b
Pike parvalbumin	Vapor diffusion		1997, June-October	US Space Shuttle Flight STS-83, STS-94	Carter et al. 1999b
EF-hand parvalbumin	Vapor diffusion	APCF, PCAM	1997, June-October	US Space Shuttle Flight STS-83	Declercq et al. 1999b
Proteinase K	Vapor diffusion, liquid-liquid diffusion		1997, July	Space Shuttle STS-94	Betzel et al. 2001
Hematopoietic prostaglandin D synthase	Vapor diffusion, liquid-liquid diffusion		1997, Mai, 10 days	STS-84, JAXA	Tanaka et al. 2011

Chaperonin-60, Macrophage migration inhibitory factor, B subunit of V-type ATPase	Vapor diffusion		1997, Mai, 10 days	STS-84, JAXA	Kitano et al. 2000
Cratylia mollis lectin (isoform 1) in complex with methyl-alpha-D-mannose	Vapor diffusion	VDA	1997, May	STS-84	De Souza et al. 2003
EF-hand Protein	Vapor diffusion, Dialysis		1997, July, 16 days	STS-94	Declercq et al. 1999a
***Thermus flavus* 5S rRNA**	Vapor diffusion		1997, July, 16 days	STS-94	Lorenz et al. 2000
***Sulfolobus solfataricus* Alcohol Dehydrogenase**	Dialysis		Until 1998, 15.5 days	US Space Shuttle, STS-73	Esposito et al. 1998
Photosystem I from *Synechococcus elongates*	Microdialysis		1998	US Space Shuttle, STS-73	Klukas et al. 1999
Beef liver catalase	Free interface diffusion		1998	Space Shuttle, STS-73	Ko et al. 1999; Lorber 2002
Surface layer glycoprotein from extremely thermophilic *Methanothermus fervidus*	Vapor diffusion		1998	Space Shuttle STS-95	Evrard et al. 1999
Human Bence–Jones protein	Vapor diffusion		1998, October, 9 days	Space Shuttle STS-95	Alvarado et al. 2001
Pro-Pro-Gly	Dialysis	APCF	1998, October, 9 days	Space Shuttle STS-95	Vitagliano et al. 2001
Collagen triple helix model [(Pro-Pro-Gly)$_{10}$]$_3$	Dialysis	APCF	1998, October, 9 days	Space Shuttle STS-95	Berisio et al. 2002; Vitagliano et al. 2001
Thaumatin	Dialysis	APCF	1998, October, 9 days	Space Shuttle STS-95	Sauter et al. 2002

NH3-dependent NAD+ synthetase from *Bacillus subtilis*	Vapor diffusion	CVDA (Commercial vapor diffusion apparatus)	1998, October, 9 days	Space Shuttle STS-95	Symersky et al. 2002
Ribonuclease S	Dialysis		1998, October,1999, July	Space Shuttle STS-93, STS-95	Travis Gallagher et al. 2003
Insulin	Vapor diffusion		1998, October, 9 days	Space Shuttle STS-95	Vahedi-Faridi et al. 2003a
Human Bence-Jones dimer	Dialysis	APCF	1998, October, 9 days	Space Shuttle STS-95	Terzyan et al. 2003
Thaumatin	Dialysis	APCF	October 1998, 8 days	STS-95	Lorber et al. 1999b; Lorber et al. 1999a; Sauter et al. 2002
Herpes Simplex Virus 1 Single-Stranded DNA Binding Protein	Vapor diffusion		October 1998, 8 days	STS-95	Mapelli and Tucker 1999
(Pro-Pro-Gly)$_{10}$	Dialysis, free interface diffusion		October 1998, 8 days	STS-95	Berisio et al. 2000
Proteinase K	Vapor diffusion		June 1998; October 1998, 8 days	STS-91; STS.95	Eschenburg et al. 2000
Insulin	Vapor diffusion		1998, October, 9 days	STS-95	Borgstahl et al. 2001
Hen egg-white lysozyme	Counter diffusion		1998, October, 9 days	STS-95	Sauter et al. 2001
(Pro-Pro-Gly)$_{10}$	Free interface diffusion, dialysis		1998, October, 9 days	STS-95	Carotenuto et al. 2001
T6-Insulin	Free interface diffusion, vapor diffusion		1998, October, 9 days	STS-95	De Mattei et al. 2001

Alcohol Dehydrogenase from The Hyperthermophilic *Archaeon Sulfolobus*	Dialysis		Until 2002	US Space Shuttle	Esposito et al. 2002; Lorber 2002
Human triosephosphate isomerase	Counter diffusion	GCF (Granada crystallization facility)	2001-2005	ISS	Kinoshita et al. 2005
Thermus flavus 5S rRNA helix B	Vapor diffusion		April 2001 to August 2001	ISS 6A, STS-100, STS-105	Vallazza et al. 2002
Mistletoe lectin I from Viscum album with adenine monophosphate	Vapor diffusion	HDPCG	2002, November, 110 days	ISS 6A, STS-113	Krauspenhaar et al. 2002; Edward and John 2005
Apocrustacyanin C(1)	Vapor diffusion		Until 2002	US Space shuttle, ISS mission	Habash et al. 2003
Myoglobin triple mutant Mb-YQR [L(B10)Y, H(E7)Q and T(E10)R]	Vapor diffusion	HDPCG (High denisty protein crystal growth)	2001, 2002	ISS 6A, ISS 8 A	Miele et al. 2003
Manganese superoxide dismutase	Vapor diffusion		December 2001 to April 2002	ISS	Vahedi-Faridi et al. 2003b
Hydrogenase maturation factor HypF N-terminal domain	Vapor diffusion		April 2002	ISS 8A/STS110	Ponassi et al. 2011
Dehydroepiandrosterone sulfotransferase (DHEA-ST), Phosphoenolpyruvate carboxykinase (PCK), Mutant of cytochrome-b5 (Cyto-b5m), Antibacterial peptide LC1, Hemorrhagin	Diffusion techniques		March 2002, 7 days	Shenzhou 3	Han et al. 2004
Liver Basic Fatty Acid-Binding Protein, Chicken liver basic Fatty Acid-binding	Vapor diffusion	HDPCG	2001	STS-100, ISS-6A	Nichesola et al. 2004

protein complexed with cholic acid					
Hematopoietic prostaglandin D synthase	Counter diffusion		January–April 2004, 13 weeks,	NASDA-GCF#3	Tanaka et al. 2011
Hen egg lysozyme, Carboxypeptidase B	Free-interface-diffusion		April-October 2005	ISS 11	Smirnova et al. 2009
Recombinant human insulin	Free-interface-diffusion		October 2005 to April 2006	ISS12-13	Smirnova et al. 2009
Thermotoga maritima triose phosphate isomerase	Counter diffusion		Until 2007	ISS	Evrard et al. 2007
Archaeal transcription termination factor NusA	Counter diffusion	GCF (Granada crystallization facility)	Until 2005	ISS, JAXA–GCF project	Tanaka et al. 2007
Mistletoe Lectin I (ML-I)	Counter diffusion	GCF (Granada crystallization facility)	2005	ISS	Małecki et al. 2012
Mistletoe Lectin I in Complex with Zeatin	Counter diffusion	GCF	2005	ISS	Meyer et al. 2008
Uridine phosphorylase from Shewanella oneidensis MR-1	free-interface-diffusion, counter diffusion		Until 2012	ISS, JAXA	Safonova et al. 2012
Mouse Lipocalin-Type Prostaglandin D Synthase	Counter diffusion		August to October 2007, 11 weeks	ISS, Russian Module-1, JAXA	Inaka et al. 2011
Recombinant Formate Dehydrogenase from Arabidopsis thaliana	Vapor diffusion		2006-2009	ISS, Russian Module	Shabalin et al. 2010
Phosphopantetheine Adenylyltransferase from Mycobacterium tuberculosis in	Vapor diffusion, Counter diffusion		2006-2009	ISS, Russian Module	Timofeev et al. 2010, 2012b

complex with Coenzyme A					
Human epidermal growth factor receptor	Counter diffusion	GCF, JCB (JAXA crystallization box)	Until 2011	ISS	Yoshikawa et al. 2013
Phosphopantetheine adenylyltransferase (PPAT) from Mycobacterium tuberculosis in the apo form, Phosphopantetheine Adenylyltransferase from Mycobacterium tuberculosis in comlex with dephosphocoenzyme A	Counter diffusion		Until 2012	ISS, Russian Module	Timofeev et al. 2012b
Phosphopantetheine adenylyltransferase (PPAT) from Mycobacterium tuberculosis in the apo form, Phosphopantetheine adenylyltransferase (PPAT) from Mycobacterium tuberculosis in the complex with ATP	Counter diffusion		Until 2012	ISS, Russian Module	Timofeev et al. 2012a
Thymidine Phosphorylase from E. coli in Complex with 3'-Azido-2'-Fluoro-2',3'-Dideoxyuridine	Counter diffusion		Until 2012	ISS, Russian Module, JAXA	Timofeev et al. 2013a
Carboxypeptidase T from Thermoactinomyces vulgaris in Complex with N-BOC-L- eucine	Counter diffusion		Until 2012	ISS, Russian Module,	Timofeev et al. 2013b
Thermostable T1 Lipase	Counter diffusion		Until 2014	ISS, JAXA	Mohamad Aris et al. 2014

Zn-insulin	Counter diffusion, free-interface diffusion		Until 2014	ISS, Russian Module	Strelov et al. 2014
Porcine carboxypeptidase B	Counter diffusion		Until 2015	ISS, Russian Module, JAXA	Akparov et al. 2015
Phosphoribosyl pyrophosphate synthetase from *E. coli*	Counter diffusion		Until 2016	ISS, Russian Module	Timofeev et al. 2016
D-tagatose 3-epimerase C66S from *Pseudomonas cichorii* in complex with 1-deoxy L-tagatose	Counter diffusion		2013-2016	ISS, JAXA-PCG	Yoshida et al. 2016
HEWL	Counter diffusion	LMM biophysics plate	2017;2018	ISS	Martirosyan et al. 2019 (to be published)
***Plasmodium falciparum* glutathione-S-transferase (*Pf*GST)**	Counter diffusion	LMM biophysics plate	2017; 2018	ISS	Martirosyan et al. 2019 (to be published)

Table 2. Biomolecules crystallized in microgravity in terms of drug design/development.

Protein	Space Mission	Function/Target	Reference
C-reactive protein	STS-61C	Binds to the phosphocholine expressed on the surface of dead or dying cells and some bacteria	DeLucas et al. 1986
Human serum albumin	STS-61C, STS-42	Maintains oncotic pressure, transports thyroid hormones, fatty acids, unconjugated bilirubin, many drugs	DeLucas et al. 1986 DeLucas et al. 1994
Purine nucleoside phosphorylase	STS-61C	Metabolizes inosine into hypoxanthine and guanosine into guanine.	DeLucas et al. 1986
TET repressor	Chinese re-entry capsule	Involved in bacterial resistance again antibiotics	Erdmann et al. 1989
Ribonuclease S	Chinese re-entry rocket	Catalyzes the degradation of RNA into smaller components	Hilgenfeld et al. 1992
Beta-Lactamase	MIR space station	Produced by bacteria that provide multi-resistance to β-lactam antibiotics	Stoddard et al. 1992

		such as penicillins, cephamycins, and carbapenems (ertapenem)	
Human Interferon-γ	STS-26, STS-28	Antiviral agent, enhance immune cells activity	Ealick et al. 1991
Bovine pancreatic trypsin inhibitor mutant	Russian unnamed re-entry capsule	Competitive inhibitor of several serine proteases, specifically trypsin, chymotrypsin. Leads to the inhibition of the formation of factor XIIa	Henning et al. 1994
HIV-1 reverse transcriptase complexed to a monoclonal antibody fragment and to a 19/18 base-paired double stranded DNA helical fragment	STS-50	One of the key players in the mechanism of infection by HIV retrovirus.	DeLucas et al. 1994
Human 1713-hydroxysteroid dehydrogenase in the complex form with NADP +	Russian MIR station	Significant target for breast and prostate cancer drug therapy	Zhu et al. 1995
T3Ri insulin hexamer, complexed with 4-hydroxybenzamide, Insulin	STS-57, STS-60, STS-95	Provide benefits to the Diabetic	Smith et al. 1996 Borgstahl et al. 2001
Acidic phospholipase A 2	Chinese space mission, re-entry capsule	Inhibition of platelet aggregation, hemolysis, presynaptic and muscular toxicity	Pan et al. 1996
Human Interferon α-2	STS-60	Hairy cell leukemia, multiple myeloma, venereal wart, AIDS related Kaposi's, sarcoma and chronic hepatitis B and C	Long et al. 1997
Human Antithrombin	STS-67	Inactivation of several enzymes of the coagulation system	Wardell et al. 1997 Skinner et al. 1997
Thaumatin	STS-73	Thaumatin production is induced in katemfe in response to an attack of viroid pathogens	Ng et al. 1997
STMV (Satellite tobacco mosaic virus)	STS-42	Plant Virus	Larson et al. 1998
Collagenase	STS-65, STS-57	Only enzyme able to cleave native collagen under physiological conditions	Broutin et al. 1997

			Broutin-L'Hermite et al. 2000
Respiratory syncytial virus (RSV) antibody	STS-85	Human respiratory syncytial virus (HRSV) is a syncytial virus that causes respiratory tract infections	Carter et al. 1999
HIV protease **complex with cyclic area based inhibitor**	STS-85	With its integral role in HIV replication, HIV protease has been a prime target for drug therapy	Carter et al. 1999
EF-hand parvalbumin	STS-83	Cell excitation and relaxation, in muscles and in neurons	Declercq et al. 1999
Herpes Simplex Virus 1 Single-Stranded DNA Binding Protein	STS-95	Herpes Simplex Virus 1 produces most cold sores by human	Mapelli and Tucker 1999
Chaperonin-60	STS-84, JAXA	Assists in protein folding in mitochondria. Plays a role in autoimmune disease	Kitano et al. 2000
***Thermus flavus* Ribosomal 5S rRNA**	STS-94	Involved in protein synthesis in Ribosome	Lorenz et al. 2000
Alcohol Dehydrogenase from the Hyperthermophilic Archaeon *Sulfolobus* ***solfataricus***	STS-73	Reversible interconversion of alcohols to aldehydes/ketones	Esposito et al. 2002
Collagen triple helix model **[(Pro-Pro-Gly)10]3**	STS-95	Main component of connective tissue, the most abundant protein in mammals	Berisio et al. 2002
NH3-dependent NAD+ synthetase from *Bacillus* ***subtilis***	STS-95	Drugs designed special for bacterial NAD+ synthetases should decrease NAD+ levels in pathogens, thereby inhibiting bacterial growth	Symersky et al. 2002
Human Bence-Jones dimer	STS-95	Amyloidogenic protein, light chains have the capacity to pass through the blood vessel endothelia and be converted into lethal, insoluble fibrils in vital organs like the kidney, heart, tongue, brain and skin	Terzyan et al. 2003 Alvarado et al. 2001
Mistletoe lectin I from *Viscum album* with adenine	ISS -6A, STS-113	Ribosome-inactivating protein of type II, depurinates specifically the ribosomal 23S/28S rRNA, causing a	Krauspenhaar et al. 2002

monophosphate		total inactivation of protein biosynthesis in eukaryotic cells	
Antibacterial peptide LC1	Chinese re-entry capsule Shenzhou 3	Antimicrobial function	Han et al. 2004
Human triosephosphate isomerase	ISS	Essential for human beings. It was inhibited by drug candidates, severe toxicity would arise	Kinoshita et al. 2005
Hematopoietic prostaglandin (PG) D synthase	JAXA; STS-84	Therapeutic target enzyme for allergy and inflammation, mediates allergic and inflammatory reactions	Tanaka et al. 2011
Hydrogenase maturation factor Hyp-F N-terminal	ISS-8A, STS-110	Hydrogen metabolism	Ponassi et al. 2011
Mouse Lipocalin-Type Prostaglandin D Synthase	ISS, JAXA	Catalyzes the isomerization of PGH2, a common precursor of various prostanoids, to produce PGD2 and is involved in the regulation of pain	Inaka et al. 2011
Phosphopantetheine Adenylyltransferase from *Mycobacterium Tuberculosis* in the Apo Form	ISS, Russian module	Involved in coenzyme A biosyn_thesis by catalyzing the penultimate and fourth step of this process	Timofeev et al. 2012
EGFR kinase domain (G719S/T790M) in the apo form	ISS	The human epidermal growth factor receptor (EGFR) is a multidomain protein	Yoshikawa et al. 2013
Thermostable T1 Lipase	ISS, JAXA	Catalyze both the hydrolysis of triglycerides and the synthesis of esters formed from alcohol and long chain fatty acids	Mohamad Aris et al. 2014
Phosphoribosyl Pyrophosphate Synthetase from *E. Coli*	ISS, Russian module	Links the pentose phosphate pathway to the biosynthesis pathway of purine and pyrimidine nucleosides	Timofeev et al. 2016
***Sa*ThiM ((*Stapilococus aerueus* Thiamin, 5-(hydroxyethyl)-4-methylthiazole kinase))**	Chinese space mission Shenzhou-8	A potential target for pro-drug compounds	Drebes et al. 2016

II Aims of this work

This work was performed in context of the LMM biophysics project. LMM Biophysics is a Glenn Research Center (GRC) and Center for the Advancement of Science in Space (CASIS) sponsored biological protein crystal growth experiment, utilizing the Fluids Integrated Rack (FIR)/Light Microscopy Module (LMM) on the International Space Station (ISS).

As in future at high intensive radiation sources for structure analysis of biomolecules mostly high quality crystals are required, the demand to produce most perfect crystals is increasing, therefore latest microgravity crystallization experiments on ISS aim to understand the inclusion of impurities, reducing the crystal quality. It is assumed that a convection-free, diffusion-controlled environment will support growth of crystals of higher quality, which can be achieved using microgravity. High-resolution three-dimensional structures obtained from crystallographic investigations are important for drug design and macromolecular engineering to optimize biomolecules for various applications in biomedical research. Microgravity crystallization experiments were performed to analyze in microgravity and under lab conditions comparative phenomena causing the incorporation of impurities, such as partially misfolded or partially denaturized proteins, or its aggregates, or other unwanted impurities in growing crystals. In this project the crystal growth rates for macromolecules covering a wide molecular weight in microgravity versus gravity will be compared. In context of this work the percentage incorporation of different molecular aggregates (protein impurities) into the crystalline lattice of growing crystals will be evaluated. Based on the percentage incorporation of larger aggregates within the crystals, the effect of molecular filtering based on differences in diffusion rates will be indirectly assessed. This will be accomplished by fluorescently tagging the aggregates.

In macromolecular protein crystallization mass transport processes are a critical determinant in the process of protein crystal growth. To investigate comparative macromolecular transport phenomena in crystallization experiments and to analyze particular the incorporation of impurities in growing crystals crystallization experiments were performed on ISS while applying the Light Microscopy Module (LMM) for monitoring and scoring the experiments. For this purpose the counter/liquid-liquid diffusion technique in capillaries of 100mm in length, 3mm in width and 0.3mm inner diameter will be applied. The investigation entails the launch of Biophysics Plates (cassettes) containing capillaries with various protein samples. The cassettes were launched aboard SpaceX in cold stowage at -80 °C. Upon reaching ISS the cassettes were transferred to ISS cold stowage while awaiting science operations. Then, the cassette were removed from cold stowage, thawed, and installed onto the LMM and operations were performed. Parallelly, science operations were performed in earth laboratories.

Once the crystals were returned to earth they were experimental analyzed subjected to X-ray crystallography, to determine the structure and hence understand the biology of the system.

III Materials and Methods

1 Material

1.1 Instrumentation

Table 3. Instrumentation.

Devise	Manufacturer
Agarose gel electrophoresis:	
Gel caster	PerfectBlueTM Mini S (Peqlab, Germany)
Power supply	PowerPac 200 (Bio-Rad, Germany)
Electrophoresis unit	PerfectBlueTM Mini S (Peqlab, Germany)
UV transilluminator	Gel iX Imager (INTAS Science Imaging Instruments, Germany)
Balance	TE3102S (Sartorius, Germany)
Centrifuges	5415R/5415C/5424/5804R/5810R MinispinPlus (Eppendorf, Germany) Multifuge X3R (Thermo Fisher Scientific, Germany)
Clean bench	Hera Safe, Thermo Electron corporation (Thermo Fisher Scientific, Germany)
Confocal laser scanning microscopes	Zeiss LSM 710 (Zeiss, Germany) Leica TCS SP – 8 (Leica Microsysteme, Germany)
Crystal imaging	Digital Sight DS-L3 (Nikon, Japan) CrystalScore (Diversified Scientific Inc., US) Microscope SZX12 (Olympus, Japan)
DLS instrumentation	SpectroSize 300 (XtalConcepts, Germany) Spectro Light 500 (XtalConcepts, Germany) Multichannel DLS system (XtalConcepts, Germany)
FPLC (Fast protein liquid chromatography)	ÄKTA Purifier P-901 (GE Healthcare, UK) ÄKTA Prime (GE Healthcare, UK)
Freezer:	
-20 °C	Liebherr premium (Liebherr, Germany)
-80 °C	B35-85 (FRYKA-Kältetechnik, Germany)

Devise	Manufacturer
Freeze-dryer	Alpha 1-4 LSC (CHRIST, Germany)
Incubator: **37 °C** **27 °C**	 Heraeus B6120 (Heraeus, Germany) Heraeus B-5060 (Heraeus, Germany)
Incubator Shaker	Innova 44® (New Brunswick Scientific, USA)
LMM microscope	Leica RXA (Leica microsystems, Germany), modified for ISS research
Mass spectrometer	Agilent 6224 ESI-TOF (Agilent, USA)
Microbalance	CP224S-0CE (Sartorius, Germany)
Microscopes	Stereo microscope SZX12 (Olympus, Japan) Axiovert 25 (Zeiss, Germany) Leica M205 C (Leica Mikrosysteme, Germany)
Micropipette	Micropipette ResearchPlus (Eppendorf, Germany)
Microplate reader	TECAN GENios XFLUOR4 (TECAN, CH)
Multiwell 384 platte	Lumox® (Sarstedt, Germany)
Microwave	NN-e202W (Panasonic, Japan)
pH-meter	SevenEasy (Mettler Toledo, US)
Roller mixer	Stuart Roller Mixer SRT9 (Stuart, UK)
Rotatory evaporator	RV 8 V-C (IKA, Germany)
SDS-PAGE: **Gel caster** **Power supply** **Electrophoresis unit**	 Four Gel Caster (SE275) EV 231 (Peqlab, Germany) SE260 Mighty Small II Deluxe Mini electrophoresis unit (Hoefer, US)
Sonifier ultrasonic cell disruptor	Sonifier S-250A analog ultrasonic processor 200 W (Emerson Electric Co, US)
Spectrophotometer	GeneQuant 1300 (GE Healthcare, UK) Nanodrop 2000c and NanoDrop Lite (Thermo Fisher Scientific, Germany) UVICON 933 (BIO-TEK Kontron Instruments, US)
Stirrer	VMS-A (VWR, US)

Devise	Manufacturer
	MR 3001 (Heidolph, Germany)
Syringes	Hamilton® standard microliter syringes, 50 ul, 100 µl, removable-needles (Hamilton, USA)
Thermocycler	Mastercycler gradient (Eppendorf, Germany) Mastercycler personal (Eppendorf, Germany) MyCycler Thermal CyclerTM (Bio-Rad, US) Primus 25 Advanced (Peqlab, Germany)
Vortex	REAX top, Heidolph Instruments, Schwabach (Germany)
UV-light source	CrystalLIGHT 100 (Nabitec, Germany)

1.2 X-ray sources

Table 4. The beamlines used to generate high resolution structural data. The rotation anode X-ray generator was used to test and score crystallization trials.

Beamlines	
P11	**DESY, PETRA III, DESY, Hamburg**
P13	**EMBL, PETRA III, DESY, Hamburg**
Home source, rotating anode	Rigaku RU 200 X-ray generator Wavelength: Cu Kα = 1.5418 Å Detector: MAR300 image plate, University Hamburg

1.3 Consumables

Table 5. Consumables.

Consumables	Manufacturer
Capillaries	Rectangle capillaries (VitroCom, USA)
Centrifugal filters	Vivaspin® 15, 50 MWCOs from 3 000 to 100000 (GE Healthcare Europe, Germany)
Chromatography columns	Size exclusion Superdex HiLoad 26/600 (GE Healthcare Europe, Germany) Glutathione sepharose (Thermo fisher scientific, USA) Size exclusion Sephadex® G-25 (Sigma Aldrich, Germany)
Coverslips	20 x 20 mm (Thermo Fischer scientific, USA)

Dialysis cassettes	Slide-A-Lyzer G2 Dialysis Cassettes (Thermo Fisher Scientific, USA)
Falcons	Sterile 15 ml/50 ml (Sarstedt, Germany)
Linbro plates	24 well plates (Jena Bioscience, Germany)
Reaction tubes	0.2 ml (Biozym Scientific, Germany) 0.5, 1.5, 2 ml (Eppendorf, Germany)
Parafilm M	Bemis®, Pechiney Plastic Packaging, Neenah (USA)
Pipette tips	Sterile Biosphere filter tips and non-sterile 10, 200, 1000 µl (Sarstedt, Germany)
Syringes	Sterile 5, 10, 20 ml, (Braun, Germany)
Syringe filters	Millex® Syringe Filters 0,22 µm (Merck Millipore, Germany)

1.4 Kits and Reagents

Table 6. Kits und Reagents

Kit, Reagent	Manufacturer
Gel Filtration Molecular Weight Markers, standard kit	Sigma-Aldrich (USA)
Alexa Fluor™ 488 Protein Labeling Kit	Thermo fisher scientific (USA)
Alexa Fluor™ 488 TFP ester	Thermo fisher scientific (USA)

1.5 Buffers and Solutions

The solutions were autoclaved at 121 ° C and 1.4 bar. Buffers were either also autoclaved or sterile filtered on heat-sensitive ingredients using 0.22 µm filter units.

1.5.1 Growth mediums

Table 7. Growth mediums

Medium	Content, Manufacturer
LB-medium (Luria/Miller)	10 g/l Tryptone 5 g/l Yeast extract

	10 g/l Sodium chloride pH 7,0 (Carl Roth Germany)
LB-Agar (Luria/Miller)	10 g/l Tryptone 5 g/l Yeast extract 10 g/l Sodium chloride 15 g/l Agar pH 7,0 (Carl Roth, Germany)

Table 8. Antibiotics und additives

Antibiotics, additives	Concentration
Ampicillin	100 mg/ml
Isopropyl-β-D-thiogalactopyranosid (IPTG)	1 M

1.5.2 Protein purification

Table 9. Protein purification

Buffer	Content
GSH affinity chromatography lysis buffer	1 x PBS
GSH affinity chromatography wash buffer	1 x PBS
GSH affinity chromatography elution buffer A	1 x PBS, 20 mM L-Glutathione, pH 7.4
GSH affinity chromatography elution buffer B	0.1 M $NaHPO_4$, 20 mM S-(p-Bromobenzyl) GSH, pH 6.7
Matrix regeneration buffer	6 M guanidine chloride, 0.1 M acetic acid
Size exclusion chromatography buffer	1 x PBS

Table 10. Chemicals und additives

Chemicals, additives	Manufacturer
4-Bromobenzyl bromide	Sigma Aldrich (Deisenhoven)
Dimethyl sulfoxide (DMSO)	Merck (Germany
Ethanol	Merck (Germany)
L-glutathione	Merck (Germany)

1.5.3 Electrophoresis

Table 11. Electrophoresis

Buffer	Content
Coomassie-staining solution	0,1 % (w/v) Coomassie Brilliant Blue R-250 40 % (v/v) Methanol 10 % (v/v) acetic acid
Coomassie-destaining solution	40 % (v/v) Methanol 10 % (v/v) acetic acid
Resolving Buffer (SDS-PAGE)	1.5 M Tris Base 0.004 % (w/v) SDS pH 8,8
SDS-PAGE loading buffer	250 mM Tris/HCl pH 6,8 20 % (w/v) Glycerol 8 % (w/v) SDS 4 mg Bromphenolblau (4% (v/v) β-Mercaptoethanol)
SDS-PAGE separating buffer (10x)	0.025 M Tris Base 0.192 M Glycin 0.1 % (w/v) SDS
Stacking Puffer (SDS-PAGE)	0,5M Tris Base 0,004% (w/v) SDS pH 6,8

1.5.4 SDS-Polyacrylamide gels

Table 12. SDS-Polyacrylamide gels

Buffer content	Stacking gel	Resolving gel 7,5% 10% 12,5%
ddH2O	3,1 ml	4,86 ml 4,18 ml 3,2 ml
Stacking buffer	1,25 ml	--
Resolving buffer	--	2,5 ml 2,5 ml 2,5 ml
30 % Acrylamid	0,65 ml	2,5 ml 3,34 ml 4,16 ml
10 % APS	50 µl	50 µl 50 µl 50 µl
TEMED	5 µl	10 µl 10 µl 10 µl

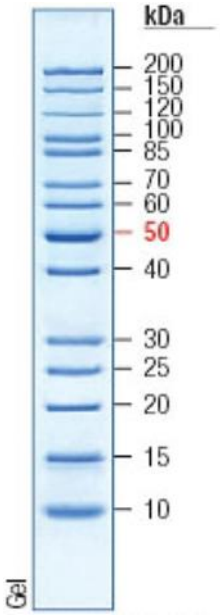

Figure 4. Page Ruler Protein ladder.
The Page Ruler Protein Ladder (Fermentas, S.T. Leon Red) was used for the protein analysis by SDS-PAGE.

1.6 Bacterial strains

Escherichia coli

Table 12. *E. coli* strain

Strain	Genotype	Manufacturer
BL21 (DE3)	F´dcm ompT hsdSB(rB-mB-)gal, l(DE3	Stratagene

1.7 Plasmids

1.7.1 Protein expression

Table 13. Plasmids for Protein expression

Plasmid	Characteristic	Reference
pJC20	Vector for prokaryotic expression of proteins	Clos and Brandau, 1994

1.8 Crystallization

Table 14. Crystallization solutions. Protein, precipitant and cryoprotectant buffers.

Buffers	Content
Protein	0.1 M $NaHPO_4$, pH 6.7
Precipitant/ reservoir (vapor diffusion technique)	0.1 M NaHPO4, 2.1 M AmSO4, pH 6.7
Precipitant (counter diffusion technique)	0.1 M $NaHPO_4$, 2.8 M $AmSO_4$, 15% glycerol, pH 6.7
Cryoprotectant (vapor diffusion technique)	0.1 M $NaPO_4$, 1.9 M $AmSO_4$, 10 mM S-(p-Bromobenzyl) GSH, 14% glycerol, pH 6.7
Cryoprotectant (Counter diffusion technique)	0.1 M $NaPO_4$, 1.9 M $AmSO_4$, 10 mM S-(p-Bromobenzyl) GSH, 14% glycerol, pH 6.7

1.9 Computational and statistical data analysis

Table 15. Software

Software	Manufacturer/ reference
Adobe Photoshop CS3	Adobe Systems GmbH (Germany)
Blast	(Altschul et al., 1997)
CCP4	(Winn et al. 2011)
Coot	(Emsley et al., 2004)
ImageJ	Developed at the National Institute of Mental Health, Maryland, USA)
iMOSFLM	(Battye et al. 2011; Leslie 2006)
IrfanView	An image viewer, editor, organizer and converter program, developed by Irfan Škiljan, initial release in 1996
MOLREP	(Vagin et al., 1997)
Office software	Microsoft, Redmond, (USA)
Origin	OriginLab Corporation, (USA)
Protein Data Bank (PDB)	(Berman et al., 2000)
ProtParam	(Gasteiger et al., 2005)
pymol	Schrödinger, Portland (USA)
Refmac5	(Murshudov et al., 2011)
UCSF Chimera	Resource for Biocomputing, Visualization, and Informatics at the University of California, San Francisco, (USA)
X-ray Detector Software (XDS)	(Kabsch, 2010)

2 Methods

2.1 Molecular biology and microbiological methods

2.1.1 Preparation of chemically competent cells

A glycerol stock (50 µl) was used to inoculate 100 ml Luria Bertani (LB)-medium and incubated at 37 °C overnight. The overnight culture was diluted to 1:50 while adding 5 ml of overnight culture to a 250 ml LB (Luria Bertani, Lennox) media supplemented with the *E. coli* specific selection antibiotics. The cells were grown at 37°C until an OD600 of 0.5 – 0.8 was reached and subsequently incubated for 10 min on ice. The solution was centrifuged at 1000 x g, 4 °C for 15 min. The supernatant was discarded and the pellet was resuspended in 10 mL 0.1 M $CaCl_2$-buffer and immediately incubated on ice for 30 min. The cell suspension was centrifuged again at 1000 x g, 4 °C for 15 min. The supernatant was discarded and the cells were resuspended in 5 ml cold 0.1 M CaCl2 buffer supplemented with 10 % (v/v) glycerol. The cell solution was distributed into 100 µL aliquots, flash-frozen in liquid nitrogen and stored at -80 °C.

2.1.2 Transformation of plasmids into *E.coli* cells

A modified method for the transformation of *E. coli* by treatment with $CaCl_2$ (Hanahan & Harbor 1983) was used. A 100 µl aliquot of chemically competent cells was slowly thawed on ice, mixed with 1-100 ng of DNA (The expression system for the *Pf*GST (Liebau et al., 2002) was kindly provided by Dr. Perbandt) and placed on ice for a further 10 min. This was followed by a heat shock (90 sec, 42 ° C) for the uptake of DNA into the cells. The cells were then transferred on ice and pipetted into 900 µl of sterile LB medium in a glass tube. Phenotypic expression of resistance was achieved by shaking the culture for 90 min at 37 ° C. After phenotypic expression, 100 µl of the suspension or appropriate dilutions were plated on selective agar plates containing corresponding antibiotics and incubated overnight at 37 ° C.

2.1.3 *E. coli* glycerol stock preparation

A Single colony of overnight culture was picked and inoculated in 100 ml LB medium and incubated/shacked at 37 °C overnight. Transformed single clones were grown to high log-phase and preserved by the addition of 30 % (v/v) glycerol to the culture (500 µl aliquots) and stored at -80 °C.

2.2 Biochemical and biophysical methods

2.2.1 Recombinant protein expression

*Pf*GST from *Plasmodium falciparum* was expressed and purified as previously reported (Liebau et al., 2002; Perbandt et al., 2015) with few modifications. The recombinant *Pf*GST was expressed in *E. coli* BL21 cells transformed with pJC20 plasmid. First, an overnight culture was applied. A single colony or 10 µl of a glycerol stock was used to inoculate a 50 ml of LB medium containing a 100 µg/ml ampicillin and incubated at 37 °C and shacked at 190 rpm overnight. For the protein expression a 1 l LB medium containing 100µg/ml ampicillin was inoculated with 1:40 overnight culture and incubated shaking at 37 °C until an optical density at 600 nm (OD600) of 0.5-0.7 reached. The protein expression was induced with 0.5-1mM IPTG and incubated at 19 ° C shaking (190 rpm) overnight. The cells were harvested by centrifugation at 17.000xg at 4 °C for 30 min, resuspended in 1xPBS buffer pH 7.4 (lysis buffer) and stored at -20 °C.

2.2.2 Synthesis of S-(p-Bromobenzyl) GSH

To stabilize the *Pf*GST dimer in solution a GSH analog the S-(p-Bromobenzyl) GSH was synthesized. S-p-bromobenzyl glutathione is a GST inhibitor and was synthesized while applying a modified method of Vince et al. (1971). The 4-Bromobenzyl bromide (12 mM) was dissolved in 500 mL of 50 % ethanol aqueous solution in a single neck round-bottom flask. Then L-glutathione (12 mM) was added into the solution with vigorous stirring. After 4-Bromobenzyl bromide and L-glutathione were completely dissolved, sodium hydroxide (5 M NaOH) was added dropwise into the mixture and the pH 9.2 was maintained stirred at RT for 3 h. Then, hydrochloric acid (10 M HCI) was slowly added into the mixture until reach the pH 2.1. The reaction was stopped. The obtained solution was removed to a 1 L round flack and the excess solvent was removed under rotary evaporator at RT 175 mbar to get white solid product (the experiment was performed at the institute of organic chemistry, University Hamburg). The white solid product was dissolved in a $NaHPO_4$ buffer. Then, 1 M NaOH was added dropwise into the solution adjusted to pH 6.7. Then, the final solution with pH 6.7 was sterile filtered. Aliquots were prepared and stored at -20 °C.

2.2.3 Mass spectrometry (MS)

The synthesized product ((S-(p-Bromobenzyl) GSH)) was analyzed by mass spectrometry, ESI-TOF. Mass spectrometry data collection and analysis was performed at the institute of organic chemistry, University Hamburg. The solution of S-(p-Bromobenzyl) GSH was diluted to 1mg/ml final concentration and was analyzed by electrospray ionization (ESI) -time-of-flight (TOF) MS (Agilent 6224 ESI-TOF) methods.

2.2.4 Protein purification

2.2.4.1 Immobilized metal affinity chromatography

A cell suspension (30 ml) was slowly thawed on ice. A spatula tip of lysozyme powder was added and the suspension incubated on ice for 5 min. Cell disruption was carried out by five times sonication for 4 min pulsed at 40 kHz on ice with 1.5 min pauses and cell debris was removed by centrifugation at 17.000x *g* at 4 ℃ for 1h. Aliquots of cell debris and supernatant were collected for further analysis on SDS-PAGE. The recombinant *Pf*GST was purified applying gravity flow glutathione affinity chromatography. The glutathione sepharose slurry was added to the column and the matrix was washed 5 times with lysis buffer. The clarified bacterial sonicate was applied to the preequilibrated glutathione sepharose column. The column was closed with a cap and incubated rotating at 10 ° C for 1h. After 1h the column was washed 3-5 times with washing buffer. The flow throughs were collected for further analysis by SDS-PAGE. Subsequently the bound protein was eluted with 20 mM GSH or S-(p-Bromobenzyl) GSH containing elution buffer. The protein eluates were stored at 4 °C.

2.2.4.2 GSH matrix regeneration

To remove precipitated or denatured substances, the matrix was washed with 2 bed volumes of 6 M guanidine hydrochloride, immediately followed by a wash with 5 bed volumes of 1 x PBS. To remove hydrophobically bund substances, the matrix was washed with 3 - 4 bed volumes of 70 % ethanol, immediately followed by a wash with 5 bed volumes of 1 x PBS. After finishing washing steps the column /matrix was stored in 20 % ethanol at 4 ℃. Before re using the column, the ethanol was removed and the matrix was equilibrated with 1 X PBS.

2.2.4.3 Size exclusion chromatography

Size exclusion chromatography (SEC) or gel filtration separates molecules by differences in size as they pass through a SEC resin packed in a column. Gel filtration resins consist of a porous matrix of spherical particles that lack reactivity and adsorptive properties. After sample has been applied, molecules larger than the pores are unable to diffuse into the beads, so they elute first and consequently the small molecules elute last. The *Pf*GST tetramer was separated by size exclusion chromatography on a Superdex HiLoad 26/600 column (GE-Healthcare). The SEC experiments are performed at 16 °C at the DEYS lab. Before sample running the column was equilibrated with 1 x PBS buffer. For evaluation, absorbance at A_{280}, A_{230} and conductivity were monitored. The standard curve was calculated from the fit of the elution volumes of the size marker proteins (GE Healthcare, calibration kit): Blue Dextran 2000, Ferritin (440 kDa), Aldolase (158 kDa), Ovalbumin (44 kDa), Ribonuclease A (13.7 kDa) and Aprotinin (6.7 kDa). Calculations for molecular weights from retention volume for proteins were done by applying standard calibration curve. The peak fractions that showed a high A_{280} absorption were collected and analyzed by SDS PAGE for purity.

2.2.4.4 Lysozyme preparation

Monomeric hen egg lysozyme (HEWL) was obtained by subjecting commercially obtained protein (Biomedicals LLC) to size exclusion chromatography (Yarra-2000 column). To produce stable aggregates the purified monomeric protein is subjected to crosslinking by using glutaraldehyde as the crosslinking agent. The fused protein was then reapplied to the size exclusion column to separate dimeric lysozyme from remaining monomeric protein (the data was provided from Dr. DeLucas, Aerospace Corporation).

2.2.5 Sodium dodecyl sulfate–polyacrylamide gel electrophoresis (SDS-PAGE)

SDS-PAGE is a fast, high-resolution method for separating protein mixtures according to their molecular weights (Laemmli, 1970). Most proteins bind the anionic surfactant SDS to negatively charged SDS-protein complexes with a constant charge-to-mass ratio (1.4 g SDS / g protein in 1% SDS solution). SDS denatures the proteins - especially after reduction with mercaptoethanol and prevents protein-protein interactions. The gel acts as a molecular sieve, which the proteins can pass at different speeds due to different sizes. Therefore, it leads to separation of proteins. To analyze protein samples SDS-PAGE gels containing 4 % polyacrylamide in stacking gel and 12 % polyacrylamide in separating gel (components listed in Table 12) were prepared. Before being applied to the gel the protein samples were mixed with SDS-PAGE 3 x loading buffer (Table 11) and denatured at 96 ° C for 10 min. The gel was placed in a gel chamber (Hoefer Inc, USA) and connected to an EV 231 power supply (Peqlab, Germany) to adjust the electric field. The denatured protein samples were inoculated into gel chambers. The applied voltage was 100 V during the run-in phase in the stacking gel and 180-200 V during the separation phase. Standard molecular weight (MW) marker (Figure 4) were used for size assessment. The gel was stained for 1 h in Coomassie staining solution and subsequently destained in destaining solution until an acceptable contrast was visualized. The gels were documented by scanning the gel using a Epson scanner.

2.2.6 Quantification of proteins

The determination of the protein concentration is based on the absorption maximum of the aromatic amino acids (phenylalanine, tryptophan and tyrosine) at 280 nm. The specific physicochemical parameters of protein sequences (Table 16) were obtained from ProtParam (Gasteiger et al., 2005). Protein concentrations were determined by measuring specific absorbance at a wavelength of A_{280}, according to the law of Lambert-Beer-equation:

$$E = \varepsilon_\lambda * c * d$$

E = measured absorbance

ε_λ = molar extinction coefficient

c = concentration of protein sample

d = layer thickness of the irradiated body

Table 16. Physicochemical parameters of proteins.

Protein	ε_{280} [M^{-1} cm^{-1}]	MW [kDa]	Theorectical pI
***Pf*GST dimer**	55700	49	6.39
***Pf*GST tetramer**	111900	97	6.40

The protein concentration was determined applying a Nanodrop 2000c instrument (Thermo Scientific, peqLab, Germany). For the measurements 1.5 µl of protein sample were applied to the sensor, elution buffer was used as blank.

2.2.7 Dynamic light scattering (DLS)

2.2.7.1 Dispersity analysis of the protein multimeric states

Dynamic light scattering is a method that can be used to determine the distribution, the hydrodynamic radius (R_H) and size of a particle in solution.

The hydrodynamic radius of the particles is calculated using the Stokes-Einstein equation

$$R_H = K_B T / 6\pi\eta D_T$$

R_H = hydrodynamic radius
K_B = Boltzmann‘s constant
T = absolute temperature
D_T = diffusion coefficient
η = viscosity

The dispersity and particle radius distribution of *Pf*GST dimer (30 mg mL−1) and tetramer (10 mg mL−1) were determined and analyzed at room temperature by Dynamic light scattering (DLS) applying the DLS system SPECTROLIGHT™ 300 (Xtal Concepts GmbH, Hamburg, Germany). Before each measurement, samples were centrifuged at 16.000x *g* for 10-30 min to remove aggregates with higher molecular weight. For time resolved measurements 10-20 µl protein sample was applied in a quartz cuvette and the sample was irradiated by a red light class 3b laser (λ = 690 nm; laser power 10-50 mW) to detect isotropic scattering at an angle of 90 degree.

2.2.7.2 Multichannel DLS system

A multichannel DLS system was developed to investigate the macromolecular crystallization process (Figure 5). It is specifically qualified to collect information about the size, shape, and dynamics of biological macromolecules and supramolecular assemblies. Structural analysis of individual biomolecules, conformational transitions, intermolecular interactions and mass transport phenomena in protein crystallization process can also be probed. The major application of the multichannel DLS

system, in comparison to other DLS systems, is the rapid determination of the translational diffusion constant in a shortened period and simultaneously at several positions in capillaries. To study macromolecular protein transport in crystallization process applying the counter diffusion method protein and precipitant solutions were filled in capillaries (VitroCom) with100mm in length, 0.3 mm inner diameter, and measurements were performed using this multichannel DLS system.

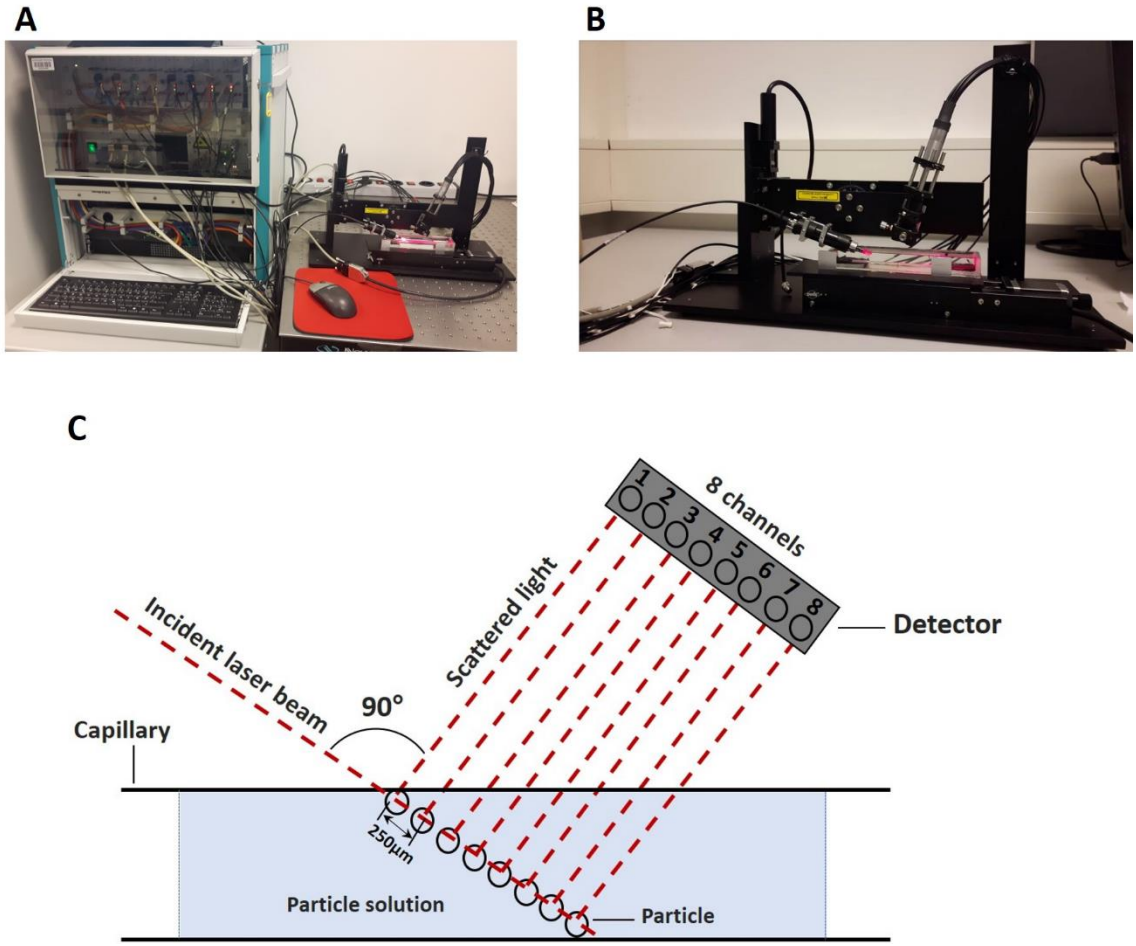

Figure 5. Multichannel DLS system. (A) Control cabinet and laser-detector hardware of the 8-channel DLS system. (B) Laser-detector optic with sample holder stage and water bath container. (C) Technical-functional description of eight-channel principle.

2.2.8 Protein aggregates acting as impurities in solution

2.2.8.1 Freeze drying of fluorescence dye

Freeze drying or lyophilization is the process of extraction of water from frozen material. The drying process takes place by avoiding the liquid state through sublimation, or direct conversion from ice to vapour. A water-soluble product which will have the same characteristics as the original product can be obtained after addition of water to the freeze-dried product. Since the drying process takes place in

a frozen state at very low temperature, denaturation of proteins is prevented. Other chemical components will be qualitatively and quantitatively unchanged.

The Alexa Fluor® 488 TFP ester, (C39H44F4N4O11S2, MW = 884.9 Da) was obtained from Thermo Fisher Scientific (life technologies). The experiments were performed in a light protected area to avoid the degradation of the light sensitive Alexa Fluor dye. The dye powder with 25 mg total mass was dissolved in 2.5 ml ddH_2O. Then, 160 µl aliquots in special light protected tubes were prepared and shock frozen in liquid nitrogen. The frozen samples were removed from the liquid nitrogen; small holes were made on the samples bags to facilitate liquid evaporation during freeze drying. Freeze drying of the Alexa Fluor 488 samples was performed in Alpha 1-4 LSC (Christ) freeze drier. The samples were immediately loaded into the freezing unit shelves and the drying chamber was closed. The drain valve was closed, the apparatus was switched on, the pump was warmed, the coil was frozen and main drying initiated. After 24 h the dried samples were removed from the chamber, put in a light protected plastic bag, and stored at -20 °C.

2.2.8.2 Fluorescently labeling of protein aggregates

To investigate the amount of impurity incorporated into growing crystals, stable fluorescently-labeled protein aggregates were prepared, and subsequently added at different percent concentrations to non-labelled monomeric protein suspensions. The *Pf*GST tetramer and lysozyme dimer, acting as impurities in the crystallization experiments, were labeled with ~~a~~ the fluorescent dyes Alexa Fluor® 488 TFP ester and Alexa Fluor® 594, respectively. The Alexa Fluor® 488 TFP ester, (C39H44F4N4O11S2, MW = 884.9 Da) and Alexa Fluor® 594 NHS Ester (C39H37N3O13S2, MW = 819.8 Da) were obtained from Thermo Fisher Scientific (life technologies). The Alexa Fluor® 488 (5mg) was dissolved in 0.5 mL of Dimethyl sulfoxide (DMSO). The reactive dye solution (80µl) was slowly added to the stirring *Pf*GST tetramer solution (10mg/ml in PBS). The reaction was incubated for 1 hour at room temperature with continuous stirring. The labeled tetramer was separated from free dye using a Sephadex® G-25 pre-packed gel filtration column. The column was first equilibrated with PBS buffer and then loaded with a reaction mixture and eluted with PBS buffer solution. Labeling degree (DOL) of tetramer was calculated due to following calculations:

Equation (1)

$$\text{Protein concentration (M)} = \frac{[A280-(CF \times A494)] \times dilution\ factor}{\varepsilon\ (protein)}$$

Equation (2)

$$\text{DOL = (moles dye)/ (mole protein)} = \frac{A494 \times dilution\ factor}{\varepsilon\ (dye) \times protein\ concentration\ (M)}$$

The protein-dye conjugate was concentrated to 10mg/ml final concentration using Millipore Amicon® ultra-centrifugal concentrators (Merckmillipore) and stored at 4 °C. For lysozyme aggregate labeling a

solution of buffered lysozyme dimer at 2mg/mL was mixed with Alexa Fluor® 594 at 22°C and incubated for one hour. Unbound dye was removed via spin concentration (500uL 30MW cutoff spin concentrator).

2.3 Crystallography

2.3.1 Protein crystallization

2.3.1.1 Vapor diffusion technique

Initial crystallization experiments were performed in 24-well Linbro plates applying the vapour diffusion technique in hanging drops, while mixing 2µl droplets of 15 mg ml^{-1} protein (*Pf*GST dimer) in a 0.1 M $NaHPO_4$, pH 6.7 solution with the same volume of precipitant, 2.1 M $AmSO_4$, 0.1M $NaHPO_4$, pH 6.7 on a cover slip and equilibrated against 1000 µl reservoir, 2.1 M $AmSO_4$, 0.1M $NaHPO_4$, pH 6.7, solution. Initial crystallization screens of *Pf*GST dimer (15 mg ml^{-1}) as well *Pf*GST dimer additionally with different percentage of fluorescence (Alexa Fluor 488) labeled *Pf*GST aggregates (10 mg ml^{-1}) were performed.

2.3.1.2 Counter diffusion technique

Initial crystallization experiments were performed using the counter/liquid-liquid diffusion technique in capillaries of 100mm in length, 3mm in width and 0.3mm inner diameter (VitroCom). Capillaries were filled with 37µl of precipitant solution, 2.8 M $AmSO_4$, 0.1M $NaHPO_4$, 15% glycerol, pH 6.7 and 37µl of protein solution, 0.1 M $NaHPO_4$, pH 6.7 (doped with different percentages of fluorescently-labelled *Pf*GST aggregate) using syringes (Hamilton). Initial crystallization screens of *Pf*GST dimer (30 mg ml^{-1}) as well *Pf*GST dimer additionally with different percentage of fluorescence (Alexa Fluor 488) labeled *Pf*GST aggregates (10 mg ml^{-1}) were performed.

2.3.2 Crystal fishing

2.3.2.1 Vapor diffusion

Crystals were grown on coverslips applying 24 well Linbro plates. Crystals were first monitored using a light microscope. Then, for diffraction data collection the appropriate crystals were fished using polymer loops (Dual-Thickness MicroMounts, Mitegen, US) or nylon loops (Mounted CryoLoop, Hampton Research, US). A cryoprotectant solution (0.1 M NaHPO4, 1.9 M AmSO4, 10 mM S-(p-Bromobenzyl) GSH, 14 % glycerol, pH 6.7) was prepared. For cryoprotection crystals were embedded in cryoprotectant solution, frozen and stored in liquid nitrogen for further X-ray experiments.

2.3.2.2 Counter diffusion

Before crystal fishing glass bowls with 500 µl protein/precipitant crystallization buffer (0.1 M $NaHPO_4$, 1.9 M $AmSO_4$, 10 mM S-(p-Bromobenzyl) GSH, 7.5 % glycerol, pH 6.7) were prepared. First, to detect the areas with crystals, the capillaries were monitored using a light microscope. The areas with crystals were marked and the capillaries were cut applying a special capillary cutting stone (Hampton research). Then, the crystals were fished/pull out from capillaries and put into glass bowls containing mother

liquor, using a plastic 15 ml syringe with a rubber tube that attaches to the syringe with the other end fit snugly over the capillary. The glass bowls were monitored for crystals using light microscope. After crystals were visualized the glass bowls were hermetically sealed (to avoid evaporation) applying cover slips and stored at RT.

2.3.3 Microscopy, crystal visualizing

2.3.3.1 Light microscope imaging

Light microscope images of crystals were recorded using the stereo SZX12 (Olympus) and Leica M205 C (Leica Mikrosystems) light microscopes. Time - laps images of growing crystals were recorded using Leica M205 C (Leica Mikrosystems) light microscope. The crystallization samples were scanned with a 2.5 x, 5 x and 10 x magnification lenses.

2.3.3.2 Confocal fluorescence imaging experiments

To investigate the incorporation of impurities into growing crystals for each protein confocal fluorescence imaging experiments were performed. Crystal fluorescence images of both protein were recorded on ISS using the LMM microscope 2.5 x and 10 x objectives. Fluorescence imaging experiments on ground were performed using the Zeiss LSM 710 (Carl Zeiss Microscopy) and Leica TCS SP – 8 (Leica Microsystems) confocal laser scanning microscopes. The capillaries were scanned with a 2.5 x and 10 x magnification lenses. To investigate the fluorescence of *Pf*GST crystals a FITC (Excitation 475~495 nm; Emission 515~545 nm) filter was used and for lysozyme crystals a Texas Red (Excitation 540~580 nm; Emission 590~630 nm) filter was used.

2.4 Biophysics 1 and Biophysics 4

2.4.1 Capillary protein/precipitant filling and sealing procedure for crystallization

Crystallization experiments were performed using the counter/liquid-liquid diffusion technique in capillaries of 100mm in length, 3mm in width and 0.3mm inner diameter (VitroCom) (Figure 6). Capillaries were filled with 37µl of precipitant and 37µl of protein solution (doped with different percentages of fluorescently labelled protein aggregate, using syringes (Hamilton). Lysozyme was prepared in 0.1 M NaOAc pH 4.6 solution with the precipitant solution consisting of 1M NaCl, 0.1M NaOAc pH 4.6. A sample of *Pf*GST dimer and tetramer was prepared in 0.1 M NaHPO4, pH 6.7 solution. The precipitant solution for *Pf*GST consisted of 2.8 M AmSO4, 0.1M NaHPO4, 15% glycerol, pH 6.7. The length and width of all flight and ground control capillaries were measured to confirm that they were within stated limits. Capillaries were visually examined before filling to ensure that there are no visual defects, e.g. cracks, jagged ends etc. One capillary end was filled with Apiezon N cryogrease (Apiezon) using a plastic 25mL syringe with a rubber or silicon tube that attaches to the syringe with the other end fit snugly over the capillary. Grease was extruded approximately 3 to 5 mm into the capillary end. All protein and precipitant solutions were degassed using “house” vacuum prior to use for the flight and ground control experiments. The capillary was filled with protein using a glass syringe

(Hamilton) with a needle small enough to fit within the width of the capillary (i.e. less than 0.3mm width). This was followed by layering the precipitant solution against the protein solution and filling the capillary to approximately 3 mm from the other end of the capillary. After completely filling the capillary with protein and precipitant solution, the opposing end was filled with Apiezon N grease using a plastic 25mL syringe with the same rubber/silicone tube as described previously. Five-minute drying Double Bubble epoxy (Hardman) was prepared and each end of the capillary was dipped into the epoxy to a depth of approximately 2-3 mm and the capillary was inspected to determine and confirm that the ends were completely sealed. The sealed capillary was then placed on a clay mount to dry for at least 5 minutes. The sealed capillary was inspected again using a dissecting microscope (at approximately 15X to 25X magnification). The sealed capillaries were placed into a specially constructed cassette (ZIN Technologies) that allows capillaries lie flat in cassette channels. After eight capillaries were positioned in the cassette, the top clamp (with the six washers previously placed in the screw holes) was carefully aligned and screws fastened using a hex wrench. To insure the capillaries were not damaged, the cassette top (clamp) was removed and the capillaries are visually inspected for possible cracks. If the capillaries were not damaged, the cassette top with the six washers (previously placed in the screw holes) was carefully aligned and re-fastened using a hex wrench. The capillary cassette was placed into a bitran bag and then bubble bag followed by immediate placement of the "bagged" cassette into a walk-in -20 °C +/- 2.0 °C freezer overnight. The capillaries were re-inspected for cracks after the overnight freezing process. Following the "slow freezing" of the "bagged" cassettes in the -20 °C freezer the bags were immediately placed into a -80 °C +/-20 °C freezer and maintained in a frozen state until on-orbit activation and observation in the LMM. In addition, the corresponding control 1G capillaries were stored at -80 °C until activation on ground.

2.4.2 On-orbit experiments

Three series of experiments were performed on ISS, one during 26.02.2017 till 18 10.03.2017, second during 16.06.2017 till 02.07 23.06.2017 (Biophysics 1) and a third during 12.07.2018 till 24.07.2018 (Biophysics 4). The cassettes (figure 6) were launched aboard SpaceX (Spx10 - Biophysics 1 and Spx15 - Biophysics 4) in cold stowage at -80 °C. Upon reaching the ISS, the cassettes were transferred to ISS cold stowage (-80 °C) while awaiting science operations.

The Light Microscopy Module (LMM) is a modified commercial Leica RXA microscope configured to operate in an automated module with interaction from the ground support staff. The microscope can house different lenses corresponding to the magnifications of 2.5 x, 4 x, 10 x, 20 x, 40 x, 50 x, 63 x and 100 x oil coupled objectives (grc.nasa.gov). The microscope includes capabilities for video and confocal microscopy. The LMM operates in the Fluids Integrated Rack (FIR), which is located in the U.S. Destiny Laboratory of the ISS. The FIR provides the LMM with the laboratory infrastructure common to different investigations, including an optics bench, temperature control, power control, illumination, imaging and trame capture, data processing and other resources (grc.nasa.gov).

The cassettes were removed from cold stowage, thawed, and installed onto the LMM Petri Plate using Velcro. The LMM Petri Plate was installed in the LMM Base Adapter and the LMM prepared for powered science operations. The initial protein crystallization experiments, LMM Biophysics-1, were performed using the ISS LMM at a temperature 20-23 °C. Powered operations began as soon as practical after installation was completed with initiation of the crystal search phase occurring within 4 hours of cassette installation. Crystals growth was monitored for several days. Crystal images were recorded with 2.5 x, 10 x objectives. To investigate crystal growth rate and the fluorescence of crystals, Texas Red and FITC fluorescence filters were used.

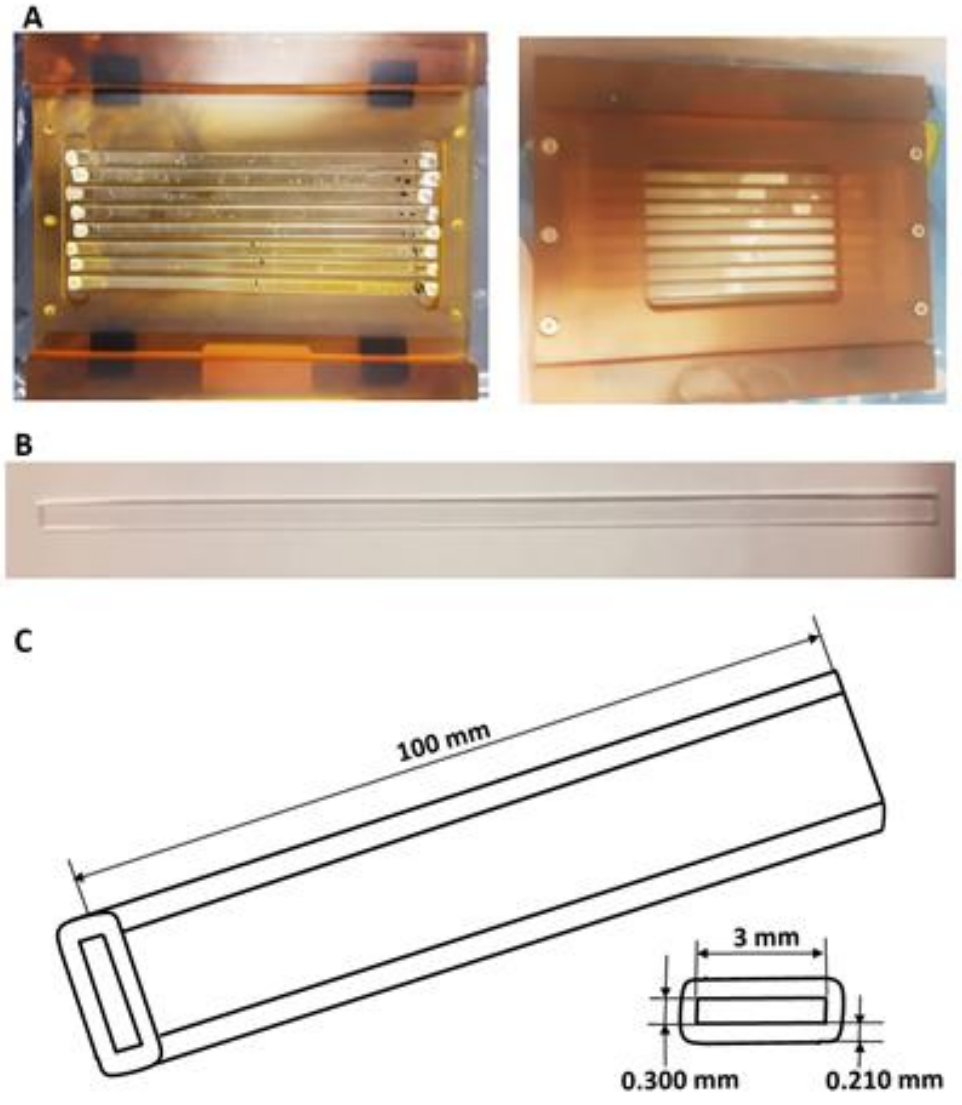

Figure 6. Hardware and capillary design for LMM Biophysics-1 protein crystallization experiments. (A) Representative images of flight cassette with eight capillaries. The left image shows a cassette with eight capillaries. The image on the right shows a cassette with aligned and fastened top cover. (B) An empty capillary. (C) Schematic diagram illustrating the capillary shape and coordinates.

2.5 X-ray Diffraction data collection

For cryo-protection crystals were embedded in cryoprotectant solution (0.1 M NaHPO4, 1.9 M AmSO4, 10 mM S-(p-Bromobenzyl) GSH, 14 % glycerol, pH 6.7). Furthermore, the crystal were mounted for diffraction data collection using polymer loops (Dual-Thickness MicroMounts, Mitegen, US) or nylon loops (Mounted CryoLoop, Hampton Research, US). Diffraction data of *Pf*GST crystals were collected using a detector PILATUS 6M (25 Hz, 450 micron sensor thickness) at the P11 beamline (PETRA III, DESY) using a wavelength of 1 Å at 100 K, at the P13 beamline (PETRA III, EMBL), using the wavelengths of 0.99 Å and 1.03 Å at 100 K and using the rotating anode generator (Rigaku RU 200 X-ray generator, University of Hamburg) using a wavelength of 1.54 Å at 100 K.

2.5.1 Diffraction data processing and model building

Diffraction data were subsequently indexed, integrated and scaled with XDS (Kabsch, 2010) and CCP4 (Winn et al., 2011) graphic programs. Datasets for crystals grown in 1G and µg were analyzed. Data were cut individual for each crystal dataset monitoring Rmeas, Rsym, I/σ and CC1/2. Optimized values of correct space group, unit cell parameters were included in further XDS runs. Molecular replacement was performed with MOLREP (Vagin and Teplyakov, 1997) implemented in the CCP4 software suite. Models were revised using Coot (Emsley and Kowtan, 2004) and refined by refmac5 (Murshudov et al., 2011).

2.6 Quantitative analysis of impurity incorporation

2.6.1 Fluorescence microplate reader

For the purpose to investigate incorporation of fluorescently labeled tetramers into growing dimer crystal quantitative analyses of total fluorescence/crystal volume were performed applying a fluorescence microplate reader. The crystals were fished and monitored for size using a light microscope. Crystals dimensions were measured and the volume calculated. Then, the crystals were 2 x washed in native buffer and dissolved in 20 µl PBS buffer for fluorescence intensity measurements. Furthermore, the solutions containing dissolved crystals were collected in light protected plastic tubes. In the next step the solutions and negative control (PBS buffer) were loaded into a Lumox® 384 - well microplate (Sarstedt, Germany). The fluorescence intensities were measured applying a microplate reader (TECAN GENios XFLUOR4, CH), using a 485 nm excitation filter and a 535 nm emission filter. Average fluorescence intensities pro μm^3 crystal were calculated.

2.7 Statistical analysis and quantification of protein and precipitant concentrations

The image-analysis software ImageJ (developed at the National Institute of Mental Health, Maryland, USA) was then used to determine the size of crystals at different positions in the capillaries. The statistical analyses were performed using Origin (OriginLab Corporation) data analysis and graphing software tools as well Microsoft Excel statistical tools (Microsoft office 365 ProPlus, Microsoft

Corporation). A two-tailed, unpaired t-test (Student's t-test) was used to determine significant difference in mean values between different crystal groups within 99% and 95% confidence intervals. The Pearson correlation was used to evaluate the relationship between data quality parameters.

To quantify the time dependent protein and precipitant concentrations changes along the capillary the following equations (derived from Fick's second law of diffusion and integrated from Crank, 1975; Garcia-Ruiz, 2003) were used:

Equation (1) (Fick's second law)

$$\frac{\partial c}{\partial t} = D\frac{\partial^2 c}{\partial x^2}$$

Equation (2)

$$c_{ppt}(x;t) = \frac{1}{2}c0(ppt)erfc\left(\frac{x}{\sqrt{2Dt}}\right)$$

Equation (3)

$$c_p(x;t) = \frac{1}{2}c0(p)erfc\left(\frac{-x}{\sqrt{2Dt}}\right)$$

∂ = Partial derivative

c = Concentration (nmol)

c0 = Start concentration

c_{ppt} = Precipitant concentration (M)

c_p = Protein concentration (nmol)

D = Diffusion coefficient ($cm^2\ s^{-1}$)

x = Distance (cm)

t = Time (s)

erfc = Complementary error function

Requirements for the equations (2) and (3): Convection must be moved

IV Results

1 Recombinant protein expression and purification

*Pf*GST was recombinantly expressed in *E. coli* BL 21 cells and purified using GSH affinity chromatography as described in chapter III.2.2. The protein fractions were eluted using a buffer solution with 20mM GSH and additionally using a buffer solution with 20mM Br-Benzyl GSH. SDS PAGE of the protein elution fractions revealed the *Pf*GST monomer single protein bands with indicated molecular weight of 25 kDa (Figure 7).

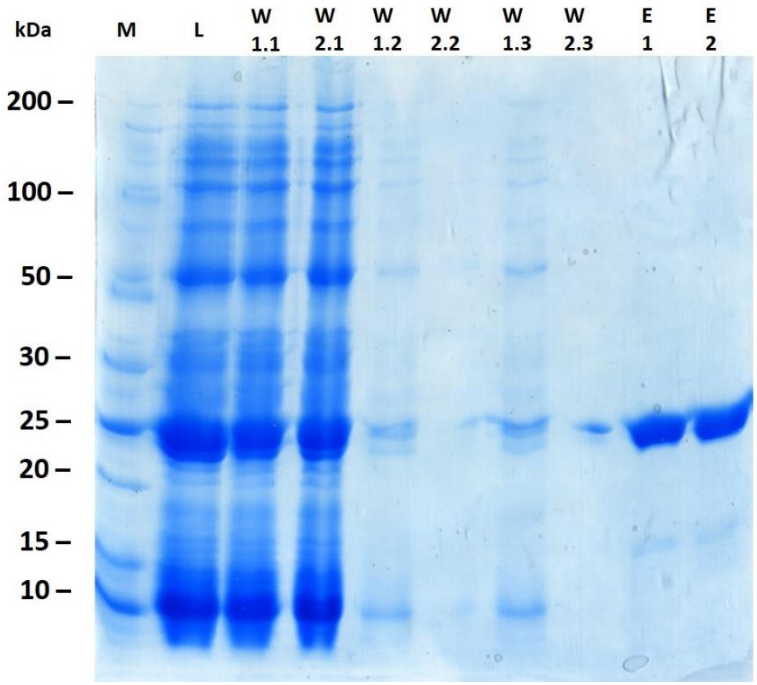

Figure 7. Affinity chromatography of *Pf*GST. SDS-PAGE patterns of the recombinantly expressed and pacificated protein of *Pf*GST. Samples from subsequent wash steps in the purification were resolved by 12 % SDS-PAGE and stained with Coomassie blue. M= PageRuler Protein Ladder (kDa); L=protein lysate; W1.1-1.3= wash steps of fraction 1; W2.1-2.3= wash steps of fraction 2; E1= the eluate with GSH; E2= the eluate with S-(p-Bromobenzyl) GSH .

1.1 Synthesis of S-(p-Bromobenzyl) GSH

To stabilize the *Pf*GST dimer in solution the GSH analog S-(p-Bromobenzyl) GSH was synthesized, as described in chapter III.2.2.2. The chemical structure of the S-(p-Bromobenzyl) GSH and GSH are presented in figure 8.

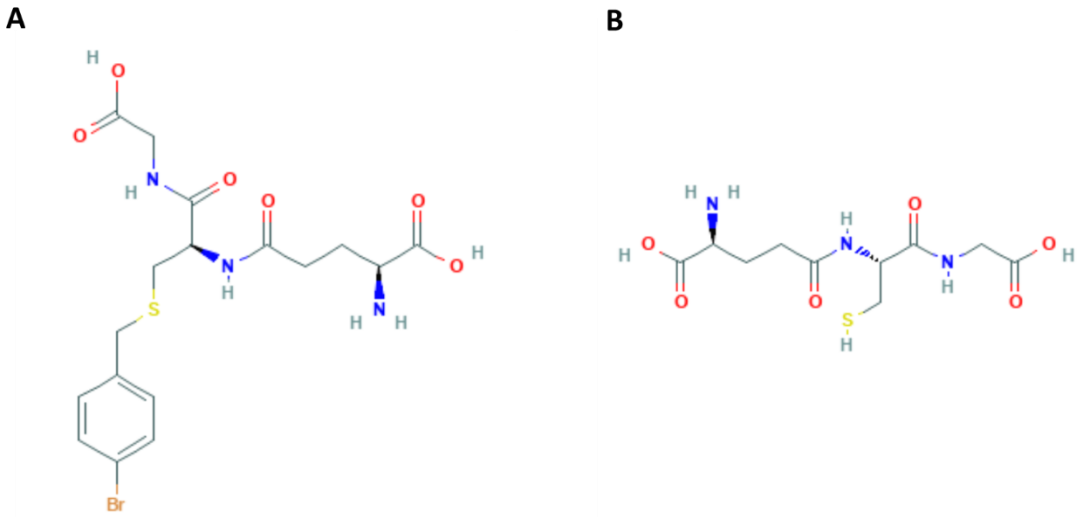

Figure 8. Chemical structures (https://pubchem.ncbi.nlm.nih.gov). (A) Chemical structure of S-(p-Bromobenzyl) GSH with an exact mass of 475.041 g/mol, molecular formula $C_{17}H_{22}BrN_3O_6S$. (B) Chemical structure of GSH with an exact mass of 307.084 g/mol, molecular formula $C_{10}H_{17}N_3O_6S$.

The synthesized substance was analyzed using the electrospray ionization mass spectrometric (ESI/MS) method.

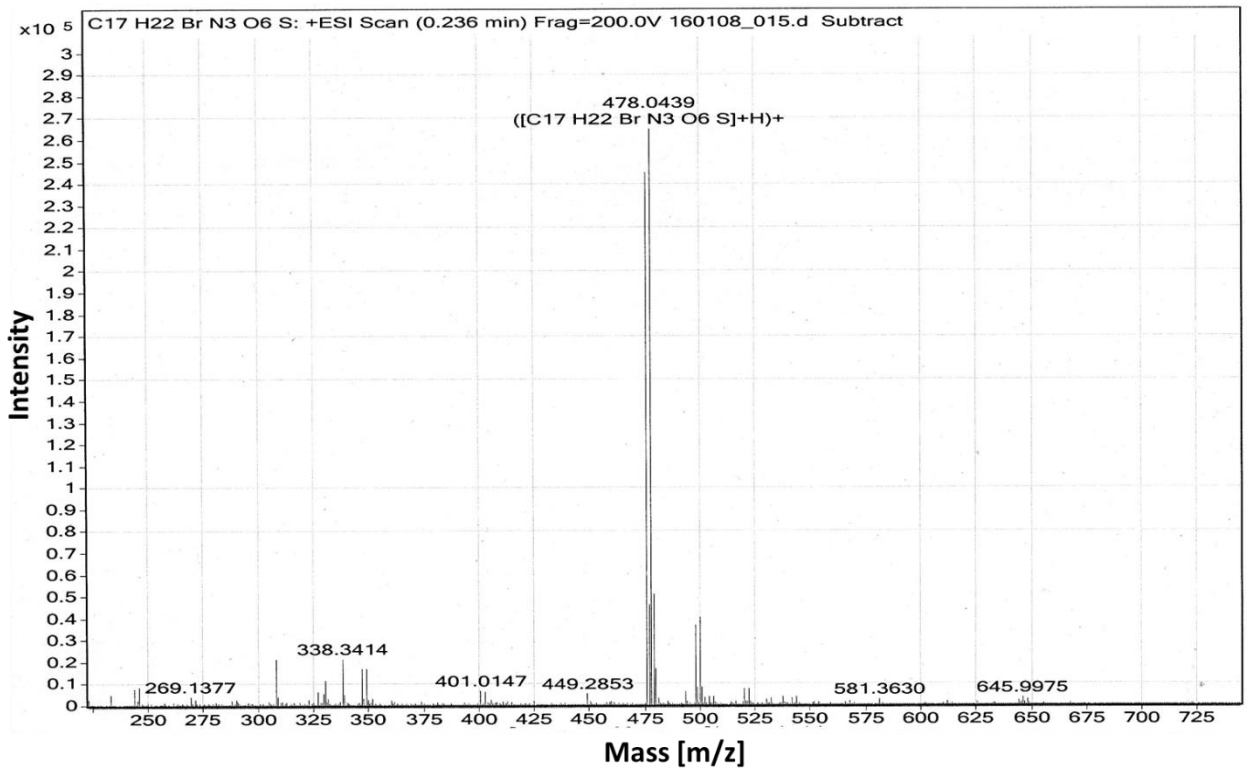

Figure 9. MS/MS spectra analysis of S-(p-Bromobenzyl) GSH.

The distribution of mass spectra of synthesized S-(p-Bromobenzyl) GSH molecule was experimental investigated (Figure 9). The main peak shows a value for a molecular size of 478 g/mol, which

corresponds approximately to the calculated molecular weight of the S-(p-Bromobenzyl) GSH. Furthermore other secondary peaks are detectable. This occurred due to possibly different isotopic compositions of the derivative.

2 Dispersity analysis of the *Pf*GST multimeric states

2.1 Analytical size determination of *Pf*GST multimeric states

Wild- type *Pf*GST is able to form dimers and tetramers in solution (Perbandt et al. (2015). Therefore

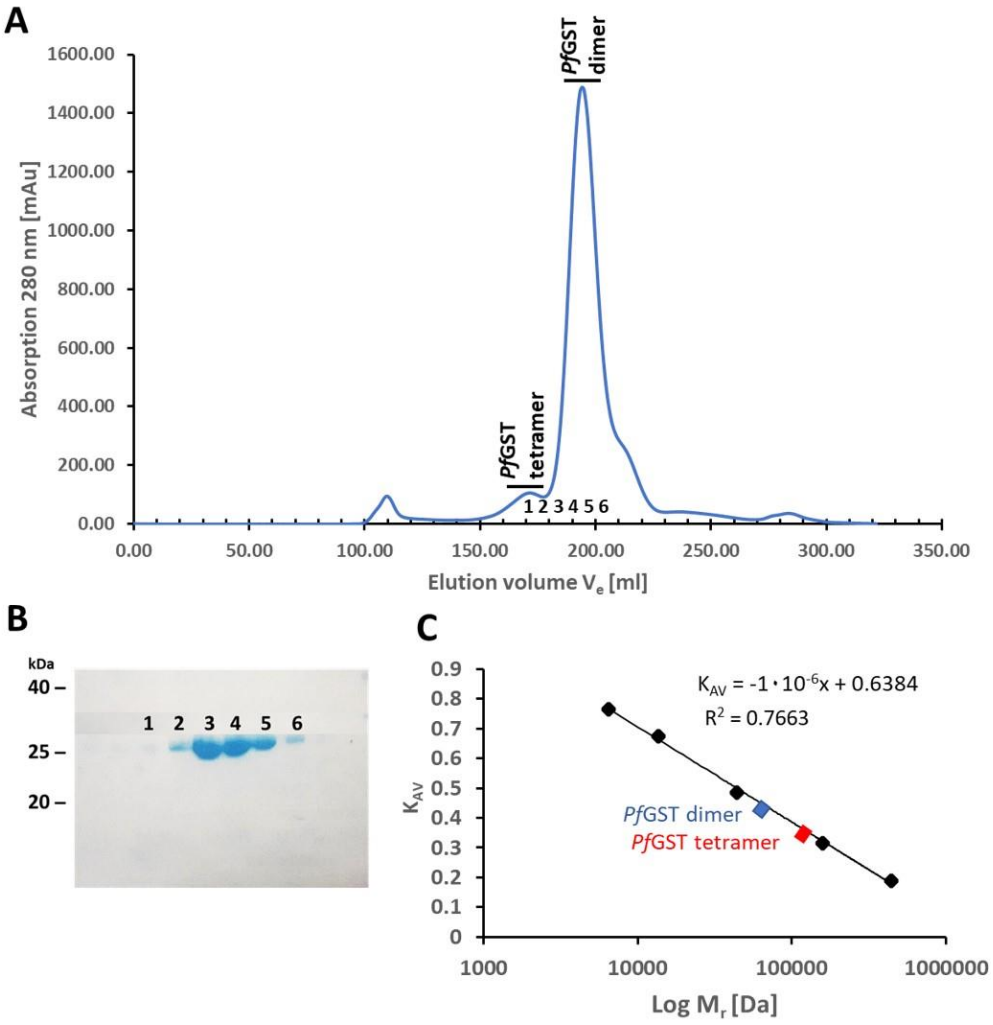

Figure 10. Analytical size exclusion chromatography (SEC) of *Pf*GST. (A) SEC traces of *Pf*GST dimer and tetramer. (B) SDS-PAGE patterns of the elution fractions of the dimer and tetramer. (C) The calibration plot showing the molecular weight of proteins. The standard curve was calculated from the fit of the elution volumes of the size marker proteins: Ferritin (440 kDa), Aldolase (158 kDa), Ovalbumin (44 kDa), Ribonuclease A (13.7 kDa) and Aprotinin (6.7 kDa).

the *Pf*GST was additionally chromatographically purified via size exclusion chromatography to separate dimer and tetramer fractions. Subsequently the eluate after GSH affinity chromatography was

applied to a Superdex HiLoad 26/600 column (GE-Healthcare) operated at 16 °C. The *Pf*GST elution shows two peaks, one small peak and other one is significantly larger (Figure 10A). The denaturing SDS PAGE of the protein elution fractions revealed *Pf*GST monomer single protein bands with indicated molecular weight of 25 kDa (Figure 10B). The relative molecular weights (MW) of the eluted protein fractions were determined from calibration plot of the calculated standard curve, from the fit of the elution volumes of the size marker proteins (Figure 10C). The calculated molecular weights indicate that the *Pf*GST forms two molecular oligomeric states in solution; a stable dimer with calculated MW ≈50 kDa and a tetramer with calculated MW ≈100 kDa, respectively.

2.2 Analysis of the *Pf*GST multimeric states using *in situ* DLS

The dimer and tetramer elution fractions after chromatographical purification were collected and concentrated by centrifugation at 4 °C (Chapter III.2.2.4.3). The dispersity and particle radius distribution of *Pf*GST dimer (10 mg ml^{-1}) and tetramer (10 mg ml^{-1}) were determined and analyzed at room temperature by Dynamic Light Scattering (DLS) applying the DLS system SPECTRO*LIGHT*™ 300 (Xtal Concepts GmbH, Hamburg, Germany).The *Pf*GST was analyzed by DLS measurements to verify the purity and dispersity of the protein and also to determine the adequate hydrodynamic radius (R_h). Time resolved measurements of hydrodynamic radius, after about 370 s, verified the monodispersity of *Pf*GST dimer and tetramer states (Figure 11, Figure 12). The observed data showed a value the hydrodynamic radii, at R_h =3.7 ± 0.1nm, for the dimer (Figure 11) and at R_h =5.7 ± 0.1nm for the tetramer (Figure 12,). The stable and similar hydrodynamic radius over time demonstrated that the *Pf*GST dimeric and tetrameric states were stable in solution. Based on this observations, this both protein solutions represent a high degree of monodispersity and no formation of protein aggregates or oligomers with higher hydrodynamic radius was observed. Furthermore, the diffusion coefficients (D) of dimer and tetramer were calculated using the Stokes-Einstein equation:

Equation (1)

$$D = \frac{kT}{6\pi\eta r}$$

k= Boltzmannconstante = 1.38 x 10-23 J/K

T= Absolute temperatur = 22°= 295.5 K

π = Archimedes Constante = 3.14

η= Dinamic viscosity of solution = 1 cP (water 20 °)

r= Hydrodynamic radius of particle ≈ 3.6 nm (*Pf*GST dimer); 5.7 nm (*Pf*GST tetramer)

D (*Pf*GST dimer) ≈ 6 x 10^{-7} cm^2 s^{-1}

D (*Pf*GST tetramer) ≈ 3.9 x 10^{-7} cm^2 s^{-1}

3 Fluorescently labeling of *Pf*GST tetramer

The purity and homogeneity of the protein samples are required to obtain protein crystals with high quality. Presence of impurities in a protein sample and therefore incorporation in the crystal lattice of growing crystal will decrease the crystal quality and thus make the crystal unsuitable for further X-ray analysis. To analyze the quantities of impurities in growing crystals fluorescently labeled *Pf*GST protein-aggregates are prepared, corresponding to impurities in solutions.

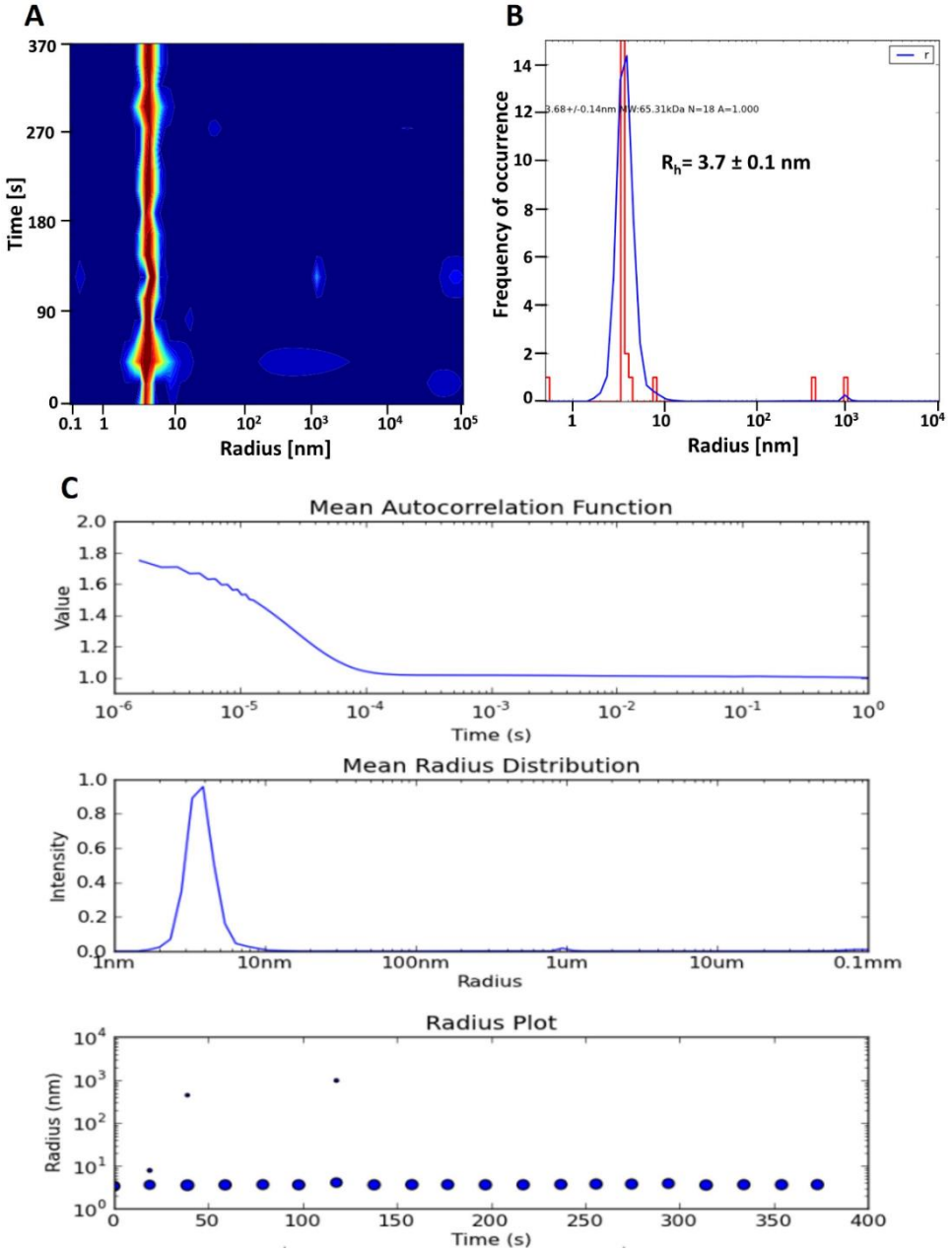

Figure 11. Real-time observation of *Pf*GST dimer sample at a concentration of 10 mg ml^{-1}, using a *in situ* DLS system. (A) The graph shows the protein radius distribution over time with a constant radius. (B) Radius distribution histogram of the *Pf*GST dimer. (C) Summary graphs of the radius distribution of a measurement series: a representative mean autocorrelation function; a representative mean radius distribution; a representative radius plot.

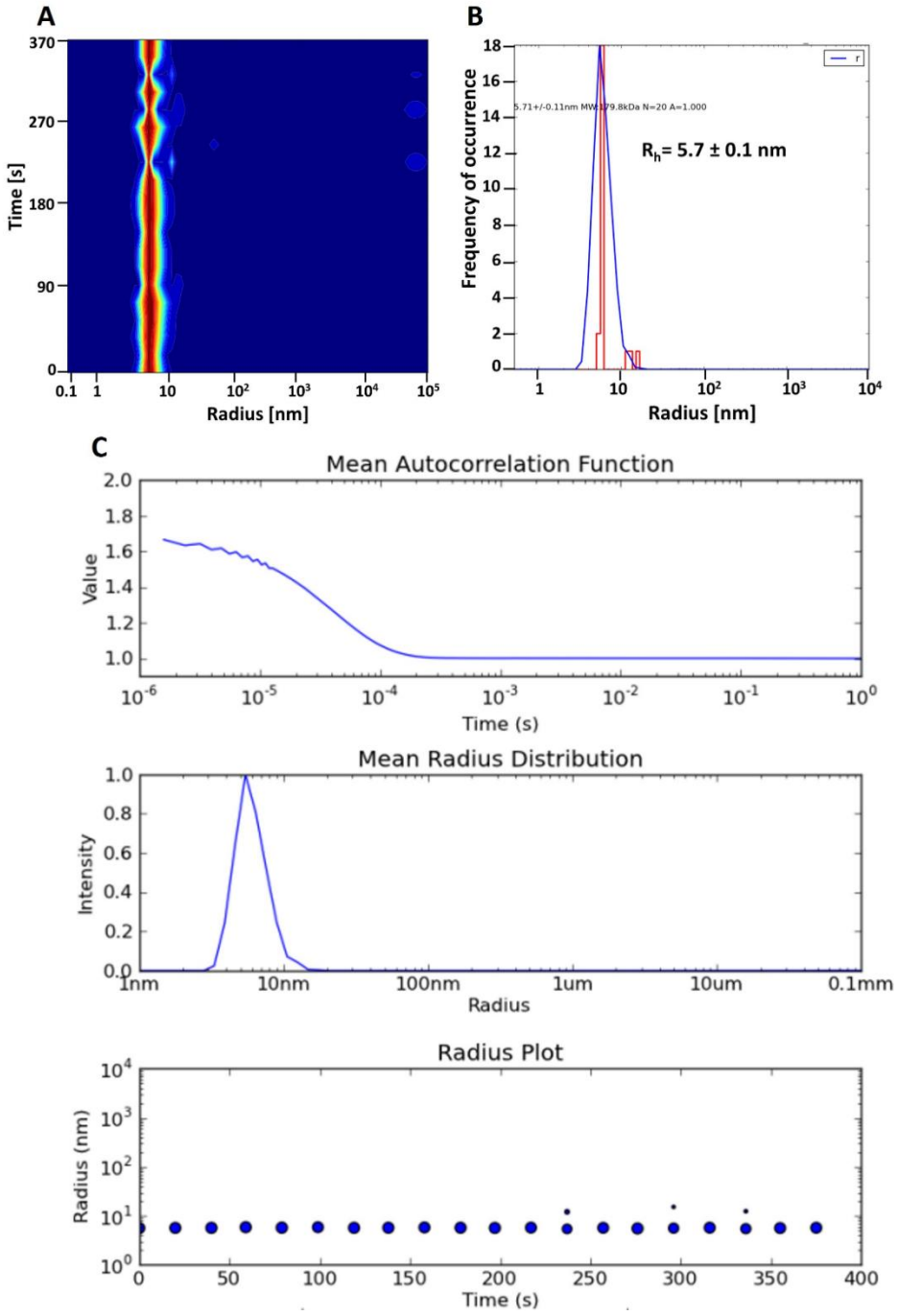

Figure 12. Real-time observation of *Pf*GST tetramer sample at a concentration of 10 mg mL^{-1}, using a *in situ* DLS system. (A) The graph shows the protein radius distribution over time with a constant radius. (B) Radius distribution histogram of *Pf*GST tetramer. (C) Summary graphs of radius distribution of a measurement series: a representative mean autocorrelation function; a representative mean radius distribution; a representative radius plot.

The *Pf*GST tetramer, acting as impurity in the crystallization experiments, was labeled with Alexa Fluor® 488 TFP ester, (C39H44F4N4O11S2, MW = 884.9 Da) fluorescent dye (chapter III.2.2.8). Figure 13 shows the labeling procedure and analysis via SDS PAGE. The labeling was confirmed by the presence of a protein band with increased molecular weight caused by the protein-dye conjugant (25 kDa +884.9 Da) compared to native protein (25 kDa) on SDS PAGE (Figure 13D). Additionally the labeling degree (DOL) of the protein – dye conjugate was determined.

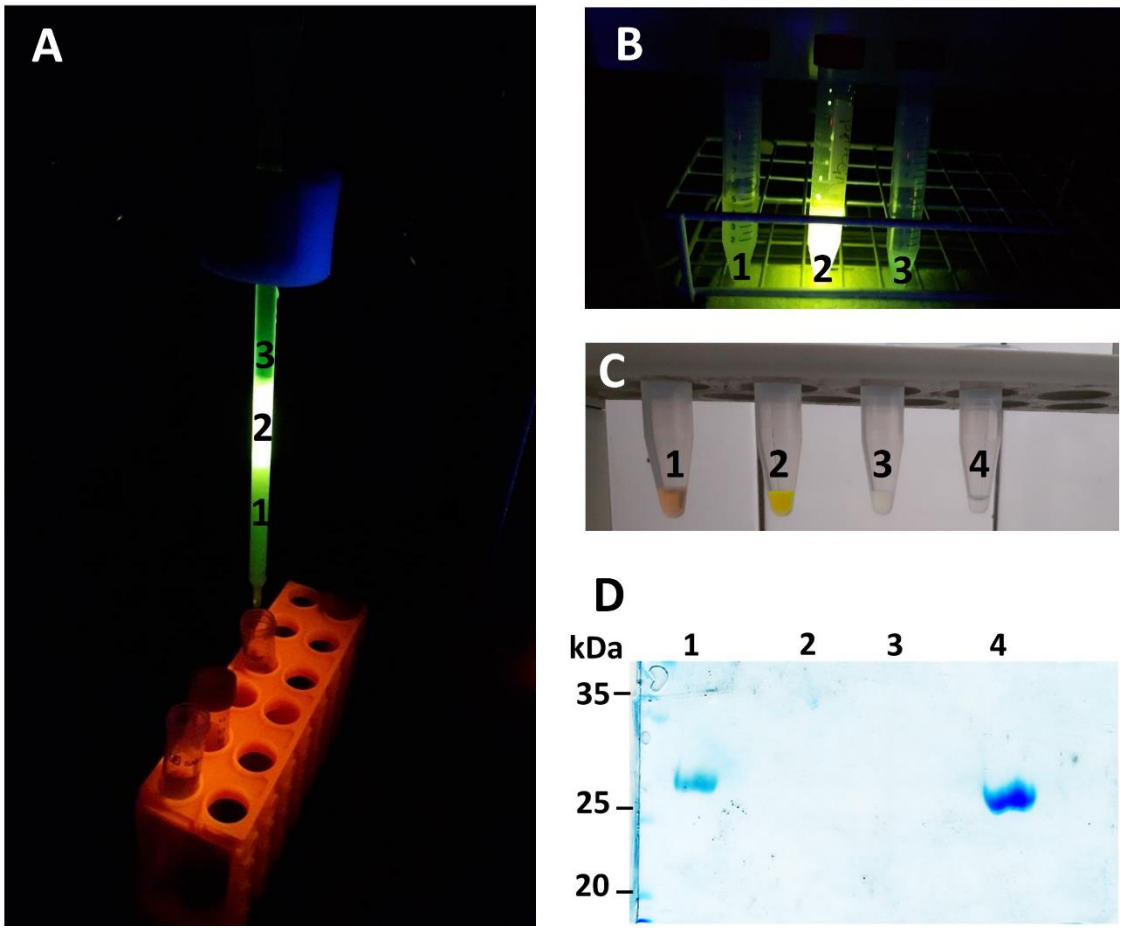

Figure 13. Fluorescently labeling of a *Pf*GST tetramer. The *Pf*GST tetramer was labeled with Alexa Fluor® 488 TFP ester, (C39H44F4N4O11S2, MW = 884.9 Da) fluorescent dye. The protein - dye conjugate was separated at 16 °C applying a prepacked Sephadex G-25 gel filtration column. (A) A total of three fractions from reaction mixture were separated: Protein – dye conjugate (1), Free dye (2), Buffer solution (3). (B) Collected elution solutions of the protein – dye conjugate, free dye and elution buffer fractions after gel filtration. (C) Aliquots of the fraction (1), fraction (2), fraction (3) and additionally unlabeled *Pf*GST tetramer (negative control) collected in 1.5 ml Eppendorf tubes. (D) SDS - PAGE patterns of the fractions (1; 2; 3) after gel filtration and additionally unlabeled *Pf*GST tetramer (4).

The conjugate was spectrophotometrically analyzed using a NanoDrop 2000c spectrophotometer. The conjugate sample was diluted 1:5 prior the measurements. The absorbance of the conjugate solution

was measured at 280 nm and at 494 nm, A_{280} = 1.16 and A_{494} = 2.21, respectively. The molar extinction coefficient (ε) of the *Pf*GST tetramer was predicted using the ExPASy (Bioinformatics resource portal) and ProtParam application. The DOL of the protein – dye conjugate was calculated due to following equations:

Equation (1)

$$\text{Protein concentration (M)} = \frac{[A280-(CF \times A494)] \times dilution\ factor}{\varepsilon\ (protein)}$$

S recource portal)

A_{280} = Absorbance of the conjugate solution at 280 nm = 1.16

A_{494} = Absorbance of the conjugate solution at 494 nm = 2.21

CF = Correction factor for the fluorophore's contribution to the A_{280} = 0.11

ε (protein) = Molar extinction coefficient of protein at 280 nm = 112000 $cm^{-1}M^{-1}$

Dilution factor = 5

$$\text{Protein concentration (M)} = \frac{[1.16-(0.11 \times 2.21)] \times 5}{112000} = 4.1 \times 10^{-5}\text{M}$$

Equation (2)

$$\text{DOL = (moles dye)/ (mole protein)} = \frac{A494 \times dilution\ factor}{\varepsilon\ (dye) \times protein\ concentration\ (M)}$$

A_{494} = Absorbance of the conjugate solution at 494 nm = 2.21

ε (dye) = molar extinction co-efficient of the Alexa Fluor® 488 dye at 494 nm = 71000 $cm^{-1}M^{-1}$

Protein concentration (M) = 4.1×10^{-5}M

Dilution factor = 5

$$\text{DOL = (moles dye)/ (mole protein)} = \frac{2.21 \times 5}{71000 \times 0.000041\ (M)} = 3.8$$

The protein-dye conjugate was concentrated to 10mg/ml final concentration, using Millipore Amicon® ultra-centrifugal concentrators (Merckmillipore).

4 Initial experiments

Initial crystallization experiments were performed to investigate and stabilize the optimal crystallization conditions of *Pf*GST, applying the vapour diffusion technique in hanging drops, as well as the counter/liquid-liquid diffusion technique in capillaries of 100mm in length, 3mm in width and 0.3mm

inner diameter (VitroCom). Furthermore, for crystallization experiments samples with different protein- fluorescence labeled aggregate ratios were prepared.

4.1 Crystallization of *Pf*GST applying vapour diffusion technique

The crystallization experiments were initially performed in 24-well Linbro plate applying the vapour diffusion technique in hanging drops while mixing 2µl droplets of 15 mg ml^{-1} protein (*Pf*GST dimer) in a 0.1 M $NaHPO_4$, pH 6.7 solution with the same volume of precipitant, 2.1 M $AmSO_4$, 0.1M $NaHPO_4$, pH 6.7 solution on a cover slip and equilibrated against 1000 µl reservoir, 2.1 M $AmSO_4$, 0.1M $NaHPO_4$, pH 6.7, solution. Initial crystallization screens of the *Pf*GST dimer (15 mg ml^{-1}) as well *Pf*GST dimer additionally with different percentage of fluorescence (Alexa Fluor 488) labeled *Pf*GST aggregates (10 mg ml^{-1}) were performed (Table 17).

Table 17. Crystallization of *Pf*GST applying vapour diffusion technique. Calculated molar quantities of dimer (15 mg ml^{-1}) additionally tetramer (10 mg ml^{-1}) solutions with different molar ratios in 2 µl droplets.

***Pf*GST dimer : tetramer molar ratio [%]**	**Molar quantity [pmol]**	
	Dimer	**Tetramer**
100 (dimer)	600	-
98 : 2	584	12
95 : 5	519	27
90 : 10	450	50
75 : 25	300	100

*Pf*GST needle-like crystals were observed for all dimer: tetramer ratios after 72 hours (Figure 14 A;B;C;D;E). The length of major axis for *Pf*GST crystals was measured to be approximately 250-550 µm for dimer (Figure 14A), 250-500 µm for dimer with the addition of tetramer with 98 : 2 molar ratio (Figure 14B), 150-250 µm for dimer with the addition of tetramer with 95 : 5 molar ratio (Figure 14C), 100-300 µm for dimer with the addition of tetramer with 90 :10 molar ratio (Figure 14D) and 30-70 µm for dimer with the addition of tetramer with 75 : 25 molar ratio (Figure 14E). Furthermore, to investigate the incorporation of impurities (fluorescence labeled *Pf*GST aggregates acting as impurity) into growing crystals confocal fluorescence images of crystals were recorded using a confocal laser scanning microscope (Leica TCS SP – 8, Leica Microsystems) with 10 x objective and FITC filter.

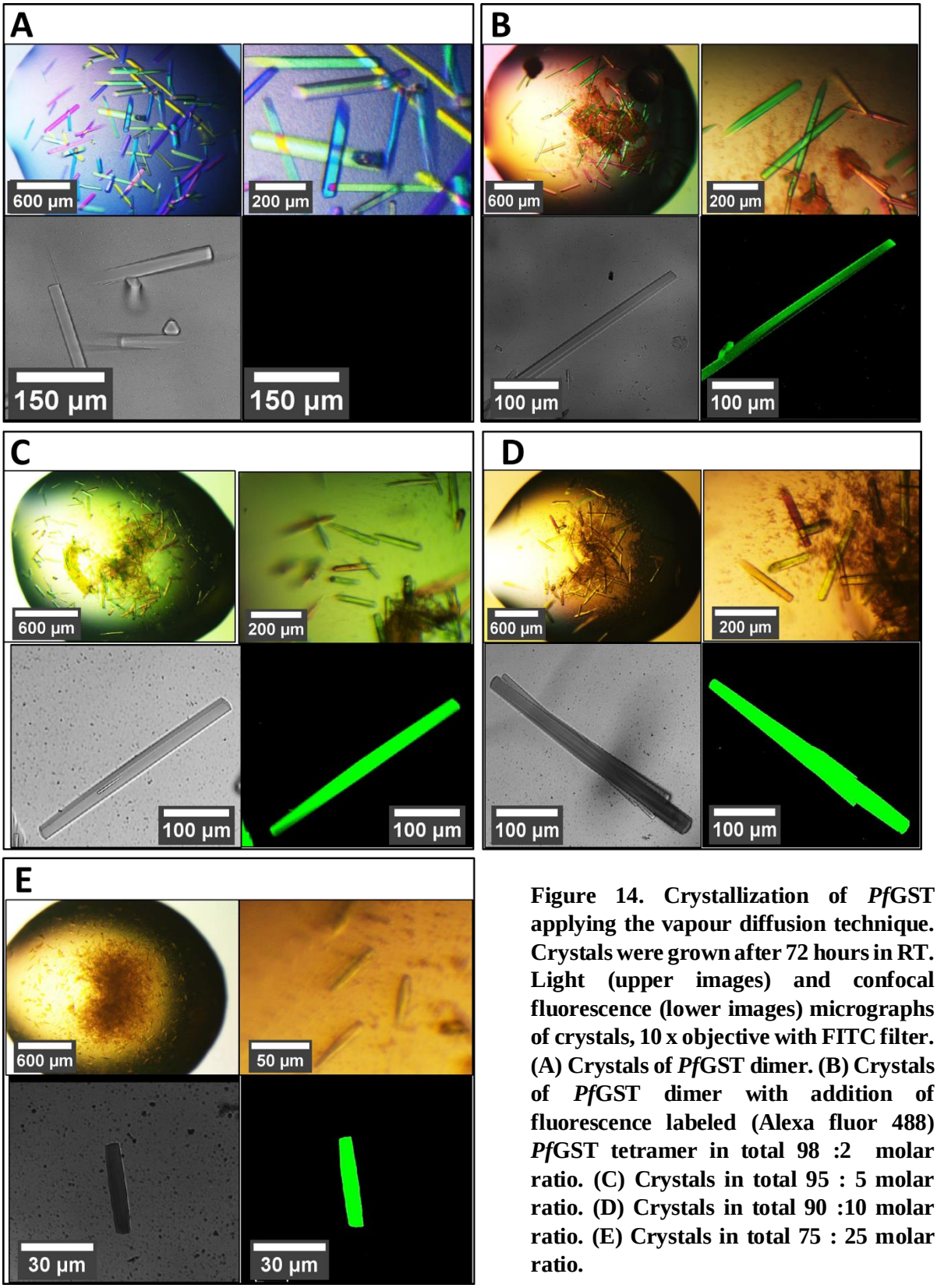

Figure 14. Crystallization of *Pf*GST applying the vapour diffusion technique. Crystals were grown after 72 hours in RT. Light (upper images) and confocal fluorescence (lower images) micrographs of crystals, 10 x objective with FITC filter. (A) Crystals of *Pf*GST dimer. (B) Crystals of *Pf*GST dimer with addition of fluorescence labeled (Alexa fluor 488) *Pf*GST tetramer in total 98 :2 molar ratio. (C) Crystals in total 95 : 5 molar ratio. (D) Crystals in total 90 :10 molar ratio. (E) Crystals in total 75 : 25 molar ratio.

The confocal fluorescence micrographs of the *Pf*GST dimer (negative control) show the absence of fluorescence (Figure 14A). The confocal fluorescence micrographs of entire samples containing *Pf*GST

dimer and additionally fluorescently labeled *Pf*GST aggregates in different molar ratios show fluorescence in crystals (Figure 14B;C;D;E).

4.2 Crystallization of *Pf*GST applying counter diffusion technique

Initial crystallization experiments were performed using the counter/liquid-liquid diffusion technique in capillaries of 100mm in length, 3mm in width and 0.3mm inner diameter (VitroCom). Capillaries were filled with 37µl of precipitant solution, 2.8 M $AmSO_4$, 0.1M $NaHPO_4$, 15% glycerol, pH 6.7 and 37µl of protein solution, 0.1 M $NaHPO_4$, pH 6.7 (doped with different percentages of fluorescently-labelled *Pf*GST aggregate) using syringes (Hamilton). Initial crystallization screens of the *Pf*GST dimer (30 mg ml^{-1}) as well *Pf*GST dimer additionally with different percentage of fluorescence (Alexa Fluor 488) labeled *Pf*GST aggregates (10 mg ml^{-1}) were performed (Table 18).

Table 18. Crystallization of *Pf*GST applying counter diffusion technique in capillaries 100mm in length, 3mm in width and 0.3mm inner diameter. Calculated molar quantities of dimer (30 mg ml^{-1}) additionally tetramer (10 mg ml^{-1}) solutions with different molar ratios in 37 µl protein solution.

***Pf*GST dimer : tetramer molar ratio [%]**	**Molar quantity [nmol]**	
	Dimer	**Tetramer**
100 (dimer)	22.2	-
99.9 : 0.1	22.1	0.022
99.8 : 0.2	21.9	0.044
99.5 : 0.5	21.5	0.11
99 : 1	20.9	0.21

*Pf*GST needle-like crystals were observed in entire dimer : tetramer ratios after 96 hours (Figure 15 A;B;C;D;E). The length of major axis for *Pf*GST crystals was measured to be approximately 500-1300 µm for larger crystals and 100-300 µm for smaller crystals in a dimer solution (Figure 15A), 100-600 µm for dimer with the addition of tetramer in 99.9 : 0.1 molar ratio (Figure 15B), 50- 500 µm for dimer with the addition of tetramer in 99.8 : 0.2 molar ratio (Figure 15C), 400-1200 µm for dimer with the addition of tetramer in 99.5 : 0.5 molar ratio (Figure 15D) and 200-1200 µm for dimer with the addition of tetramer in 99 : 1 molar ratio (Figure 15E). Furthermore to investigate the incorporation of impurities (fluorescence labeled *Pf*GST aggregates acting as impurity) into growing crystals confocal fluorescence images of crystals were recorded using a confocal laser scanning microscope (Leica TCS SP – 8, Leica Microsystems) 10 x objective with FITC filter and photo-documented. The confocal fluorescence micrograph of *Pf*GST dimer sample (negative control) of fluorescence (Figure 15A). The confocal fluorescence micrographs of entire samples containing *Pf*GST dimer and additionally fluorescently

labeled *Pf*GST aggregates in different molar ratios show the presence of fluorescence in crystals (Figure 15B;C;D;E).

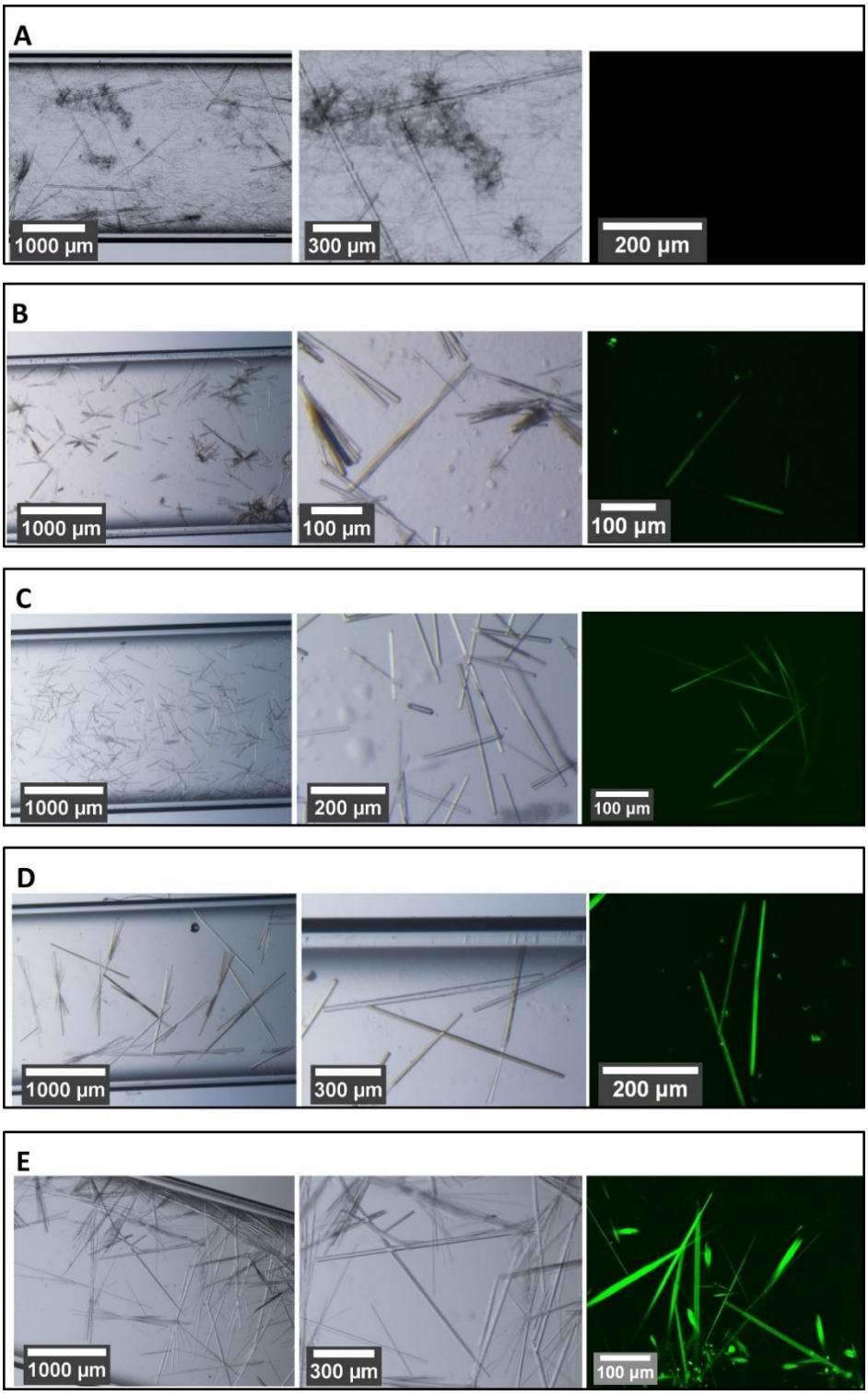

Figure 15. Crystallization of *Pf*GST applying counter diffusion technique. Crystals were grown after 96 h in RT. Light and confocal fluorescence micrographs of crystals. (A) Crystals of *Pf*GST dimer. (B) Crystals of *Pf*GST dimer with addition of fluorescence labeled (Alexa fluor 488) *Pf*GST tetramer in a total 99.9:0.1 molar ratio. (C) Crystals in a total 99.8: 0.2 molar ratio. (D) Crystals in a total 99.5:0.5 molar ratio. (E) Crystals in total 99: 1 molar ratio.

4.3 Diffraction data collection, processing, refinement and model building of *Pf*GST

Diffraction data of *Pf*GST crystals were collected at 100 K temperature using an in-house Rigaku RU-200 rotating anode X-ray generator. Diffraction data for crystals with approximately 300 – 600 µm length of major axis were collected. For cryoprotection the crystals were soaked with precipitant solution supplemented with 14 % (v/v) glycerol. Diffraction data were subsequently indexed, integrated and scaled with XDS and aimless/ccp4 graphic programs. Data were cut individual for a crystal dataset to 2.7 Å monitoring Rmeas, Rsym, I/σ and CC1/2. The crystal belonged to the orthorhombic space group $P2_12_12_1$ with unit cell dimensions of 57.9 Å, 69.1 Å, 123.9 Å and α, β, γ angles of 90.0°, 90.0°, 90.0° (Table 19). Further diffraction data of *Pf*GST crystals were collected at 100 K temperature at PETRA III P13 EMBL beamline at DESY, Hamburg. Data were cut individual for a crystal dataset to 2.1 Å monitoring Rmeas, I/σ and CC1/2. The crystal belonged to the orthorhombic space group $P2_12_12_1$ with unit cell dimensions of 57.7 Å, 69.1 Å, 123.7 Å and α, β, γ angles of 90.0°, 90.0°, 90.0° (Table 19).

The homologue structure of a *Pf*GST dimer (PDB code: 3FRC) was used as a search model for molecular replacement, refinement and Matthews coefficient probability. 5 % of reflections were used for the calculation of R free to monitor the progress of refinement. The refinement analysis showed a R-factor of 21.9 % and an R free-factor of 26.2 % for the data set collected at the home-source and a R-factor of 22.7 % and an R free-factor of 26.2 % for the dataset collected at beamline P13. The Matthews coefficient was determined for both dataset, home-source and beamline P13, 2.63 $Å^2\,Da^{-1}$ and 2.61 $Å^2\,Da^{-1}$ respectively. The solvent content was calculated to be 53 % for two *Pf*GST monomers in the respective asymmetric unit. Data collection and refinement parameters are summarized in Table 19. The asymmetric unit consist a *Pf*GST homodimer with two identical monomer chains (Figure 16).

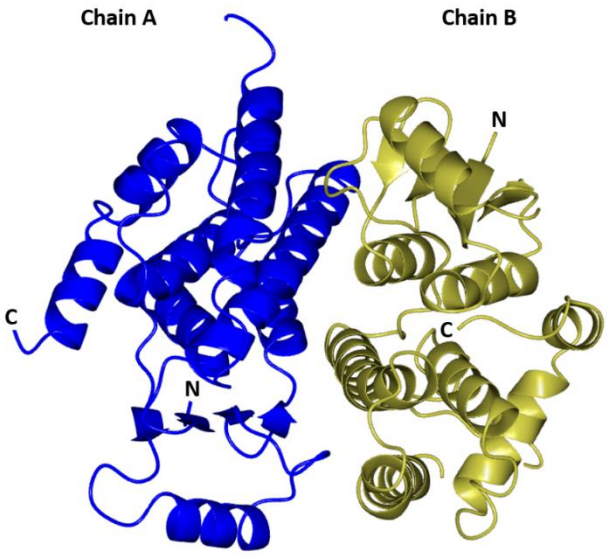

Figure 16. Structure of *Pf*GST homodimer. Cartoon representation of the *Pf*GST homodimer structure. Blue is used for chain A, gold for chain B; labels of the N- and C-terminus are shown.
Table 19. Data collection and refinement statistics for *Pf*GST.

Data collection statistics		
Beamline/Source	PETRA III, P13	In-House rotating anode
Wavelength [Å]	0.9762	1.5418
Space group	P 2_1 2_1 2_1	P 2_1 2_1 2_1
Unit cell parameters: a, b, c [Å]	57.7, 69.1, 123.7	57.9, 69.1, 123.9
α, β, γ [°]	90.0, 90.0, 90.0	90.0, 90.0, 90.0
Resolution [Å]	46.1 – 2.1 (2.16 – 2.10)	28.9 – 2.7 (2.84 – 2.71)
Temperature [K]	100	100
Rmerge [%]	12.7 (44.1)	12.7 (39.6)
Rmeas [%]	13.8 (47.8)	16.2 (50.5)
Measured reflections	389308	55946
Unique reflections	29665	14071
Average I/σ(I)	15.2 (5.5)	11.1 (3.6)
Mn(I) half-set correlation CC(1/2) [%]	99.8 (95.3)	98.6 (78.0)
Completeness [%]	100.0 (100.0)	99.4 (99.6)
Mosaicity [°]	0.06	0.16
Redundancy	13.1 (13.1)	4.0 (4.0)
Refinement statistics		
Resolution range [Å]	46.1 – 2.1	28.3 – 2.7
R/ Rfree [%]	22.7/26.2	21.9/26.2
Overall *B* factor [Å^2]	21.57	15.99
Rms deviation		
Bond-length [Å]	0.009	0.007
Bond angle [°]	1.671	1.540
Nr. of atoms		
Protein	3389	3389
Brom	2	2
Matthews coefficient [Å^3 Da^{-1}]	2.61	2.63
Solvent content [%]	53	53
Molecules in the asymmetric unit	2	2

*Values in parentheses are for the highest resolution shell. Rmerge: Σhkl Σi | *Ii* (hkl) – ⟨*I* (*hkl*)⟩ |/Σ$_{hkl}$Σi *Ii* (*hkl*), where *I* (*hkl*) is the mean intensity of the reflections hkl, Σ$_{hkl}$ is the sum over all reflections and Σi is the sum over i measurements of reflection hkl.

5 Biophysics 1

5.1 Mission SpaceX 10

Crystallization experiments were performed using the counter/liquid-liquid diffusion technique in capillaries of 100mm in length, 3mm in width and 0.3mm inner diameter (VitroCom). Capillaries were filled with 37µl of precipitant solution, 2.8 M $AmSO_4$, 0.1M $NaHPO_4$, 15% glycerol, pH 6.7 and 37µl of protein solution, 0.1 M $NaHPO_4$, pH 6.7 (doped with different percentages of fluorescently-labelled *Pf*GST aggregate) using syringes (Hamilton). Initial crystallization screens of *Pf*GST dimer (30 mg ml^{-1}) as well *Pf*GST dimer additionally with different percentage of fluorescence (Alexa Fluor 488) labeled *Pf*GST aggregates (10 mg ml^{-1}) were performed (Table 20).

Table 20. Crystallization of *Pf*GST applying counter diffusion technique in capillaries 100mm in length, 3mm in width and 0.3mm inner diameter. Calculated molar quantities of dimer (30 mg ml^{-1}) additionally tetramer (10 mg ml^{-1}) solutions with different molar ratios in à 37 µl protein solutions.

***Pf*GST dimer : tetramer molar ratio [%]**	**Molar quantity [nmol]**	
	Dimer	**Tetramer**
100 (dimer)	22.2	-
99.9 : 0.1	22.1	0.022
99.8 : 0.2	21.9	0.044
99.5 : 0.5	21.5	0.11
99 : 1	20.9	0.21
95 :5	16.8	0.88
90 : 10	13.2	1.36
75 : 25	6.9	2.29
60 : 40	4.2	2.7

5.1.1 Round 1

5.1.1.1 LMM monitoring of crystal growth in microgravity, 99.9 : 0.1 ratio

The flight cassettes were adapted to the LMM microscope after sample thawing to perform crystallization experiments. Grown *Pf*GST crystals showed nearly similar morphologies in each capillary and were photo-documented with the LMM. *Pf*GST needle-like crystals in the capillary area 21 - 40 mm from the precipitant solution end were observed for dimer with the addition of tetramer in 99.9 : 0.1 ratio (Figure 17). Furthermore, crystals of different sizes were observed. The length of the major axis for crystals was measured to be 50 to 150 µm (Figure 17). Time-lapse images for different capillary areas were recorded with 2.5 x and 10 x magnification to investigate crystal growth rates for

crystals grown in microgravity. The first image was taken t = 303 min after sample thawing with 2.5 x magnification. The imaging time extended to t = 2461 min, images were taken t1 = 303 min, t2 = 579

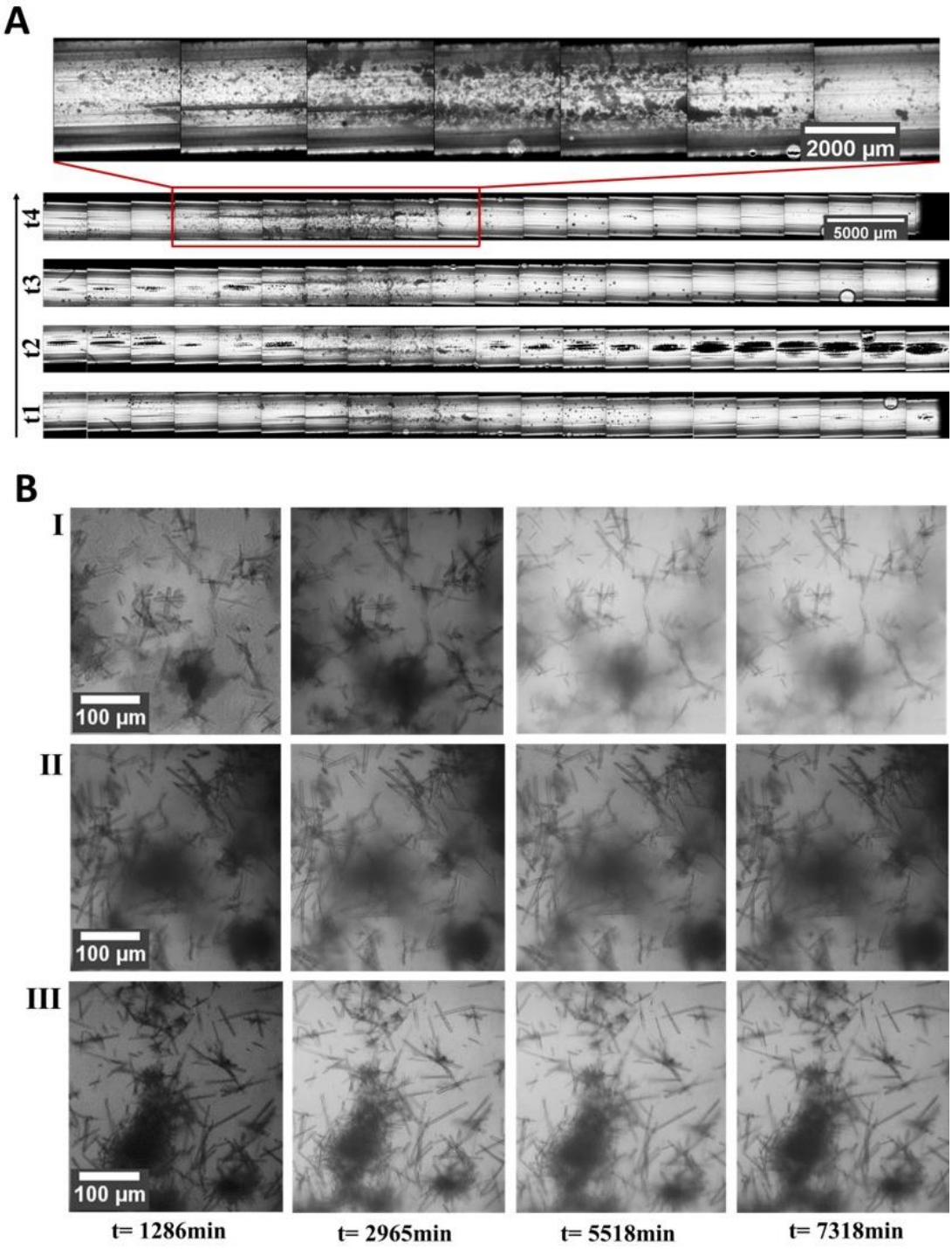

Figure 17. Protein crystallization in microgravity applying the counter diffusion technique in capillaries. Images were recorded using the ISS LMM microscope. *Pf*GST dimer crystals additionally fluorescence labeled *Pf*GST aggregates in 99.9:0.1 total ratio. (A) Time-lapse images were recorded with 2.5 x magnification. The imaging time extended to t = 2461 min, images were taken t1 = 303 min, t2 = 579 min, t3 = 823 and t4 = 2461 min after sample thawing. (B) Time-lapse images were recorded for 3 different areas (I, II, III) with 10 x magnification. The imaging time extended to t = 7318 min, first image was taken t = 1286 min after sample thawing.

min, t3 = 823 and t4 = 2461 min after sample thawing. Protein precipitation was observed at the time points t1 – t4, however a subsequent growth of crystals was not observed for the images recorded with 2.5 x magnification (Figure 17A; 18). Furthermore, at time points t = 1286-, 2965-, 5518- and 7318 min crystals were observed and photo-documented with 10 x magnification (Figure 17B).

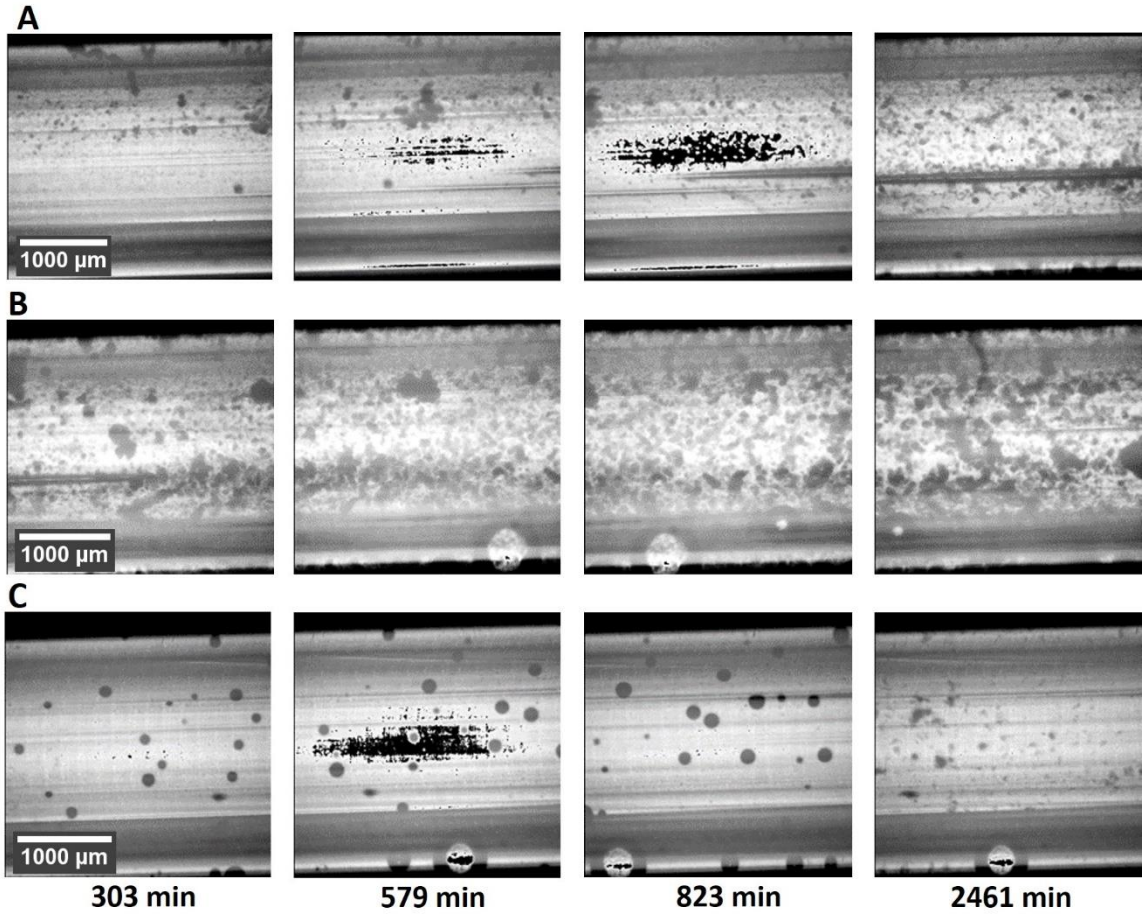

Figure 18. Growth of *Pf*GST crystals in microgravity. *Pf*GST dimer additionally fluorescence labeled *Pf*GST aggregates in 99.9:0.1 total ratio. Time-lapse images were recorded for 3 different areas (A, B, C) in the capillary using the LMM microscope with 2.5x magnification. The imaging time extended to t = 2461 min, first image was taken t = 303 min after sample thawing.

5.1.1.2 Crystal growth in 1G vs microgravity, 99.9 : 0.1 ratio

Since samples returned to the earth, light microscope images of crystals grown in µg and 1G were recorded and photo-documented. Crystal images were recorded t = 31 days after sample thawing with 2.5 x and 10 x magnification (Figure 19). Crystal dimensions vary for µg and 1G grown crystals. In µg grown crystals showed on average larger dimensions, particular the length of major axis, compared to 1G (figure 19).

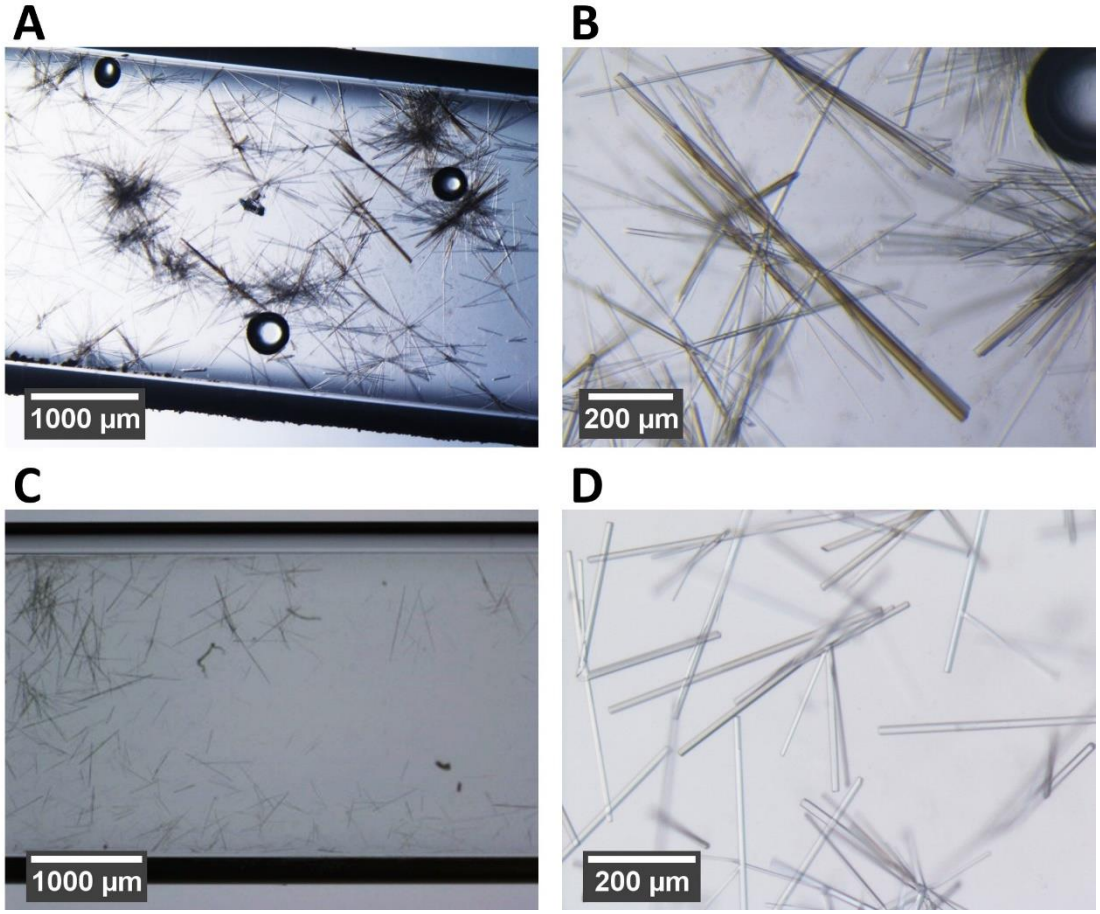

Figure 19. Crystals of *Pf*GST dimer additionally fluorescence labeled *Pf*GST aggregates in 99.9:0.1 total ratio grown in µg and 1G. Crystal images were recorded using a light microscope t = 31 days after sample thawing, after µg samples returned on the earth. (A) Crystals grown in µg, images were recorded with 2.5 x objective. (B) Crystals grown in µg, recorded with 10 x objective. (C) Crystals grown in 1G, recorded with a 2.5 x objective. (D) Crystals grown in 1G, recorded with a 10 x objective.

5.1.1.3 LMM monitoring of crystal growth, 99 : 1 ratio

Needle-like crystals in the capillary area 27 - 43 mm from the protein solution end were observed for the dimer with the addition of tetramer in 99 : 1 ratio (Figure 20). Furthermore, crystals of different sizes at different capillary areas were observed. The length of the major axis for crystals was measured to be 30 to 80 µm for smaller crystals and 100 to 200 µm for larger crystals (Figure 20). Time-lapse images for different capillary areas were recorded with 2.5 x and 10 x magnification to investigate crystal growth rates for crystals grown in microgravity. The first image was taken t = 312 min after sample thawing with 2.5 x magnification. The imaging time extended to t = 2499 min, images were taken t1 = 312 min, t2 = 588 min, t3 = 832 and t4 = 2499 min after sample thawing. Protein precipitation was observed at the time points

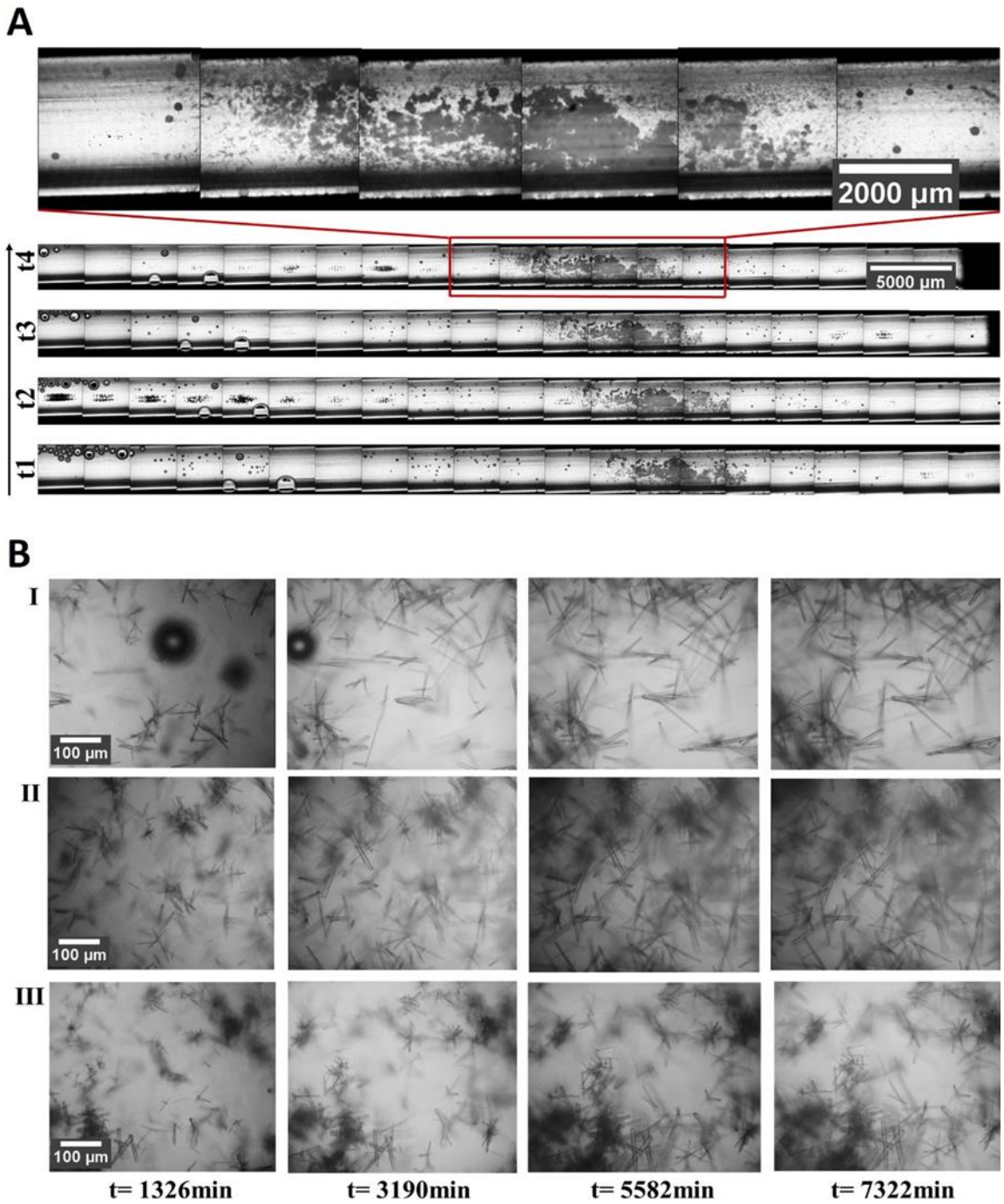

Figure 20. Protein crystallization in microgravity applying the counter diffusion technique in capillaries. Images were recorded using the ISS LMM microscope. *Pf*GST dimer crystals with fluorescence labeled *Pf*GST aggregates in a 99:1 total ratio. (A) Time-lapse images were recorded with 2.5 x magnification. The imaging time extended to t = 2499 min, images were taken t1 = 312 min, t2 = 588 min, t3 = 832 and t4 = 2461 min after sample thawing. (B) Time-lapse images were recorded for 3 different areas (I, II, III) with 10 x magnification. The imaging time extended to t = 7322 min, first image was taken t = 1326 min after sample thawing.

t1 - t4. Furthermore nucleation and subsequent growth of crystals was observed at the time points t = 842 – 2499 min for the images recorded with 2.5 x magnification (Figure 21). Additionally at time

points t = 1326-, 3190-, 5582- and 7322 min crystals of different dimensions at 3 different areas were observed and photo-documented for the images with 10 x magnification (Figure 20).

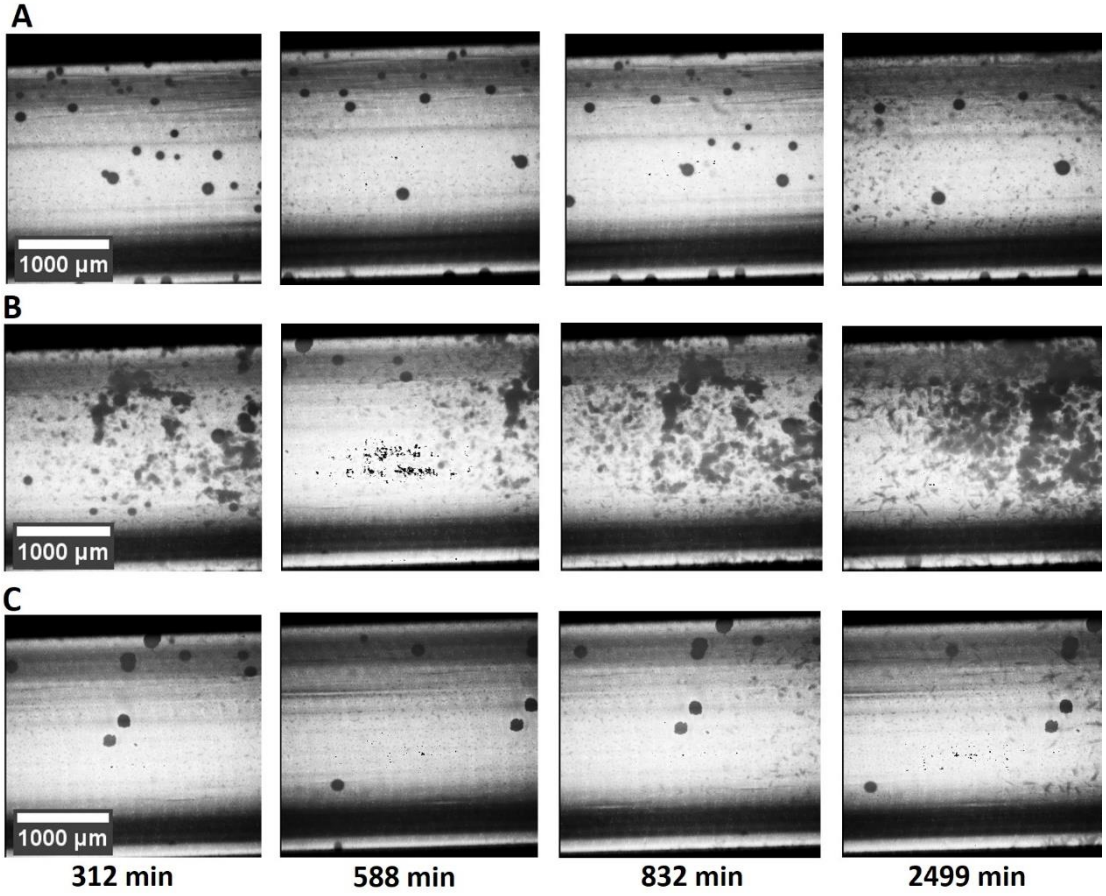

Figure 21. Growth of *Pf*GST crystals in microgravity. *Pf*GST dimer with fluorescence labeled *Pf*GST aggregates in 99:1 total ratio. Time-lapse images were recorded for 3 different areas (A, B, C) using the LMM microscope with 2.5x magnification. The imaging time extended to t = 2499 min, first image was taken t = 312 min after sample thawing.

5.1.1.4 Crystal growth in 1G vs microgravity, 99 : 1 ratio

In parallel time-lapse images for a capillary area, 15 – 20 mm from the protein end, were recorded with 10 x magnification to investigate crystal growth rates for crystals grown in 1G. First image was taken t = 720 min after sample thawing. The imaging time extended to t = 1320 min, images were taken t = 720-, t = 895-, t = 970-, t = 1060-, t = 1170- and t = 1320 min after sample thawing (Figure 22). The growth rate for a single crystal with final length of the major axis 420 µm was calculated to 17.2 µm/h (Figure 23).

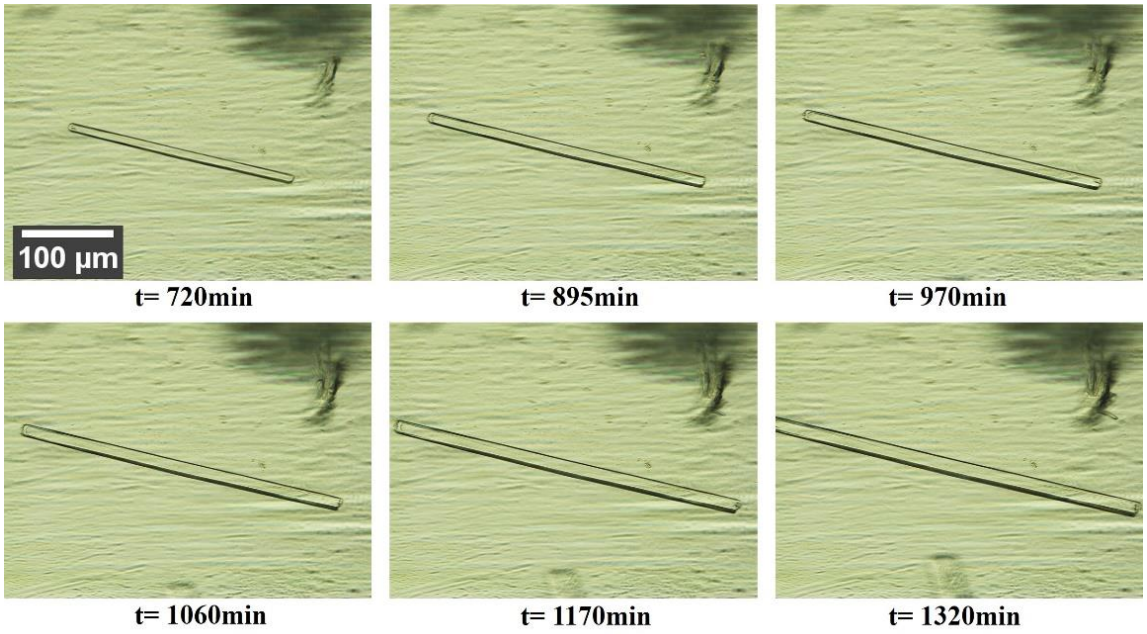

Figure 22. Growth of *Pf*GST crystals in 1G. *Pf*GST dimer with fluorescence labeled *Pf*GST aggregates in 99:1 total ratio. Time-lapse images were recorded for an area in capillary using the Leica M205 C light microscope. The imaging time extended to t = 1320 min, the first image was taken t = 720 min after sample thawing.

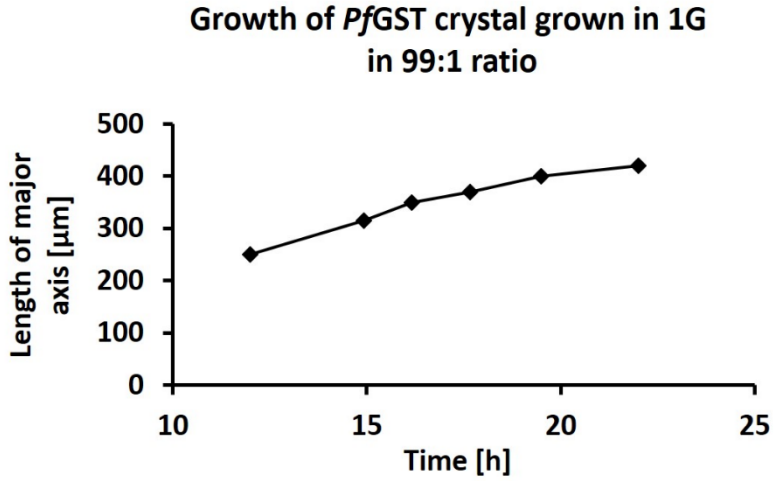

Figure 23. The growth of crystals in 1G. Dimer crystal with fluorescence labeled *Pf*GST aggregates in 99:1 total ratio. The growth was measured for a single area in the capillary, 15-20 mm from the protein end.

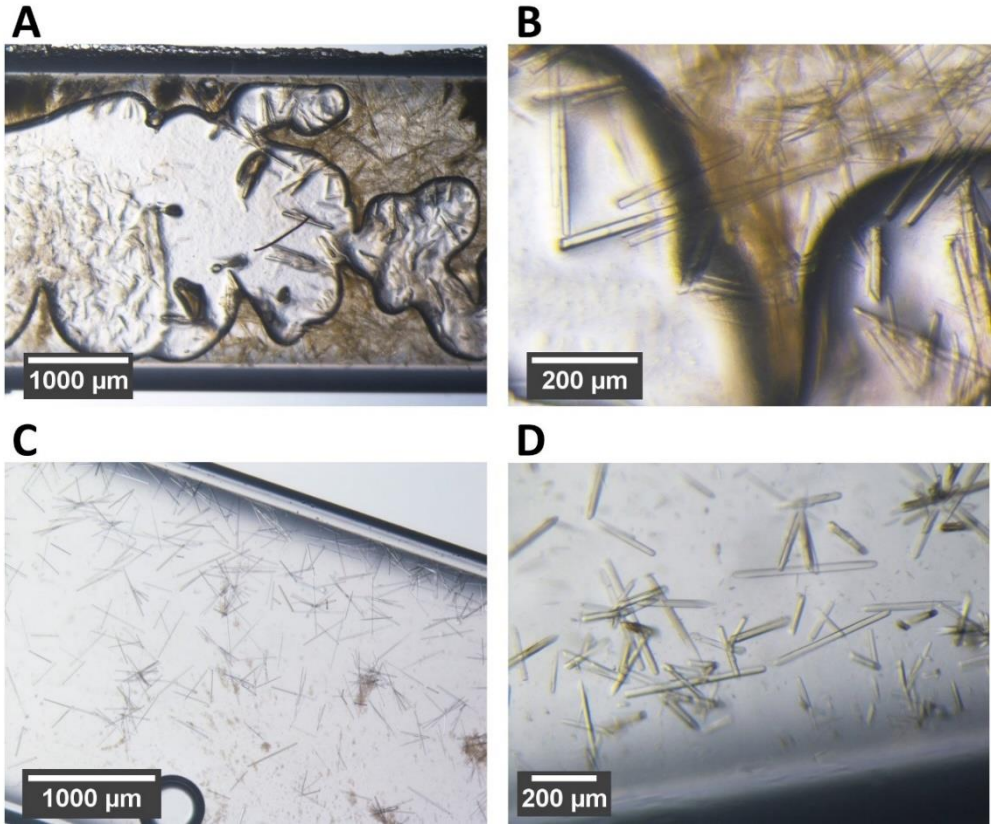

Figure 24. Crystals of *Pf*GST dimer with fluorescence labeled *Pf*GST aggregates in 99:1 total ratio grown in µg and 1G. Crystal images were recorded using a light microscope t = 31 days after sample thawing, after µg samples returned on the earth. (A) Crystals grown in µg, images were recorded with a 2.5 x objective. (B) Crystals grown in µg, recorded with a 10 x objective. (C) Crystals grown in 1G, recorded with a 2.5 x objective. (D) Crystals grown in 1G, recorded with a 10 x objective.

Since samples returned to the earth light microscope images of crystals grown in µg and 1G were recorded and photo-documented. Crystal images were recorded t = 31 days after sample thawing with 2.5 x and 10 x magnification (Figure 24). Crystal dimensions, 200 – 500 µm, are similar for µg and 1G grown crystals (Figure 24).

5.1.1.5 LMM monitoring of crystal growth in microgravity, 95 : 5 ratio

*Pf*GST needle-like crystals in the capillary area 24 - 37 mm from the protein solution end were observed for the dimer with the addition of tetramer in 95 : 5 ratio (Figure 25). Furthermore, crystals of different sizes were observed. (Figure 25). The length of the major axis for crystals was measured to be 50 to 80 µm for smaller crystals and 100 to 170 µm for larger crystals (Figure 25). Time-lapse images for different capillary areas were recorded with 2.5 x and 10 x magnification to investigate crystal growth rates for crystals grown in microgravity. The first image was taken t = 321 min after sample thawing with 2.5 x magnification.

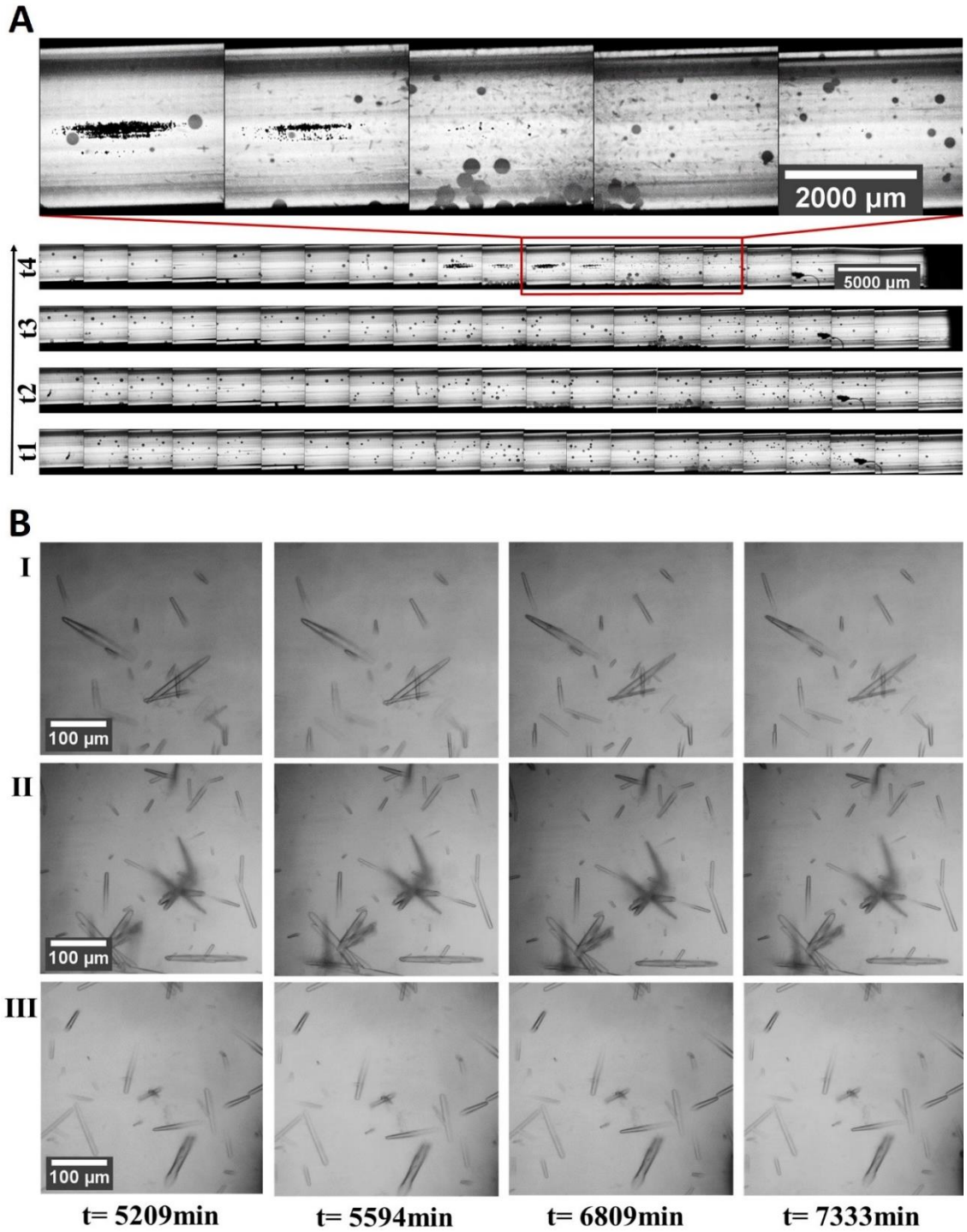

Figure 25. Protein crystallization in microgravity applying counter diffusion technique in capillaries. Images were recorded using the ISS LMM microscope. *Pf*GST dimer crystals with fluorescence labeled *Pf*GST aggregates in 95:5 total ratio. (A) Time-lapse images were recorded with 2.5 x magnification. The imaging time extended to t = 2566 min, images were taken t1 = 321 min, t2 = 597 min, t3 = 841 and t4 = 2566 min after sample thawing. (B) Time-lapse images were recorded for 3 different areas (I, II, III) in capillary with 10 x magnification. The imaging time extended to t = 7333 min, first image was taken t = 5209 min after sample thawing.

The imaging time extended to t = 2566 min, images were taken t1 = 321 min, t2 = 597 min, t3 = 841 and t4 = 2566 min after sample thawing. Protein precipitation was observed at the time point t4 and at

the same time a subsequent growth of crystals was observed for the images recorded with 2.5 x magnification (Figure 26). However, at time points t = 5209-, 5594-, 6809- and 7333 min, crystals were observed and photo-documented with 10 x magnification (Figure 25).

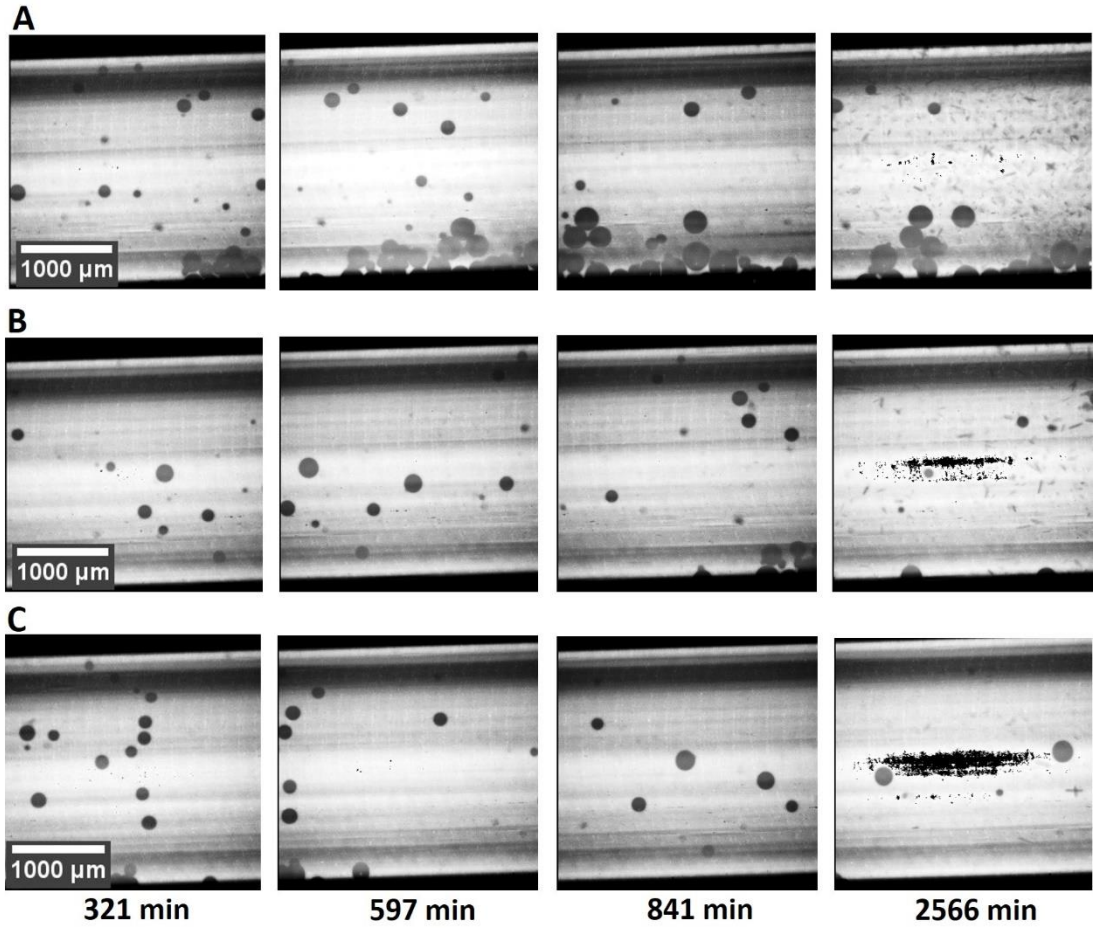

Figure 26. Growth of *Pf*GST crystals in microgravity. *Pf*GST dimer with fluorescence labeled *Pf*GST aggregates in 95:5 total ratio. Time-lapse images were recorded for 3 different areas (A, B, C) in capillary using LMM microscope with 2.5x magnification. The imaging time extended to t = 2566 min. The first image was taken t = 321 min after sample thawing.

5.1.1.6 Crystal growth in 1G vs microgravity, 95 :5 ratio

In parallel time-lapse images for a capillary area, 10– 15 mm from the protein end, were recorded with 10 x magnification to investigate crystals growth rates for crystals grown in 1G. The first image was taken t = 240 min, after sample thawing. The imaging time extended to t = 3640 min. Images were taken t = 240-, t = 700-, t = 930-, t = 1230-, t = 2040- and t = 3640 min after sample thawing (Figure 27). The average growth rate for crystals with length of major axis 146 ± 23 µm was calculated to 2.9 ± 0.6 µm/h (Figure 28).

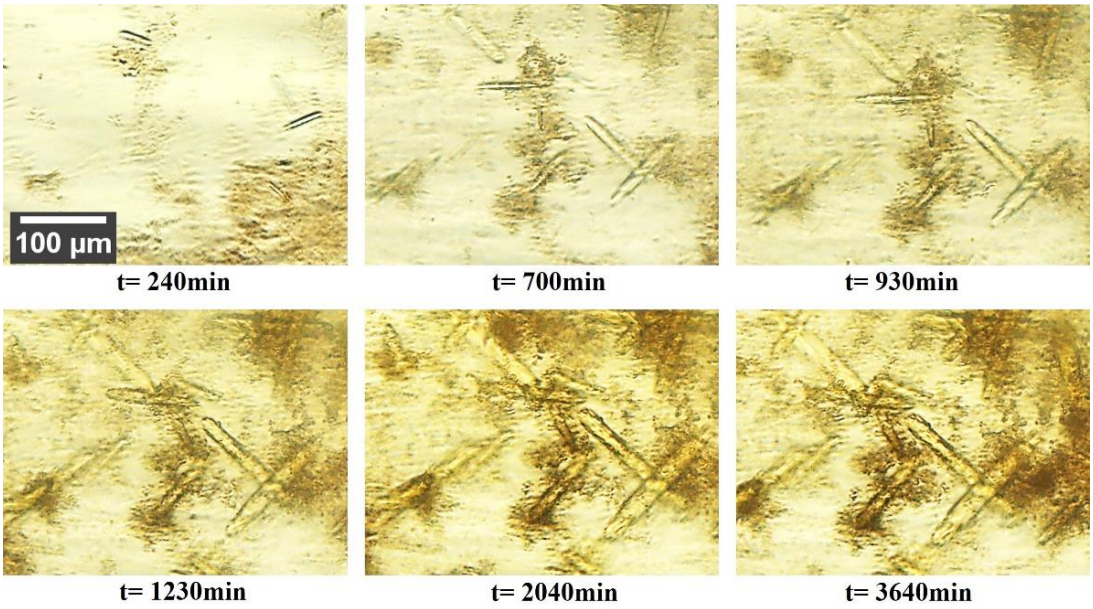

Figure 27. Growth of *Pf*GST crystals in 1G. *Pf*GST dimer additionally fluorescence labeled *Pf*GST aggregates in 95:5 total ratio. Time-lapse images were recorded for a single area in a capillary using the Leica M205 C light microscope. The imaging time extended to t = 3640 min. The first image was taken t = 240 min, after sample thawing.

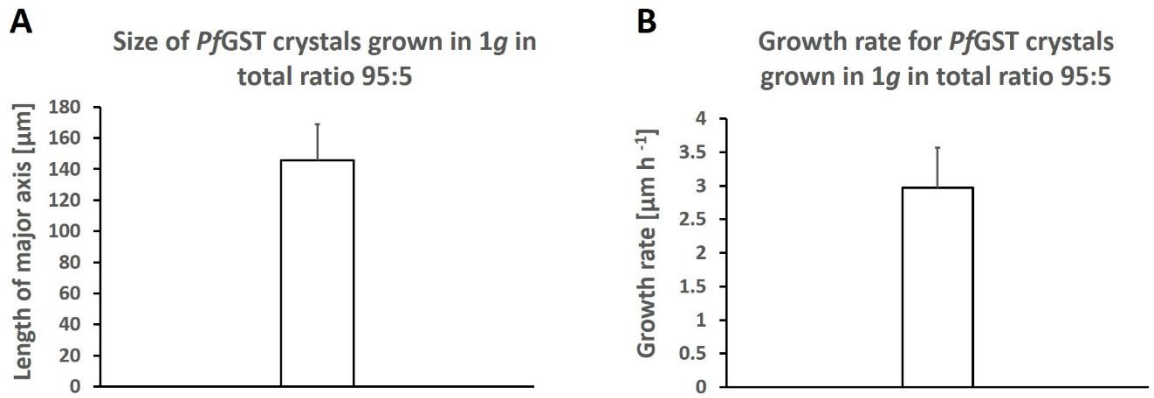

Figure 28. Growth of crystals in 1G. Growth rate and size values (the length of major axis) of dimer crystals with fluorescence labeled *Pf*GST aggregates in 95:5 total ratio for a single area in the capillary, 10-15 mm from the protein end of capillary, were measured. Error bars represent standard deviations of the average. (A) Average size of crystals. The sample size is n = 4 crystals. (B) Average growth rate with standard deviation of crystals with lengths of major axis 146 ± 23 µm. The sample size is n = 4 crystals.

Since samples returned to the earth light microscope images of crystals grown in µg and 1G were recorded and photo-documented. Crystal images were recorded t = 31 days after sample thawing with 2.5 x and 10 x magnification (Figure 29). The crystal dimensions vary for µg and 1G grown crystals.

The µg grown crystals showed on average larger dimensions, with lengths of major axis for larger crystals ~ 1200 µm, compared to 1G with lengths of major axis for larger crystals ~ 500 µm (Figure 29).

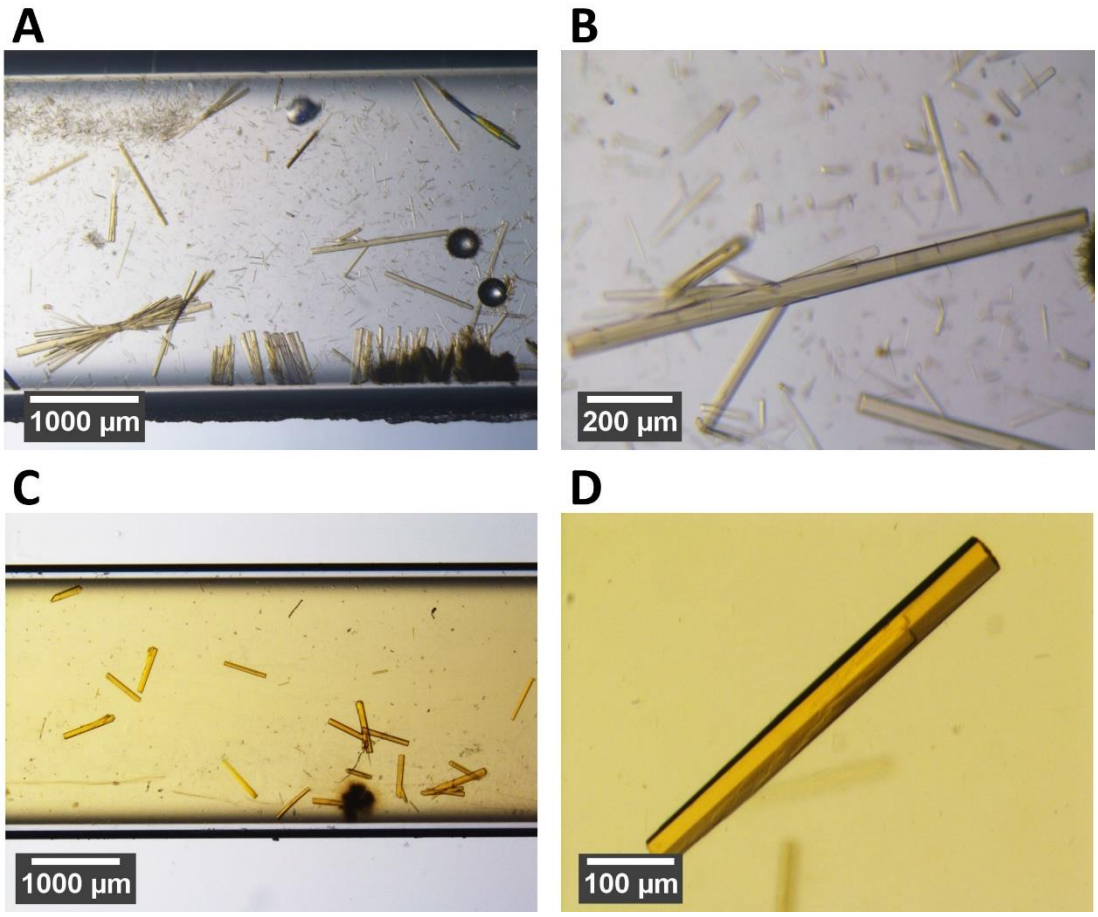

Figure 29. Crystals of *Pf*GST dimer with fluorescence labeled *Pf*GST aggregates in 95:5 total ratio grown in µg and 1G. Crystal images were recorded using a light microscope t = 31 days after sample thawing, after µg samples returned on the earth. (A) Crystals grown in µg, images were recorded with a 2.5 x objective. (B) Crystals grown in µg, recorded with 10 x objective. (C) Crystals grown in 1G, recorded with a 2.5 x objective. (D) Crystals grown in 1G, recorded with a 10 x objective.

5.1.2 Round 2

5.1.2.1 LMM monitoring of crystal growth in microgravity, *Pf*GST dimer

*Pf*GST needle-like crystals in the capillary area 18 - 34 mm from the protein solution end were observed for the dimer (Figure 30). The crystal dimensions and amount of crystals vary for several observed areas in the capillary (Figure 30). Time-lapse images for different capillary areas were recorded with 2.5 x and 10 x magnification to investigate crystal growth rates for crystals grown in microgravity. First image was taken t = 301 min, after sample thawing with 2.5 x magnification. The imaging time extended to t = 8803 min, images were taken t1 = 301 min, t2 = 824 min, t3 = 3266 and t4 = 8803 min after sample thawing. Protein precipitation was observed at the time point t1 and nucleation and subsequent growth of smaller crystals was observed for the images recorded with 2.5 x magnification (Figure 31). However, at the time points t3 – t4 growth of larger crystals was observed (Figure 30). Furthermore, at time points t = 3765-, 3875-, 4390-, 4695-, 7380-, 7450-, 9430-, 9812-, 10208- and 10550 min, crystals of different sizes at different areas in capillary were observed and photo-documented with 10 x magnification (Figure 30). The crystal sizes at different positions in the capillaries were measured and comparative statistically analyzed. The area in the capillary was measured from the end of capillary (i.e. the protein). Temporarily the length of the major axis values for n = 30 dimer crystals were measured. The average size of crystals was calculated in the 3 areas from the capillary end, 18-25 mm, 25-29 mm and 29 -34 mm with crystal sizes 117 ± 21 µm, 196 ± 29 µm and 381 ± 28 µm, respectively. Significant differences for the average crystal sizes from all 3 capillary areas (Student's t-test: $p < 0.01$); Significance for the area 18-25 mm and 25-29 mm ($p < 0.01$); Significance for the area 18-25 mm and 29-34 mm ($p < 0.01$); Significance for the area 25-29 mm and 29-34 mm ($p < 0.01$) was indicated (Figure 32). The average growth rate (1.8 ± 0.1 µm /h) for crystals with length of major axis 303 ± 21 µm were calculated (Figure 32).

Furthermore, the precipitant and protein concentrations for the capillary area with larger crystals were estimated (Chapter III 2.7). The average concentrations at the time point 6034 ± 2768 min (Start of crystal growth) for the capillary area 32 ± 1.1 mm were calculated to 19.9 ± 0.8 nmol for *Pf*GST dimer and 1.1 ± 0.1 M for precipitant.

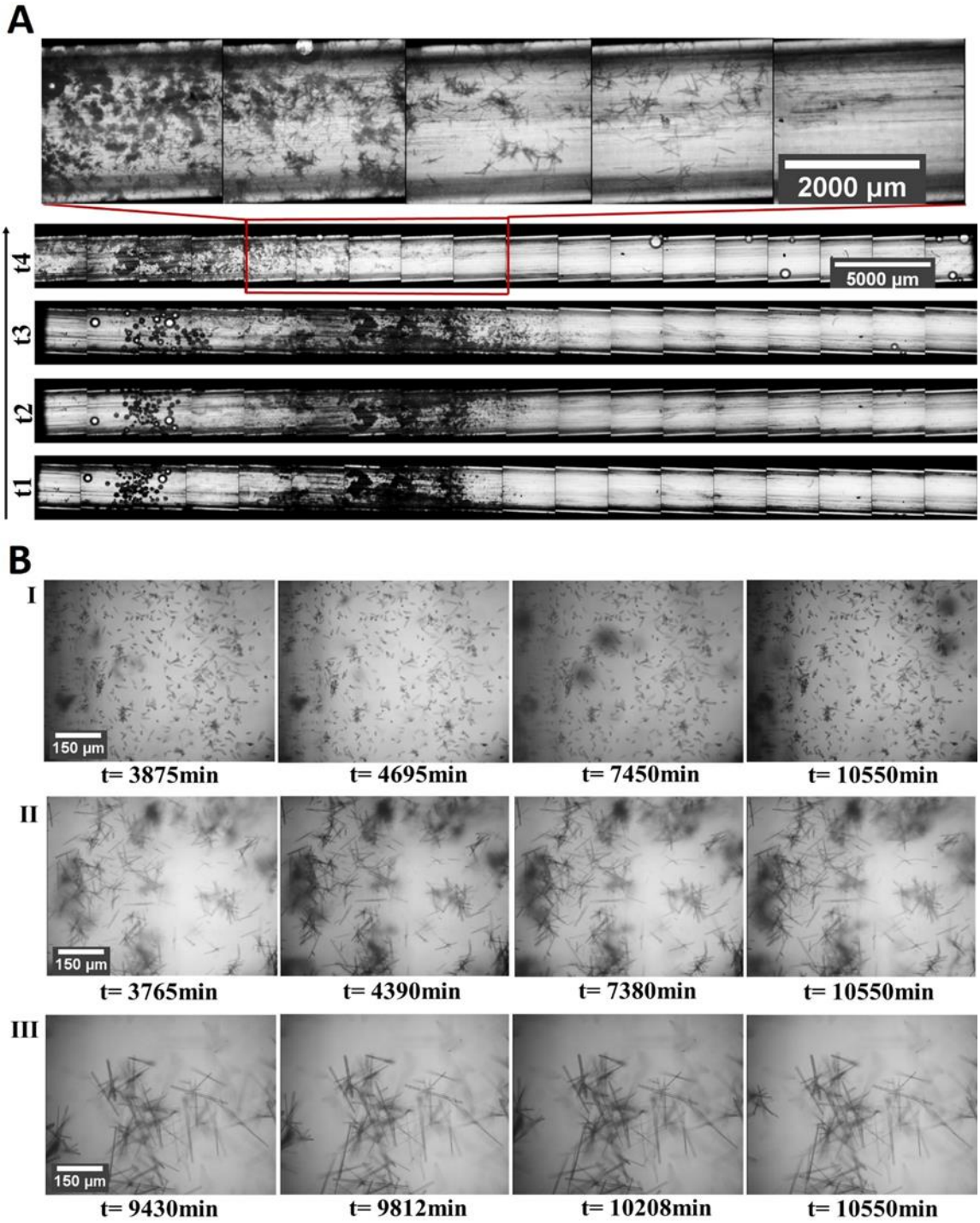

Figure 30. Protein crystallization in microgravity applying counter diffusion technique in capillary. Images were recorded using the ISS LMM microscope. *Pf*GST dimer crystals. (A) Time-lapse images were recorded with 2.5 x magnification. The imaging time extended to t = 8803 min, images were taken t1 = 301 min, t2 = 824 min, t3 = 3266 and t4 = 8803 min after sample thawing. (B) Time-lapse images were recorded for 3 different areas (I, II, III) in capillary with 10 x magnification. The imaging time extended to t = 10550 min, first images were taken t = 3875 min for area I, t = 3765 min for area II and t = 9430 min for area III after sample thawing.

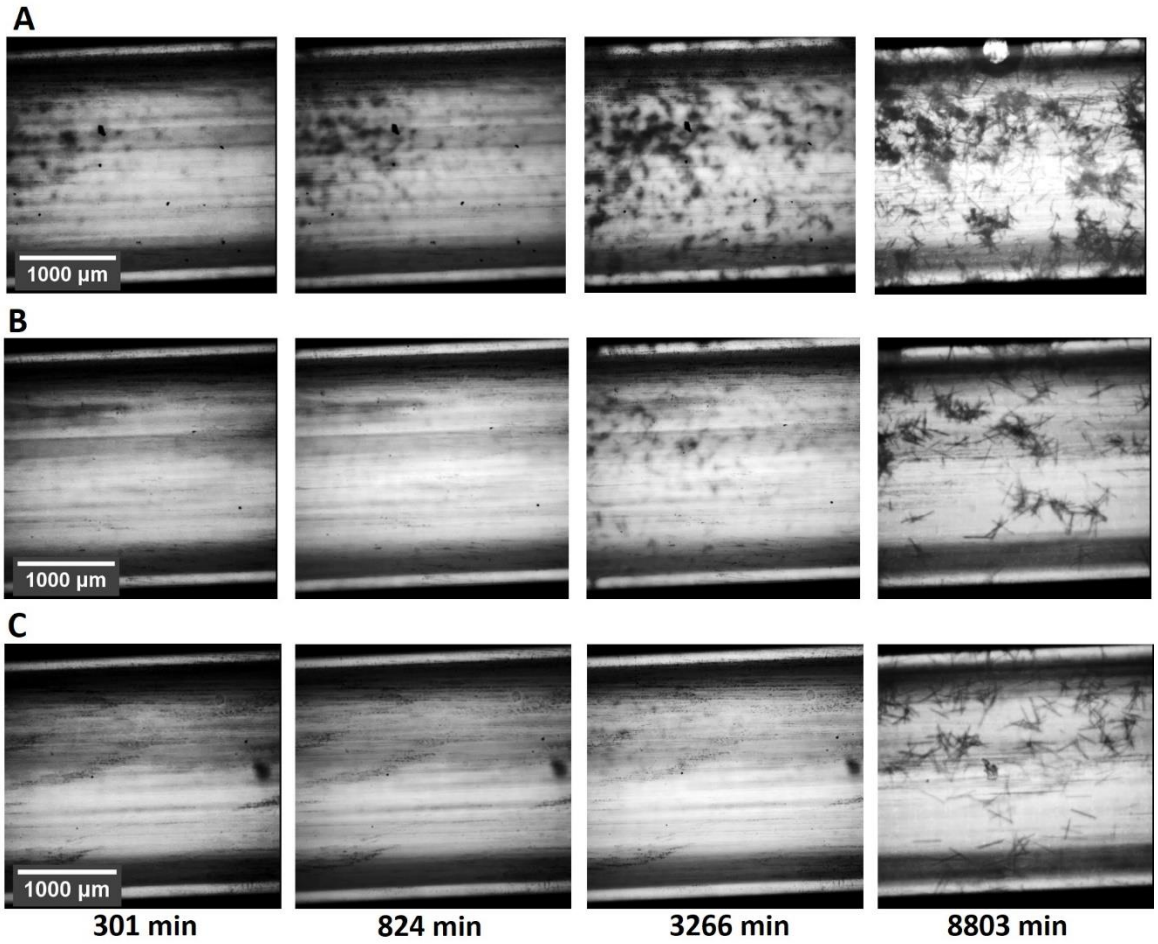

Figure 31. Growth of *Pf*GST crystals in microgravity. *Pf*GST dimer. Time-lapse images were recorded for 3 different areas (A, B, C) in capillary using the LMM microscope with 2.5x magnification. The imaging time extended to t = 8803 min, first image was taken t = 301 min after sample thawing.

5.1.2.2 Crystal growth in 1G vs microgravity, *Pf*GST dimer

In parallel time-lapse images for a capillary area, 7– 12 mm from the protein end, were recorded with 10 x magnification to investigate crystals growth rates for dimer crystals grown in 1G. First image was taken t = 150 min after sample thawing. The imaging time extended to t = 3640 min, images were taken t = 150-, t = 250-, t = 400-, t = 610-, t = 1270- and t = 1900 min after sample thawing (Figure 33). The average growth rate for crystals with length of major axis 84 ± 3 µm was calculated to 3.1 ± 0.1 µm/h (Figure 34).

Since samples returned to the earth, light microscope images of crystals grown in µg and 1G were recorded and photo-documented. Crystal images were recorded t = 25 days after sample thawing with 2.5 x and 10 x magnification (Figure 35). The crystal dimensions, length of major axis 50 - 900 µm, vary at different areas of capillary for µg and 1G grown crystals (Figure 35).

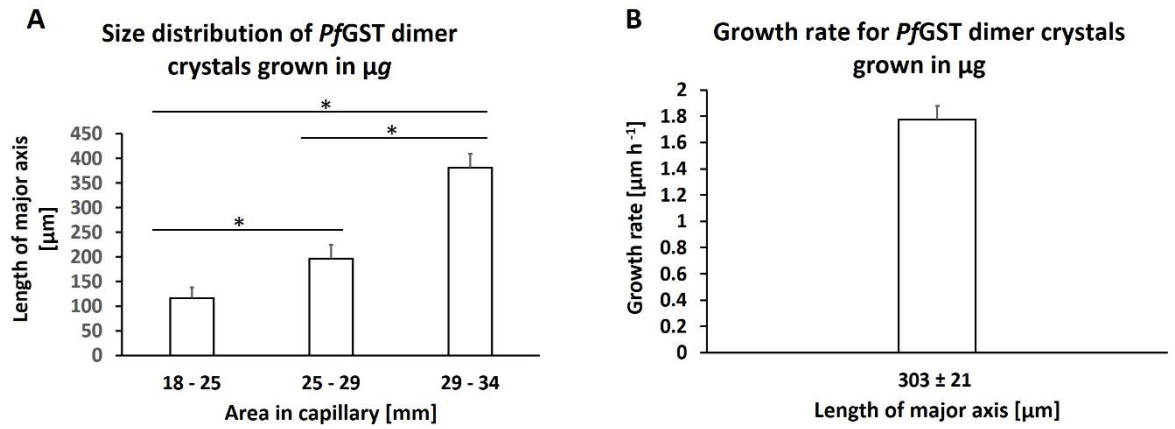

Figure 32. Growth of dimer crystals in µg. Comparative size distribution and growth rate values (the length of major axis) of crystals along the capillary. Different regions (areas) along the capillary were measured from the protein end of the capillary toward the protein-precipitant interface. Error bars represent standard deviations of the average. Significance within a 99% confidence interval was determined using Student's *t*-test and is denoted by asterisk (* = $p < 0.01$). (A) Average size distribution of crystals for the areas from the capillary end, 18-25 mm, 25-29 mm and 29-34 mm. The sample sizes for crystals in the areas, 18-25 mm, 25-29 mm and 29-34 mm are n = 10, n = 10 and n = 10, respectively. (B) Average growth rate with standard deviation of crystals with lengths of major axis 303 ± 21 µm. The sample number is n = 4 crystals.

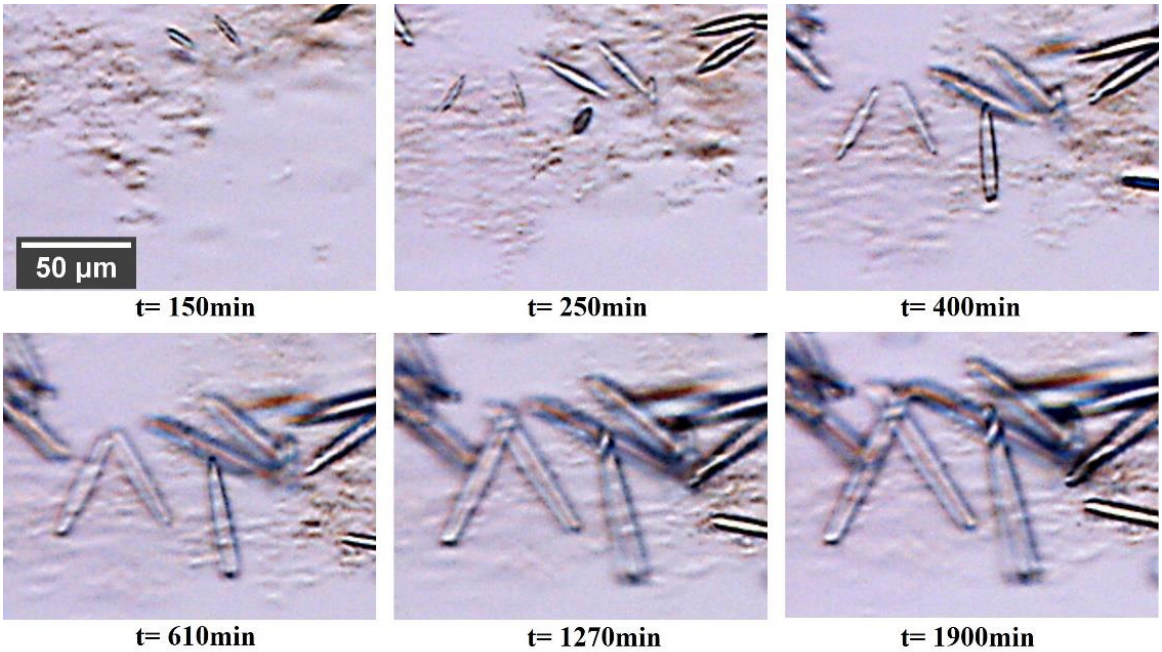

Figure 33. Growth of *Pf*GST crystals in 1G. *Pf*GST dimer. Time-lapse images were recorded for a single area in capillary, 7-12 mm from the protein end of capillary, using the Leica M205 C light microscope. The imaging time extended to t = 1900 min, first image was taken t = 150 min after sample thawing.

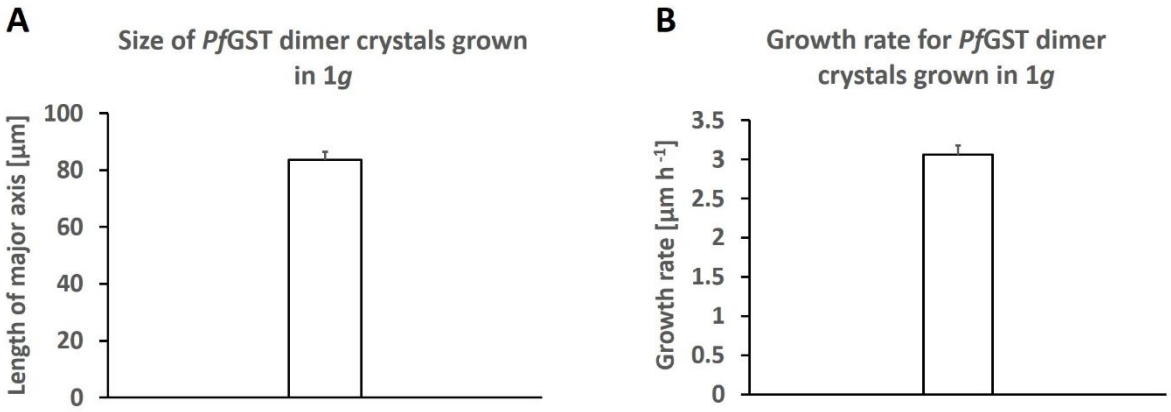

Figure 34. Growth of crystals in 1*g*. Growth rate and size values (the length of major axis) of dimer crystals for a single area in the capillary, 7-12 mm from the protein end of capillary, were measured. Error bars represent standard deviations of the average. (A) Average size of crystals. The sample number is n = 4 crystals. (B) Average growth rate with standard deviation of crystals with lengths of major axis 84 ± 3 µm. The sample number is n = 4 crystals.

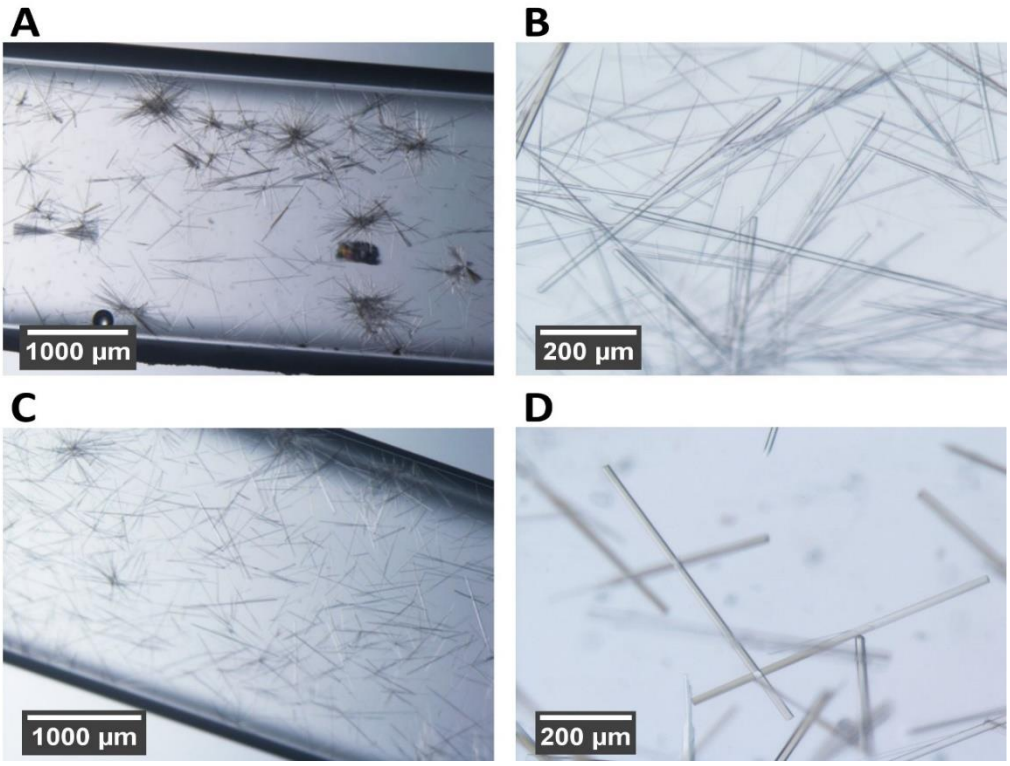

Figure 35. Crystals of *Pf*GST dimer grown in µg and 1G. Crystal images were recorded using a light microscope t = 25 days after sample thawing, after µg samples returned on the earth. (A) Crystals grown in µg, images were recorded with a 2.5 x objective. (B) Crystals grown in µg, recorded with 10 x objective. (C) Crystals grown in 1G, recorded with a 2.5 x objective. (D) Crystals grown in 1G, recorded with a 10 x objective

5.1.2.3 LMM monitoring of crystal growth in microgravity, 99.8 : 0.2 ratio

*Pf*GST needle-like crystals in the capillary area 17 - 38 mm from the protein solution end were observed for the dimer with the addition of tetramer in 99.8 : 0.2 ratio (Figure 36). The crystal dimensions and amount of crystals vary for several observed areas in the capillary (Figure 36). Time-lapse images for different capillary areas were recorded with 2.5 x and 10 x magnification to investigate crystal growth rates for crystals grown in microgravity. First image was taken t = 293 min, after sample thawing with 2.5 x magnification. The imaging time extended to t = 8666 min, images were taken t1 = 293 min, t2 = 790 min, t3 = 3258 and t4 = 8666 min after sample thawing. Protein precipitation was observed at the time point t2 and nucleation and subsequent growth of smaller crystals was observed for the images recorded with 2.5 x magnification (Figure 36; 37). However, at the time points t3 – t4 growth of larger crystals was observed (Figure 36; 37). Furthermore, at time points t = 915-, 1124-, 1855-, 4033-, 4614-, 6229-, 9355-, 9562-, 9800- and 10485 min, crystals of different sizes at different areas in capillary were observed and photo-documented with 10 x magnification (Figure 36). The crystal sizes at different positions in the capillaries were measured and comparative statistically analyzed. The area in the capillary was measured from the end of the capillary (i.e. the protein). Temporarily the length of the major axis values for n = 31 crystals were measured. The average size of crystals was calculated in the 4 areas from the capillary end, 17-25 mm, 25-30 mm, 30-35 mm and 35 -38 mm with crystal sizes 111 ± 9 µm, 424 ± 26 µm, 698 ± 23 µm and 505 ± 23 µm, respectively. Significant differences for the average crystal sizes from all 4 capillary areas (Student's t-test: $p < 0.01$); Significance for the area 17-25 mm and 25-30 mm ($p < 0.01$); Significance for the area 17-25 mm and 30-35 mm ($p < 0.01$); Significance for the area 17-25 mm and 35-38 mm ($p < 0.01$); Significance for the area 25-30 mm and 30-35 mm ($p < 0.01$); Significance for the area 25-30 mm and 35-38 mm ($p < 0.01$); Significance for the area 30-35 mm and 35-38 mm ($p < 0.01$) is indicated (Figure 38). The average growth rate for crystals with lengths of major axis 111 ± 5 µm and 425 ± 14 µm were calculated (Figure 38). The average growth rate (1.8 ± 0.2 µm/h) for crystals with length of major axis 111 ± 5 µm were significantly higher (Student's t-test: $p < 0.01$), than the average growth rate (1.3 ± 0.1 µm/h) for crystals with the length of the major axis 425 ± 14 µm (Figure 38).

Furthermore, the precipitant and protein concentrations for the capillary area with larger crystals were estimated (Chapter III 2.7). The average concentrations at the time point 5962 ± 2704 min (Start of crystal growth) for the capillary area 32 ± 1.1 mm were calculated to 20.7 ± 0.8 nmol for *Pf*GST dimer and 1.1 ± 0.1 M for precipitant.

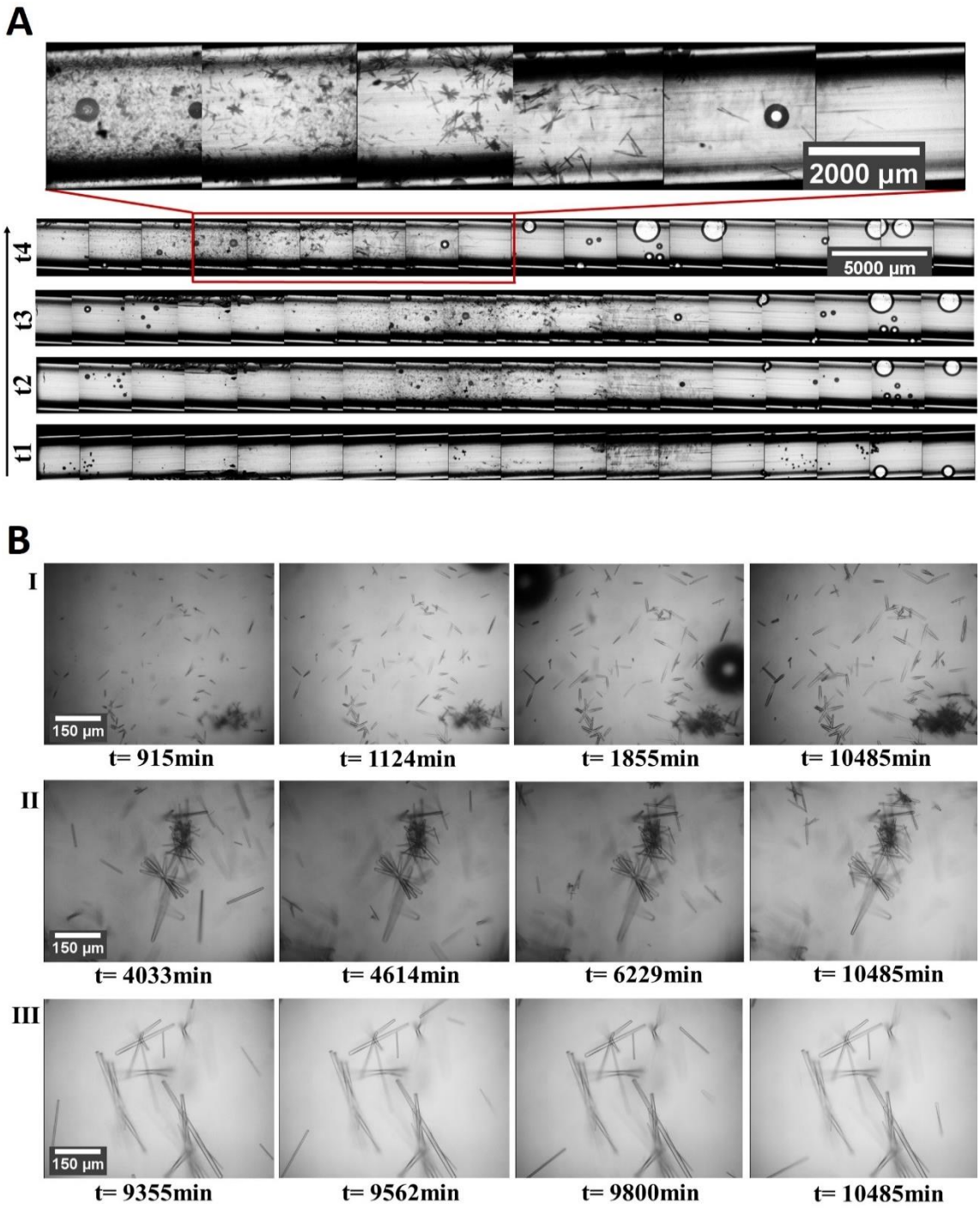

Figure 36. Protein crystallization in microgravity applying the counter diffusion technique in capillaries. Images were recorded using the ISS LMM microscope. *Pf*GST dimer crystals additionally fluorescence labeled *Pf*GST aggregates in 99.8:0.2 total ratio. (A) Time-lapse images were recorded with 2.5 x magnification. The imaging time extended to t = 8666 min, images were taken t1 = 293 min, t2 = 790 min, t3 = 3258 and t4 = 8666 min after sample thawing. (B) Time-lapse images were recorded for 3 different areas (I, II, III) in capillary with 10 x magnification. The imaging time extended to t = 10485 min, first images were taken t = 915 min for area I, t = 4033 min for area II and t = 9355 min for area III after sample thawing.

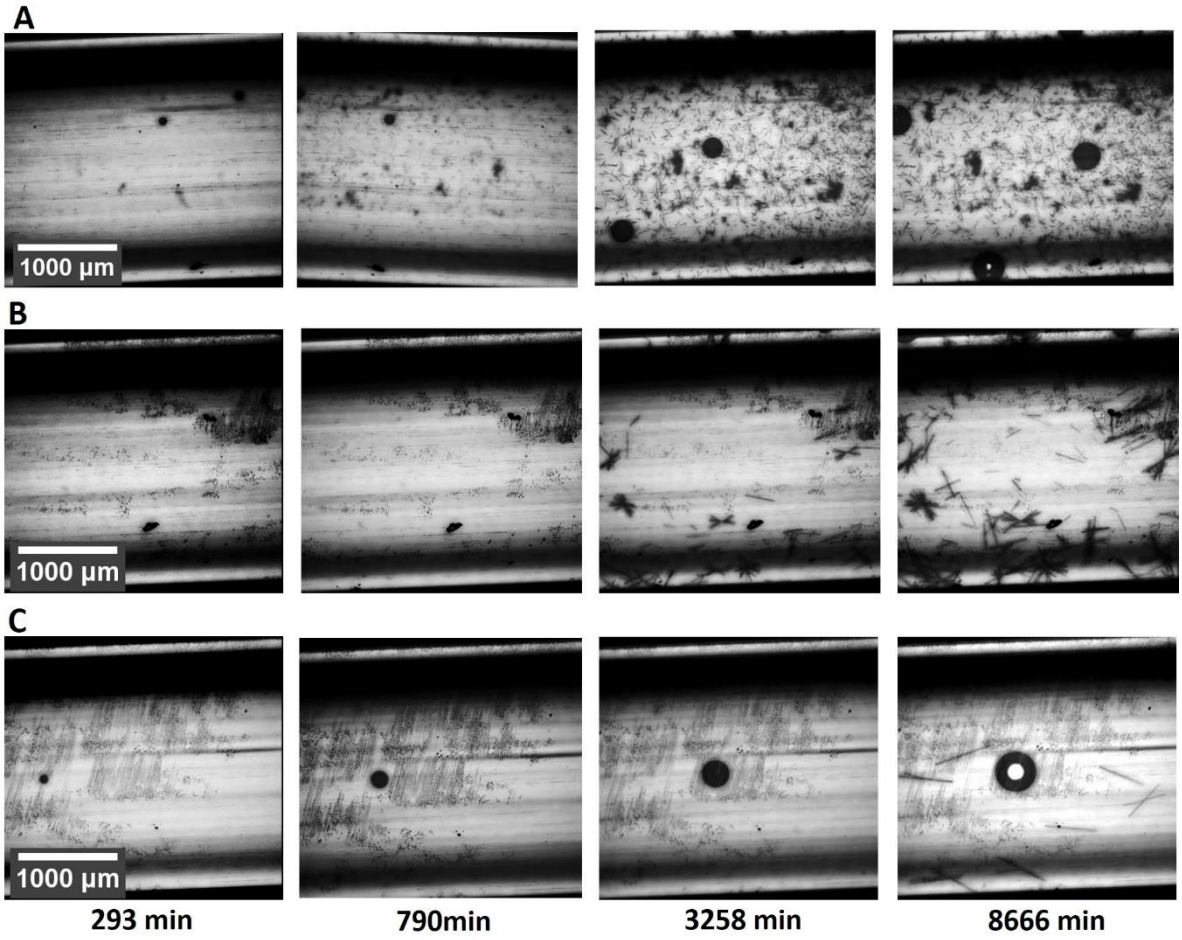

Figure 37. Growth of *Pf*GST crystals in microgravity. *Pf*GST dimer additionally fluorescence labeled *Pf*GST aggregates in 99.8:0.2 total ratio. Time-lapse images were recorded for 3 different areas (A, B, C) in a capillary using the LMM microscope with 2.5x magnification. The imaging time extended to t = 8666 min, first image was taken t = 293 min after sample thawing.

5.1.2.4 Crystal growth in 1G vs microgravity, 99.8 : 0.2 ratio

Since samples returned to the earth light microscope images of crystals grown in µg and 1G were recorded and photo-documented. Crystal images were recorded t = 25 days after sample thawing with 2.5 x and 10 x magnification (Figure 39). The crystal dimensions, length of major axis 50 - 1600 µm, vary at different areas of the capillaries for µg and 1G grown crystals (Figure 39). The µg grown crystals showed on average larger dimensions, with lengths of major axis for larger crystals ~ 1500 µm, compared to 1G, with lengths of the major axis for larger crystals ~ 650 µm (Figure 39).

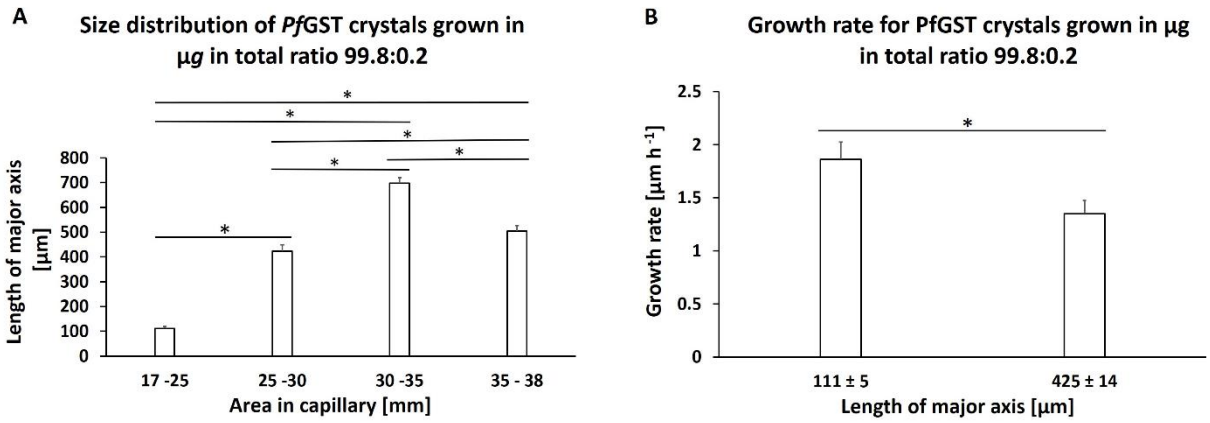

Figure 38. Crystals grown in µg. *Pf*GST dimer crystals additionally fluorescence labeled *Pf*GST aggregates in 99.8:0.2 total ratio. Comparative growth rate and size distribution values (the length of major axis) of crystals along the capillary. Different regions (areas) along the capillary were measured from the protein end of the capillary toward the protein-precipitant interface. Error bars represent standard deviations of the average. Significance within a 99% confidence interval was determined using Student's *t*-test and is denoted by asterisk (* = p < 0.01). (A) Average size distribution of crystals for the areas from the capillary end, 17-25 mm, 25-30 mm, 30-35 mm and 35-38 mm. The sample sizes for crystals in the areas, 17-25 mm, 25-30 mm, 30-35 mm and 35-38 mm are n = 10, n = 10, n = 6 and n = 5, respectively. (B) Average growth rates with standard deviations of crystals with lengths of major axis 111 ± 5 µm and 425 ± 14 µm. The sample sizes for crystals 111 ± 5 µm and 425 ± 14 µm are n = 4 and n = 4 respectively.

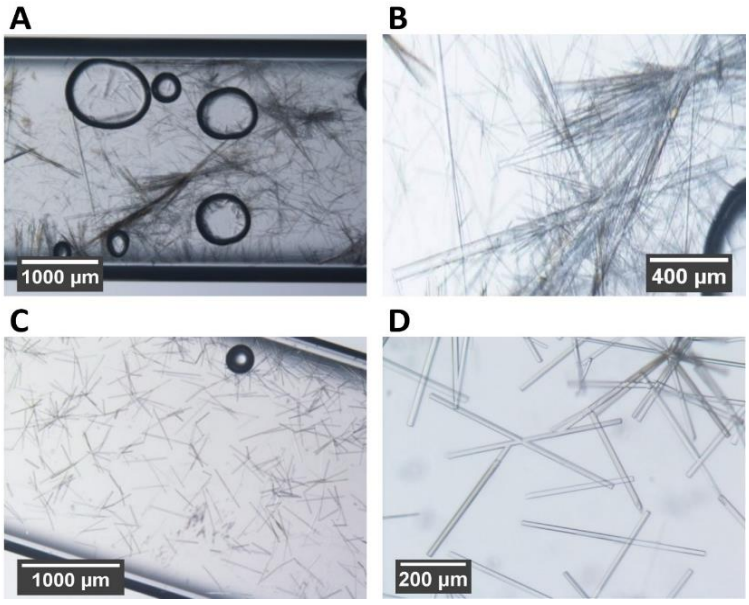

Figure 39. Crystals of the *Pf*GST dimer with fluorescence labeled *Pf*GST aggregates in 99.8:0.2 total ratio grown in µg and 1G. Crystal images were recorded using a light microscope t = 25 days after sample thawing, after µg samples returned on the earth. (A) Crystals grown in µg, images were recorded with a 2.5 x objective. (B) Crystals grown in µg, recorded with a 10 x objective. (C) Crystals grown in 1G, recorded with a 2.5 x objective. (D) Crystals grown in 1G, recorded with a 10 x objective.

5.1.2.5 LMM monitoring of crystal growth in microgravity, 99.5 :0.5 ratio

*Pf*GST needle-like crystals in the capillary area 26 - 44 mm from the protein solution end were observed for the dimer with the addition of tetramer solution in 99.5 : 0.5 ratio (Figure 40). The crystal dimensions and amount of crystals vary for several observed areas in the capillary (Figure 40). Time-lapse images for different capillary areas were recorded with 2.5 x and 10 x magnification to investigate crystal growth rates for crystals grown in microgravity. First image was taken t = 301 min after sample thawing with 2.5 x magnification. The imaging time extended to t = 8674 min, images were taken t1 = 301 min, t2 = 824 min, t3 = 3266 and t4 = 8674 min after sample thawing. Protein precipitation was observed at the time point t1 and at the time points t3 – t4 nucleation and subsequent growth of crystals was observed for the images recorded with 2.5 x magnification (Figure 40; 41). Furthermore, at time points t = 900-, 1277-, 1307-, 1965-, 2012-, 2560-, 3590-, 4061-, 6435- and 10515 min, crystals of different sizes at different areas in the capillary were observed and photo-documented with 10 x magnification (Figure 40). The crystal sizes at different positions in the capillaries were measured and comparative statistically analyzed. The area in the capillary was measured from the end of the capillary (i.e. the protein). Temporarily the length of major axis values for n = 61 crystals were measured. The average size of crystals was calculated in 4 areas from the capillary end, 26-29 mm, 29-35 mm, 35-41 mm and 41-44 mm with crystal sizes 158 ± 30 µm, 380 ± 54 µm, 770 ± 55 µm and 571 ± 54 µm, respectively. Significant difference for the average crystal sizes from all 4 capillary areas (Student's t-test: $p < 0.01$); Significance for the area 26-29 mm and 29-35 mm ($p < 0.01$); Significance for the area 26-29 mm and 35-41 mm ($p < 0.01$); Significance for the area 26-29 mm and 41-44 mm ($p < 0.01$); Significance for the area 29-35 mm and 35-41 mm ($p < 0.01$); Significance for the area 29- 35 mm and 41-44 mm ($p < 0.01$); Significance for the area 35-41 mm and 41-44 mm ($p < 0.01$) was indicated (Figure 42). The average growth rates for crystals with lengths of major axis < 200 µm and 300-400 µm were calculated (Figure 42). The average growth rate (2.4 ± 0.28 µm/h) for crystals with length of major axis < 200 µm were significantly higher (Student's t-test: $p < 0.01$), than the average growth rate (1.2 ± 0.13 µm/h1) for crystals with the length of major axis 300-400 µm (Figure 42).

Furthermore, the precipitant and protein concentrations for the capillary area with larger crystals were estimated (Chapter III 2.7). The average concentrations at the time point 5970 ± 2704 min (Start of crystal growth) for the capillary area 38 ± 1.4 mm were calculated to 15.5 ± 1.9 nmol for *Pf*GST dimer and 1.3 ± 0.1 M for precipitant.

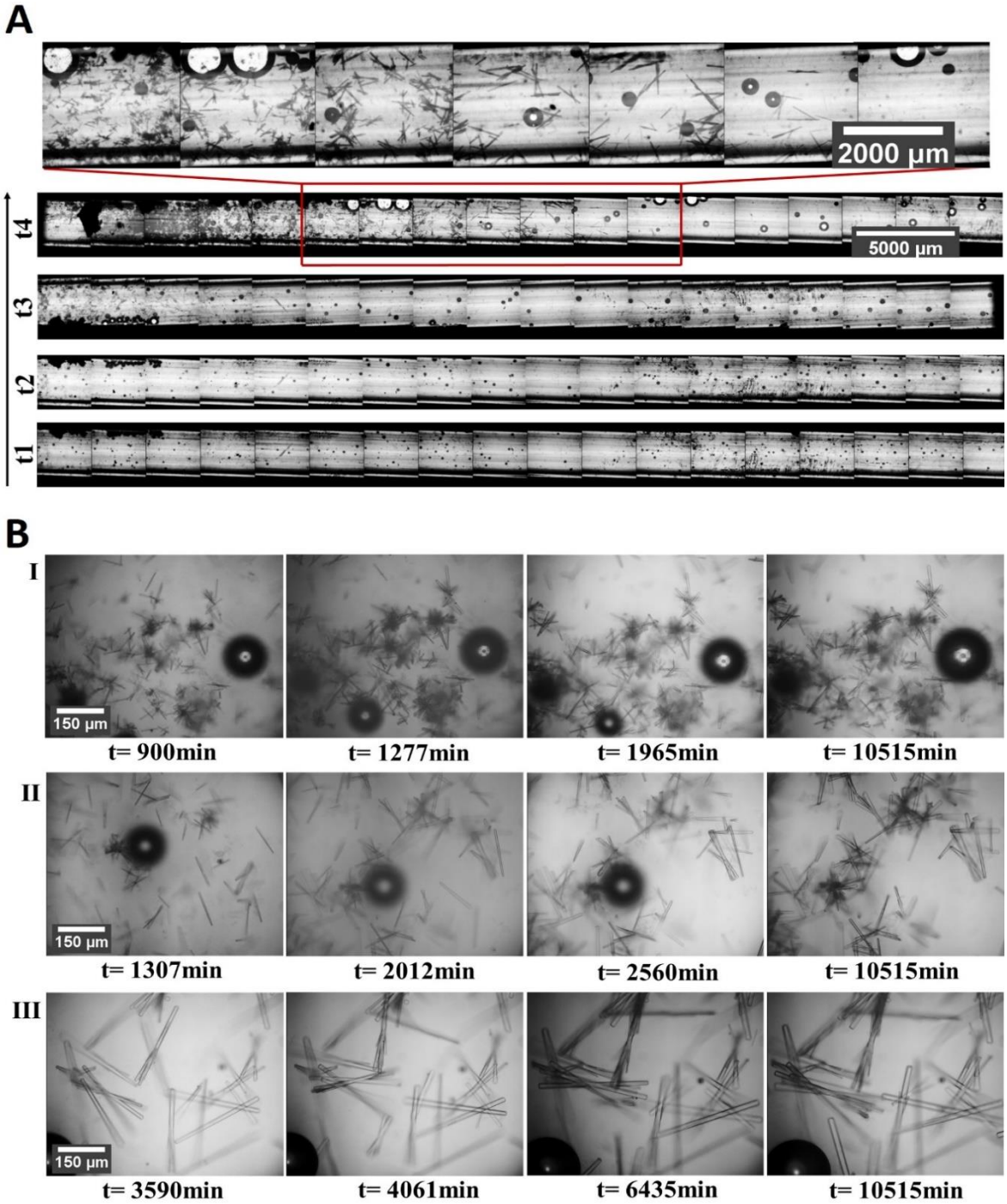

Figure 40. Protein crystallization in microgravity applying the counter diffusion technique in capillaries. Images were recorded using the ISS LMM microscope. *Pf*GST dimer crystals with fluorescence labeled *Pf*GST aggregates in 99.5:0.5 total ratio. (A) Time-lapse images were recorded with 2.5 x magnification. The imaging time extended to t = 8674 min, images were taken t1 = 301 min, t2 = 824 min, t3 = 3266 and t4 = 8674 min after sample thawing. (B) Time-lapse images were recorded for 3 different areas (I, II, III) in capillary with 10 x magnification. The imaging time extended to t = 10515 min, first images were taken t = 900 min for area I, t = 1307 min for area II and t = 3590 min for area III after sample thawing.

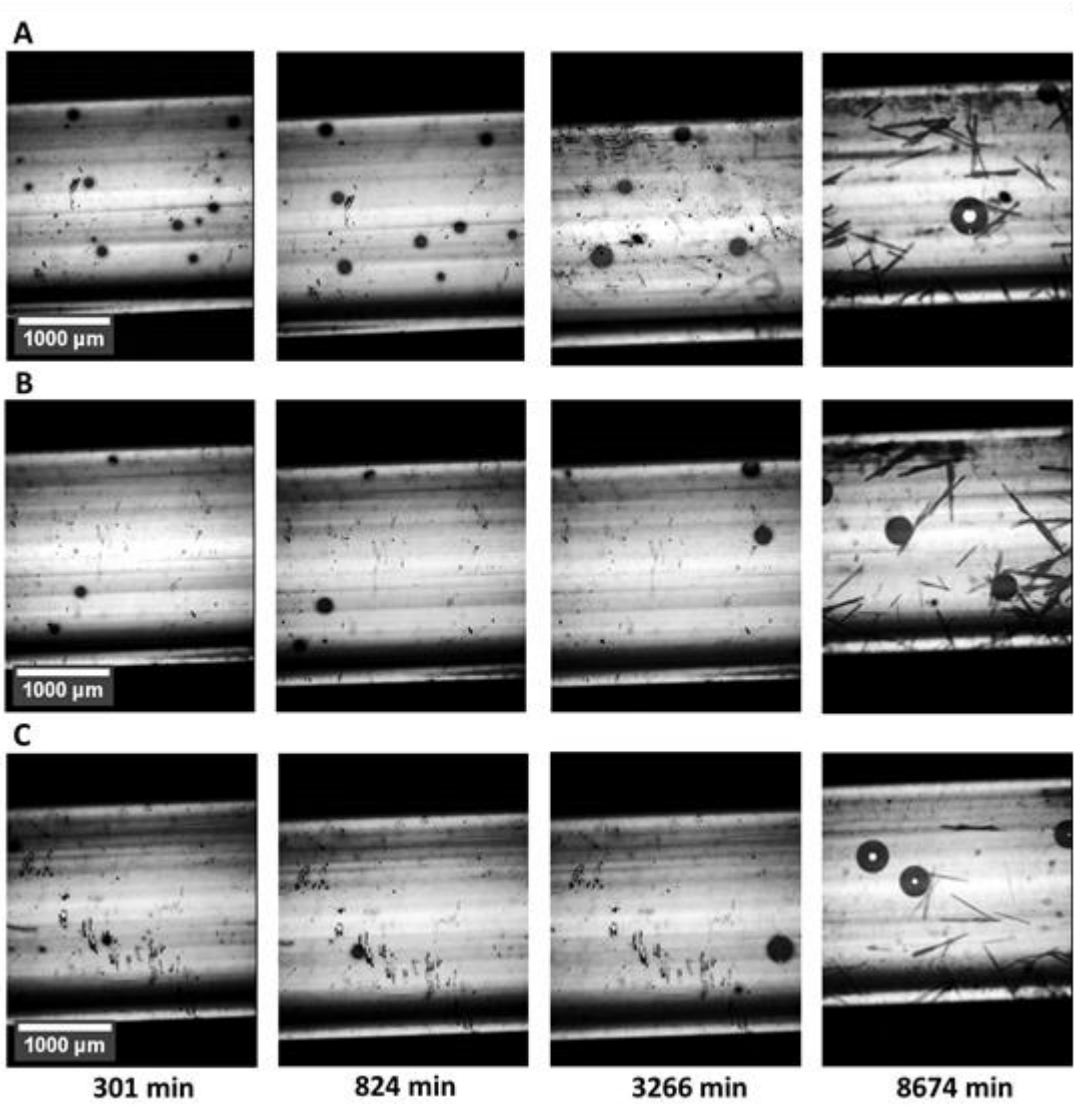

Figure 41. Growth of *Pf*GST crystals in microgravity. *Pf*GST dimer with fluorescence labeled *Pf*GST aggregates in 99.5:0.5 total ratio. Time-lapse images were recorded for 3 different areas (A, B, C) in capillary using the LMM microscope with 2.5x magnification. The imaging time extended to t = 8674 min. The first image was taken t = 301 min after sample thawing.

5.1.2.6 Crystal growth in 1G vs microgravity, 99.5 :0.5 ratio

Since samples returned to the earth light microscope images of crystals grown in µg and 1G were recorded and photo-documented. Crystal images were recorded t = 25 days after sample thawing with 2.5 x and 10 x magnification (Figure 43). The crystal dimensions, length of major axis 100 - 1100 µm, vary at different areas of capillary for µg and 1G grown crystals (Figure 43). The µg grown crystals showed on average larger dimensions, with lengths of the major axis for larger crystals ~ 1100 µm, compared to 1G, with lengths of major axis for larger crystals ~ 600 µm (figure 43).

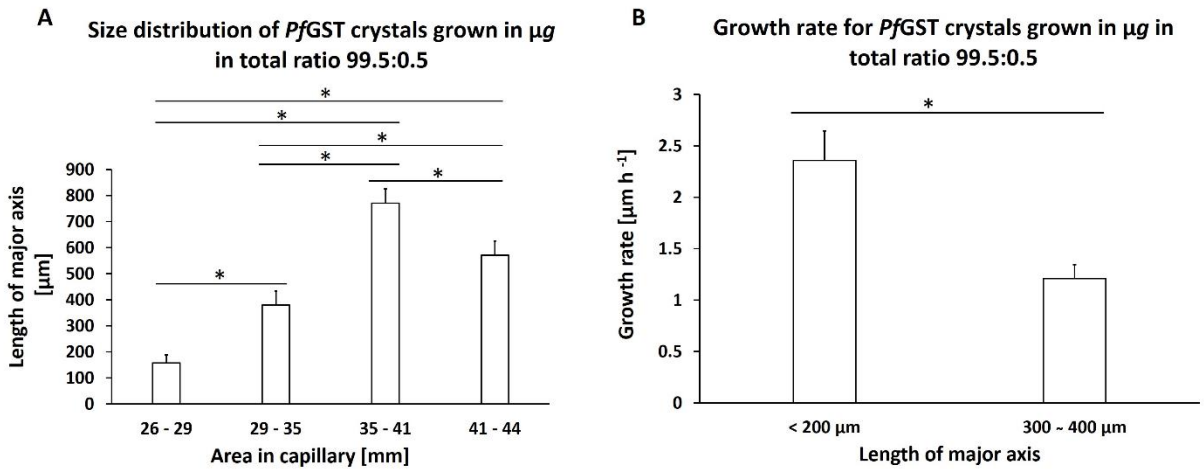

Figure 42. Crystals grown in µg. *Pf*GST dimer crystals with fluorescence labeled *Pf*GST aggregates in 99.5:0.5 total ratio. Comparative growth rate and size distribution values (the length of major axis) of crystals along the capillary. Different regions (areas) along the capillary were measured from the protein end of the capillary toward the protein-precipitant interface. Error bars represent standard deviations of the average. Significance within a 99% confidence interval was determined using Student's *t*-test and is denoted by asterisk (* = p < 0.01). (A) Average size distribution of crystals for the areas from the capillary end, 26-29 mm, 29-35 mm, 35-41 mm and 41-44 mm. The sample sizes for crystals in the areas, 26-29 mm, 29-35 mm, 35-41 mm and 41-44 mm are n = 15, n = 20, n = 18 and n = 8, respectively. (B) Average growth rates with standard deviations of crystals with lengths of major axis < 200 µm and 300 - 400 µm. The sample number for crystals < 200 µm and 300 - 400 µm are n = 3 and n = 3 respectively.

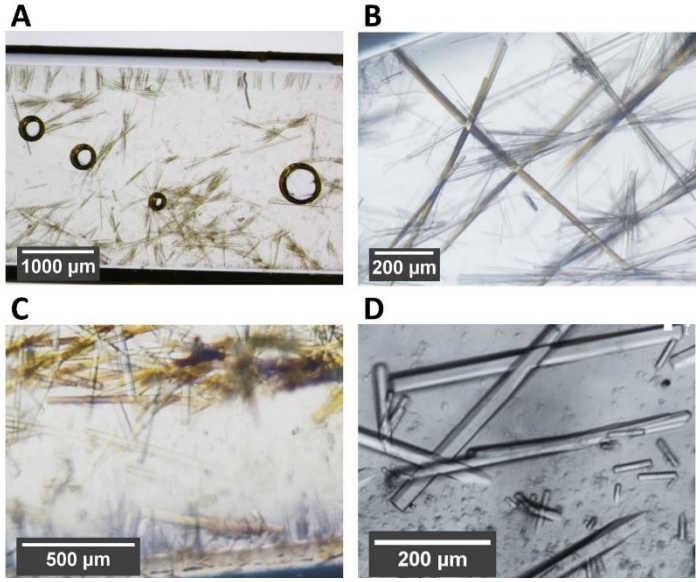

Figure 43. Crystals of *Pf*GST dimer with fluorescence labeled *Pf*GST aggregates in 99.5:0.5 total ratio grown in µg and 1G. Crystal images were recorded using a light microscope t = 25 days after sample thawing, after µg samples returned on the earth. (A) Crystals grown in µg, images were recorded with a 2.5 x objective. (B) Crystals grown in µg, recorded with a 10 x objective. (C) Crystals grown in 1G, recorded with a 2.5 x objective. (D) Crystals grown in 1G were recorded with a 10 x objective.

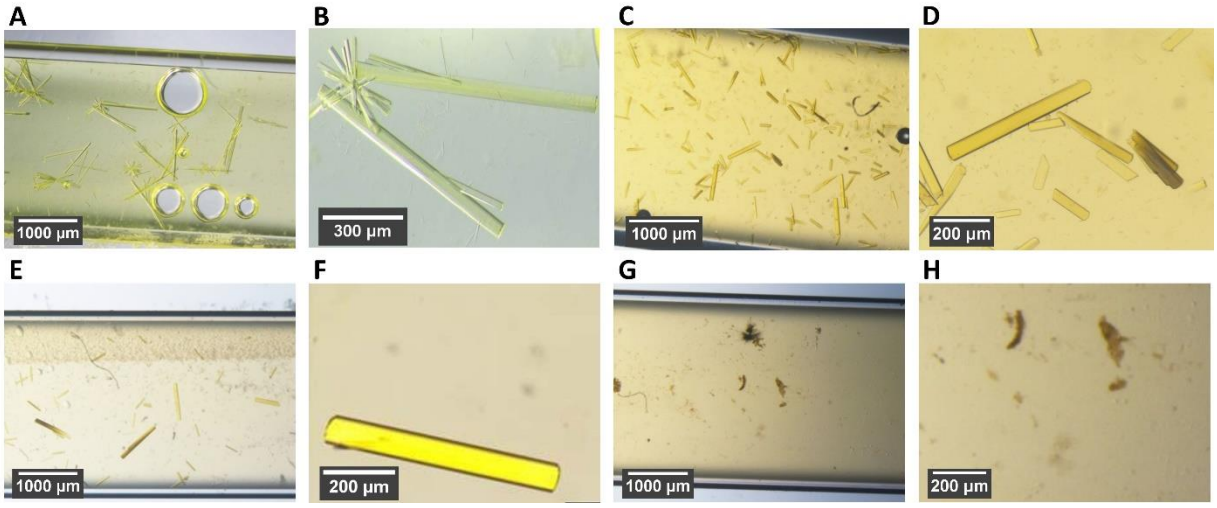

Figure 44. Crystals of *Pf*GST dimer with fluorescence labeled *Pf*GST aggregates in 90:10 and 72:25 total ratios grown in µg and 1G. Crystal images were recorded using a light microscope t = 25 days after sample thawing, after µg samples returned on the earth. (A) Crystals grown in µg in 90:10 total ratio, images were recorded with a 2.5 x objective. (B) Crystals grown in µg in 90:10 total ratio, recorded with a 10 x objective. (C) Crystals grown in µg in 75:25 total ratio, recorded with a 2.5 x objective. (D) Crystals grown in µg in 75:25 total ratio, recorded with a 10 x objective. (E) Crystals grown in 1G in 90:10 total ratio, recorded with a 2.5 x objective. (F) Crystals grown in 1G in 90:10 total ratio, recorded with a 10 x objective. (G) 1G, 75:25 total ratio, recorded with a 2.5 x objective. (H) 1G, 75:25 total ratio, recorded with a 10 x objective.

5.1.2.7 Crystal growth in 1G vs microgravity, 90 : 10 and 75 :25 ratios

The flight cassette with the ratios 90 : 10; 75 : 25 was not installed to the LMM microscope after sample thawing, so that the crystal growth in µg was not photo documented. Since samples returned to the earth light microscope images of crystals grown in µg and 1G were recorded and photo-documented. Crystal images were recorded t = 25 days after sample thawing with 2.5 x and 10 x magnification (Figure 44). The crystal dimensions, length of major axis 50 - 900 µm, vary at different areas of capillary for µg and 1G grown crystals for dimer with the addition of tetramer in 90 : 10 ratio (Figure 44). The µg grown crystals showed on average larger dimensions, with lengths of major axis for larger crystals ~ 900 µm, compared to 1G, with lengths of major axis for larger crystals ~ 500 µm (figure 44). Furthermore, crystals grown in µg with lengths of major axis 50 – 500 µm were observed and photo documented for the dimer with the addition of tetramer in 75 : 25 ratio (Figure 44). On the other hand crystals in 1G capillary with similar ratio (75 : 25) were not observed (Figure 44).

5.1.2.8 LMM monitoring of crystal growth in microgravity, lysozyme

Lysozyme crystals in the capillary area 13 - 44 mm from the protein solution end were observed (Figure 45). The crystal dimensions and amount of crystals vary for several observed areas in the capillary (Figure 45; 46). Time-lapse images for different capillary areas were recorded with 2.5 x and 10 x magnification to investigate crystal growth rates for crystals grown in microgravity. First image was taken t = 253 min after sample thawing with 2.5 x magnification. The imaging time extended to t = 8725 min, images were taken t1 = 253 min, t2 = 612 min, t3 = 3214 and t4 = 8725 min after sample thawing. At the time points t2 – t4 nucleation and subsequent growth of crystals was observed for the images recorded with 2.5 x magnification (Figure 45; 46). Furthermore, at time points t = 1610-, 2700-, 4145- and 10390 min crystals of different sizes at different areas in capillary were observed and photo-documented with 10 x magnification (Figure 45). The crystal sizes at different positions in the capillaries were measured and comparative statistically analyzed. The area in the capillary was measured from the end of the capillary (i.e. the protein). Temporarily the length of major axis values for n = 39 crystals were measured. The average dimensions (length of major axis) of lysozyme crystals were calculated in the 2 areas from the capillary end, 13-25 mm and 25-44 mm with crystal sizes 277 ±27 µm and 495 ± 47 µm, respectively. The average size of lysozyme crystals was significantly lower (Student's t-test: $p < 0.01$) for the capillary area between 13-25 mm than the average size for the capillary area between 25-44 mm (Figure 47). The average growth rates for crystals with lengths of major axis < 350 µm and > 350 µm were calculated. The average growth rate (1.9 ± 0.23 µm /h) for lysozyme crystals with length of major axis < 350 µm were significantly lower (statistical t-test: $p < 0.01$) than the average growth rate (2.6 ± 0.24 µm/h) for crystals with the length of major axis > 350 µm (Figure 47).

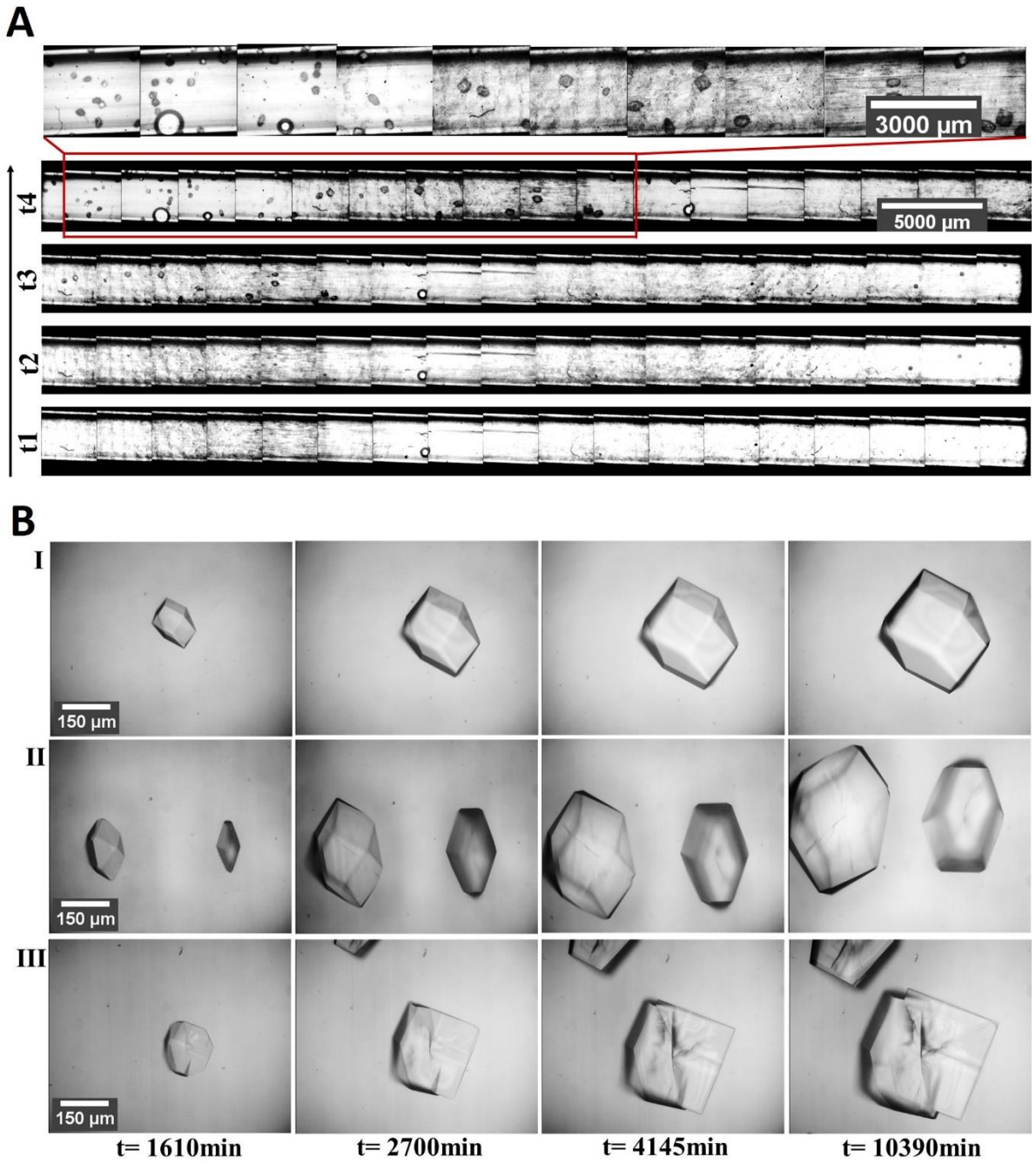

Figure 45. Protein crystallization in microgravity applying the counter diffusion technique in capillaries. Images were recorded using the ISS LMM microscope. Lysozyme crystals. (A) Time-lapse images were recorded with 2.5 x magnification. The imaging time extended to t = 8725 min, images were taken t1 = 253 min, t2 = 1416 min, t3 = 3214 and t4 = 8725 min after sample thawing. (B) Time-lapse images were recorded for 3 different areas (I, II, III) in the capillary with 10 x magnification. The imaging time extended to t = 10390 min. The first images was taken t = 1610 min after sample thawing.

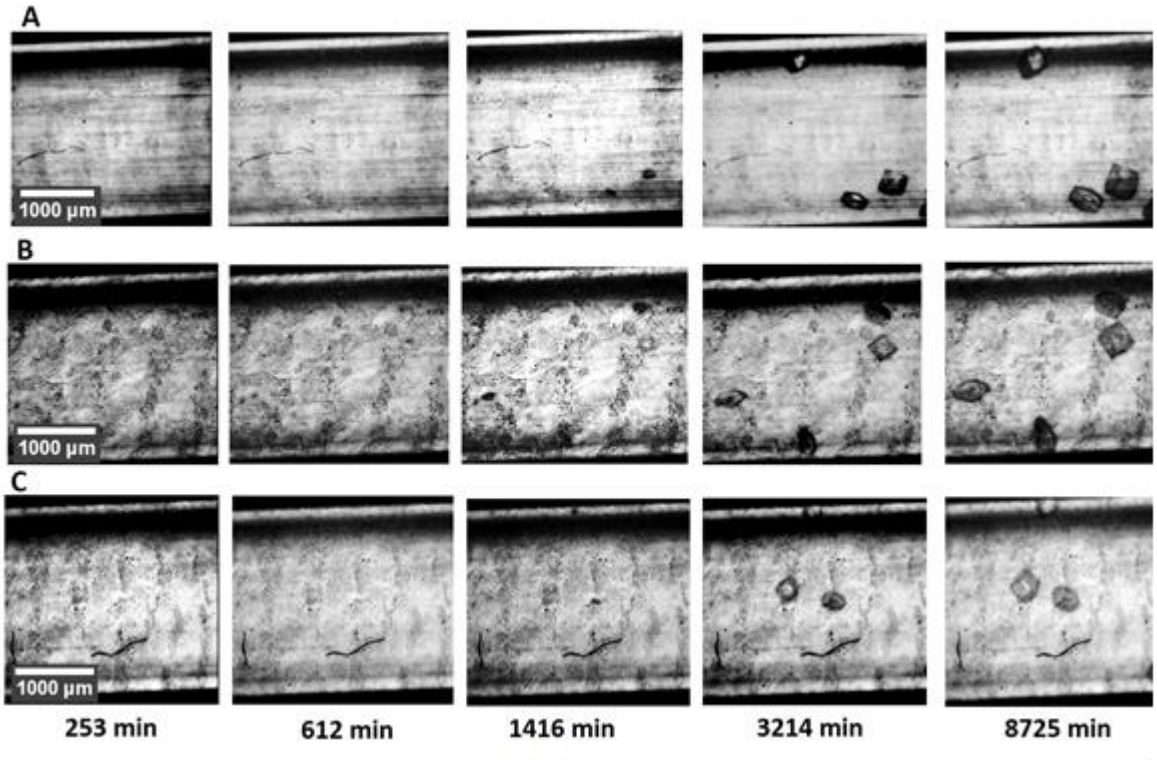

Figure 46. Growth of lysozyme crystals in microgravity. Time-lapse images were recorded for 3 different areas (A, B, C) in the capillary using the LMM microscope with 2.5x magnification. The imaging time extended to t = 8725 min, first image was taken t = 253 min, after sample thawing.

5.1.2.9 Crystal growth in 1G vs microgravity, lysozyme

Since samples returned to the earth light microscope images of crystals grown in µg and 1G were recorded and photo-documented. Crystal images were recorded t = 25 days after sample thawing with 2.5 x and 10 x magnification (Figure 48). The crystal dimensions, length of major axis 150 - 580 µm, vary at different areas of capillary for µg and 1G grown crystals (Figure 48). The µg grown crystals showed on average larger dimensions, with lengths of major axis for larger crystals ~ 550 µm, compared to 1G, with lengths of major axis for larger crystals ~ 350 µm (figure 48).

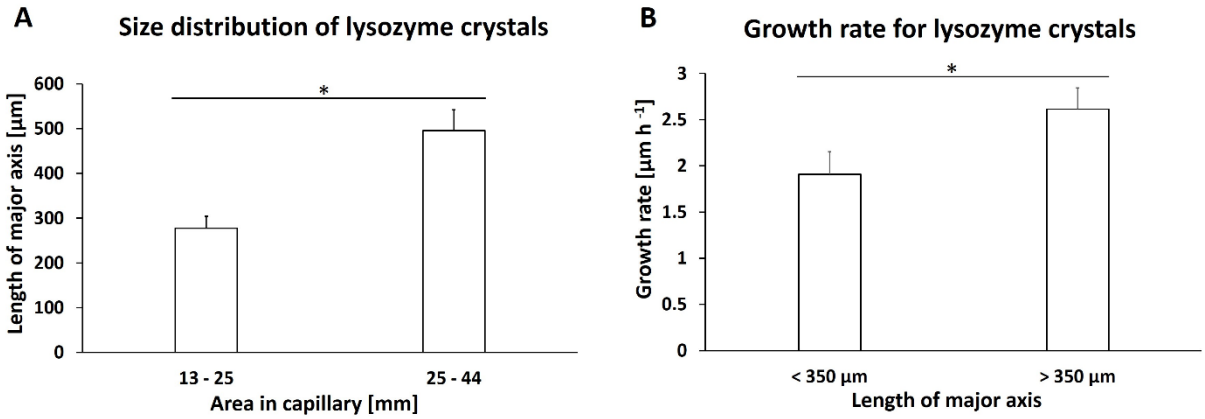

Figure 47. Crystals grown in µg. Lysozyme crystals. Comparative growth rate and size distribution values (the length of major axis) of crystals along the capillary. Different regions (areas) along the capillary were measured from the protein end of the capillary toward the protein-precipitant interface. Error bars represent standard deviations of the average. Significance within a 99% confidence interval was determined using Student's *t*-test and is denoted by asterisk (* = $p < 0.01$). (A) Average size distribution of lysozyme crystals for the areas from the capillary end 13-25 mm and 25-44 mm. The sample sizes for crystals in the areas 13-25 mm and 25-44 mm are n = 24 and n = 15, respectively. (B) Average growth rates with standard deviations of lysozyme crystals with lengths of major axis < 350 µm and > 350 µm. The sample sizes for crystals < 350 µm and > 350 µm are n = 6 and n = 9 respectively.

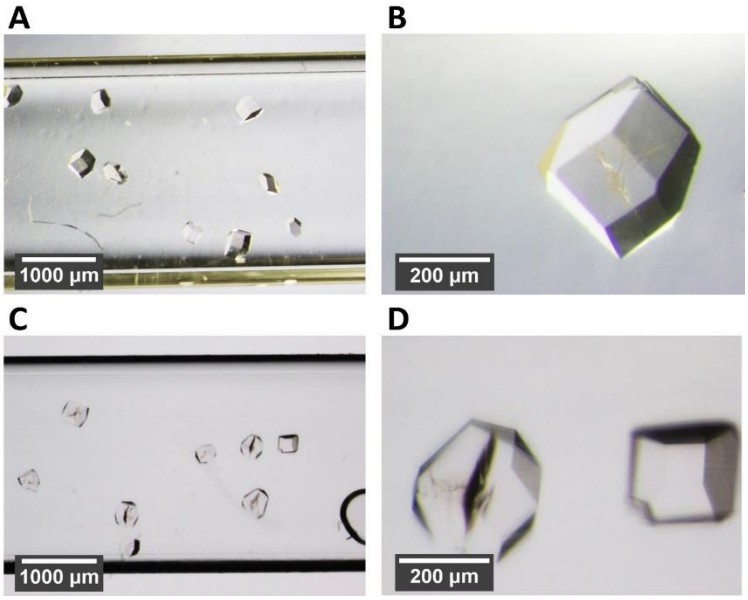

Figure 48. Lysozyme crystals grown in µg and 1G. Crystal images were recorded using a light microscope t = 25 days after sample thawing, after µg samples returned on the earth. (A) Crystals grown in µg, images were recorded with a 2.5 x objective. (B) Crystals grown in µg, recorded with a 10 x objective. (C) Crystals grown in 1G, recorded with a 2.5 x objective. (D) Crystals grown in 1G, recorded with a 10 x objective.

5.2 Impurity incorporation

5.2.1 LMM monitoring of impurity incorporation into crystals in microgravity

To investigate the incorporation of impurities into growing crystals fluorescently labeled protein-aggregates were prepared which simulate protein aggregate impurities in solution. For crystallization experiments in microgravity, samples with different protein-aggregate ratios were prepared.

The LMM fluorescence micrographs of capillaries samples containing *Pf*GST dimer and additionally fluorescently labeled *Pf*GST aggregates recorded with 2.5 x magnification show the presence of fluorescence in crystals for the dimer with the addition of tetramer in 99.5 : 0.5 ratio (Figure 49). However, the micrographs of capillaries samples containing dimer (negative control) and dimer additionally fluorescently labeled tetramer with 99.8 :0.2 ratio show the absence of fluorescence (Figure 49). On the other hand the micrograph of crystals with 99.8 : 0.2 ratio recorded with 10 x magnification show week presence of fluorescence (Figure 49). Furthermore, the micrographs of crystals with 99.5 : 0.5, 99 :1 and 95 : 5 ratios recorded with 10 x magnification show the presence of fluorescence (Figure 49). The micrographs of crystals with dimer and dimer : tetramer in 99.9 : 0.1 ratio recorded with 10 x magnification show the absence of fluorescence (Figure 49). Initial crystallization experiments showed that fluorescently labeled *Pf*GST aggregates are not crystallizing under same conditions as *Pf*GST dimers.

5.2.2 Impurity incorporation in 1G vs microgravity grown crystals

Since samples returned to the Earth confocal images of crystals in the capillaries grown in µg and 1G were recorded and photo-documented. The confocal fluorescence micrograph of *Pf*GST dimer sample (negative control) shows the absence of fluorescence for µg and 1G crystals (Figure 50). The *Pf*GST crystals grown in µg and 1G in presence of fluorescent labeled protein aggregates in 99.9 : 0.1, 99.8 :0.2, 99.5 : 0.5, 99 : 1, 95 : 5, 90 : 10 and 75 : 25 (µg) ratios show the presence of green fluorescence (Figure 50). In addition the lysozyme crystals show the presence of red fluorescence (Figure 50).

Based on confocal laser scanning fluorescence microscopy analysis, there appears to be presence also incorporation of fluorescently labeled tetramers into growing dimer crystals. Therefore, incorporation of fluorescently labeled tetramers into growing dimer crystal can be investigated applying appropriate methods and techniques. For this purpose quantitative analyses of total fluorescence/crystal volume were performed applying a fluorescence microplate reader. Temporarily the fluorescence intensities values for n = 65 crystals grown in 1G and µg were measured. The average fluorescence intensities of crystals grown in 1G for a crystal volume of μm^3 was calculated for the 7 different ratios, dimer, 99.9 :0.1, 99.8 : 0.2, 99.5 : 0.5, 99 : 1, 95 : 5 and 90 : 10 with fluorescence intensity values 0-, 0.003 ± 0.001-, 0.03 ± 0.01-, 0.03 ± 0.02-, 0.24 ± 0.06-, 0.23 ± 0.03- and 0.17 ± 0.02 a.u, respectively (Figure 51). The average fluorescence intensities of crystals grown in µg for a crystal volume of μm^3 was calculated for the 8 different ratios, dimer, 99.9 :0.1, 99.8 : 0.2, 99.5 : 0.5, 99 : 1, 95 : 5, 90 : 10 and 75 : 25 with

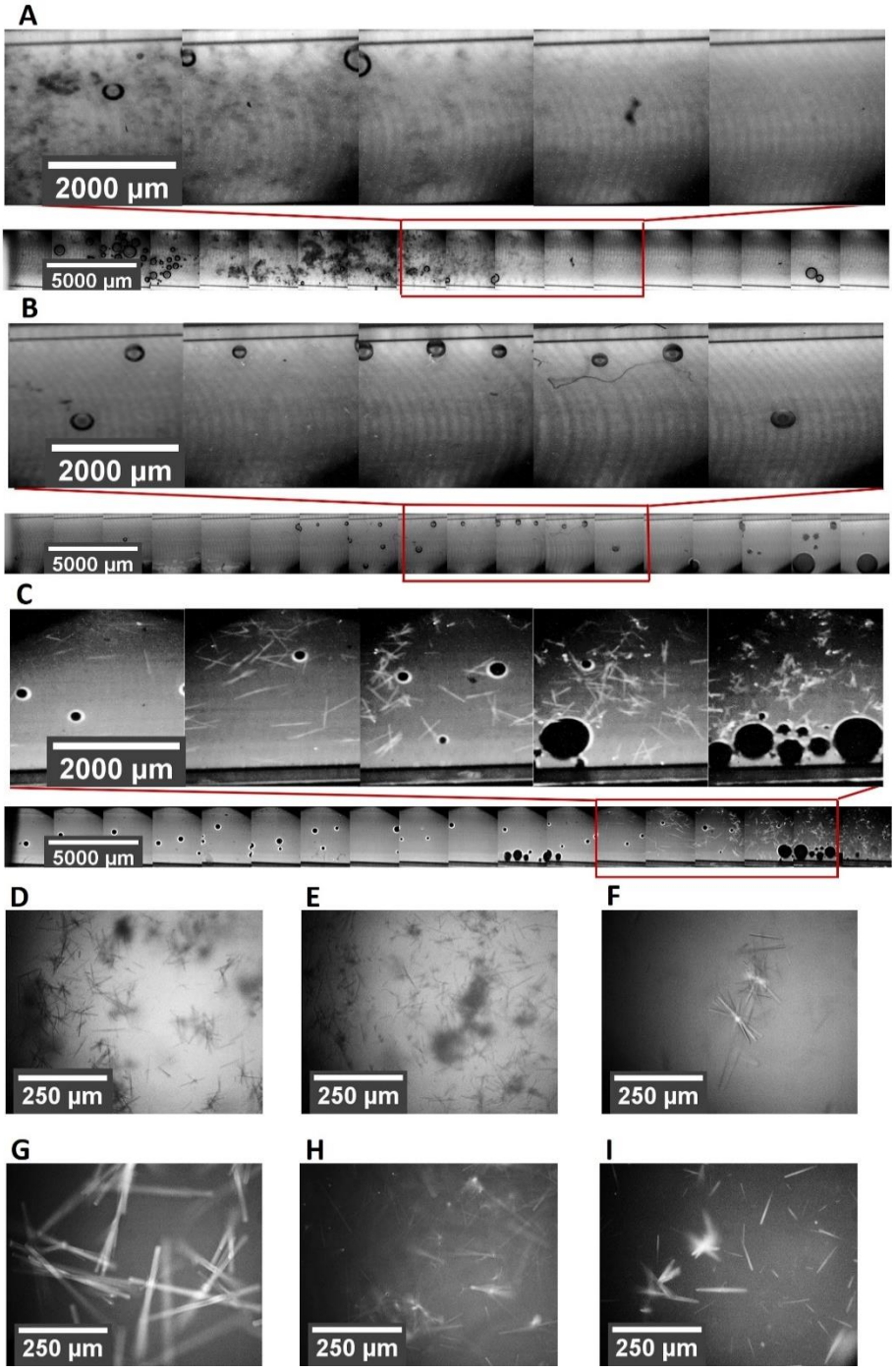

Figure 49. Crystals grown in µg. Crystals of *Pf*GST with additionally fluorescence labeled (Alexa fluor 488) aggregates in 5 different ratios. Crystal images were recorded on ISS using the LMM microscope 2.5 x and 10 x objective with FITC fluorescence filter. (A;B;C) Images were recorded with 2.5 x objective t = 8742 min after sample thawing. (A) dimer. (B) dimer additionally tetramer in 99.8:0.2 ratio. (C) dimer additionally tetramer in 99.5:0.5 ratio. (D;E;F;G;H;I) Images were recorded with a 10 x objective. (D) dimer, t = 4709 min. (E) dimer additionally tetramer in 99.9:0.1 ratio, t = 5807 min. (F) dimer additionally tetramer in 99.8:0.2 ratio. t = 4900 min. (G) dimer additionally tetramer in 99.5:0.5 ratio. t = 10500 min. (H) dimer additionally tetramer in 99:1 ratio. t = 7286 min. (I) dimer additionally tetramer in 95:5 ratio. t = 7349 min.

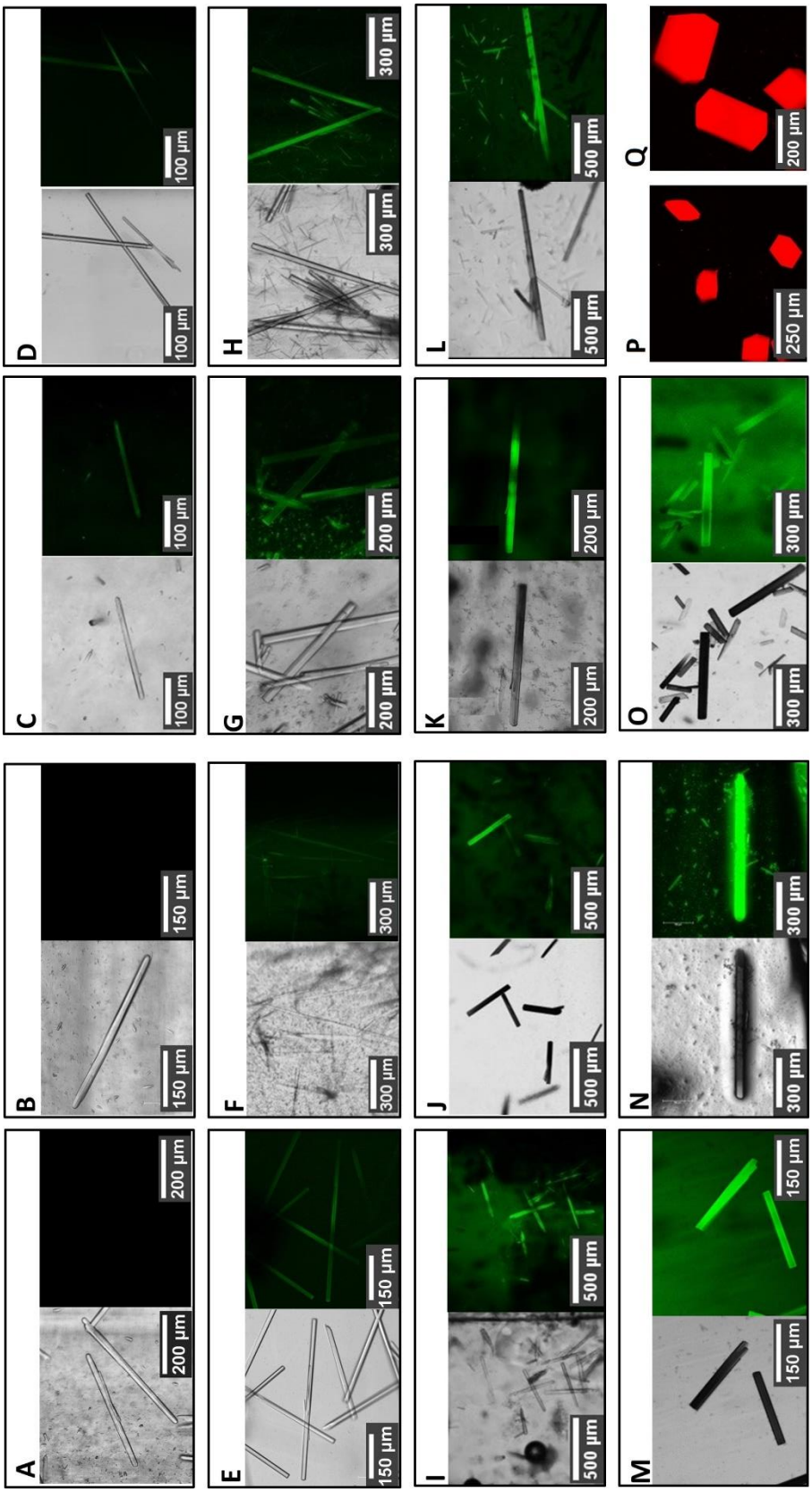

Figure 50. Crystals grown in 1G vs µg. Images were recorded after return of the samples on the earth. Crystals of *Pf*GST and lysozyme with additionally fluorescence labeled, Alexa Fluor 488 (*Pf*GST) and Alexa fluor 594 (lysozyme), aggregates in different ratios. Crystal images were recorded using a confocal laser microscope 10 x objective with FITC (*Pf*GST) and Texas Red (lysozyme) fluorescence filter. (A) *Pf*GST dimer crystals grown in 1G. (B) *Pf*GST dimer crystals grown in µg. (C) Dimer additionally tetramer in 99.9:0.1 ratio, 1G. (D) dimer additionally tetramer in 99.9:0.1 ratio, µg. (E) Dimer : tetramer in 99.8:0.2 ratio, 1G. (F) Dimer : tetramer in 99.8:0.2 ratio, µg. (G) 99.5:0.5 ratio, 1G. (H) 99.5:0.5 ratio, µg. (I) 99:1 ratio, 1G. (J) 99:1 ratio, µg. (K) 95:5 ratio, 1G. (L) 95:5 ratio, µg. (M) 90:10 ratio, 1G. (N) 90:10 ratio, µg. (O) 75:25 ratio, µg. (P, Q) Lysozyme crystals.

fluorescence intensity values 0-, 0.002 ± 0.001-, 0.001 ± 0.0004-, 0.01 ± 0.002-, 0.10 ± 0.01-, 0.08 ± 0.01-, 0.04 ± 0.01 and 0.11 ± 0.09 a.u, respectively (Figure 51). Significant difference for the average fluorescence intensities from 4 ratios 1G vs µg (Student's t-test: $p < 0.01$); Significance for the ratio

99.8 : 0.2 ($p < 0.01$); Significance for the ratio 99 : 1 ($p < 0.01$); Significance for the ratio 95 : 5 ($p < 0.01$); Significance for the ratio 90 : 10 ($p < 0.01$) was indicated (Figure 51). In the other hand, not significant difference for the average fluorescence intensities from 2 ratios 1G vs µg (Student's t-test: $p < 0.01$; $p < 0.05$); Not significance for the ratio 99.9 : 0.1 ($p > 0.05$); Not significance for the ratio 99.5 : 0.5 ($p > 0.05$ was indicated (Figure 51).

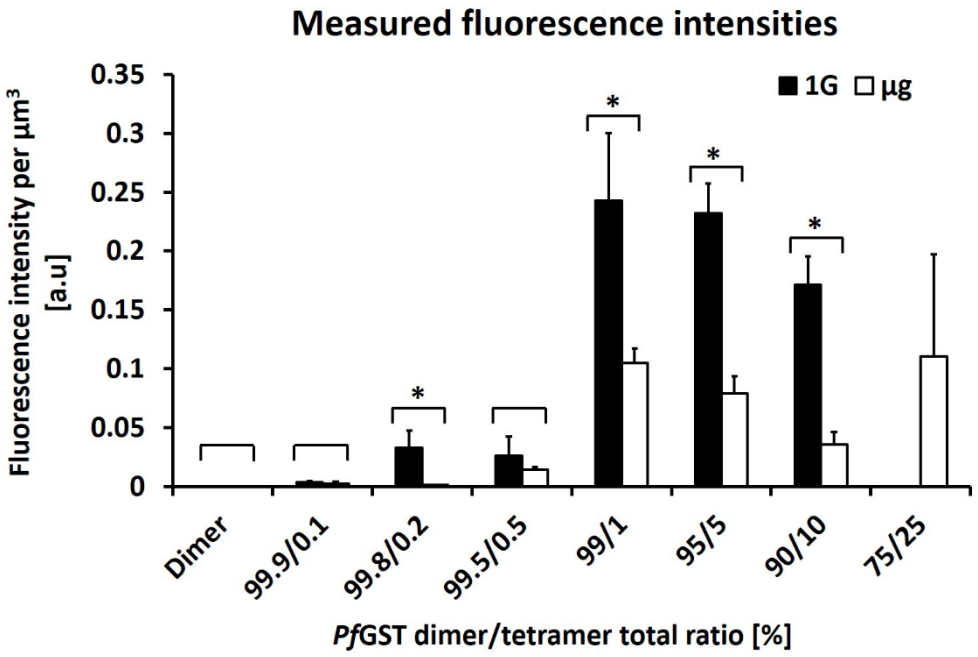

Figure 51. Comparative analysis of fluorescence intensities of crystals grown in µg versus 1G grown *Pf*GST crystals. In total n = 5 1G grown and n = 5 µg grown crystals in similar sizes from each dimer : tetramer ratio (in total n = 65 crystals) were 2 x washed in native buffer and resolved in 1xPBS buffer for fluorescence intensity measurements. Fluorescence intensities were measured applying a fluorescence microplate reader. Error bars represent standard deviations of the average. Significance within a 99% confidence interval was determined using Student's *t*-test and is denoted by asterisks (* = p < 0.01). Measured average fluorescence intensities correspond to a crystal volume of µm³. Data of dimer and 7 different dimer/tetramer ratios are shown.

5.3 X-ray diffraction data collection, processing and structure of *Pf*GST

Diffraction data of *Pf*GST crystals grown in 1G and µg were collected at 100 K temperature at PETRA III, beamlines P11 and P13 EMBL at DESY, Hamburg. X-ray data for dimer and dimer : tetramer in 8 different ratios were collected and statistical (via crystal quality factors) analyzed. Data for crystals with

approximately similar dimensions for each ratio were collected. For cryoprotection the crystals were soaked with precipitant solution supplemented with 14 % (v/v) glycerol. Diffraction data were subsequently indexed, integrated and scaled with XDS and ccp4 graphic programs. Datasets for n = 58 crystals grown in 1G and µg were analyzed (Figure 52; 53). Datasets were cut individual for each crystal dataset monitoring Rmeas, Rsym, I/σ and CC1/2. The crystals belonged to the monoclinic space group $P2_1$ with unit cell dimensions ~ 61 Å, ~ 69 Å, ~ 100 Å and β angle of ~ 92.0° (Tables 21-28). The µg grown crystals for dimer and for the ratios 99.8 : 0.2, 99.5 : 0.5, 95 : 5 diffracted to higher resolutions compared to the 1G (Tables 21; 22; 23; 25). To investigate the quality differences of 1G vs µg grown crystals the average signal-to-noise ratios (I/σ(I)) vs resolutions for each crystal was calculated and statistical analyzed (Figure 52; 53). Significant difference for the average I/σ(I) values from dimer and 1 ratio 1G vs µg (Student's t-test: $p < 0.05$); Significance for the resolution range 2.26 – 5.94 Å for dimer ($p < 0.05$); Significance for the resolution range 2.1 – 3.0 Å for the ratio 99.8 : 0.2 ($p < 0.05$) was indicated (Figure 52; 53). However, no significant difference for the average I/σ(I) values from 4 ratios 1G vs µg (Student's t-test: $p < 0.05$); No significance for the ratio 99.5 : 0.5 ($p > 0.05$); No significance for the ratio 99 : 1 ($p > 0.05$); No significance for the ratio 95 : 5 ($p > 0.05$) and No significance for the ratio 90 : 10 ($p > 0.05$) was indicated (Figures 52; 53). Additionally to investigate the number of protein molecules in unit cell and the structure, one dataset each of 1G and µg grown crystals were analyzed. Data were cut individual for 1 x 1G and 1 x µg crystal datasets to 2.3 Å and 2.1 Å, respectively. The crystals belonged to the monoclinic space group $P2_1$ with unit cell dimensions of 61.6 Å, 69.6 Å, 101.6 Å and β angle of 92.3° for 1G crystals and with unit cell dimensions of 61.5 Å, 69.6 Å, 101.6 Å and α, β, γ angles of 90.0°, 92.3°, 90.0° for µg crystals (Table 29). The homologue structure of the *Pf*GST dimer (PDB code: 3FRC) was used as a search model for molecular replacement. The Matthews coefficient was determined for both dataset, 1G and µg, 2.18 $Å^2\ Da^{-1}$ and 2.17 $Å^2\ Da^{-1}$ respectively. The solvent content was calculated to be 43 % for each dataset with 4 *Pf*GST monomers in the respective asymmetric unit. Data collection parameters are summarized in Table 29. The asymmetric unit for 1G and µg consist 2 x *Pf*GST homodimer with 4 identical monomer chains (Figure 54A, B).

Table 21. Data collection statistics (via XDS) for *Pf*GST dimer crystals grown in 1G vs µg. In total X-ray data for n = 6 1G grown and n = 6 µg grown crystals with similar dimensions were analyzed.

	***Pf*GST dimer**											
Data collection statistics	**1G**						**µg**					
	Crystal 1	**Crystal 2**	**Crystal 3**	**Crystal 4**	**Crystal 5**	**Crystal 6**	**Crystal 1**	**Crystal 2**	**Crystal 3**	**Crystal 4**	**Crystal 5**	**Crystal 6**
Wavelength	0.9919	0.9919	0.9919	0.9919	0.9919	1.0332	0.9919	0.9919	0.9919	0.9919	1.0332	1.0332
Space group	P 2_1	P 2_1	P 2_1	P 2_1	P 2_1	P 2_1	P 2_1	P 2_1	P 2_1	P 2_1	P 2_1	P 2_1
Unit cell parameters a/b/c [Å]	61.3 69.8 98.8	61.2 69.6 100.3	61.5 69.8 100.7	61.6 69.9 101.5	61.8 70.1 101.3	61.2 70.1 99.3	61.6 69.7 101.8	61.5 69.9 100.6	61.4 69.8 99.6	61.1 69.5 99.5	60.1 69.6 98.9	61.2 69.7 99.3
β [°]	90.2	90.1	90.2	89.9	90.1	92.1	92.4	92.4	91.9	91.8	92.2	92.2
Total reflections	38264	49046	72528	56700	55681	80197	164488	45729	125680	71728	103053	166916
Unique reflections	11385	14755	14429	17230	16855	12204	48857	13653	37211	14937	15341	24889
Resolution range [Å]	50-3.42 (3.62-3.42)	50-3.14 (3.33-3.14)	50-3.19 (3.38-3.19)	50-3.00 (3.18-3.00)	50-3.03 (3.22-3.03)	50-3.35 (3.55-3.35)	50-2.12 (2.25-2.12)	50-3.24 (3.43-3.24)	50-2.30 (2.44-2.30)	50-3.10 (3.28-3.10)	50-3.09 (3.27-3.09)	50-2.63 (2.79- 2.63)
R means [%]	7.9 (55.9)	16.2 (58.2)	14.9 (55.3)	5.4 (8.6)	15.7 (51.2)	15.5 (55.2)	9.9 (56.6)	18.6 (56.8)	8.0 (60.1)	15.1 (50.9)	13.7 (54.4)	9.0 (54.3)
R symm [%]	6.6 (47.4)	13.6 (48.4)	13.4 (49.6)	4.2 (6.8)	13.1 (51.4)	14.3 (50.6)	8.3 (49.9)	15.6 (49.5)	6.7 (50.3)	13.4 (44.8)	12.7 (50.1)	8.3 (49.8)
Mean I/σ (I)	12.44 (2.49)	7.57 (2.28)	9.96 (3.28)	8.25 (2.61)	7.77 (2.14)	9.73 (3.33)	12.09 (2.57)	7.47 (2.45)	12.82 (2.30)	8.48 (2.33)	11.09 (3.77)	15.33 (3.26)
CC (1/2) [%]	99.9 (94.4)	99.7 (86.8)	99.7 (88.1)	100 (99.9)	99.8 (94.6)	99.9 (91.5)	99.8 (83.4)	99.6 (94.9)	99.8 (85.6)	99.6 (99.6)	99.9 (95.6)	99.9 (95.5)
Average mosaictiy [°]	0.14	0.34	0.27	0.33	0.33	0.33	0.12	0.11	0.12	0.34	0.31	0.24
Completeness [%]	99.2 (98.9)	98.8 (96.3)	99.7 (99.7)	98.8 (97.0)	99.1 (98.8)	99.2 (96.5)	99.5 (99.4)	98.9 (96.7)	99.4 (98.8)	97.0 (96.7)	99.5 (97.5)	99.6 (98.1)

Table 22. Data collection statistics (via XDS) for *Pf*GST crystals in dimer : tetramer 99.9:0.1 ratio grown in 1G vs µg. In total X-ray data for n = 6 1G grown and n = 1 µg grown crystals with similar dimensions were analyzed.

	***Pf*GST dimer additionally tetramer in 99.9/ 0.1 total ratio**						
Data collection statistics	**1G**						**µg**
	Crystal 1	**Crystal 2**	**Crystal 3**	**Crystal 4**	**Crystal 5**	**Crystal 6**	**Crystal 1**
Wavelength	1.0332	1.0089	1.0332	1.0332	1.0332	1.0332	1.0089
Space group	P 2_1	P 2_1	P 2_1	P 2_1	P 2_1	P 2_1	P 2_1
Unit cell parameters a/b/c [Å]	60.7 69.1 93.5	61.2 68.7 89.9	60.8 69.7 98.3	61.1 69.9 99.2	60.1 69.7 98.4	61.0 69.5 99.5	61.7 69.7 100.7
β [°]	90.1	90.2	92.1	92.2	91.8	92.4	92.6
Total reflections	143428	132439	126837	132694	91440	83046	63621
Unique reflections	21563	41537	18759	19429	21850	12459	19114
Resolution range [Å]	50-2.69 (2.85-2.69)	50-2.11 (2.24-2.11)	50-2.88 (3.05-2.88)	50-2.86 (3.04-2.86)	50-2.74 (2.90-2.74)	50-3.32 (3.52-3.32)	50-2.87 (3.05-2.87)
R means [%]	5.5 (54.6)	11.8 (57.3)	12.3 (54.3)	11.3 (55.2)	8.4 (50.1)	15.4 (51.9)	13.0 (56.5)
R symm [%]	5.1 (50.2)	9.9 (47.3)	11.4(50.1)	10.5 (51.0)	7.3 (43.6)	14.2(47.6)	10.9 (47.7)
Mean I/σ (I)	22.21 (3.22)	9.21 (2.20)	12.97 (3.48)	14.02 (3.41)	12.51 (2.90)	9.44 (3.40)	9.22 (2.36)
CC (1/2) [%]	100 (93.3)	99.8 (99.7)	99.8 (96.0)	99.9 (95.5)	99.9 (93.5)	99.9 (92.8)	99.6 (87.0)
Average mosaictiy [°]	0.27	0.18	0.29	0.26	0.39	0.19	0.12
Completeness [%]	99.6 (98.0)	97.0 (87.3)	99.4 (97.1)	99.7 (98.9)	99.4 (97.8)	99.5 (97.6)	97.0 (92.9)

Table 23. Data collection statistics (via XDS) for *Pf*GST crystals in dimer : tetramer 99.8:0.2 ratio grown in 1G vs µg. In total X-ray data for n = 5 1G grown and n = 5 µg grown crystals with similar dimensions were analyzed.

	***Pf*GST dimer additionally tetramer in 99.8/ 0.2 total ratio**									
Data collection statistics	**1G**					**µg**				
	Crystal 1	**Crystal 2**	**Crystal 3**	**Crystal 4**	**Crystal 5**	**Crystal 1**	**Crystal 2**	**Crystal 3**	**Crystal 4**	**Crystal 5**
Wavelength	1.0332	1.0332	1.0332	1.0332	1.0332	1.0332	1.0332	1.0332	1.0332	1.0332
Space group	P 2_1	P 2_1	P 2_1	P 2_1	P 2_1	P 2_1	P 2_1	P 2_1	P 2_1	P 2_1
Unit cell parameters a/b/c [Å]	61.2 69.3 99.8	61.0 69.3 99.2	61.2 69.5 99.5	61.2 69.8 100.2	61.3 69.6 99.9	60.1 69.3 98.5	60.1 69.3 99.4	61.1 69.6 98.8	61.1 69.7 99.5	61.1 69.6 98.6
β [°]	92.2	92.1	92.2	92.3	92.2	91.9	92.3	91.8	92.0	91.9
Total reflections	103533	127345	142274	101249	106086	113202	138518	145519	189840	156059
Unique reflections	15319	18534	24899	14813	15441	16505	20080	21494	28128	23031
Resolution range [Å]	50-3.10 (3.28-3.10)	50-2.90 (3.07-2.90)	50-2.63 (2.79-2.63)	50-3.14 (3.33-3.14)	50-3.10 (3.28-3.10)	50-3.00 (3.18-3.00)	50-2.82 (2.99-2.82)	50-2.76 (2.92-2.76)	50-2.53 (2.68-2.53)	50-2.69 (2.85-2.69)
R means [%]	20.2 (54.0)	12.9 (52.3)	11.5 (55.5)	18.0 (52.7)	20.4 (53.7)	12.8 (52.4)	13.2 (53.6)	12.0 (53.6)	10.7 (53.8)	11.0 (52.5)
R symm [%]	18.7 (49.9)	11.9 (48.4)	10.4 (50.2)	16.6 (48.7)	18.9 (49.7)	11.9 (48.5)	12.2 (49.7)	11.1 (49.4)	9.9 (49.6)	10.1 (48.3)
Mean I/σ (I)	8.52 (3.65)	13.92 (4.13)	13.97 (3.22)	10.03 (3.65)	8.78 (3.33)	13.81 (4.12)	13.70 (3.83)	12.05 (3.91)	12.98 (3.66)	14.75 (3.87)
CC (1/2) [%]	99.2 (93.6)	99.8 (94.9)	99.8 (91.6)	99.6 (92.9)	99.2 (91.9)	99.8 (94.5)	99.8 (93.8)	99.8 (94.4)	99.9 (94.3)	99.9 (94.8)
Average mosaictiy [°]	0.31	0.25	0.12	0.12	0.07	0.34	0.15	0.23	0.18	0.36
Completeness [%]	99.6 (98.7)	99.8 (99.3)	99.2 (98.7)	99.3 (97.1)	99.7 (99.6)	98.6 (95.0)	99.4 (98.9)	99.6 (97.9)	99.5 (97.5)	99.0 (96.0)

Table 24. Data collection statistics (via XDS) for *Pf*GST crystals in dimer : tetramer 99.5:0.5 ratio grown in 1G vs µg. In total X-ray data for n = 3 1G grown and n = 4 µg grown crystals with similar dimensions were analyzed.

	***Pf*GST dimer additionally tetramer in 99.5/ 0.5 total ratio**						
Data collection statistics	**1G**			**µg**			
	Crystal 1	**Crystal 2**	**Crystal 3**	**Crystal 1**	**Crystal 2**	**Crystal 3**	**Crystal 4**
Wavelength	1.0332	1.0332	1.0332	1.0332	1.0332	1.0332	1.0332
Space group	P 2_1	P 2_1	P 2_1	P 2_1	P 2_1	P 2_1	P 2_1
Unit cell parameters a/b/c [Å]	61.4 69.6 99.7	61.3 69.5 99.5	61.3 69.4 98.9	61.2 69.5 98.9	61.2 69.5 99.5	61.3 69.5 99.8	61.2 69.5 99.5
β [°]	92.1	92.1	92.0	92.1	92.2	92.1	92.1
Total reflections	132494	126894	155924	118946	311846	42903	139130
Unique reflections	19432	18609	22691	34075	45654	16198	20225
Resolution range [Å]	50-2.87 (3.04-2.87)	50-2.91 (3.08-2.91)	50-2.71 (2.88-2.71)	50-2.94 (3.12-2.94)	50-2.15 (2.28-2.15)	50-2.96 (3.14-2.96)	50-2.82 (2.99-2.82)
R means [%]	11.5 (53.0)	12.5 (54.3)	11.4 (54.9)	16.4 (57.8)	7.8 (53.1)	18.1 (58.7)	12.7 (51.2)
R symm [%]	10.7 (49.1)	11.5 (50.3)	10.6 (50.7)	13.8 (49.1)	7.2 (48.9)	14.6 (47.2)	11.7 (47.4)
Mean I/σ (I)	15.77 (3.94)	14.64 (3.87)	14.53 (3.29)	7.64 (2.41)	17.60 (3.37)	6.33 (2.14)	13.34 (3.68)
CC (1/2) [%]	99.9 (95.6)	99.9 (95.3)	99.9 (94.7)	99.6 (91.5)	99.9 (92.4)	99.0 (90.7)	99.9 (95.1)
Average mosaictiy [°]	0.38	0.37	0.17	0.22	0.09	0.12	0.18
Completeness [%]	99.6 (98.1)	99.7 (98.7)	99.8 (99.3)	98.1 (93.8)	99.9 (99.7)	91.9 (90.8)	99.8 (99.5)

Table 25. Data collection statistics (via XDS) for *Pf*GST crystals in dimer : tetramer 99:1 ratio grown in 1G vs µg. In total X-ray data for n = 3 1G grown and n = 3 µg grown crystals with similar dimensions were analyzed.

	***Pf*GST dimer additionally tetramer in 99/ 1 total ratio**					
Data collection statistics	**1G**			**µg**		
	Crystal 1	**Crystal 2**	**Crystal 3**	**Crystal 1**	**Crystal 2**	**Crystal 3**
Wavelength	1.0089	1.0089	1.0089	1.0089	1.0089	1.0332
Space group	P 2_1	P 2_1	P 2_1	P 2_1	P 2_1	P 2_1
Unit cell parameters a/b/c [Å]	61.4 69.7 100.6	61.1 69.6 98.7	61.8 69.9 102.5	60.7 69.3 97.6	60.1 69.9 99.5	61.4 69.9 99.4
β [°]	91.1	92.2	92.6	89.9	91.2	91.7
Total reflections	32777	27846	71134	37077	29252	104867
Unique reflections	9870	9467	40196	21271	9039	15536
Resolution range [Å]	50-3.53 (3.75-3.53)	50-3.59 (3.81-3.59)	50-2.73 (2.90-2.73)	50-3.27 (3.47-3.27)	50-3.62 (3.84-3.62)	50-3.09 (3.28-3.09)
R means [%]	29.4 (57.9)	29.4 (63.8)	17.2 (68.9)	23.2 (64.9)	23.3 (58.1)	10.1 (54.9)
R symm [%]	24.6 (48.0)	24.0 (52.1)	12.2 (48.8)	16.5 (46.0)	19.4 (48.1)	9.3 (50.7)
Mean I/σ (I)	4.07 (2.33)	4.35 (1.71)	6.75 (1.59)	5.38 (1.46)	4.82 (1.90)	14.88 (3.82)
CC (1/2) [%]	97.2 (69.0)	97.4 (77.7)	98.3 (75.7)	97.4 (79.6)	99.3 (92.2)	99.9 (96.3)
Average mosaictiy [°]	0.37	0.44	0.51	0.77	0.61	0.25
Completeness [%]	94.1 (74.4)	96.2 (89.7)	88.4 (85.7)	87.1 (70.3)	92.9 (60.2)	99.4 (97.0)

Table 26. Data collection statistics (via XDS) for *Pf*GST crystals in dimer : tetramer 95:5 ratio grown in 1G vs µg. In total X-ray data for n = 3 1G grown and n = 4 µg grown crystals with similar dimensions were analyzed.

	***Pf*GST dimer additionally tetramer in 95/ 5 total ratio**						
Data collection statistics	**1G**			**µg**			
	Crystal 1	**Crystal 2**	**Crystal 3**	**Crystal 1**	**Crystal 2**	**Crystal 3**	**Crystal 4**
Wavelength	1.0089	1.0089	1.0089	1.0089	1.0089	1.0332	1.0332
Space group	P 2_1	P 2_1	P 2_1	P 2_1	P 2_1	P 2_1	P 2_1
Unit cell parameters a/b/c [Å]	61.3 70.2 101.2	61.4 70.0 97.6	61.4 70.5 99.0	61.8 70.2 99.4	60.4 69.4 94.2	61.3 69.7 99.6	61.2 69.8 99.3
β [°]	92.2	91.9	91.6	91.7	89.8	92.2	91.6
Total reflections	31396	48626	41703	68641	39688	155774	74350
Unique reflections	10453	27761	24230	39050	22787	32601	11248
Resolution range [Å]	50-3.48 (3.69-3.48)	50-3.08 (3.26-3.08)	50-3.23 (3.42-3.23)	50-2.74 (2.91-2.74)	50-3.17 (3.37-3.17)	50-2.41 (2.55-2.41)	50-3.42 (3.63-3.42)
R means [%]	19.6 (54.9)	10.9 (68.5)	14.9 (69.6)	20.5 (64.6)	15.5 (66.4)	7.5 (53.9)	16.1 (55.1)
R symm [%]	16.0 (44.9)	7.8 (49.2)	10.7 (50.4)	14.7 (46.3)	11.1 (47.8)	6.7 (48.0)	14.8 (50.5)
Mean I/σ (I)	5.91 (2.36)	7.93 (2.01)	5.35 (1.43)	3.91 (1.77)	5.09 (1.37)	14.42 (3.05)	8.85 (3.29)
CC (1/2) [%]	91.1 (98.6)	99.6 (71.6)	99.0 (77.3)	98.1 (82.0)	98.8 (64.5)	99.9 (92.0)	99.9 (95.2)
Average mosaictiy [°]	0.48	0.52	0.73	0.25	0.65	0.15	0.51
Completeness [%]	93.5 (74.2)	92.0 (79.6)	90.7 (79.8)	89.5 (80.4)	88.3 (61.5)	99.5 (98.2)	98.0 (88.5)

Table27. Data collection statistics (via XDS) for *Pf*GST crystals in dimer : tetramer 90:10 ratio grown in 1G vs µg. In total X-ray data for n = 3 1G grown and n = 3 µg grown crystals with similar dimensions were analyzed.

	***Pf*GST dimer additionally tetramer in 90/ 10 total ratio**					
Data collection statistics	**1G**			**µg**		
	Crystal 1	**Crystal 2**	**Crystal 3**	**Crystal 1**	**Crystal 2**	**Crystal 3**
Wavelength	1.0332	1.0332	1.0332	1.0332	1.0332	1.0332
Space group	P 2_1	P 2_1	P 2_1	P 2_1	P 2_1	P 2_1
Unit cell parameters a/b/c [Å]	61.6 69.6 101.6	61.5 69.8 100.6	61.1 69.6 97.9	61.3 69.5 99.6	61.3 69.6 99.9	60.6 68.9 97.9
β [°]	92.3	92.1	90.1	92.2	92.2	91.8
Total reflections	295032	189514	120502		149810	139846
Unique reflections	44018	28127	36725	37117	22044	20941
Resolution range [Å]	50-2.19 (2.33-2.19)	50-2.54 (2.70-2.54)	50-2.84 (3.01-2.84)	50-2.30 (2.44-2.30)	50-2.75 (2.91-2.75)	50-2.75 (2.75-2.92)
R means [%]	10.4 (53.6)	9.8 (53.0)	15.5 (58.9)	7.9 (53.7)	10.8 (50.8)	10.6 (51.2)
R symm [%]	9.6 (49.2)	9.1 (48.8)	12.9 (49.6)	7.3 (49.7)	9.9 (46.9)	9.7 (47.2)
Mean I/σ (I)	14.39 (3.34)	14.91 (3.43)	6.18 (1.58)	18.54 (3.74)	15.93 (3.93)	13.67 (4.01)
CC (1/2) [%]	99.9 (96.0)	99.9 (93.4)	99.6 (90.3)	99.9 (93.7)	99.9 (93.6)	99.9 (95.2)
Average mosaictiy [°]	0.25	0.23	0.31	0.21	0.35	0.37
Completeness [%]	99.7 (98.6)	99.6 (98.1)	96.4 (91.7)	99.7 (99.1)	99.7 (98.5)	99.4 (97.5)

Table 28. Data collection statistics (via XDS) for *Pf*GST crystals in dimer : tetramer 75:25 ratio grown in µg. In total X-ray data for n = 3 µg grown crystals with similar dimensions were analyzed.

	***Pf*GST dimer additionally tetramer in 75/ 25 total ratio**		
Data collection statistics	**µg**		
	Crystal 1	**Crystal 2**	**Crystal 3**
Wavelength	1.0332	1.0332	1.0332
Space group	P 2_1	P 2_1	P 2_1
Unit cell parameters a/b/c [Å]	61.5 69.6 101.6	61.1 69.5 99.4	61.3 69.6 98.6
β [°]	92.3	92.1	91.8
Total reflections	393164	168552	84174
Unique reflections	57627	24897	22443
Resolution range [Å]	50-2.00 (2.13-2.00)	50-2.63 (2.79-2.63)	50-2.71 (2.88-2.71)
R means [%]	6.5 (50.5)	7.9 (49.8)	9.4 (57.7)
R symm [%]	6.0 (46.7)	7.3 (45.8)	8.0 (49.4)
Mean I/σ (I)	21.40 (3.87)	18.29 (3.73)	12.73 (2.69)
CC (1/2) [%]	100 (94.5)	100 (94.8)	99.7 (90.2)
Average mosaictiy [°]	0.11	0.17	0.33
Completeness [%]	99.8 (99.4)	99.6 (98.5)	98.7 (96.1)

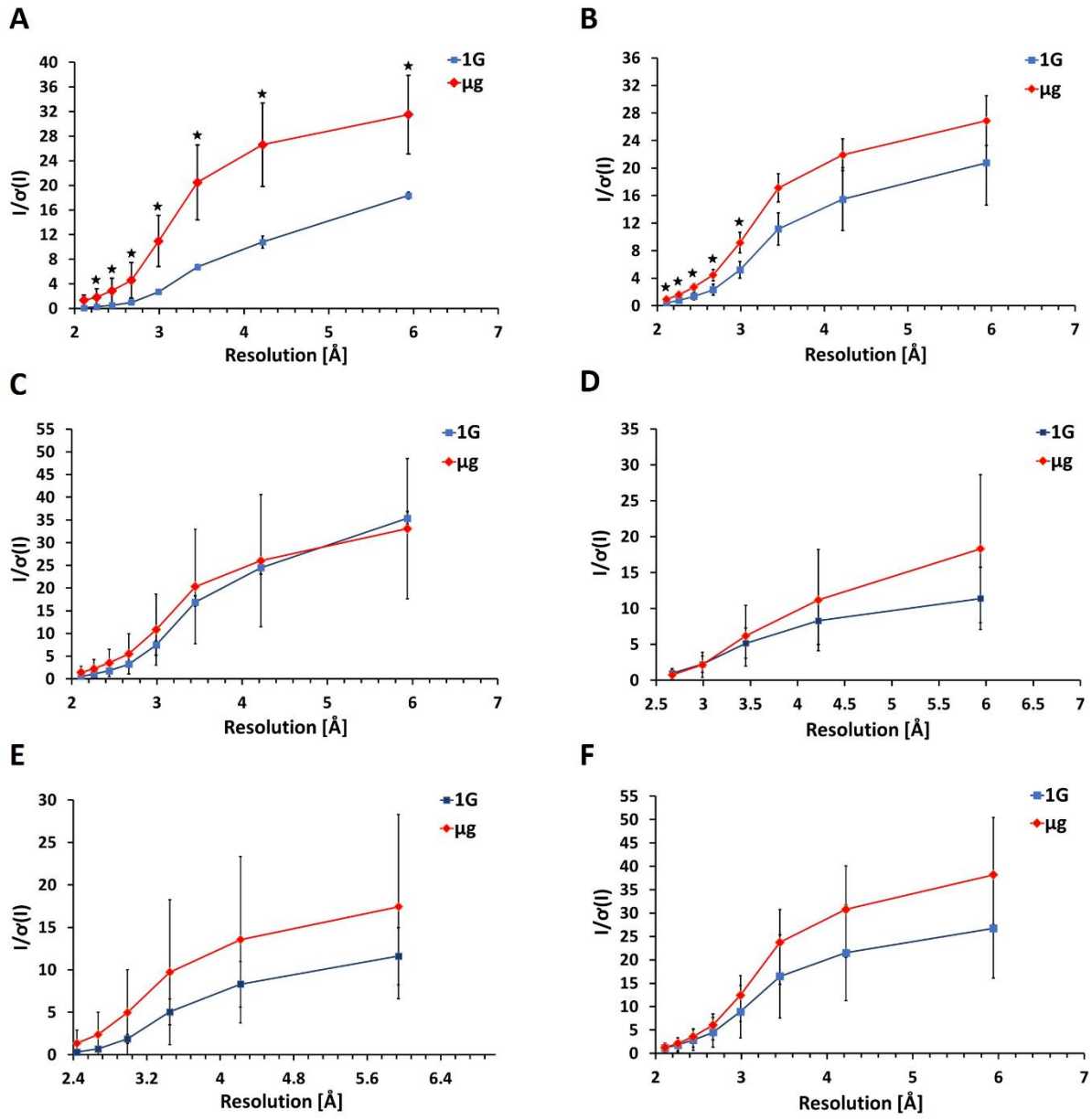

Figure 52. Comparative analysis of the merged X-ray diffraction datasets of µg grown vs 1G grown *Pf*GST crystals. Distribution of signal-to-noise ratio (I/σ(I)) vs resolution. Data of dimer and 5 different dimer/ tetramer ratios are shown. In total X-ray datasets for n = 22 microgravity grown and n = 22 1G grown crystals (in total n = 44 crystals) were analyzed. Line graphs with whiskers. Error bars represent standard deviations of the average. Significance within a 95% confidence interval was determined using Student's t-test and is denoted by asterisks (* = $p < 0.05$). (A) PfGST dimer crystals. (B) Dimer/tetramer in 99.8:0.2 ratio. (C) Dimer/tetramer in 99.5:0.5 ratio. (D) Dimer/tetramer in 99:1 ratio. (E) Dimer/tetramer in 95:5 ratio. (F) Dimer/tetramer in 90:10 ratio.

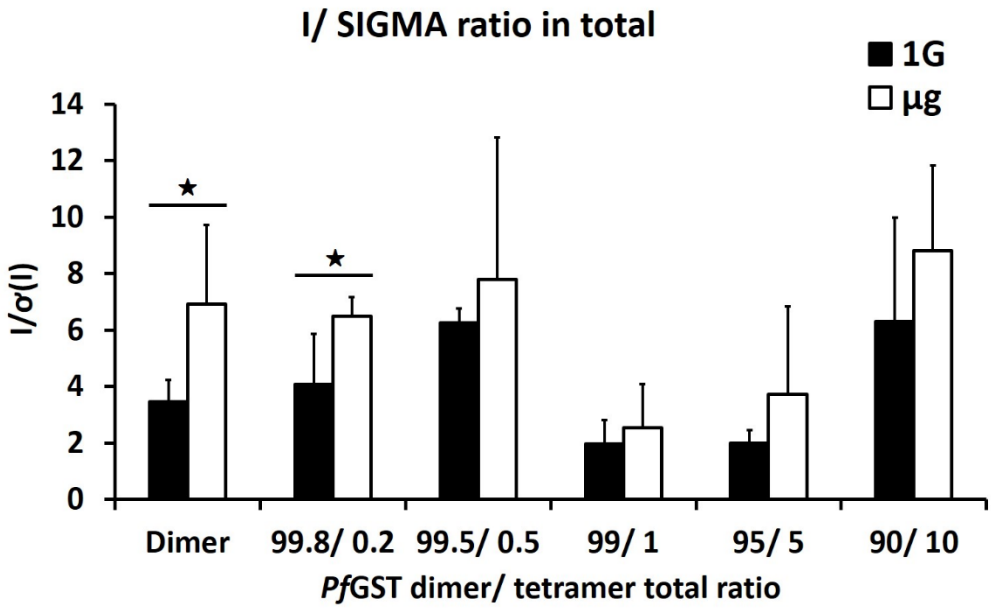

Figure 53. Comparative analysis of the merged X-ray diffraction datasets of µg grown vs 1G grown *Pf*GST crystals. Distribution of signal-to-noise ratio (I/σ(I)) in total for each ratio. Data of dimer and 5 different dimer/ tetramer ratios are shown. In total X-ray datasets for n = 22 microgravity grown and n = 22 1G grown crystals (in total n = 44 crystals) were analyzed. Error bars represent standard deviations of the average. Significance within a 95% confidence interval was determined using Student's *t*-test and is denoted by asterisks (*= p < 0.05).

Table 29. Data collection statistics for *Pf*GST crystals grown in 1G vs µg .

Data collection statistics	**1G**	**µg**
Beamline/Source	PETRA III, P11	PETRA III, P11
Wavelength [Å]	1.0332	1.0332
Space group	P 2_1	P 2_1
Unit cell parameters: a, b, c [Å] β [°]	61.6, 69.6, 101.6 92.3	61.5, 69.6, 101.6 92.3
Resolution [Å]	46.1 – 2.3 (2.38 – 2.30)	46.1 – 2.1 (2.16 – 2.10)
Temperature [K]	100	100
Rmerge [%]	9.8 (45.0)	5.7 (36.7)
Rmeas [%]	10.8 (49.4)	6.2 (40.2)
Measured reflections	258897	341906
Unique reflections	38378	50213
Average I/σ(I)	14.4 (4.4)	22.3 (5.1)
Mn(I) half-set correlation CC(1/2) [%]	99.8 (96.5)	99.9 (96.6)
Completeness [%]	99.9 (99.9)	99.9 (99.8)
Mosaicity [°]	0.25	0.11
Redundancy	6.7 (6.8)	6.8 (6.8)
Nr. of atoms		
Protein	6778	6778
Brom	4	4
Matthews coefficient [$Å^3$ Da^{-1}]	2.18	2.17
Solvent content [%]	43	43
Molecules in the asymmetric unit	4	4

*Values in parentheses are for the highest resolution shell. Rmerge: Σhkl Σi | *Ii* (hkl) – ⟨*I* (*hkl*)⟩ | / Σ_{hkl}Σi *Ii* (*hkl*), where *I* (*hkl*) is the mean intensity of the reflections hkl, Σ_{hkl} is the sum over all reflections and Σi is the sum over i measurements of reflection hkl.

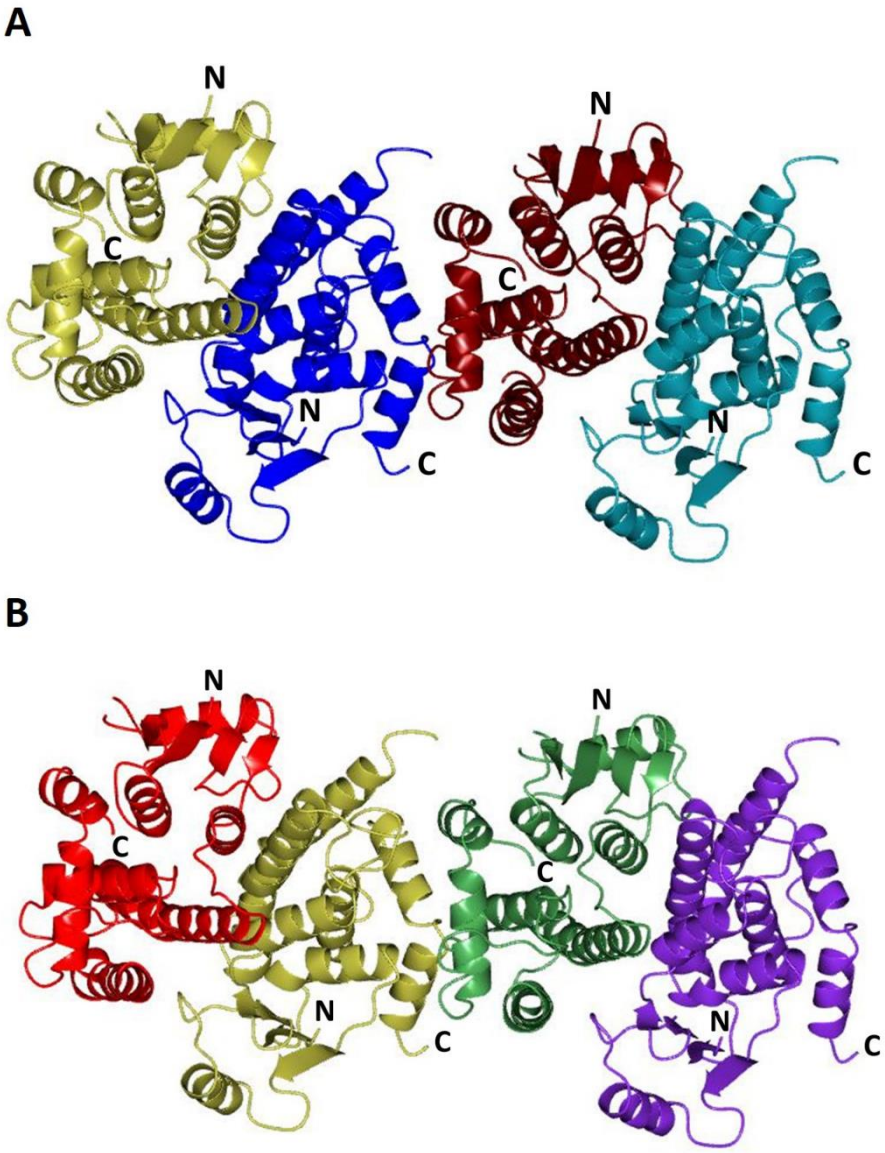

Figure 54. Structure of *Pf*GST 1G vs µg .
Cartoon representations of the *Pf*GST structure. (A) Structure in 1G, 2 x *Pf*GST homodimer with 4 identical monomer chains. Gold is used for chain A, blue for chain B, brown for chain C and cyan for chain D; labels of the N- and C-terminus are shown. (B) Structure in µg, 2 x *Pf*GST homodimer with 4 identical monomer chains. Red is used for chain A, gold for chain B, green for chain C and purple for chain D; N- and C-terminus are indicated.

6 Biophysics 4

Complementary crystallization experiments were performed in 1G and µg. Experiments were performed using the counter/liquid-liquid diffusion technique in capillaries of 100mm in length, 3mm in width and 0.3mm inner diameter (VitroCom). Capillaries were filled with 37µl of precipitant solution, 2.8 M $AmSO_4$, 0.1M $NaHPO_4$, 15% glycerol, pH 6.7 and 37µl of protein solution, 0.1 M $NaHPO_4$, pH 6.7 (doped with different percentages of fluorescently-labelled *Pf*GST aggregate) using syringes (Hamilton). Initial crystallization screens of *Pf*GST dimer (25 mg ml^{-1}) as well *Pf*GST dimer additionally with different percentage of fluorescence (Alexa Fluor 488) labeled *Pf*GST aggregates (10 mg ml^{-1}) were performed (Table 30).

Table 30. Crystallization of *Pf*GST applying counter diffusion technique in capillaries 100mm in length, 3mm in width and 0.3mm inner diameter. Calculated molar quantities of dimer additionally tetramer solutions with different molar ratios in 37 µl protein solutions.

***Pf*GST dimer : tetramer molar ratio [%]**	**Molar quantity [nmol]**	
	Dimer	**Tetramer**
100 (dimer)	18.5	-
100 (dimer) + 0.5 (tetramer)	18.5	0.0925
100 (dimer) + 1 (tetramer)	18.5	0.185

6.1 LMM monitoring of crystal growth in microgravity, *Pf*GST dimer

The flight cassettes were installed to the LMM microscope after sample thawing to perform and monitor crystallization experiments. *Pf*GST crystals grown in µg showed nearly similar morphologies in each capillary and were photo-documented in the LMM. *Pf*GST needle-like crystals in the capillary area 22 - 38 mm from the protein solution end were observed for the dimer (Figure 55). The crystal dimensions and amount of crystals vary for several observed areas in capillary (Figure 55). Time-lapse images for different capillary areas were recorded with 2.5 x magnification to investigate crystal growth rates for crystals grown in microgravity. The first image was taken t = 8510 min, after sample thawing with 2.5 x magnification. The imaging time extended to t = 17713 min, images were taken t1 = 8510 min, t2 = 8942 min, t3 = 11840, t4 = 14769 and t5 = 17713 min after sample thawing. Protein precipitation was observed at the time point t1. At the time points t1 – t4 nucleation and subsequent growth of crystals was observed (Figure 55). The crystal dimensions at different positions in the capillaries were measured and comparative statistically analyzed. The area in the capillary was measured from the end of capillary (i.e. the protein). Temporarily the length of major axis values for n = 29 crystals were measured. The average dimensions (length of major axis) of microgravity grown crystals were calculated in the 4 areas from the capillary end, 22- 28 mm, 28 – 31 mm, 31 – 34 mm and 34 – 38 mm with crystal sizes 146 ±26 µm, 340 ±36 µm, 715 ±62 µm and 355 ± 30 µm, respectively (Figure 57).

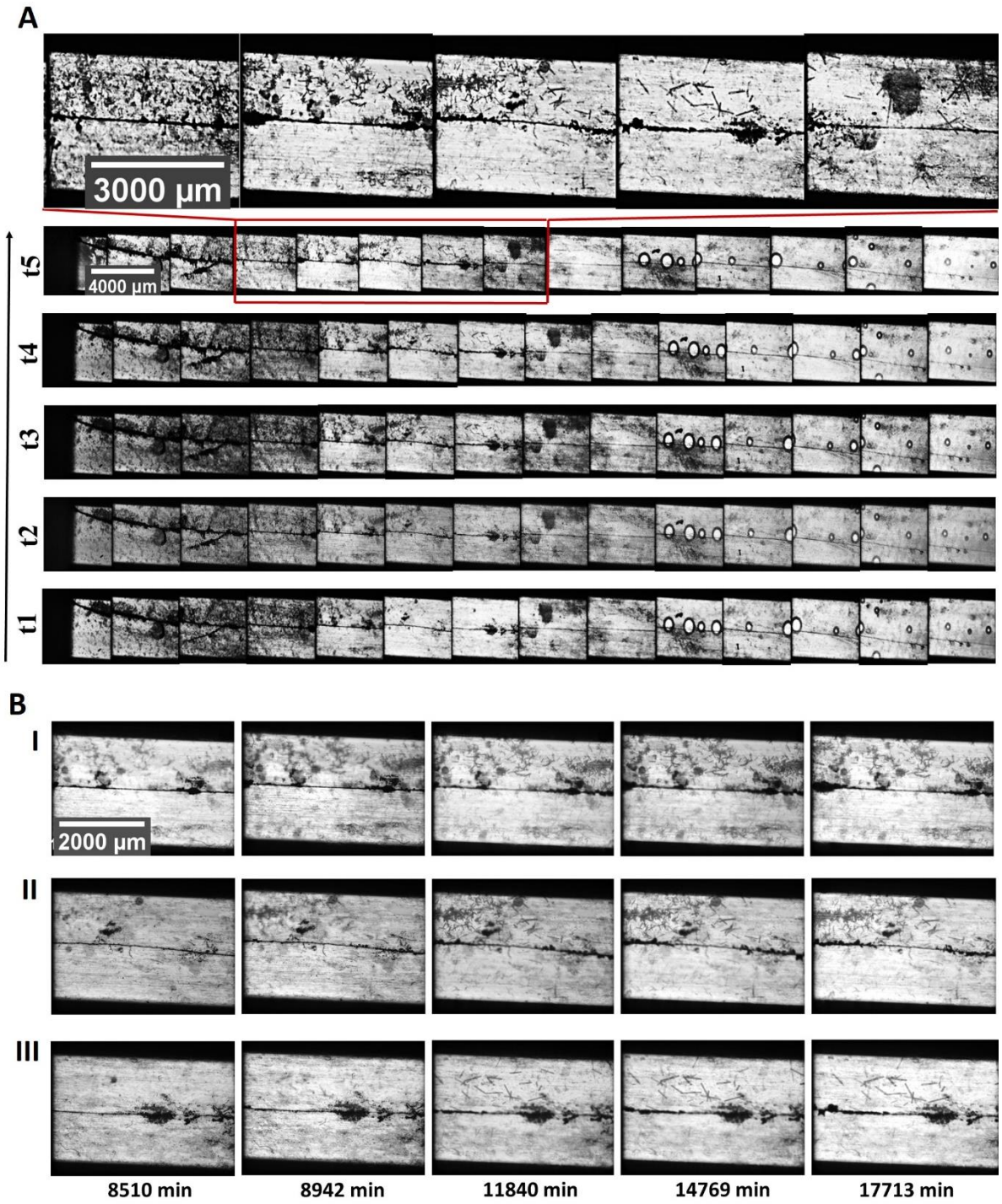

Figure 55. Protein crystallization in microgravity applying the counter diffusion technique in capillaries. Images were recorded using the ISS LMM microscope. *Pf*GST dimer crystals. (A) Time-lapse images were recorded with 2.5 x magnification. The imaging time extended to t = 17713 min, images were taken t1 = 8510 min, t2 = 8942 min, t3 = 11840, t4 = 14769 min and t5 = 17713 min after sample thawing. (B) Time-lapse images were recorded for 3 different areas (I, II, III) with 2.5 x magnification.

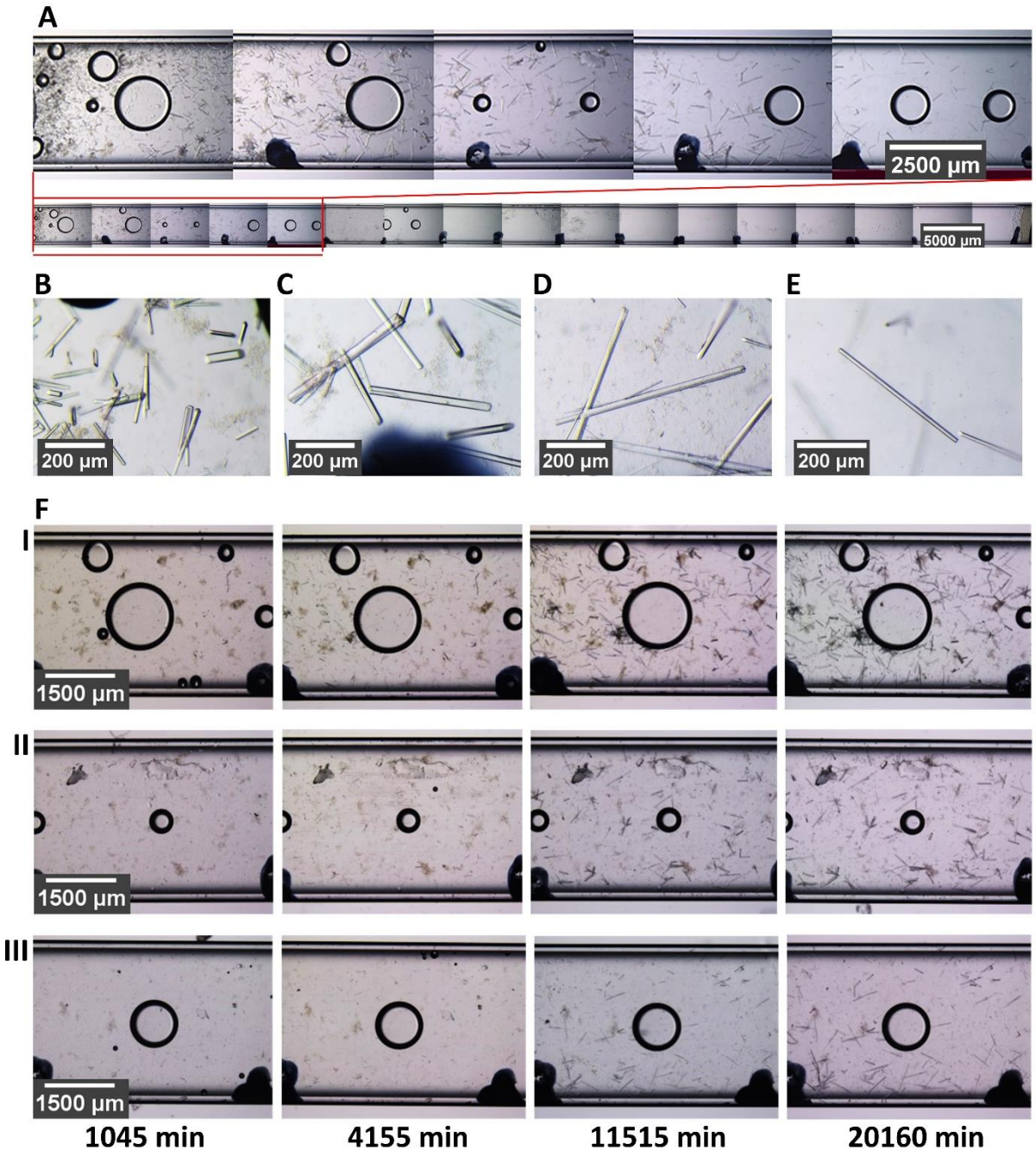

Figure 56. Protein crystallization in 1G applying the counter diffusion technique in capillaries. Images were recorded using a light microscope. PfGST dimer crystals. (A) Images were recorded t = 20160 min after sample thawing with 2.5 x magnification. (B,C,D,E) Images were recorded for 4 different areas in the capillary with 10 x magnification. (F) Time-lapse images were recorded for 3 different areas (I, II, III) in capillary with 2.5 x magnification. The imaging time extended to t = 20160 min, first image was taken t = 1045 min, after sample thawing.

Significant difference for the average microgravity grown crystal sizes from capillary areas (Student's *t*-test: $p < 0.01$); Significance for the area 22 – 28 mm and 28 -31 mm ($p < 0.01$); Significance for the area 22 -28 mm and 31 - 34 mm ($p < 0.01$); Significance for the area 22 -28 mm and 34 – 38 mm ($p <$

0.01); Significance for the area 28 – 31 mm and 31 – 34 mm ($p < 0.01$); No significance for the area 28 – 31 mm and 34 – 38 mm ($p > 0.05$); Significance for the area 31 – 34 mm and 34 – 38 mm ($p < 0.01$) is indicated (Figure 57). The average growth rate for crystals with lengths of major axis 446 ± 63 µm was calculated to 0.017 ± 0.003 µm h^{-1} (Figure 57).

Furthermore, the precipitant and protein concentrations for the capillary area with larger crystals were estimated (Chapter III 2.7). The average concentrations at the time point 8726 ± 216 min (Start of crystal growth) for the capillary area 32 ± 1.1 mm were calculated to 17.2 ± 0.6 nmol for *Pf*GST dimer and 1.1 ± 0.1 M for precipitant.

6.2 Crystal growth in 1G vs microgravity, *Pf*GST dimer

*Pf*GST dimer crystals grown in 1G showed nearly similar morphologies in each capillary and were photo-documented with a light microscope. *Pf*GST needle-like crystals in the capillary area 4 - 35 mm from the protein solution end were observed for dimer (Figure 56). The crystal dimensions and amount of crystals vary for several observed areas in capillary (Figure 56). Time-lapse images for different capillary areas were recorded with 2.5 x magnification to investigate crystal growth rates for crystals grown in microgravity. First image was taken t = 1045 min after sample thawing with 2.5 x magnification. The imaging time extended to t = 20160 min, images were taken t1 = 1045 min, t2 = 4155 min, t3 = 11515 and t4 = 20160 min after sample thawing. Protein precipitation was observed at the time point t1. At the time points t2 – t4 nucleation and subsequent growth of crystals was observed (Figure 56). The crystal dimensions at different positions in the capillaries were measured and comparative statistically analyzed. The area in the capillary was measured from the end of capillary (i.e. the protein). Temporarily the length of the major axis values for n = 37 crystals were measured. The average dimensions (length of major axis) of 1G grown crystals were calculated in the 4 areas from the capillary end, 2- 4 mm, 4 – 12 mm, 12 – 20 mm and 20 – 35 mm with crystal sizes 124 ±14 µm, 347 ±76 µm, 683 ±56 µm and 498 ± 19 µm, respectively (Figure 57). Significant difference for the average ground grown crystal sizes from capillary areas (Student's *t*-test: $p < 0.01$); Significance for the area 2 – 4 mm and 4 -12 mm ($p < 0.01$); Significance for the area 2 -4 mm and 12 - 20 mm ($p < 0.01$); Significance for the area 2 -4 mm and 20 – 35 mm ($p < 0.01$); Significance for the area 4 – 12 mm and 12 – 20 mm ($p < 0.01$); Significance for the area 4 – 12 mm and 20 – 35 mm ($p < 0.01$); Significance for the area 12 – 20 mm and 20 – 35 mm ($p < 0.01$) is indicated (Figure 57). The average growth rate for crystals with lengths of major axis 545 ± 34 µm was calculated to 0.022 ± 0.003 µm h^{-1} (Figure 57).

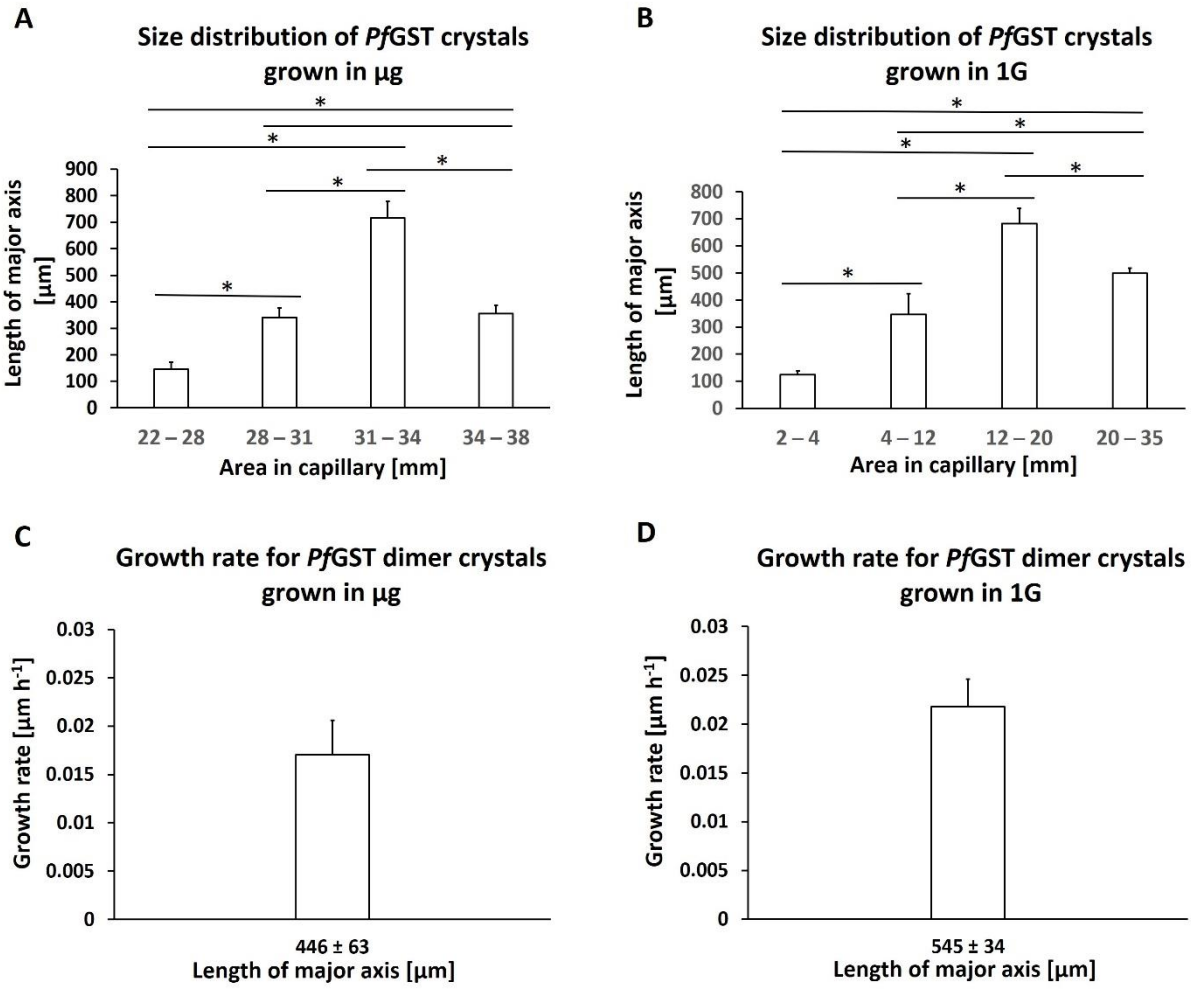

Figure 57. Comparative growth rate and size distribution values (the length of major axis) of *Pf*GST dimer crystals along the capillary. Different regions (areas) along the capillary were measured from the protein end of the capillary toward the protein-precipitant interface. Error bars represent standard deviations of the average. Significance within a 99% confidence interval was determined using Student's *t*-test and is denoted by asterisk (* = $p < 0.01$). (A) Average size distribution of crystals grown in µg for the areas from the capillary end, 22- 28 mm, 28 -31 mm, 31 – 34 mm and 34 – 38 mm. The sample numbers for crystals in the areas, 22 -28 mm, 28 – 31 mm, 31 -34 mm and 34 – 38 mm are n = 10, n = 11, n = 4 and n = 4, respectively. (D) Average size distribution of crystals grown in 1G for the areas from the capillary end, 2 - 4 mm, 4 – 12 mm, 12 – 20 mm and 20 – 35 mm. The sample sizes for crystals in the areas, 2 -4 mm, 4 – 12 mm, 12 – 20 mm and 20 – 35 mm are n = 10, n = 12, n = 5 and n = 10, respectively. (C) Average growth rate with standard deviations of crystals grown in µg with lengths of major axis 446 ± 63 µm. The sample number for crystals 446 ± 63 µm is n = 5. (D) Average growth rate with standard deviation of crystals grown in 1G with lengths of major axis 545 ± 34 µm. The sample number for crystals 545 ± 34 µm is n = 12.

6.3 Crystal growth in 1G vs microgravity, *Pf*GST dimer plus 0.5% tetramer

*Pf*GST needle-like crystals grown in µg were observed for the dimer with addition of 0.5 % tetramer (Figure 58). The capillary with growing crystals indicated damages, thus the solution have been evaporated as well running out over the time (figure 58). Time-lapse images for different capillary areas were recorded with 2.5 x and 10 x magnification to investigate crystal growth rates for crystals grown in µg. First image was taken t = 8511 min after sample thawing with 2.5 x magnification. The imaging time extended to t = 17725 min, images were taken t1 = 8511 min, t2 = 8952 min, t3 = 11848, t4 = 13408 and t5 = 17725 min after sample thawing. A subsequent growth of crystals with dimensions 100 – 400 µm was observed for the images recorded with 2.5 x magnification (Figure 58). Furthermore, at time points t = 9325 – 17891 min, crystals of different dimensions, 100-400 µm, at different areas in the capillary were observed and photo-documented with 10 x magnification (Figure 59).

*Pf*GST dimer crystals with addition of 0.5 % tetramer grown in 1G showed similar dimensions in capillary and were photo-documented with a light microscope. A total of 5 - 6 crystals in the capillary area 2 - 25 mm from the protein solution end were observed (Figure 60). Time-lapse images for different capillary areas were recorded with 2.5 x and 10 x magnification to investigate crystal growth rates for crystals grown in µg. First image was taken t = 1045 min after sample thawing with 2.5 x magnification. The imaging time extended to t = 20160 min. Images were taken t1 = 1045 min, t2 = 4155 min, t3 = 11515 and t5 = 20160 min after sample thawing. At time point t4 a subsequent growth of crystals with dimensions 100 – 300 µm was observed for the images recorded with 2.5 x and 10 magnifications (Figure 60).

6.4 Crystal growth in 1G vs microgravity, dimer plus 1% tetramer

Time-lapse images for different capillary areas with dimer plus 1 % tetramer were recorded with 2.5 x magnification to investigate crystal growth rates for crystals grown in µg. First image was taken t = 8972 min, after sample thawing with 2.5 x magnification. The imaging time extended to t = 16204 min, images were taken t1 = 8972 min, t2 = 11856 min, t3 = 13414, t4 = 14796 and t5 = 16204 min, after sample thawing. A subsequent growth of crystals was not observed for the images recorded with 2.5 x magnification (Figure 61).

*Pf*GST dimer crystals with the addition of 1 % tetramer grown in 1G showed similar dimensions in the capillary and were photo-documented with a light microscope. A total of 5 - 6 crystals in the capillary area 2 - 20 mm from the protein solution end were observed (Figure 62). Time-lapse images for different capillary areas were recorded with 2.5 x and 10 x magnification to investigate crystal growth rates for crystals grown in µg. First image was taken t = 1045 min after sample thawing with 2.5 x magnification. The imaging time extended to t = 20160 min, images were taken t1 = 1045 min, t2 = 4155 min, t3 = 11515 and t5 = 20160 min after sample thawing. At time point t4 a subsequent growth of crystals with dimensions 300 – 450 µm was observed for the images recorded with 2.5 x and 10 magnifications (Figure 62).

Figure 58. Protein crystallization in microgravity applying the counter diffusion technique in capillaries. Images were recorded using the ISS LMM microscope. *Pf*GST dimer crystals plus fluorescence labeled *Pf*GST aggregates in 0.5 %. (A) Time-lapse images were recorded with 2.5 x magnification. The imaging time extended to t = 17725 min, images were taken t1 = 8511 min, t2 = 8952 min, t3 = 11848, t4 = 13408 min and t5 = 17725 min after sample thawing. (B) Time-lapse images were recorded for 3 different areas (I, II, III) in the capillary with 2.5 x magnification.

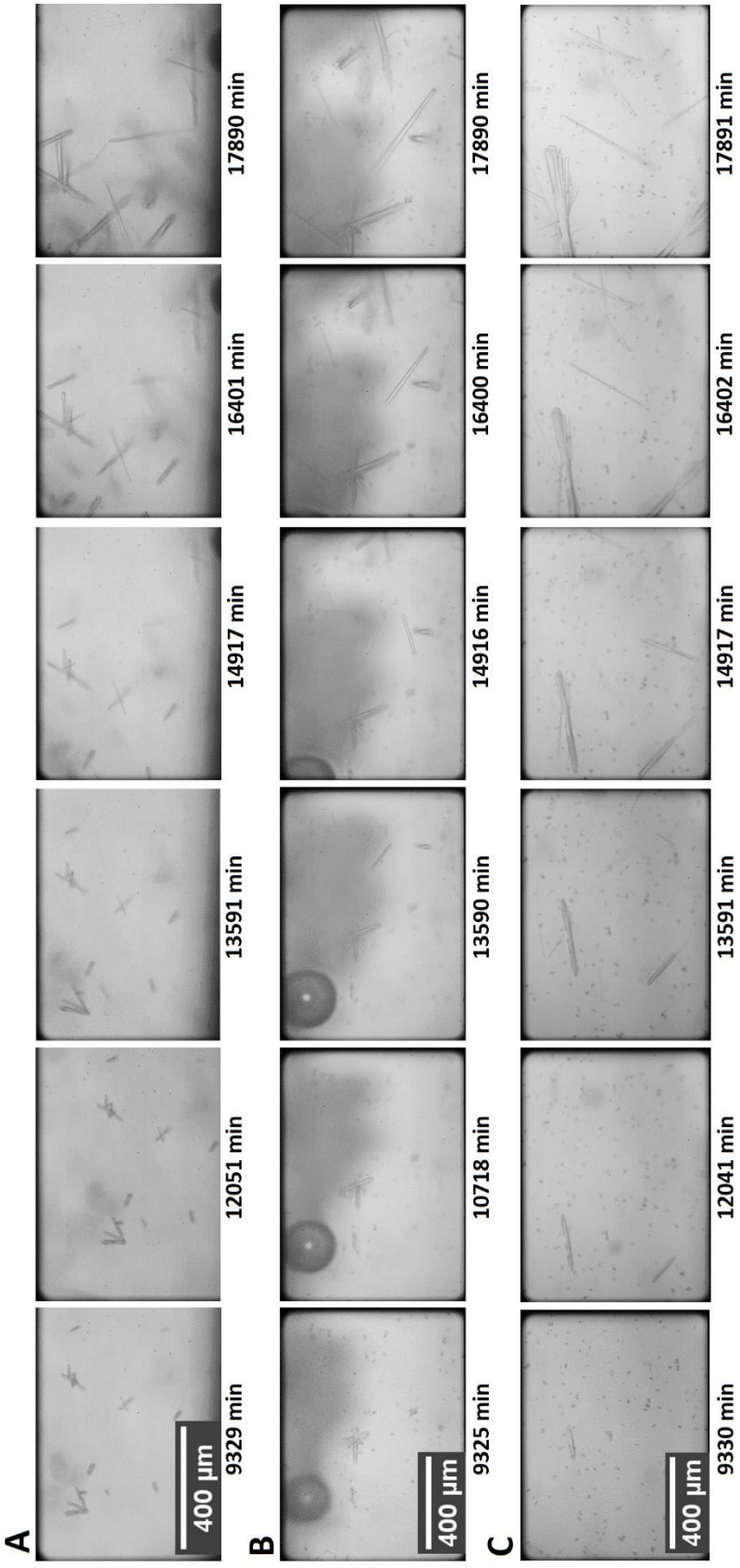

Figure 59. Growth of *Pf*GST crystals in microgravity. *Pf*GST dimer plus fluorescence labeled *Pf*GST aggregates in 0.5 %. Time-lapse images were recorded for 3 different areas (A, B, C) in capillary using the LMM microscope with 10 x magnification. The imaging time extended to t = 17890-17891 min, first images were taken t = 9325-9330 min after sample thawing.

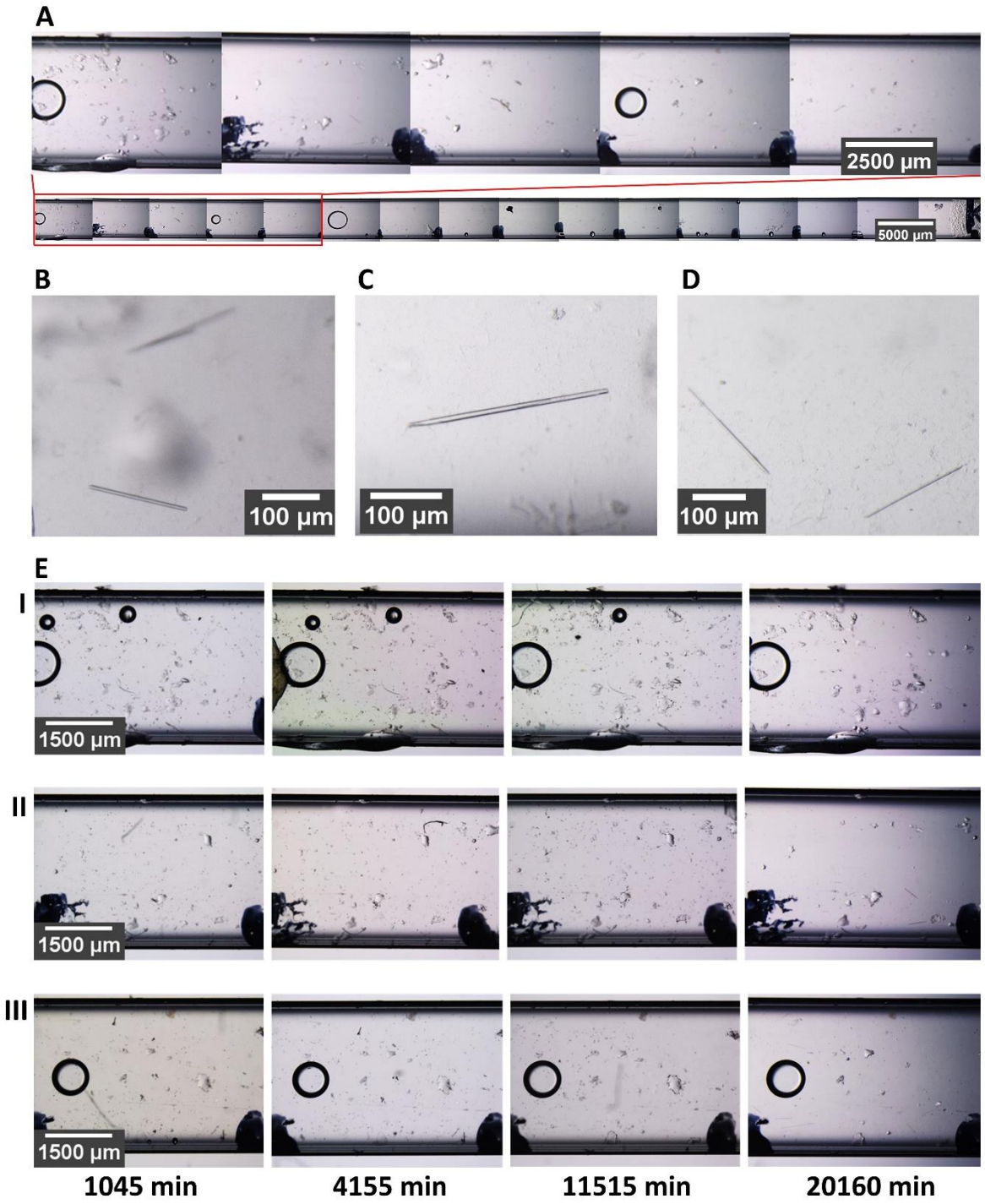

Figure 60. Protein crystallization in 1G applying the counter diffusion technique in capillaries. Images were recorded using a light microscope. *Pf*GST dimer crystals plus fluorescence labeled *Pf*GST aggregates in 0.5 %. (A) Images were recorded t = 20160 min after sample thawing with 2.5 x magnification. (B,C,D,)Images were recorded for 3 different areas in the capillary with 10 x magnification. (E) Time-lapse images were recorded for 3 different areas (I, II, III) in the capillary with 2.5 x magnification. The imaging time extended to t = 20160 min, first image was taken t = 1045 min after sample thawing.

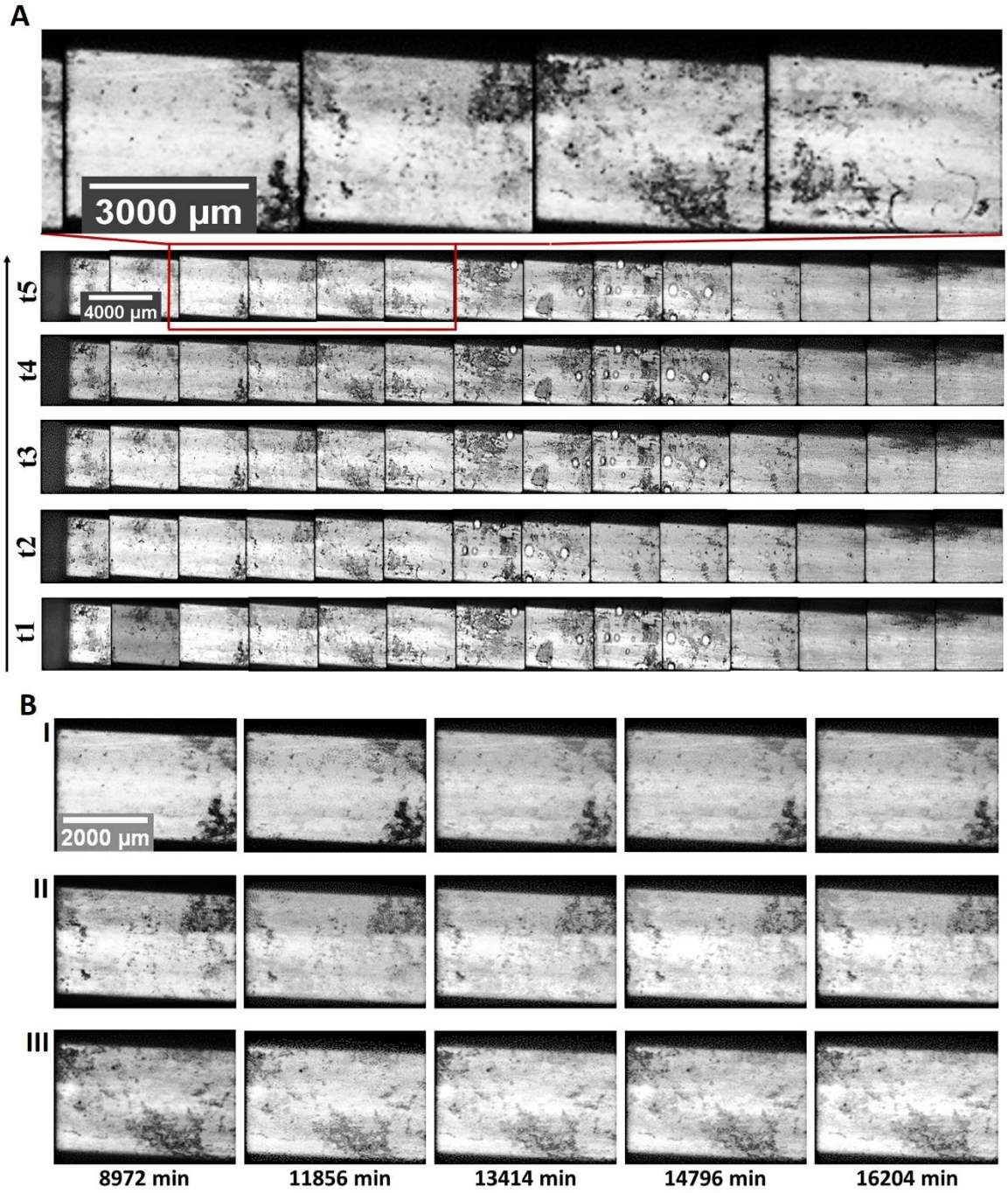

Figure 61. Images were recorded using the ISS LMM microscope. *Pf*GST dimer plus fluorescence labeled *Pf*GST aggregates in 1 %. (A) Time-lapse images were recorded with 2.5 x magnification. The imaging time extended to t = 16204 min, images were taken t1 = 8972 min, t2 = 11856 min, t3 = 13414, t4 = 14796 min and t5 = 16204 min after sample thawing. (B) Time-lapse images were recorded for 3 different areas (I, II, III) with 2.5 x magnification.

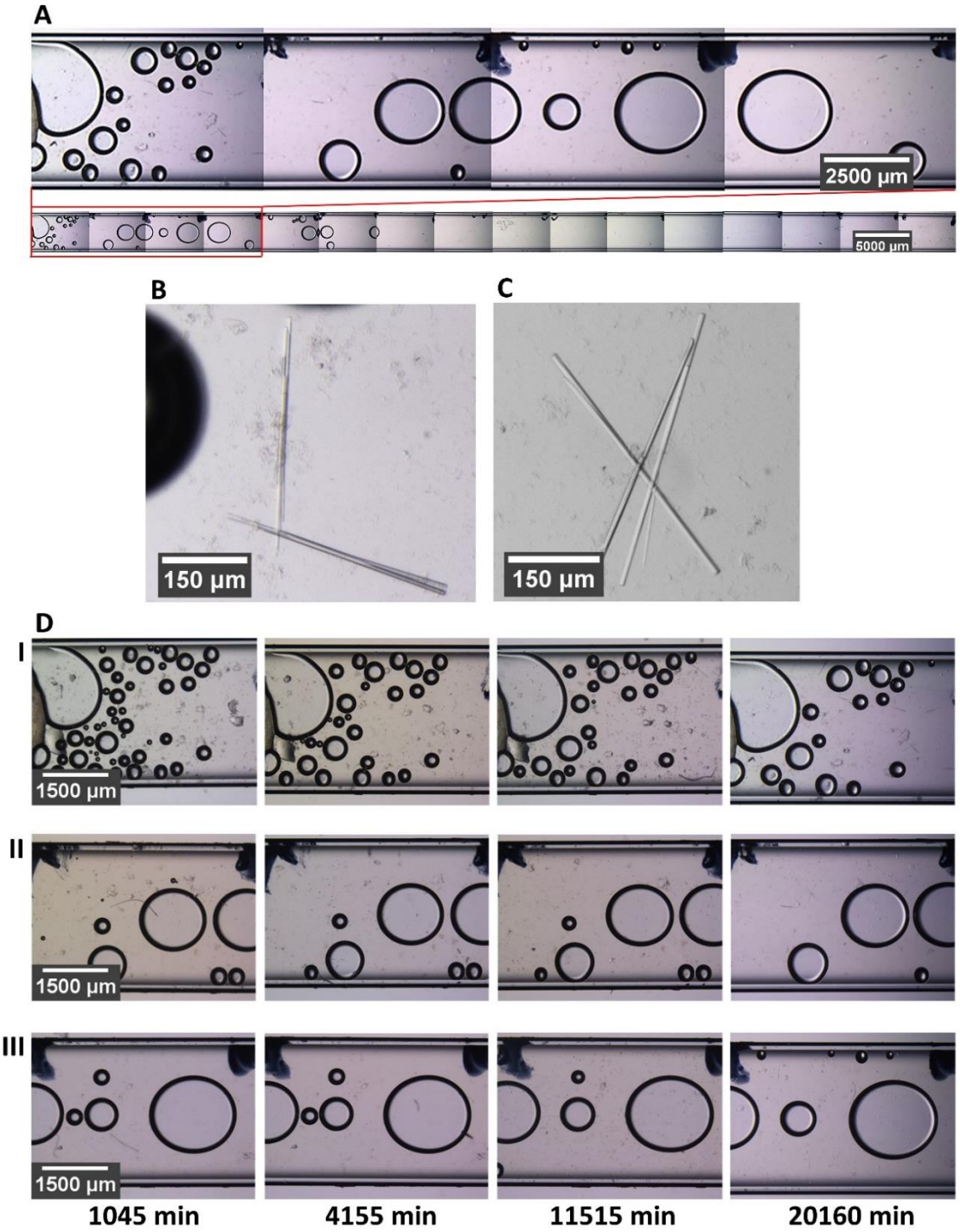

Figure 62. Protein crystallization in 1G. Images were recorded using a light microscope. *Pf*GST dimer crystals plus fluorescence labeled *Pf*GST aggregates in 1 %. (A) Images were recorded t = 20160 min after sample thawing with 2.5 x magnification. (B,C,) Images were recorded for 2 different areas in the capillary with 10 x magnification. (D) Time-lapse images were recorded for 3 different areas (I, II, III) with 2.5 x magnification. The imaging time extended to t = 20160 min, first image was taken t = 1045 min after sample thawing.

6.5 Analysis of µg grown crystals after returnto the earth

After samples returned to the earth light microscope images of crystals in the capillaries grown in µg were recorded and photo-documented. Images were recorded t = 28 days after sample thawing with 2.5 x and 10 x magnification (Figure 63). The crystal dimensions, length of major axis 80 ~1300 µm, vary at different areas of capillary for the dimer crystals (Figure 63). The dimensions, length of major axis, for larger crystals were measured to 1200 ~1300 µm. Crystals lengths of major axis 80 ~700 µm were observed and photo documented for the dimer with addition of 0.5 % tetramer (Figure 63). Furthermore, 8-10 crystals with lengths of major axis 80 ~300 µm were observed and photo documented for the dimer with addition of 1 % tetramer (Figure 63).

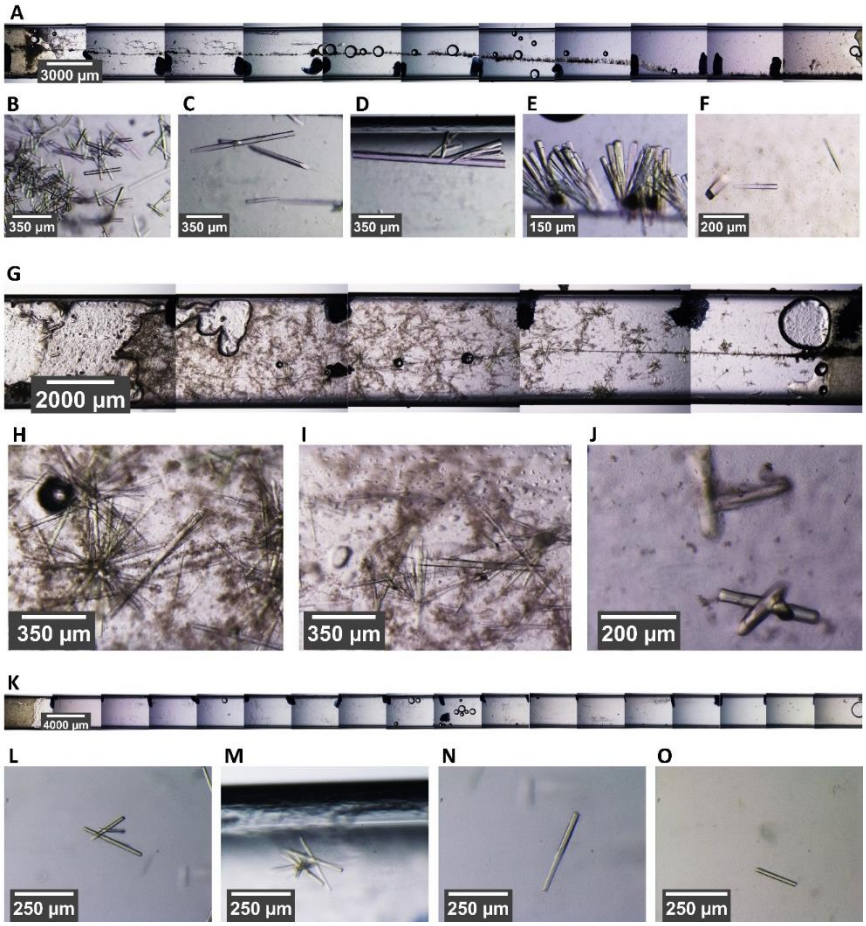

Figure 63. *Pf*GST crystals grown in µg. Dimer and dimer plus fluorescence labeled *Pf*GST aggregates in 2 different ratios. Images were recorded using a light microscope t = 29 days after sample thawing, after µg samples returned on the earth. (A) Dimer crystals in capillary, images were recorded with a 2.5 x objective. (B,C,D,E,F) Dimer crystals, recorded with a 10 x objective in different areas in the capillary. (G) Dimer plus tetramer in 0.5 % ratio, recorded with a 2.5 x objective. (H,I,J) Dimer plus tetramer in 0.5 % ratio, recorded with a 10 x objective. (K) Dimer plus tetramer in 1 % ratio, recorded with a 2.5 x objective. (L,M,N,O) Dimer plus tetramer in 1 % ratio, recorded with a 10 x objective.

6.6 Impurity incorporation into crystals grown in 1G vs microgravity

To investigate the incorporation of impurities into growing crystals for each protein fluorescently labeled protein-aggregates were prepared, which simulate protein aggregate impurities in solution. For crystallization experiments in µg and 1G samples with different protein-aggregate ratios were prepared. Initial crystallization experiments showed that fluorescently labeled *Pf*GST aggregates are not crystallizing under same conditions as *Pf*GST dimers. Since samples returned to earth confocal images of crystals in the capillaries grown in µg and 1G were recorded and photo-documented. The confocal fluorescence micrograph of *Pf*GST dimer sample (negative control) shows the absence of fluorescence for µg and 1G crystals (Figure 64). The *Pf*GST crystals grown in µg and 1G in presence of fluorescent labeled protein aggregates in 0.5 % and 1 % ratios showed the presence of green fluorescence (Figure 64).

Based on confocal laser scanning fluorescence microscopy analysis, the incorporation of fluorescently labeled tetramers into growing dimer crystals was analyzed. Therefore, incorporation of fluorescently labeled tetramers into growing dimer crystal can be investigated applying appropriate methods and techniques. For this purpose quantitative analyses of total fluorescence/crystal volume were performed applying a fluorescence microplate reader. Temporarily the fluorescence intensities values for n = 20 crystals grown in 1G and µg were measured. The average fluorescence intensities of crystals grown in 1G for a crystal volume of μm^3 was calculated for the dimer and dimer plus 1 % tetramer with fluorescence intensity values 0 and 0.57±0.16 a.u, respectively (Figure 65). The average fluorescence intensities of crystals grown in µg for a crystal volume of μm^3 was calculated for the dimer and dimer plus 1 % tetramer with fluorescence intensity values 0 and 0.22±0.11 a.u, respectively (Figure 65). Significant difference for the average fluorescence intensities for the samples with 1 % tetramer 1G vs µg (Student's t-test: $p < 0.01$); Significance ($p < 0.01$) was indicated (Figure 65).

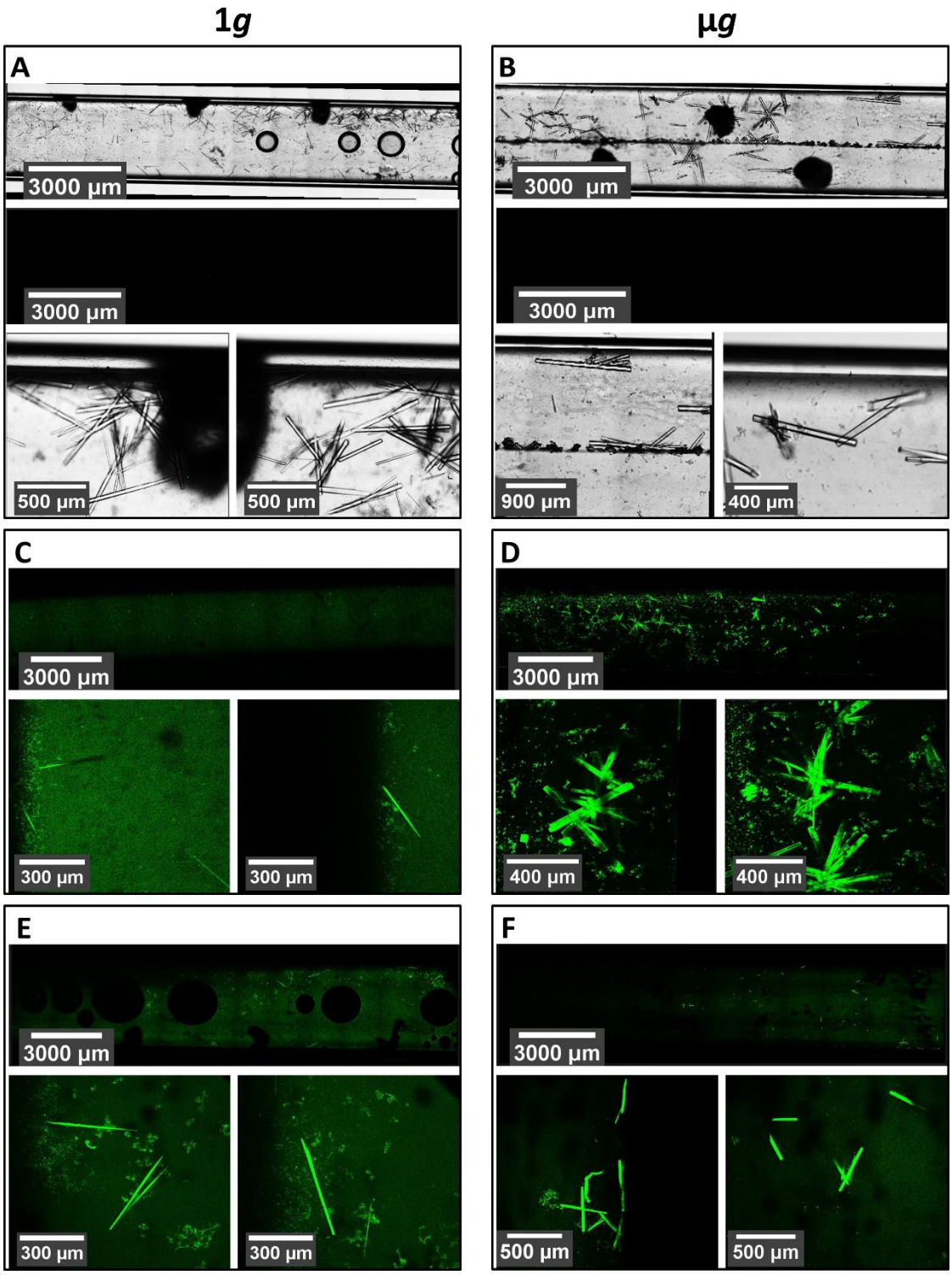

Figure 64. Crystals grown in 1G vs µg. Images were recorded after return of the samples to the earth. Crystals of *Pf*GST dimer plus fluorescence labeled, Alexa Fluor 488, aggregates in different ratios. Crystal images were recorded using a confocal laser microscope 2.5 x and 10 x objective with FITC (*Pf*GST) fluorescence filter. (A) Dimer crystals grown in 1G. (B) Dimer crystals grown in µg. (C) Dimer : tetramer in 0.5 % ratio, 1G. (D) Dimer : tetramer in 0.5 % ratio, µg. (E) Dimer : tetramer in 1 % ratio, 1G. (F) Dimer : tetramer in 1 % ratio, µg.

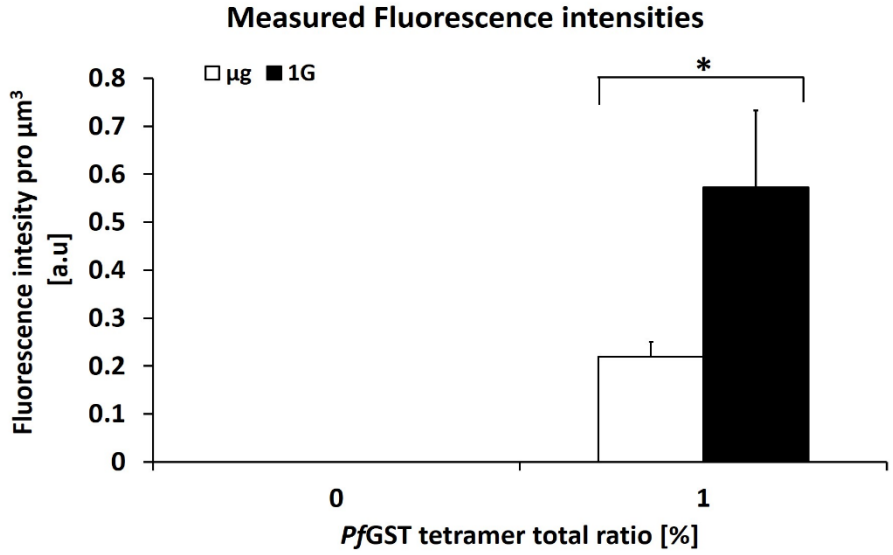

Figure 65. Comparative analysis of fluorescence intensities of crystals grown in microgravity versus 1g grown *Pf*GST crystals. In total n = 5 1G grown and n = 5 µg grown crystals with similar dimensions from each *Pf*GST tetramer ratio (in total n = 20 crystals) were 2 x washed in native buffer and resolved in 1xPBS buffer for fluorescence intensity measurements. Fluorescence intensities were measured applying a fluorescence microplate reader. Error bars represent standard deviations of the average. Significance within a 99% confidence interval was determined using Student's *t*-test and is denoted by asterisks (* = p < 0.01). Measured average fluorescence intensities correspond to a crystal volume of µm^3. Data of the dimer (0) and the tetramer ratio (1%) are shown.

6.7 X-ray diffraction data collection, processing and structure of *Pf*GST

Diffraction data of *Pf*GST crystals grown in 1G and µg were collected at 100 K temperature at the PETRA III, beamline P11 EMBL. X-ray data for dimer and dimer plus 0.5 % tetramer were collected and statistical (via crystal quality factors) analyzed. Data for crystals with approximately similar dimensions for each ratio were collected. For cryoprotection the crystals were soaked with precipitant solution supplemented with 14 % (v/v) glycerol. Diffraction data were subsequently indexed, integrated and scaled with XDS and ccp4 programs. Datasets for n = 17 crystals grown in 1G and µg were analyzed (Tables 31; 32). Datasets were cut individual for each crystal dataset monitoring Rmeas, Rsym, I/σ and CC1/2. The crystals belonged to the monoclinic space group $P2_1$ with unit cell dimensions ~ 61 Å, ~ 69 Å, ~ 100 Å and β angle of ~ 92.0° (Tables 31; 32). However, two µg grown crystals with 0.5 % ratio belonged to orthorhombic space group $P2_1P2_1P2_1$ with unit cell dimensions 57.9 Å, 69.1 Å, 123.8 Å and β angle of 90.0° (Table 32; 33). To investigate the quality differences of 1G vs µg grown crystals the average signal-to-noise ratios (I/σ(I)) vs resolutions for each crystal was calculated and statistical analyzed (Figure 66). Significant difference for the average I/σ(I) values for dimer 1G vs µg (Student's t-test: $p < 0.05$); Significance for the resolution range 5.96 Å ($p < 0.05$) was indicated (Figure 66). However, no significant difference for the average I/σ(I) values 1G vs µg (Student's t-test: $p < 0.05$);

No significance for the resolution ranges 2.11 - 4.23 Å ($p > 0.05$) was indicated (Figure 66). To investigate the number of protein molecules in unit cell and the structure of crystals with 2 different space groups one dataset each of crystals were analyzed. Data were cut individual 1 x for crystals with space group $P2_1P2_1P2_1$ and 1 x for crystals with space group $P2_1$ to 1.8 Å and 2.1 Å, respectively (Tables 31-33). The homologue structure of *Pf*GST dimer (PDB code: 3FRC) was used as a search model for molecular replacement and Matthews coefficient probability. The Matthews coefficient was determined for both datasets, $P2_1P2_1P2_1$ and $P2_1$, to 2.48 $Å^3\ Da^{-1}$ and 2.19 $Å^3\ Da^{-1}$ respectively. The solvent content was calculated to be 50 % for dataset 1 with 2 *Pf*GST monomers in the respective asymmetric unit. The solvent content was calculated to be 43 % for dataset 2 with 4 *Pf*GST monomers in the respective asymmetric unit. Data collection parameters are summarized in Table 33. The asymmetric unit for crystal 1 consists 1 x *Pf*GST homodimer with 2 identical monomer chains and the asymmetric unit for crystal 2 consists of 2 x *Pf*GST homodimers with 4 identical monomer chains (Figure 67A, B).

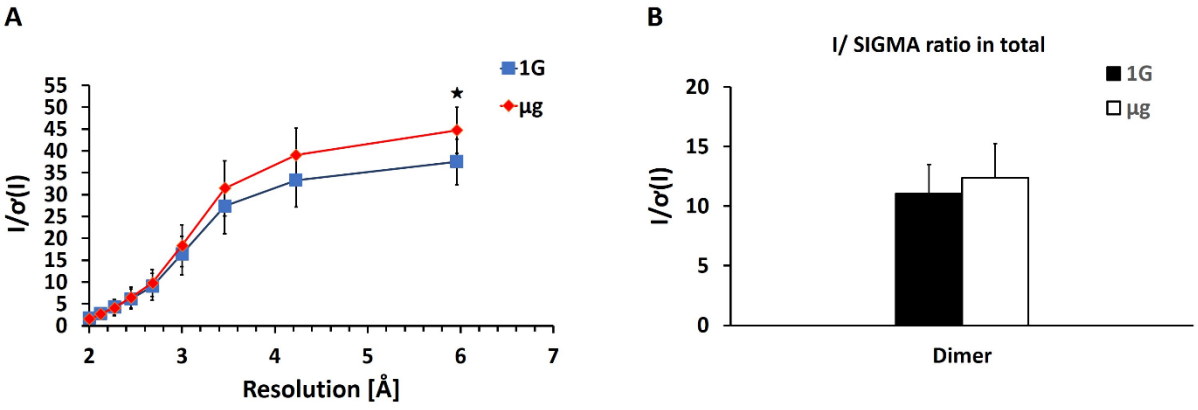

Figure 66. Comparative analysis of the merged X-ray diffraction datasets of µg grown vs 1G grown *Pf*GST dimer crystals. In total X-ray datasets for n = 5 microgravity grown and n = 6 1G grown crystals (in total n = 11 crystals) were analyzed. Error bars represent standard deviations of the average. Significance within a 95% confidence interval was determined using Student's *t*-test and is denoted by asterisks (*= $p < 0.05$). (A) Line graph with whiskers. Distribution of signal-to-noise ratio (I/σ(I)) vs resolution. (B) Distribution of signal-to-noise ratio (I/σ(I)) in total.

Table 31. Data collection statistics (via XDS) for *Pf*GST dimer crystals grown in 1G vs µg. In total X-ray data for n = 6 1G grown and n = 6 µg grown crystals with similar dimensions were analyzed.

	***Pf*GST dimer**											
Data collection statistics	**1G**						**µg**					
	Crystal 1	**Crystal 2**	**Crystal 3**	**Crystal 4**	**Crystal 5**	**Crystal 6**	**Crystal 1**	**Crystal 2**	**Crystal 3**	**Crystal 4**	**Crystal 5**	**Crystal 6**
Wavelength	1.0332	1.0332	1.0332	1.0332	1.0332	1.0332	1.0332	1.0332	1.0332	1.0332	1.0332	1.0332
Space group	P 2_1	P 2_1	P 2_1	P 2_1	P 2_1	P 2_1	P 2_1	P 2_1	P 2_1	P 2_1	P 2_1	P 2_1
Unit cell parameters a/b/c [Å]	61.7 69.6 101.8	61.8 69.6 102.1	61.7 69.7 102.1	61.7 69.4 102.2	61.6 69.7 101.9	61.5 69.9 101.7	61.5 70.0 101.7	61.4 69.6 100.5	61.5 69.9 101.9	61.3 69.6 99.9	61.4 69.6 100.7	61.3 69.6 99.8
β [°]	92.6	92.6	92.7	92.6	92.5	92.5	92.4	92.3	92.4	92.2	92.4	92.1
Total reflections	145822	166986	89958	189029	220956	157385	203500	167731	191621	128111	122194	142342
Unique reflections	38372	43965	24006	50304	57699	41447	54174	44765	50462	33883	32212	37603
Resolution range [Å]	50-2.30 (2.44-2.30)	50-2.20 (2.33-2.20)	50-2.70 (2.86-2.70)	50-2.10 (2.23-2.10)	50-2.00 (2.12-2.00)	50-2.24 (2.38-2.24)	50-2.05 (2.17-2.05)	50-2.17 (2.30-2.17)	50-2.10 (2.23-2.10)	50-2.38 (2.52-2.38)	50-2.43 (2.57-2.43)	50-2.30 (2.44-2.30)
R means [%]	7.7 (43.4)	7.3 (42.5)	9.3 (46.9)	7.3 (43.5)	7.7 (45.4)	8.6 (45.9)	6.2 (43.5)	6.2 (45.1)	7.2 (38.7)	6.5 (45.1)	8.0 (47.5)	6.3 (46.1)
R symm [%]	6.6 (37.4)	6.3 (36.4)	8.0 (40.1)	6.3 (37.3)	6.6 (39.2)	7.4 (39.4)	5.3 (37.4)	5.3 (38.5)	6.2 (34.2)	5.6 (38.7)	6.9 (43.0)	5.4 (39.7)
Mean I/σ (I)	14.57 (3.40)	15.96 (3.14)	13.83 (3.16)	13.97 (2.98)	14.19 (3.41)	13.94 3.42)	18.35 (3.70)	16.71 (3.40)	15.04 (3.67)	16.42 (3.51)	14.50 (3.13)	15.94 (3.26)
CC (1/2) [%]	99.9(93.9)	99.9 (91.7)	99.8 (90.1)	99.9 (93.9)	99.8 (88.5)	99.9 (92.7)	99.9 (93.3)	99.9 (91.6)	99.9 (93.7)	99.9 (93.4)	99.9 (90.2)	99.9 (92.0)
Average mosaictiy [°]	0.11	0.11	0.42	0.13	0.07	0.14	0.22	0.22	0.09	0.12	0.10	0.18
Completeness [%]	99.6 (99.1)	99.0 (97.9)	99.5 (98.5)	99.2 (97.1)	98.8 (97.6)	99.6 (98.8)	99.5 (99.0)	99.4 (98.6)	99.5 (98.5)	99.5 (98.4)	99.5 (98.6)	99.7 (99.1)

Table 32. Data collection statistics (via XDS) for *Pf*GST crystals in tetramer total ratio 0.5 % grown in µg. In total X-ray data for n = 5 µg grown crystals with similar dimensions were analyzed.

	***Pf*GST tetramer total ratio 0.5 %**				
Data collection statistics	**µg**				
	Crystal 1	**Crystal 2**	**Crystal 3**	**Crystal 4**	**Crystal 5**
Wavelength	1.0332	1.0332	1.0332	1.0332	1.0332
Space group	P 2_1	P 2_1 2_1 2_1	P 2_1 2_1 2_1	P 2_1	P 2_1
Unit cell parameters a/b/c [Å]	61.3 69.6 99.84	57.9 69.1 123.8	57.9 69.0 123.8	61.4 69.9 101.4	61.5 69.9 101.9
β [°]	92.5	90.0	90.0	92.5	92.5
Total reflections	110852	395543	215.759	99518	164867
Unique reflections	29214	55299	29621	26571	43934
Resolution range [Å]	50-2.50 (2.65-2.50)	50-1.70 (1.80-1.70)	50-1.70 (2.23-2.10)	50-2.60 (2.76-2.60)	50-2.20 (2.33-2.20)
R means [%]	8.4 (47.5)	3.8 (31.7)	2.9 (7.7)	8.1 (46.9)	7.9 (47.0)
R symm [%]	7.2 (40.8)	3.5 (29.0)	2.7 (7.1)	6.9 (40.0)	6.8 (40.2)
Mean I/σ (I)	13.37 (3.29)	31.10 (4.84)	48.90 (21.95)	15.42 (2.87)	15.17 (3.08)
CC (1/2) [%]	99.9 (92.1)	100.0 (97.3)	100.0 (99.8)	99.9 (90.9)	99.9 (92.5)
Average mosaictiy [°]	0.12	0.05	0.06	0.19	0.21
Completness [%]	99.6 (98.5)	99.7 (98..4)	99.9 (99..6)	99.6 (98.9)	99.6 (98.9)

Table 33. Data collection statistics for *Pf*GST in two different space groups.

Data collection statistics		
Beamline/Source	PETRA III, P11	PETRA III, P11
Wavelength [Å]	1.0332	1.0332
Space group	P 2_1 2_1 2_1	P 2_1
Unit cell parameters: a, b, c [Å] β [°]	57.9, 69.1, 123.9 90.0	61.5, 69.8, 101.8 92.4
Resolution [Å]	46.1 – 1.8 (1.84 – 1.80)	46.1 – 2.1 (2.16 – 2.10)
Temperature [K]	100	100
Rmerge [%]	3.1 (20.5)	5.5 (34.5)
Rmeas [%]	3.6 (23.7)	7.4 (46.1)
Measured reflections	343330	191581
Unique reflections	46831	50458
Average I/σ(I)	33.9 (7.6)	14.3 (3.4)
Mn(I) half-set correlation CC(1/2) [%]	100 (98.4)	99.8 (91.4)
Completeness [%]	99.8 (98.2)	99.5 (97.2)
Mosaicity [°]	0.05	0.09
Redundancy	7.3 (7.4)	3.8 (3.8)
Nr. of atoms		
Protein	3389	6778
Brom	2	4
Matthews coefficient [$Å^3$ Da^{-1}]	2.48	2.19
Solvent content [%]	50	43
Molecules in the asymmetric unit	2	4

*Values in parentheses are for the highest resolution shell. Rmerge: Σhkl Σi | *Ii* (hkl) – ⟨*I* (*hkl*)⟩ | / Σ_{hkl}Σi *Ii* (*hkl*), where *I* (*hkl*) is the mean intensity of the reflections hkl, Σ_{hkl} is the sum over all reflections and Σi is the sum over i measurements of reflection hkl.

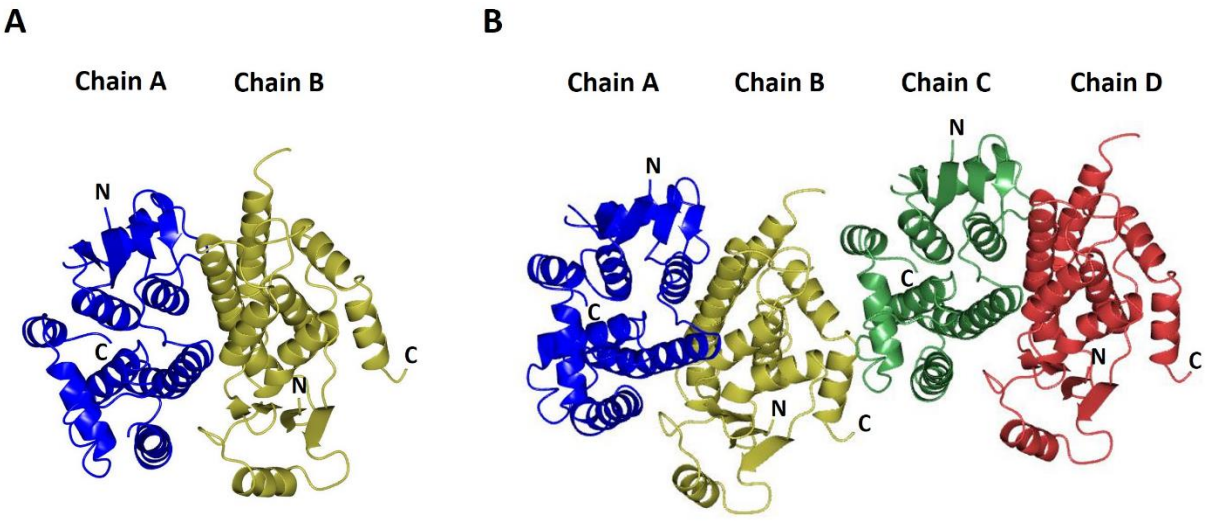

Figure 67. Structure of *Pf*GST homodimer in 2 different space groups. (A) Cartoon representation of the *Pf*GST homodimer structure for space group 19. Blue is used for chain A, gold for chain B; labels of the N- and C-terminus are shown. (B) Cartoon representation of the *Pf*GST homodimer (2 x homodimer) structure for space group 4. Blue is used for chain A, gold for chain B, green for chain C and red for chain D; N- and C-terminals are indicated.

7 Multichannel DLS system

The major advantage of a multichannel DLS system in comparison to other DLS systems (Chapter III 2.2.7.2), is possibility rapid determine the translational diffusion constant and simultaneously in several positions in a capillary. The protein solution are filled in capillaries 100mm in length, 3mm in width, 0.3mm inner diameter and the measurements are performed with a multichannel DLS system. The dispersity and particle radius distribution of Glucose isomerase (10 mg ml^{-1}), *Pf*GST dimer (10 mg ml^{-1}) and a sample of synthetic gold nanoparticles (10 mg ml^{-1}) were determined and analyzed at room temperature by the multichannel DLS system. The samples were analyzed by DLS measurements to verify the purity and dispersity of protein and also to determine the adequate hydrodynamic radius (R_h). Time resolved measurements of hydrodynamic radius, verified the monodispersity of Glucose isomerase, *Pf*GST dimer and synthetic gold nanoparticles solutions (Figures 68; 69; 70). The observed data showed similar values of hydrodynamic radii for entirely 8 channels for each protein/particles (Table 34).

Further multichannel DLS experiments were performed to investigate the protein crystallization (Figure 71). The observed data showed similar values of hydrodynamic radiuses, about 4 ± 30nm, for entirely 6 channels (Figure 71).

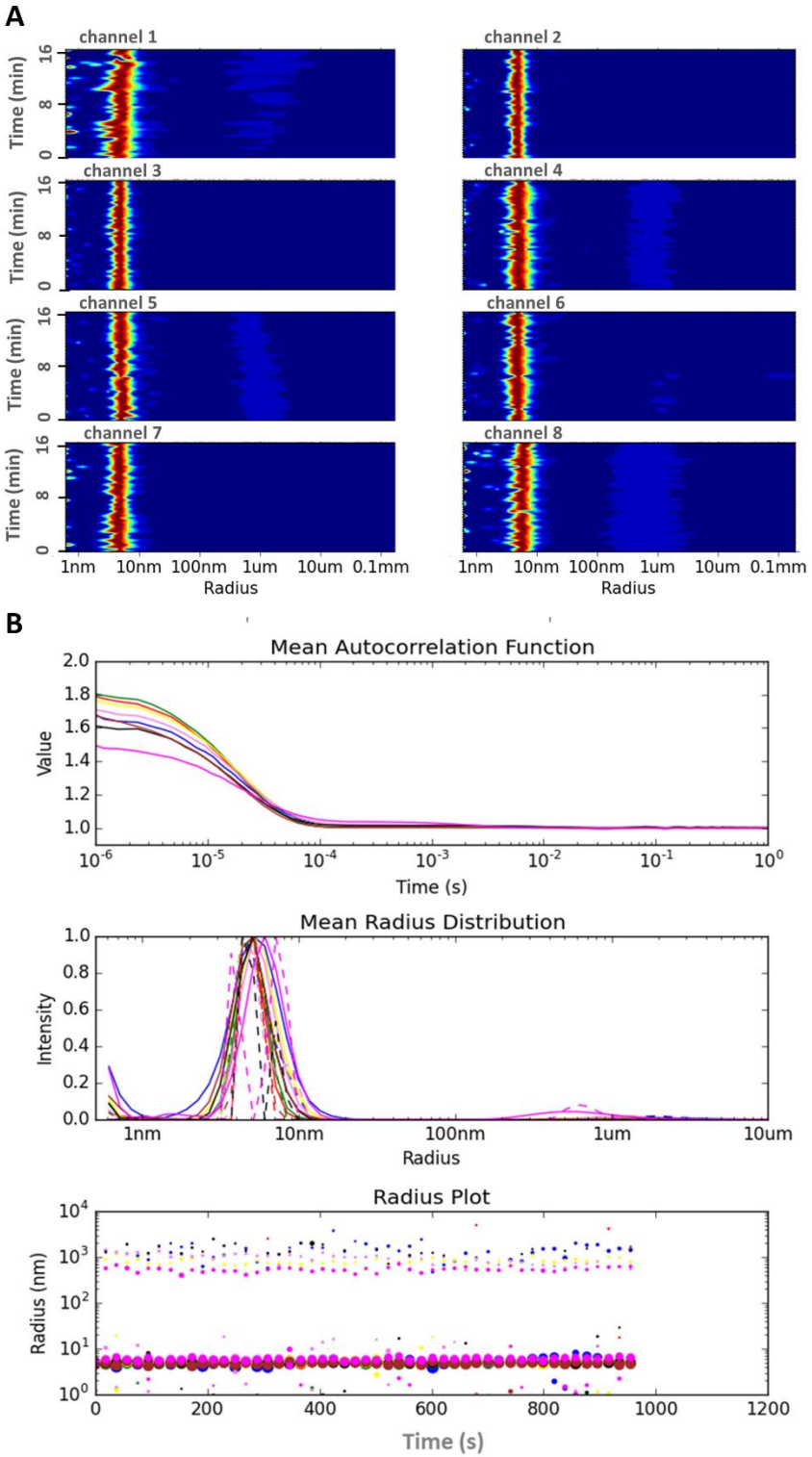

Figure 68. Real-time observation of glucose isomerase sample at a concentration of 10 mg mL^{-1}, using *in situ* multichannel DLS system. (A) The graphs in 8 boxes show the protein radius distribution dependence on time with a constant radius in the capillary. (B) Summary graphs of radius distribution of a measurement series: a representative mean autocorrelation function; a representative mean radius distribution; a representative radius plot.

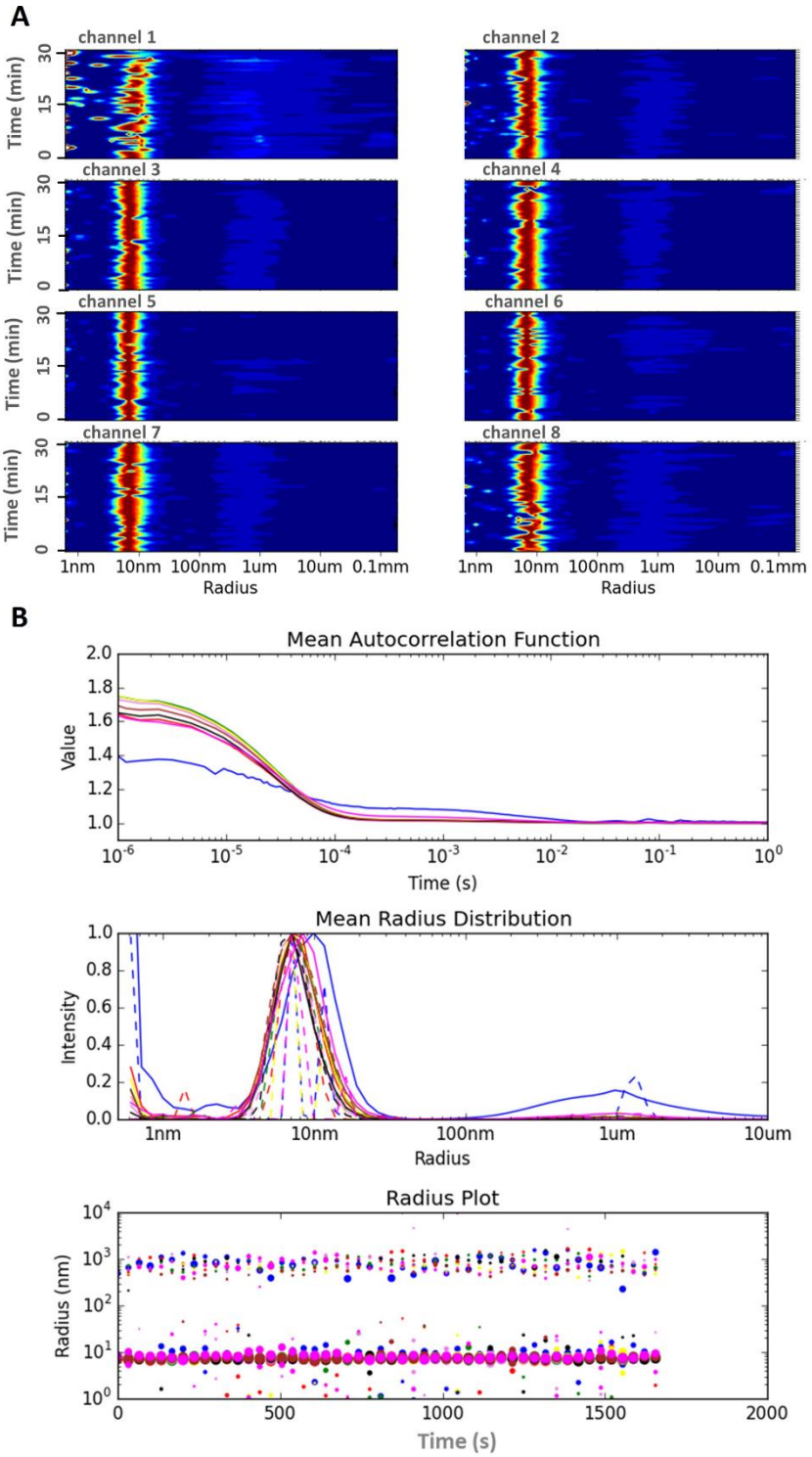

Figure 69. Real-time observation of *Pf*GST dimer sample at a concentration of 10 mg mL^{-1}, using *in situ* multichannel DLS system. (A) The graphs in 8 boxes show the protein radius distribution dependence on time with a constant radius in the capillary. (B) Summary graphs of radius distribution of a measurement series: a representative mean autocorrelation function; a representative mean radius distribution; a representative radius plot.

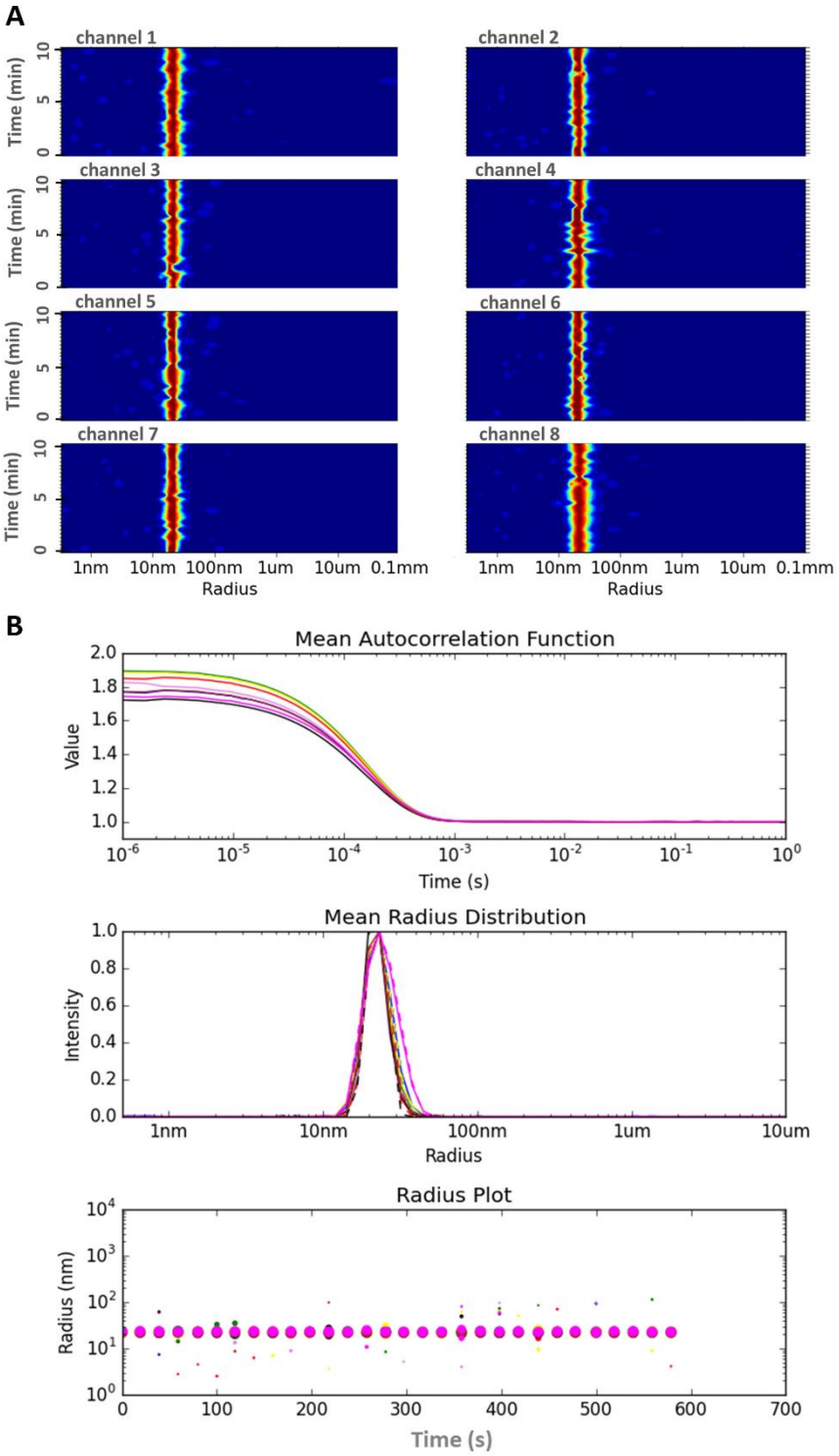

Figure 70. Real-time observation of synthetic nanoparticles sample at a concentration of 50 mg mL^{-1}, using *in situ* multichannel DLS system. (A) The graphs in 8 boxes show the protein radius distribution dependence on time with a constant radius in the capillary. (B) Summary graphs of radius distribution of a measurement series: a representative mean autocorrelation function; a representative mean radius distribution; a representative radius plot.

Table 34. Hydrodynamic radius (R_h) and count rate with standard deviations for glucose isomerase, *Pf*GST and synthetic nanoparticles measured applying multichannel DLS system.

Channel	Glucose isomerase		*Pf*GST		Synthetic gold nanoparticles	
	Hydrodynamic radius [nm]	Count rate [kHz]	Hydrodynamic radius [nm]	Count rate [kHz]	Hydrodynamic radius [nm]	Count rate [kHz]
1	5.0 ± 0.5	9.3 ± 0.5	9.1 ± 1.6	4.5 ± 0.8	22.4 ± 0.4	75.6 ± 4.5
2	4.9 ± 0.2	24.9 ± 0.8	7.4 ± 0.6	12.3 ± 1.0	22.2 ± 1.2	157.3 ± 8.6
3	4.9 ± 0.1	30.1 ± 0.8	7.5 ± 0.4	21.7 ± 1.4	22.9 ± 2.8	208.9 ± 11.8
4	5.3 ± 0.2	26.6 ± 1.2	7.6 ± 0.9	23.4 ± 2.3	22.4 ± 1.8	213.7 ± 12.9
5	5.3 ± 0.2	55.3 ± 2.8	7.1 ± 0.4	52.9 ± 3.1	21.9 ± 0.5	547.9 ± 28.8
6	4.9 ± 0.2	34.4 ± 3.4	7.2 ± 0.5	45.1 ± 3.6	21.9 ± 1.1	446.1 ± 21.4
7	4.8 ± 0.3	17.5 ± 0.6	7.4 ± 0.6	27.2 ± 1.8	21.9 ± 0.2	254.9 ± 13.2
8	5.9 ± 0.5	20.3 ± 1.1	7.9 ± 1.1	19.9 ± 2.4	23.1 ± 1.3	147.5 ± 8.4

For the crystallization experiment the capillary containing 37 µl *Pf*GST solution (25mg/ml) was injected additionally with 37µl precipitant (2.8M AmSO4; 0.1M PO4 Buffer, pH 6.7) and immediately set for multichannel DLS measurements. In comparison to the hydrodynamic radius (4nm ± 0.30) of a protein solution before adding the precipitant (Figure 71), after the addition of the precipitant, an increase of hydrodynamic radii to 10-12nm was detected in entirely 6 channels (Figure). Furthermore, the hydrodynamic radii of aggregates remained constant afterwards for 20-22h. However from a certain point in time, after 20 - 22h, the radius distribution started to disperse or disappear and the R_h rapidly increased for all channels between 100nm and 1µm comparably (Figure 71). The indicated ratio between small oligomers and larger assemblies with R_H > 100 nm remains approximately constant for all channels (Figure 71). Furthermore, the *Pf*GST crystals obtained in the capillary were observed using a light microscope (Figure 71).

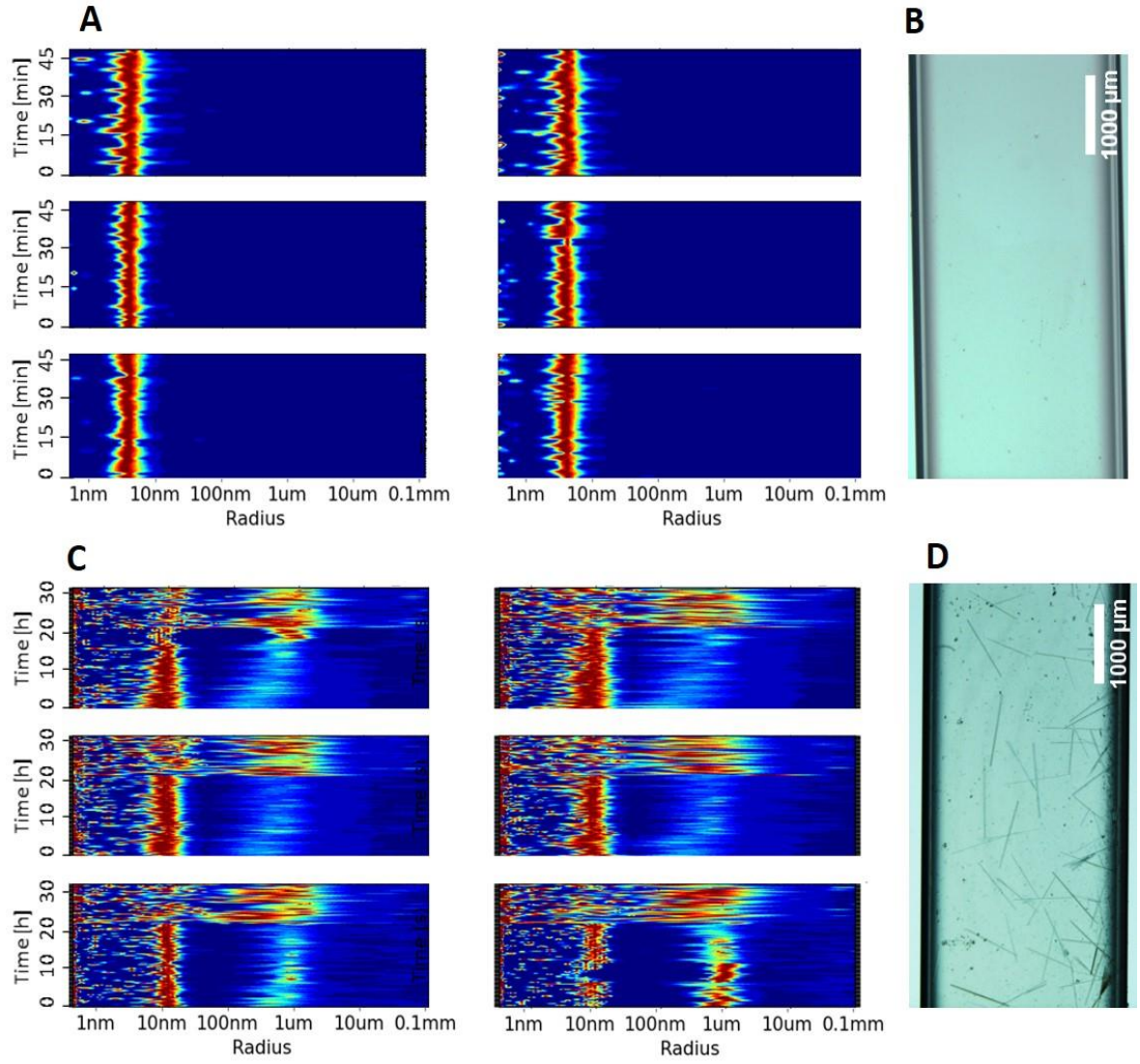

Figure 71. Real-time observation of *Pf*GST crystallization in capillary using multichannel *in situ* DLS system. Summary of radii observed for 6 channels in two measurements series. (A) The graphs in 6 boxes show the protein radius distribution dependence on time with a constant radius in the capillary before adding the precipitant. (B) The capillary with *Pf*GST protein solution. (C) The graphs show the formation of aggregates after adding the precipitant solution to the capillary and the start of nucleation/crystallization process after 20-22 hours. (D) Crystals in the capillary are shown.

V Discussion

1 Effect of Macromolecular mass transport on crystal growth

Since 1984 protein crystallization experiments have been conducted in microgravity to obtain crystals of higher X-ray diffraction quality (DeLucas et. al. 1986; Kundrot et al., Littke et John, 1984; McPherson et al., 1999; Snell et al., 1997). It is assumed that a convection-free, diffusion-controlled environment will support growth of crystals of higher quality, which can be achieved using microgravity. For example, the crystals of the collagen-like polypeptide (PPG) grown in 1G and microgravity conditions revealed on average larger dimensions for microgravity grown crystals (Vergara et al., 2002). The capillary counter diffusion method is an efficient technique to investigate diffusion-limited mass transport phenomena in macromolecular crystallization (Garcia-Ruiz et al., 2001; Garcia-Ruiz, 2003).

This investigation addresses the following hypothesis:

Improved quality of microgravity-grown protein crystals is the result of two macromolecular characteristics that exist in a buoyancy-free, diffusion-dominated solution:

1) Slower crystal growth rates, due to slower protein transport to the growing crystal surface.

2) Predilection of growing crystals to incorporate protein monomers versus higher protein aggregates due to differences in transport rates.

Experiments were performed in microgravity and in laboratory controls to compare the effect of diffusional mass transport on crystal growth rate, crystal size, impurity incorporation and crystal quality. The results for both proteins, lysozyme and *Pf*GST, reveal growth of crystals with different sizes at different positions along the capillary. The concentration variations of the protein-precipitant solution along the length of the capillary influences the interaction of protein precipitation. In addition, the diffusive macromolecular mass transport leads to a supersaturation gradient along the capillary resulting in crystals of different size ranges along the length of the capillary (Garcia-Ruiz, 2003; Garcia-Ruiz et al., 2016). This is due to a gradient of crystallization conditions produced along the capillary. Changes in average size of the lysozyme crystals was only observed in 2 areas within the capillary. Crystals growing between 25-44 mm along the capillary (from the capillary end) are on average, significantly larger compared to crystals grown in the area between 13-25 mm. Analogous to the lysozyme crystallization results, changes in the average sizes of the *Pf*GST crystals grown in 1G and µg were observed such that the average sizes of *Pf*GST dimer crystals grown in µg increase in the capillary area from 18 -34 mm from the capillary end, the average sizes of µg grown crystals for dimer with the addition of tetramer in 99.8 : 0.2 and 99.5 : 0.5 ratios increase in the capillary area from 17 - 35 mm and 26 -41 mm, respectively, from the capillary end (also it starts to decrease again in the area from 35 -38 mm and 41-44 mm, respectively, along the capillary). Furthermore, the complementary crystallization experiments performed in the context of biophysics 4 project showed analogous results. Because of technical problems with the imaging system of the LMM microscope onboard the ISS, the image analysis was available only after 8500 min after sample thawing. Therefore, more than 90 % of

images proved poor quality recorded with 10 x magnification. Changes in the average sizes of the *Pf*GST crystals grown in 1G and µg were observed, such that the average sizes of *Pf*GST dimer crystals grown in µg increase in the capillary area from 22-34 mm from the capillary end, also it starts to decrease again in the area from 34-38 mm (Chapter IV 6.2). On the other hand, the average sizes of *Pf*GST dimer crystals grown in 1G increase in the capillary area from 2-20 mm from the capillary end, also it starts to decrease again in the area from 20-35 mm (Chapter IV 6.2). As the counter diffusion method in capillary is based on mixing protein and precipitate solution by diffusion in opposite directions, it is assumed that protein molecules diffuse an order of magnitude more slowly than the precipitant. This is caused by the fact that proteins reveal lower diffusion coefficient values in liquid environments compared to the diffusion coefficient values of the small molecule (salt ions) precipitant (Brune and Kim, 1993; Tyn and Gusek, 1990). Therefore, the concentration of precipitant in a capillary containing protein increases at a faster rate than the concentration reduction of protein in the same area of the capillary. In this context, the concentration of protein in the area of the capillary initially containing the precipitant increases at a slower rate than the reduction of concentration of the precipitant in the same area of the capillary. This process produces an initial supersaturation wave in the protein area/side of the capillary, subsequently generating nucleation events and crystal growth (Garcia-Ruiz et al., 2001). This explains the observed growth of lysozyme and *Pf*GST crystals in the initial protein area within the capillaries. It is supposed that nucleation and subsequent crystal growth occurs at high protein and precipitant concentration values (at the interface between the protein and precipitant), also at a high value of supersaturation and nucleation degree (Otálora et al., 2009). The supersaturation degree as well as the diffusion coefficient values change along the capillary over time, generating additional nucleation events. The supersaturation rate decreases with time and the nucleation process and crystal growth occurs at slower rates (Otálora et al., 2009; Garcia-Ruiz et al., 2016). This effect of diffusional mass transport on nucleation and crystal growth is responsible for the observation of different crystal dimensions and different average growth rates for crystals in different positions along the capillary. In addition, *Pf*GST crystals grown in µg in the capillary area 22-38 mm from the protein solution end were observed for dimer. However, the crystals grown within the same time period in 1G in the capillary area 2-35 mm from the protein end were observed. It is assumed that in comparison to convection-controlled environment, in a convection-free, diffusion-controlled environment due to slower macromolecular mass transport rates thereby slower particle/protein transport to the growing crystal surface the crystals will grow slower. This effect explains the difference of the distribution areas of crystals in the 1G and µg capillaries, namely 33 mm for 1G and 16 mm for µg grown crystals, for the same time period. Furthermore, the experimental observations indicate that the crystal growth for 1G grown crystals starts prior to the crystal growth of µg grown crystals. For example from the time point 4155 min after sample thawing nucleation and subsequent growth of crystals grown in 1G was observed. However, from the time point 8510 min after sample thawing growth of crystals grown in µg was observed.

Since samples were returned to earth, light microscope images of earth-grown (1G-grown) and microgravity-grown (µg-grown) crystals in capillaries were recorded and photo-documented for the purpose of identifying and quantifying the positions in the capillary that had the largest crystals. The 2D measurements of the crystals in the capillaries were performed using a light microscope with an integrated measurement software. The dimensions of a total of 4 earth-grown and 4 microgravity-grown crystals from each *Pf*GST dimer/tetramer ratio were measured. For the measurements, the largest crystals in terms of the length of the major axis for each ratio of the 1G and µg-grown crystals was preferably selected. Changes in the length of the major axis of the *Pf*GST crystals were observed in all dimer/tetramer ratios for 1G and µg-grown crystals. Compared to the 1G-grown crystals, the µg-grown crystals were, on average, larger. Within the diffusional gradients, crystal dimensions presumably change proportionally to changes in nucleation and the growth rates of the crystals. As a result, the gradient concentration of the precipitant naturally results in a position in the capillary with specific nucleation and growth rates that produce larger and improved crystal quality. For example, for lysozyme, the estimated position with the specific conditions optimal for crystallization corresponds to the area 25-44 mm from the capillary end. The size distribution of the *Pf*GST dimer crystals grown in µg shows that, on average, the largest crystals were grown in the 29-34 mm area; for the dimer with tetramer addition in a 99.8/0.2 ratio, the largest crystals were grown in the 30-35 mm area and for the dimer/tetramer ratio of 99.5/0.5, the largest crystals were grown in the 35-41 mm area (see Figures X). In addition, the complementary crystallization experiments performed in the context of the biophysics 4 project showed analogous results. The size distribution of *Pf*GST dimer crystals grown in µg shows that, on average, the largest crystals were grown in the 31-34 mm area. In comparison, the size distribution of dimer crystals grown in 1G shows that, on average, the largest crystals were grown in the 12-20 mm area. It is assumed that in these areas, conditions optimal for crystallization originated over time through diffusion-controlled macromolecular mass transport for µg-grown crystals, and through convection/diffusion-controlled macromolecular mass transport for 1G-grown crystals. The effect of slower macromolecular mass transport rates and thus slower particle/protein transport to the crystal growth surface in a convection-free, diffusion-controlled environment is likely to be the reason for the difference in the areas between the larger crystals grown in the 1G and µg capillaries with similar start conditions and the same time period.

In conclusion, the comparative crystallization experiments at the ISS LMM facility were successfully performed in 1G and µg using an innovative capillary counter-diffusion technique. The effect of macromolecular mass transport in protein crystallization in the context of the counter-diffusion method when growing crystals in different dimensions with correspondingly different growth kinetics along the capillary areas could be investigated. For the crystallization samples with similar start conditions for both 1G and µg, assuming optimal crystallization conditions, the diffusion-controlled mass transport and thus the slower crystal growth in µg led to the growth of larger crystals. The experiments indicate that the growth of crystals with different dimensions in different areas of the capillary were successful

for different time periods. Furthermore, for the growth of crystals with similar dimensions, the crystals grown in 1G started prior to the crystals grown in µg. Determining growth rate values for crystals with different dimensions due to different growth kinetics in different areas of the capillary is required for a further precise quantitative analysis of crystal growth of 1G vs µg crystals,.

2 Impurity incorporation into crystals grown in 1G vs microgravity

In previously studies, crystallization experiments were performed to investigate the relationship between impurity incorporation and protein crystal growth and quality (Adawy et al., 2015; Carter et al., 1999; Snell et al., 2001). In these studies, hen egg white lysozyme (HEWL) crystals were grown in 1G and µg in the presence of various amounts of a lysozyme dimer acting as an impurity. In most crystallization experiments, the vapor-diffusion, liquid-liquid-diffusion and dialysis methods were used. To characterize the incorporation and distribution of the impurity in the crystals, quantitative impurity portioning partitioning analysis was conducted to calculate the effective partitioning coefficient (Keff) as a ratio of the concentration of the impurity in the solid crystal relative to the major protein concentration in the crystal divided by the same ratio in a solution (Carter et al., 1999; Snell et al., 2001; Thomas et al, 1998; Vekilov et al, 1996).

Our study involves fluorescently labeling protein aggregates to represent the impurities in the growth solution for first time. The *Pf*GST protein solutions contained different ratios of fluorescently labeled *Pf*GST aggregates. The analyzed data with respect to impurity incorporation into the growing crystals is given in chapter IV 5.2 and 6.6. The LMM fluorescence micrograph together with the confocal microscopy images of *Pf*GST and lysozyme crystals shows the presence of fluorescence in the crystals. This initial data indicates that the crystals incorporated notable quantities of fluorescently labeled impurities. Initial crystallization experiments showed that fluorescently labeled *Pf*GST aggregates do not crystallize under same conditions as *Pf*GST dimers. Therefore, the incorporation of fluorescently labeled tetramers into the growing dimer crystal could be investigated using the appropriate methods and techniques. For this purpose, a quantitative analyses of total fluorescence/crystal volume was performed using a fluorescence microplate reader. The statistical analysis of the percentage incorporation of impurities (via a quantitative analysis of total fluorescence/crystal volume) for µg vs 1G-grown crystals indicated that the crystals with the addition of different ratios of fluorescently labeled aggregates incorporated different quantities of impurities. Compared to the earth-grown *Pf*GST crystals, the microgravity-grown crystals, on average, had a significantly lower (Student's t-test, $p < 0.05$) fluorescence intensity in samples with different impurity ratios. In 1G conditions, there is regular density-driven convective mixing in the crystallization solution. In the microgravity environment, there is no convective mixing of the crystallization solution and protein and impurity transport are dominated solely by diffusion. It has been suggested that while a crystal grows from solution, a draft of the protein and salt molecules from the surrounding solution generates a depletion zone resulting in areas with different concentrations. Therefore, the concentration of protein near the crystal is lower than that of

the bulk solution and the crystal grows in an environment with a lower supersaturation. In the absence of gravity in a diffusion-controlled microgravity environment, the transport of protein molecules occurs in the quasi-stable depletion zones and the protein molecules diffuse slowly towards the growing crystal surface (McPherson et al., 1999). In addition, large impurity molecules diffuse even more slowly than the monomeric protein molecules, thus the development of depletion zones act as a diffusion filter that prevents the incorporation of impurities into the growing crystals. This diffusion-controlled effect on its own could explain the occurrence of a decreased amount of impurities in the *Pf*GST crystals grown in microgravity.

In addition, the data of the earth and microgravity-grown crystals were statistically evaluated and graphically represented in order to investigate the relationship between the quantity of the incorporated impurity (via fluorescence intensity values) and the crystal quality parameters. As reported, the incorporation of impurities into growing crystals in different quantities increased the mosaicity of the crystals and decreased the signal-to-noise ratio of the X-ray data. For example, CEWL crystals grown in 1G and µg with the addition of different ratios of naturally occurring dimers showed, on average, increased mosaicity and decreased signal-to-noise values in crystallization samples with a higher percentage of dimers (Snell et al., 2001).

A total of 49 earth-grown and 50 space-grown crystal data sets were analyzed. The relationships between fluorescence intensity values and crystal mosaicity as well as the signal-to-noise (I/σ(I)) values were evaluated using the Pearson correlation. The correlation between fluorescence intensity (impurity quantities in the crystals) and the I/σ(I) values for 1G and µg-grown crystals were determined from the negative correlation coefficients: r = -0.84 (84%) and r = -0.96 (96%), respectively (Figure 72). The I/σ(I) values decrease with increasing values of fluorescence intensity (Figure 72). Furthermore, the correlation between fluorescence intensity (impurity quantities in the crystals) and mosaicity values for 1G and µg-grown crystals were determined from the positive correlation coefficients: r = 0.75 (75%) and r = 0.92 (92%), respectively (Figure 72). The mosaicity values increase with increasing values of fluorescence intensity (Figure 72). The correlation between fluorescence intensity and I/σ(I) values suggested a fairly strong relationship between fluorescence intensity values and crystal quality parameter values, and therefore the importance of the incorporated impurity effect on crystal quality for both 1G and µg-grown crystals. Additionally, the µg-grown crystals proved to be more sensitive to incorporated impurity. In previous experiments with the target impurity effect on the quality of the growing crystal, the highest signal-to-noise ratio for the highest diffraction resolution data and the lowest symmetry-related reflection mosaicity was reported for lysozyme and thaumatin and was observed for crystals grown from pure solution (Carter et al., 1999; Ng et al., 1997; Snell et al., 1995; Snell et al., 2001).

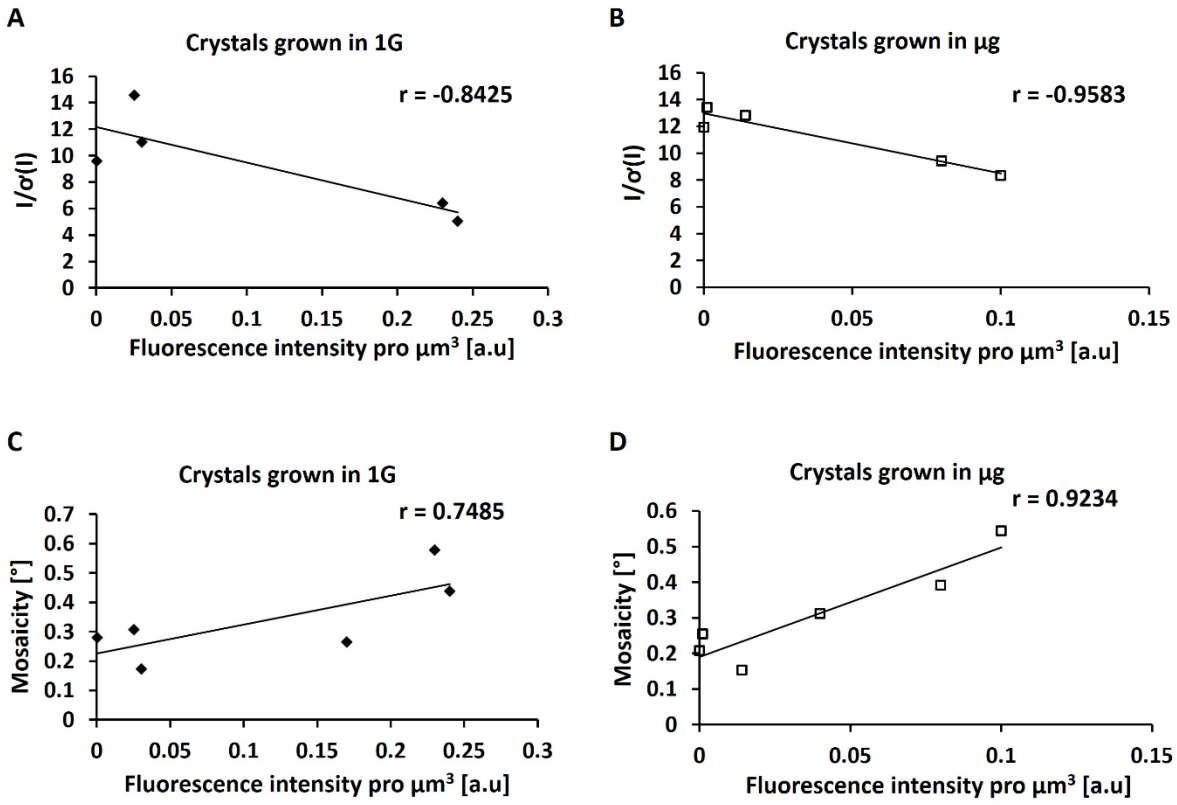

Figure 72. Effect of impurity on crystals grown in 1G and µg.

Correlation between average of fluorescence intensity values and the corresponding average of crystal quality parameters derived from measured values 49 crystals grown in 1G and of 50 crystals grown in µg. The correlation level was determined using Pearson correlation coefficient ($0 < r < 1$; $-1 < r < 0$). (A) Correlation between fluorescence intensity values and signal-to-noise ratio ($I/\sigma(I)$) for crystals grown in 1G. (B) Correlation between fluorescence intensity values and signal-to-noise ratio ($I/\sigma(I)$) for crystals grown in µg. (C) Correlation between fluorescence intensity and mosaicity values for crystals grown in in 1G. (D) Correlation between fluorescence intensity and mosaicity values for crystals grown in in µg.

In conclusion, the observed microscopic and measured intensity data indicated that the crystals incorporated notable quantities of fluorescently labeled impurities. Thus, the effect of impurities in a protein crystallization experiment on the quality of crystals grown in 1G and µg, in context of the counter-diffusion method could be investigated. The crystals with higher amounts of incorporated impurities had substantially decreased signal-to-noise and increased mosaicity values. Consequently, purifying the crystallization solutions to the highest level possible could increase the possibility of obtaining crystals with improved quality. For an additional precise quantitative analysis of impurities effect on the quality of growing crystals, in the context of the counter-diffusion method in a capillary, the determination of the incorporated impurity quantities and thus the corresponding crystal quality

parameter values for crystals with different dimensions and different growth kinetics, and probably also with different quantities of incorporated impurities in different areas of capillary, is required.

3 X-ray diffraction data collection and crystal quality

Comparative protein crystallization experiments in microgravity and on earth were conducted in a large number of studies with the purpose of investigating the effect of a diffusion-controlled environment in microgravity on crystal growth and the improvement of crystal quality (Eschenburg et al., 2000; Evrard et al., 2007; Snell and Helliwell, 2005). Furthermore, most studies performed in microgravity reported an improvement in the specific quality parameters. These includes a high degree of diffraction data measured throughout a higher resolution range, enhanced signal-to-noise ratios, improved electron densities and water structure, improvements in data agreement between the model and experimental data and notable improvements in the crystals mosaicity (Carter et al., 1999, Eschenburg et al., 2000; McPherson et al., 1999; Vergara et al., 2003).

In our study, comparative protein crystallization experiments in microgravity and on earth were performed. X-ray data for dimer crystals and dimer with the addition of tetramer in different ratios were collected and statistically (using crystal quality parameters) analyzed. Data sets for individual crystal data sets were measured for Rmeas, Rsym, I/σ and CC1/2. Statistical analysis of the diffraction data showed that the microgravity-grown dimer crystals and the dimer with the lower quantities of impurities delivered, on average, significantly enhanced signal-to-noise ratios (I/σ(I)) vs resolution than the reference crystals grown in 1G.

However, no significant difference for the average I/σ(I) values from crystals with the addition of higher quantities of impurities for 1G vs µg was found. The improvement of the crystal quality parameters for the µg-grown crystals may be associated with the diffusion-controlled microgravity environment effects since the transport of protein molecules occurs in the quasi-stable depletion zone and the protein molecules diffuse slowly towards the growing crystal surface (McPherson et al., 1999).

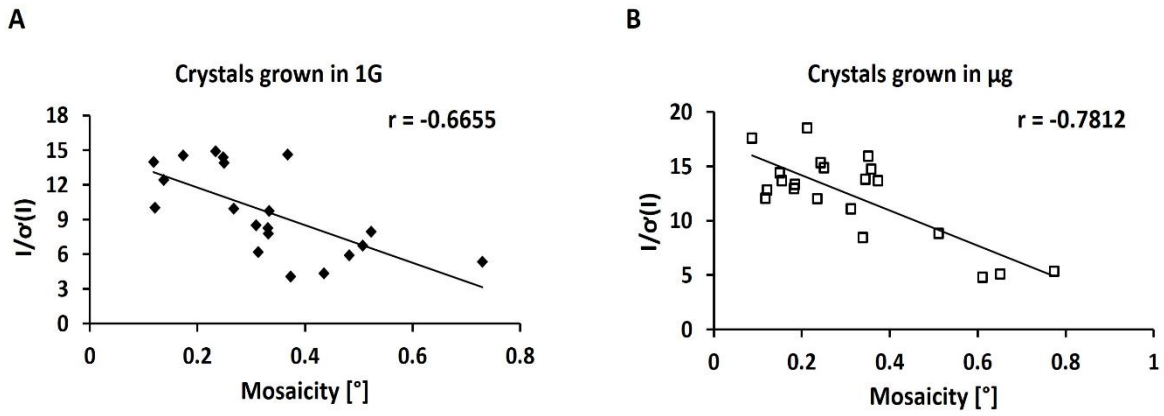

Figure 73. X-ray data quality analysis for crystals grown in 1G and µg.
Correlation between mosaicity and the corresponding signal-to-noise ratio (I/σ(I)) values derived from 20 crystals grown in 1G and 21 crystals grown in µg. The correlation level was determined using Pearson correlation coefficient (0 < r <1; -1< r <0). (A) Correlation between mosaicity and signal-to-noise ratio (I/σ(I)) for crystals grown in 1G. (B) Correlation between mosaicity and signal-to-noise ratio (I/σ(I)) for crystals grown in µg.

Furthermore, to investigate the relationship between mosaicity and signal-to-noise ratio values, the data of the earth and microgravity-grown crystals were statistically evaluated and graphically represented. As reported previously, the incorporation of different quantities of impurities into growing crystals increased crystal mosaicity and reduced the signal-to-noise ratio of the X-ray data. A total of 20 earth-grown and 21 space-grown crystal datasets were analyzed. The relationship between crystal mosaicity and signal-to-noise (I/σ(I) values was evaluated using the Pearson correlation. The correlation between mosaicity and I/σ(I) values for 1G and µg-grown crystals was determined from the negative correlation coefficients: r = -0.66 (66%) and r = -0.78 (78%), respectively (Figure 73). The I/σ(I) values decreased with increasing values of mosaicity (Figure 73). The correlation between crystal mosaicity and I/σ(I) values suggested a strong to moderate relationship between the crystal quality parameters for both 1G and µg-grown crystals. Additionally, µg-grown crystals proved to be more sensitive in the context of the relationship between the crystal quality parameters. Previous studies indicated a potential correlation of changes in crystal mosaicity with changes in the other (resolution and signal-to-noise-ratio) diffraction data quality parameters and that the crystals grown in µg were more sensitive to changes in the quality parameters (Carter et al., 1999; Evrard et al., 2007; Snell et al., 2001).

In addition, complementary crystallization experiments were performed on the ISS during the "Biophysics 4" project. The analysis of diffraction data reveals changes in space groups for crystals from the same capillary grown in µg (Chapter IV 6.7). The 3 crystals measured belonged to space group $P2_1$, while the other 2 crystals measured belonged to space group $P2_1P2_1P2_1$, having similar space group parameters to the crystals obtained in the hanging drop method in the experiments performed on earth (laboratory). All crystals measured showed similar shapes and dimensions. The solvent content in the

unit cell was calculated to be 50% with 2 *Pf*GST monomers (homodimer) for the crystals in space group $P2_1P2_1P2_1$. On the other hand, the solvent content was calculated to be 43% for 4 *Pf*GST monomers (2 homodimers) in space group $P2_1$. It should be noted that the capillary with growing crystals had some damaged areas, thus solution evaporated over time. The crystals in space group $P2_1P2_1P2_1$ were grown in the immediate vicinity of the capillary area with the cracks, while the crystals in space group $P2_1$ were grown in the capillary area away from the cracks. Therefore, the crystals were grown in the presence of different crystallization conditions. In other words, two different techniques were used: vapor-diffusion for the crystals growing near the cracked area and counter-diffusion for the crystals growing away from cracked areas. This could also be responsible for the different rates at which supersaturation was achieved in different areas of the capillary (Garcia-Ruiz et al., 2016; Zegers et al., 2006). For example, a change of space group in vapor and counter-diffusion samples was observed for the anti-polyQ antigen-binding fragment (MW1 Fab) and for Thermotoga maritima triosephosphate isomerase (TIM) crystals grown in 1G and µg (Evrard et al., 2007; Owens et al., 2016).

In conclusion, the results of the diffraction data indicated that diffusion-limited mass transport in crystallization can be beneficial for the quality of growing crystals. Furthermore, the statistical analysis of diffraction data indicated a fairly strong relationship between the crystal quality parameter values for both 1G and µg crystals. Depending on the crystallization technique used the space group changed. Further quantitative analysis of diffraction data for crystals with different dimensions and different growth kinetics, and probably with different qualities in different areas of the capillary, is required to investigate the effect of macromolecular mass transport on crystal quality in the context of the counter-diffusion method.

4 Multichannel DLS system

A multichannel DLS system was developed to improve the experimental investigation of the macromolecular crystallization process. The major use of the multichannel DLS system compared to other DLS systems is the rapid determination of the translational diffusion constant in a short period, simultaneously and in several positions for macromolecules in solution in capillaries. To study macromolecular protein transport in the crystallization process in the counter-diffusion method, the protein solution was filled into the capillaries and measurements were performed with the multichannel DLS system. Glucose isomerase, a *Pf*GST dimer and synthetic gold nanoparticles were analyzed using multichannel dynamic light scattering measurements to verify the purity and dispersity of protein and also to determine the adequate hydrodynamic radius (R_h). Time-resolved measurements of the hydrodynamic radius verified the monodispersity of glucose isomerase, the *Pf*GST dimer and the synthetic gold nanoparticle solutions. The data showed similar values of hydrodynamic radiuses for all 8 channels for each protein/particle solution. The stable and similar hydrodynamic radii over time in all 8 channels demonstrated that the protein/particles were stable in solution. Based on this observation, these protein solutions represent a high degree of monodispersity and do not form protein aggregates

or oligomers with higher hydrodynamic radiuses. GST or *Pf*GST is well known to form stable dimers in solution, having a hydrodynamic radius of about 3.7 nm (gyration radius of 2.9 nm), calculated using the assumption of a globular molecular shape (Bulone et al. 2006; Perbandt et al. 2004; Perbandt et al. 2015). The experimental radius measured for *Pf*GST (4 ± 0.30 nm) is therefore in excellent agreement with the presence of the dimer in solution. Further multichannel DLS experiments were performed to investigate protein crystallization as well as macromolecular mass transport. For the crystallization experiment, the capillary containing 37 µl of *Pf*GST solution (25 mg/ml) was injected with an additional 37 µl of precipitant (2.8M AmSO4; 0.1M PO4 buffer, pH 6.7) and multichannel DLS measurements were performed immediately. In comparison to the hydrodynamic radius (4 nm ± 0.30) of the protein solution before adding the precipitant, an increase in the hydrodynamic radiuses (about 10-12 nm) was detected in all 6 channels after the addition of the precipitant. An increase in the hydrodynamic radiuses is associated with the formation of larger aggregates after adding the precipitant. This change could be caused by a change in the protein diffusivity, which in turn is caused by a change in the ionic environment or due to precipitation. In previous experiments performed using 1 channel DLS and lysozyme and glucose isomerase crystallization solutions, similar behavior of the hydrodynamic radii was observed (Dierks et al. 2008; Oberthuer et al. 2012). Furthermore, the hydrodynamic radii of aggregates remained constant for 20-22 h afterwards. However, after a certain point in time (i.e. after 20-22 h) the radius distribution started to disperse or disappear and the R_h rapidly increased for all channels between 100 nm and 1 µm. The rapid dispersion or disappearance and consequent formation of larger aggregates indicated the start of nucleation as well as the start of the crystallization process (Dierks et al. 2008). The ratio of small oligomers and larger assemblies with R_h > 100 nm remained approximately constant for all channels. In addition, the light microscope crystal images of the capillary area with increased or disappeared radii confirms that the technique for the investigation of protein crystallization in fluid systems using a multichannel DLS system is appropriate.

Further development and optimization of the multichannel DLS system is required to establish measurement procedures for the systematical measurements of radius distribution and transport of particles in protein/crystallization solutions.

VI Summary

To investigate the effect of macromolecular transport and the incorporation of protein aggregate impurities in growing crystals, experiments were performed on the International Space Station (ISS) and compared with control experiments perform in a 1G laboratory environment. Crystal growth experiments for hen egg lysozyme (HEWL) and *Plasmodium falciparum* Glutathione S-Transferase (*Pf*GST) were monitored using the ISS Light Microscopy Module (LMM). Crystallization solutions containing different protein-aggregate ratios were prepared. Experiments were performed applying the liquid-liquid counter diffusion crystallization method using rectangular, optically transparent capillaries. The crystallization samples were launched to the ISS via SpaceX-10 and SpaceX-15 missions. Three series of crystallization experiments were performed on ISS, one during 26.02.2017 until 10.03.2017, second during 16.06.2017 until 23.06.2017 (both Biophysics 1) and a third during 12.07.2018 until 24.07.2018 (Biophysics 4).

A comparison of crystal growth rates and size showed different calculated average growth rates, as well different dimensions for crystals growing in different positions along the capillary. The effect of macromolecular mass transport on crystal growth in microgravity was experimentally investigated. For the crystallization samples with similar start conditions for both 1G and µg, assuming optimal crystallization conditions, the diffusion-controlled mass transport and thus the slower crystal growth in µg led to the growth of larger crystals. The experiments indicate that the growth of crystals with different dimensions in different areas of the capillary were successful for different time periods. Furthermore, for the growth of crystals with similar dimensions, the crystals grown in 1G started prior to the crystals grown in µg.

In parallel, the percentage of incorporated fluorescent aggregate into the crystals was monitored utilizing the fluorescent Light Microscopy Module (LMM) and ground-based fluorescent microscopes. The observed microscopic and measured intensity data indicated that the crystals incorporated notable quantities of fluorescently labelled impurities. Thus, the effect of impurity in protein crystallization on the quality of crystals grown in 1G and µg in the context of the counter-diffusion method could be investigated. The crystals with higher amounts of incorporated impurities had substantially decreased signal-to-noise and increased mosaicity values. Consequently, purifying the crystallization solutions to the highest level possible could increase the possibility of obtaining crystals with improved quality.

The results of the diffraction data indicated that diffusion-limited mass transport in crystallization can be beneficial for the quality of growing crystals. The statistical analysis of diffraction data indicated a fairly strong relationship between the crystal quality parameter values for both 1G and µg crystals.

The hydrodynamic radii of three different proteins in capillary samples were determined using a multichannel DLS system. Furthermore, the crystallization process of a *Pf*GST sample were observed using multichannel DLS system. The observations confirm that the technique for the investigation of protein crystallization in fluid systems using a multichannel DLS system is appropriate.

VII Zusammenfassung

Um den Effekt des makromolekularen Transports und damit auch den Einbau von Proteinverunreinigungen in wachsende Protein Kristalle zu untersuchen, wurden Experimente auf der Internationalen Raumstation (ISS) durchgeführt und mit Kontrollexperimenten auf der Erde verglichen, Zu diesem Zweck wurden Hühnerei-Lysozym (HEWL) und *Plasmodium falciparum* Glutathion-S-Transferase (*Pf*GST) ausgewählt. Kristallwachstum wurde unter Verwendung des ISS–Lichtmikroskopiemoduls überwacht und dokumentiert. Kristallisationsansätze mit unterschiedlichen Protein-Verunreinigungs-Verhältnissen wurden hergestellt. Die Experimente wurden mit der Counter – Diffusions-Methode unter Verwendung von rechteckigen, optisch transparenten Kapillaren durchgeführt. Die Kristallisationsproben wurden mit SpaceX-10- und SpaceX-15-Missionen zur ISS gebracht. Drei Reihen von Kristallisationsexperimenten wurden auf der ISS durchgeführt, eine vom 26.02.2017 bis 10.03.2017, eine zweite vom 16.06.2017 bis 23.06.2017 (beide Biophysik 1) und eine dritte vom 12.07.2018 bis 24.07.2018 (Biophysik 4).

Ein Vergleich der Kristallwachstumsrate und auch der Größe ergab unterschiedliche berechnete, durchschnittliche Wachstumsraten sowie unterschiedliche Dimensionen für Kristalle, die an unterschiedlichen Positionen entlang der Kapillare wuchsen. Die Auswirkung des makromolekularen Massentransports auf das Kristallwachstum in den Mikrogravitätsbedingungen wurde experimentell berechnet. Bei den Kristallisationsproben mit ähnlichen Startbedingungen sowohl für 1G als auch für µg führte der diffusionskontrollierte Massentransport und damit das langsamere Kristallwachstum in µg bei optimalen Kristallisationsbedingungen zum Wachstum größerer Kristalle. Die Experimente zeigten, dass das Wachstum von Kristallen mit unterschiedlichen Dimensionen in verschiedenen Bereichen der Kapillare für verschiedene Zeiträume erfolgreich war. Das Wachstum von in 1G gewachsenen Kristallen mit ähnlichen Abmessungen im Unterschied zu den in µg gewachsenen Kristallen begann zu einem früheren Zeitpunkt.

Parallel dazu wurde der Prozentsatz der in die Kristalle eingebauten fluoreszierenden Aggregate unter Verwendung des Lichtmikroskopiemoduls (LMM) und bodenbasierter Mikroskope ermittelt. Die absolvierten mikroskopischen Bilder und gemessenen Intensitätsdaten zeigten, dass die Kristalle bemerkenswerte Mengen fluoreszenzmarkierter Verunreinigungen enthielten. So konnte der Einfluss von Verunreinigungen bei der Proteinkristallisation auf die Qualität von in 1G und µg gewachsenen Kristallen im Rahmen der angewendeten Methode untersucht werden. Die Kristalle mit höheren Mengen an eingebauten Verunreinigungen hatten ein wesentlich geringeres Signal-Rausch-Verhältnis und erhöhte Mosaizitätswerte. Folglich kann die Reinigung der Kristallisationslösungen auf das höchstmögliche Niveau die Möglichkeit erhöhen Kristalle mit verbesserter Qualität zu erhalten.

Die Ergebnisse der Beugungsdaten zeigten, dass nur der diffusionsgeführte Massentransport bei der Kristallisation für die Qualität wachsender Kristalle vorteilhaft sein kann. Die statistische Analyse der Beugungsdaten zeigte eine ziemlich starke Beziehung zwischen den Kristallqualitätsparametern sowohl für 1G als auch für µg Kristalle.

Zusammenfassung

Der hydrodynamische Radius von drei verschiedenen Proteinen in Kapillarproben wurde unter Verwendung eines Mehrkanal-DLS-Systems bestimmt. Weiterhin wurde die Kristallisation einer *Pf*GST-Probe unter Verwendung eines Mehrkanal-DLS-Systems beobachtet. Die Beobachtungen bestätigen, dass die Technik zur Untersuchung der Proteinkristallisation in Fluidsystemen geeignet ist.

VIII References

Adawy A, van der Heijden EG, Hekelaar J, van Enckevort WJ, de Grip WJ, Vlieg E (2015) A comparative study of impurity effects on protein crystallization: diffusive versus convective crystal growth. Crystal Growth & Design 15(3): 1150-1159

Adkins JN, Varnum SM, Auberry KJ, Moore RJ, Angell NH, Smith RD, Springer DL and Pounds JG (2002) Toward a human blood serum proteome: analysis by multidimensional separation coupled with mass spectrometry. Molecular & Cellular Proteomics 1(12): 947-955

Aibara S, Shibata K, Morita Y (1997) Protein crystallization in microgravity. Biological Sciences in Space 11 (4):339-345

Akparov VK, Timofeev VI, Kuranova IP (2015) Crystallization and preliminary X-ray diffraction study of porcine carboxypeptidase B. Crystallography Reports 60 (3):367-369

Alvarado UR, DeWitt CR, Shultz BB, Ramsland PA, Edmundson AB (2001) Crystallization of a human Bence–Jones protein in microgravity using vapor diffusion in capillaries. Journal of Crystal Growth 223 (3):407-414

Altschul SF, Madden TL, Schäffer AA, Zhang J, Zhang Z, Miller W, Lipman DJ (1997) Gapped BLAST and PSI-BLAST: A new generation of protein database search programs. Nucleic Acids Res (25):3389–3402

Asano K, Fujita S, Senda T, Mitsui Y (1992) Crystal growth of ribonuclease S under microgravity. Journal of Crystal Growth 122 (1):323-329

Ataka M (1993) Protein crystal growth: an approach based on phase diagram determination. Phase Transitions: A Multinational Journal 45(2-3): 205-219

Battye TGG, Kontogiannis L, Johnson O, Powell HR, Leslie AGW (2011) iMOSFLM: A new graphical interface for diffraction-image processing with MOSFLM. Acta Crystallogr Sect D Biol Crystallogr (67):271–281

Berisio R, Vitagliano L, Mazzarella L, Zagari A (2002) Crystal structure of the collagen triple helix model [(Pro-Pro-Gly)(10)](3). Protein Sci 11 (2):262-270

Berisio R, Vitagliano L, Sorrentino G, Carotenuto L, Piccolo C, Mazzarella L, Zagari A (2000) Effects of microgravity on the crystal quality of a collagen-like polypeptide. Acta Crystallographica Section D 56 (1):55-61

Berman HM, Westbrook J, Feng Z, Gilliland G, Bhat TN, Weissig H, Shindyalov IN and Bourne PE (2000) The protein data bank Nucleic Acid Res (28): 235–242

Bernal JD, & Crowfoot D (1934) X-ray photographs of crystalline pepsin. Nature 133(3369): 794

Betzel C, Gourinath S, Kumar P, Kaur P, Perbandt M, Eschenburg S, Singh TP (2001) Structure of a Serine Protease Proteinase K from Tritirachium album limber at 0.98 Å Resolution. Biochemistry 40 (10):3080-3088

Borgstahl GEO, Vahedi-Faridi A, Lovelace J, Bellamy HD, Snell EH (2001) A test of macromolecular crystallization in microgravity: large well ordered insulin crystals. Acta Crystallographica Section D 57 (8):1204-1207

Borisova SN, Birnbaum GI, Rose DR, Evans SV (1996) Experiments in Microgravity: A Comparison of Crystals of a Carbohydrate-Binding Fab Grown on the Ground, on Space Shuttle Discovery and on Space Staion Mir. Acta Crystallographica Section D 52 (2):267-271

Böck A, Forchhammer K, Heider J, Leinfelder W, Sawers G, Veprek B, & Zinoni F (1991) Selenocysteine: the 21st amino acid. Molecular microbiology 5(3): 515-520

Bragg WH (1915) XXX. The structure of the spinel group of crystals. The London, Edinburgh, and Dublin Philosophical Magazine and Journal of Science 30(176): 305-315

Bragg WH, & Bragg WL (1918) X-rays and Crystal Structure. G. Bell and sons, Limited

Branden C, & Tooze J (1999) O991) Introduction to Protein Structure

Broutin I, Riès-Kautt M, Ducruix A (1997) Crystallographic analyses of lysozyme and collagenase microgravity grown crystals versus ground controls. Journal of Crystal Growth 181 (1):97-108

Broutin-L'Hermite I, Ries-Kautt M, Ducruix A (2000) 1.7 A X-ray structure of space-grown collagenase crystals. Acta Crystallographica Section D 56 (3):376-378

Brune D, Kim S (1993) Predicting protein diffusion coefficients. Proceedings of the National Academy of Sciences 90(9): 3835-3839

Brunori M, Giardina B, Antonini E, Benedetti PA & Bianchini G (1974) Distribution of the haemoglobin components of trout blood among the erythrocytes: observations by single-cell spectroscopy. Journal of molecular biology 86(1): 165-169

Bulone D, Masino L, Thomas DJ, San Biagio PL, & Pastore A (2006) The interplay between PolyQ and protein context delays aggregation by forming a reservoir of protofibrils. PLoS One 1(1): e111

Carotenuto L, Berisio R, Piccolo C, Vitagliano L, Zagari A (2001) Video observation of protein crystal growth in the advanced protein crystallization facility aboard the space shuttle mission STS-95. Journal of Crystal Growth 232 (1–4):481-488

Carter DC, Lim K, Ho JX, Wright BS, Twigg PD, Miller TY, Chapman J, Keeling K, Ruble J, Vekilov PG, Thomas BR, Rosenberger F, Chernov AA (1999a) Lower dimer impurity incorporation may result in higher perfection of HEWL crystals grown in microgravity: A case study. Journal of Crystal Growth 196 (2–4):623-637

Carter DC, Wright B, Miller T, Chapman J, Twigg P, Keeling K, Moody K, White M, Click J, Ruble JR, Ho JX, Adcock-Downey L, Dowling T, Chang C-H, Ala P, Rose J, Wang BC, Declercq J-P, Evrard C, Rosenberg J, Wery J-P, Clawson D, Wardell M, Stallings W, Stevens A (1999b) PCAM: a multi-user facility-based protein crystallization apparatus for microgravity. Journal of Crystal Growth 196 (2–4):610-622

Carotenuto L, Cartwright JHE, Castagnolo D, Ruiz JG, Otálora F (2002). Theory and simulation of buoyancy-driven convection around growing protein crystals in microgravity. Microgravity science and technology 13(3): 14

Chayen NE, Gordon EJ, Zagalsky PF (1996) Crystallization of apocrustacyanin on the International Microgravity Laboratory (IML-2) mission. Acta Crystallographica Section D 52 (1):156-159

Chayen NE, Snell EH, Helliwell JR, Zagalsky PF (1997) CCD video observation of microgravity crystallization: apocrustacyanin C1. Journal of Crystal Growth 171 (1):219-225

Chayen NE (1998) Comparative studies of protein crystallization by vapour-diffusion and microbatch techniques. Acta Crystallographica Section D: Biological Crystallography 54(1): 8-15

Chayen NE (2005) Methods for separating nucleation and growth in protein crystallisation. Progress in biophysics and molecular biology 88(3): 329-337

Chayen NE, & Saridakis E (2008) Protein crystallization: from purified protein to diffraction-quality crystal. Nature methods 5(2): 147

Clos J, & Brandau S (1994) pJC20 and pJC40-two high-copy-number vectors for T7 RNA polymerase-dependent expression of recombinant genes in Escherichia coli. Protein expression and purification 5(2): 133-137

Crank J (1975) The mathematics of difiusion. 2nd end

Day J, McPherson A (1992) Macromolecular crystal growth experiments on international microgravity laboratory – 1. Protein Science 1 (10):1254-1268

De Mattei RC, Feigelson RS, Bray TL, DeLucas LJ, Symersky J (2001) A preliminary study of space- and ground-grown insulin crystals by X-ray diffraction and by light scattering tomography. Journal of Crystal Growth 232 (1–4):511-519

De Souza GA, Oliveira PS, Trapani S, Santos ACO, Rosa JC, Laure HJ, Faça VM, Correia MT, Tavares GA, Oliva G (2003) Amino acid sequence and tertiary structure of Cratylia mollis seed lectin. Glycobiology 13 (12):961-972

Declercq J-P, Evrard C, Carter DC, Wright BS, Etienne G, Parello J (1999a) A crystal of a typical EF-hand protein grown under microgravity diffracts X-rays beyond 0.9 Å resolution. Journal of Crystal Growth 196 (2–4):595-601

Declercq JP, Evrard C, Lamzin V, Parello J (1999b) Crystal structure of the EF-hand parvalbumin at atomic resolution (0.91 A) and at low temperature (100 K). Evidence for conformational multistates within the hydrophobic core. Protein Sci 8 (10):2194-2204

DeLucas LJ, Suddath FL, Snyder R, Naumann R, Broom MB, Pusey M, Yost V, Herren B, Carter D, Nelson B, Meehan EJ, McPherson A, Bugg CE (1986) Preliminary investigations of protein crystal growth using the space shuttle. Journal of Crystal Growth 76 (3):681-693

DeLucas L, Smith C, Smith H, Vijay-Kumar S, Senadhi S, Ealick S, Carter D, Snyder R, Weber P, Salemme F, al. e (1989) Protein crystal growth in microgravity. Science 246 (4930):651-654

DeLucas LJ, Long MM, Moore KM, Rosenblum WM, Bray TL, Smith C, Carson M, Narayana SVL, Harrington MD, Carter D, Clark AD, Nanni RG, Ding J, Jacobo-Molina A, Kamer G, Hughes SH, Arnold E, Einspahr HM, Clancy LL, Rao GSJ, Cook PF, Harris BG, Munson SH, Finzel BC, McPherson A, Weber PC, Lewandowski FA, Nagabhushan TL, Trotta PP, Reichert P, Navia MA, Wilson KP, Thomson JA, Richards RN, Bowersox KD, Meade CJ, Baker ES, Bishop SP, Dunbar BJ, Trinh E, Prahl J, Sacco A, Bugg CE (1994) Recent results and new hardware developments for protein crystal growth in microgravity. Journal of Crystal Growth 135 (1):183-195

DeLucas LJ (2001) Protein crystallization – is it rocket science? Drug Discovery Today 6 (14):734-744

Dierks K, Meyer A, Einspahr H, & Betzel C (2008) Dynamic light scattering in protein crystallization droplets: adaptations for analysis and optimization of crystallization processes. Crystal Growth and Design 8(5): 1628-1634

Dong J, Boggon TJ, Chayen NE, Raftery J, Bi RC, Helliwell JR (1999) Bound-solvent structures for microgravity-, ground control-, gel- and microbatch-grown hen egg-white lysozyme crystals at 1.8 A resolution. Acta crystallographica Section D, Biological crystallography 55 (Pt 4):745-752

Dong J, Wang Y, Han Q, Bi R (1998) Structural study on hen egg-white lysozyme crystals grown in gravity and microgravity. Science in China Series C: Life Sciences 41 (3):238-244

Drebes J, Künz M, Windshügel B, Kikhney AG, Müller IB, Eberle RJ, Oberthür D, Cang H, Svergun DI, Perbandt M, Betzel C, Wrenger C (2016) Structure of ThiM from Vitamin B1 biosynthetic pathway of Staphylococcus aureus – Insights into a novel pro-drug approach addressing MRSA infections. Scientific Reports 6:22871

Ducruix A, & Giegé R (Eds.) (1999) Crystallization of nucleic acids and proteins: a practical approach (No. 210). Practical Approach Series

Ealick S, Cook W, Vijay-Kumar S, Carson M, Nagabhushan T, Trotta P, Bugg C (1991) Three-dimensional structure of recombinant human interferon-gamma. Science 252 (5006):698-702

Eckert M (2012) Max von Laue and the discovery of X-ray diffraction in 1912. Annalen der Physik, 524(5): A83-A85

Edward HS, John RH (2005) Macromolecular crystallization in microgravity. Reports on Progress in Physics 68 (4):799

Emsley P, Cowtan K (2004) Coot: model-building tools for molecular graphics. Acta Crystallogr D Biol Crystallogr (60): 12 Pt 1):2126–32

Erdmann VA, Lippmann C, Betzel C, Dauter Z, Wilson K, Hilgenfeld R, Hoven J, Liesum A, Saenger W, Müller-Fahrnow A, Hinrichs W, Düvel M, Schulz GE, Müller CW, Wittmann HG, Yonath A, Weber G, Stegen K, Plaas-Link A (1989) Crystallization of proteins under microgravity. FEBS Letters 259 (1):194-198

Eschenburg S, Degenhardt M, Moore K, DeLucas LJ, Peters K, Fittkau S, Weber W, Betzel C (2000) Crystallization of proteinase K complexed with substrate analogue peptides on US space missions STS-91 and STS-95. Journal of Crystal Growth 208 (1–4):657-664

Esposito L, Sica F, Sorrentino G, Berisio R, Carotenuto L, Giordano A, Raia CA, Rossi M, Lamzin VS, Wilson KS, Zagari A (1998) Protein Crystal Growth in the Advanced Protein Crystallization Facility on the LMS Mission: a Comparison of Sulfolobus solfataricus Alcohol Dehydrogenase Crystals Grown on the Ground and in Microgravity. Acta Crystallographica Section D 54 (3):386-390

Esposito L, Sica F, Raia CA, Giordano A, Rossi M, Mazzarella L, Zagari A (2002) Crystal structure of the alcohol dehydrogenase from the hyperthermophilic archaeon Sulfolobus solfataricus at 1.85 A resolution. J Mol Biol 318 (2):463-477

Evans P (2006) Scaling and assessment of data quality. Acta Crystallographica Section D: Biological Crystallography, 62(1): 72-82

Evans P. (2011) An introduction to data reduction: space-group determination, scaling and intensity statistics. Acta Crystallographica Section D: Biological Crystallography, 67(4): 282-292

Evrard C, Declercq J-P, Fastrez J (1997) Crystallization and preliminary X-ray analysis of bacteriophage lambda lysozyme in which all tryptophans have been replaced by aza-tryptophans. Acta Crystallographica Section D 53 (2):217-219

Evrard C, Fastrez J, & Declercq JP (1998) Crystal structure of the lysozyme from bacteriophage lambda and its relationship with V and C-type lysozymes. Journal of molecular biology 276(1): 151-164

Evrard C, Declercq J-P, Debaerdemaeker T, König H (1999) The first successful crystallization of a prokaryotic extremely thermophilic outer surface layer glycoprotein. Zeitschrift für Kristallographie 214 (8):427-429

Evrard C, Maes D, Zegers I, Declercq JP, Vanhee C, Martial J, Wyns L, Weerdt CVD (2007) TIM Crystals Grown by Capillary Counterdiffusion: Statistical Evidence of Quality Improvement in Microgravity. Crystal Growth & Design 7 (11): 2161-2166

Fronticelli C, Sanna MT, Perez-Alvarado GC, Karavitis M, Lu AL, & Brinigar WS (1995) Allosteric Modulation by Tertiary Structure in Mammalian Hemoglobins introduction of the functional chracteristics of bovine hemoglobin into human hemoglbin by five amino acid substittutions. Journal of Biological Chemistry, 270(51): 30588-30592

García-Ruiz JM, Otálora F, Novella M, Gavira JA, Sauter C, Vidal O (2001) A supersaturation wave of protein crystallization. Journal of Crystal Growth 232(1-4): 149-155

Garcıa-Ruiz JM, Novella ML, Moreno R, Gavira JA (2001a) Agarose as crystallization media for proteins: I: Transport processes. Journal of Crystal Growth 232(1-4): 165-172

García-Ruiz JM (2003) Counterdiffusion methods for macromolecular crystallization. In Methods in Enzymology, Vol. 368, pp 130-154. Academic Press

García-Ruiz JM, Otálora F, García-Caballero A (2016) The role of mass transport in protein crystallization. Acta Crystallographica Section F: Structural Biology Communications 72(2): 96-104

Gasteiger E, Hoogland C, Gattiker A, Duvaud S, Wilkins MR, Appel RD, Bairoch A *Protein Identification and Analysis Tools on the ExPASy Server;* (In) John M. Walker (ed): The Proteomics Protocols Handbook, Humana Press (2005) pp. 571-607

Giege R, Dock AC, Kern D, Lorber B, Thierry JC, Moras D (1986) The role of purification in the crystallization of proteins and nucleic acids. Journal of Crystal Growth 76(3): 554-561

Gromiha MM (2010) Protein bioinformatics: from sequence to function. Academic Press

Habash J, Boggon TJ, Raftery J, Chayen NE, Zagalsky PF, Helliwell JR (2003) Apocrustacyanin C(1) crystals grown in space and on earth using vapour-diffusion geometry: protein structure refinements and electron-density map comparisons. Acta crystallographica Section D, Biological crystallography 59 (Pt 7):1117-1123

Han Y, Cang HX, Zhou JX, Wang YP, Bi RC, Colelesage J, Delbaere LTJ, Nahoum V, Shi R, Zhou M, Zhu DW, Lin SX (2004) Protein crystal growth on board Shenzhou 3: a concerted effort improves crystal diffraction quality and facilitates structure determination. Biochemical and Biophysical Research Communications 324 (3):1081-1086

Harp JM, Hanson BL, Timm DE, Bunick GJ (2000) Asymmetries in the nucleosome core particle at 2.5 A resolution. Acta Crystallographica Section D 56 (12):1513-1534

Helliwell JR, Snell E, Weisgerber S (1996) An investigation of the perfection of lysozyme protein crystals grown in microgravity and on earth. In: Ratke L, Walter H, Feuerbacher B (eds) Materials and Fluids Under low Gravity: Proceedings of the IXth European Symposium on

Gravity-Dependent Phenomena in Physical Sciences Held at Berlin, Germany, 2–5 May 1995. Springer Berlin Heidelberg, Berlin, Heidelberg, pp 155-170

Henning M, Visanji M, Weber W, Janczikowski H, Plaas-Link A, Betzel C (1994) COSIMA — protein crystal growth facility for automatic processing on unmanned satellites. Journal of Crystal Growth 135 (3):513-522

Hilgenfeld R, Liesum A, Storm Rd, Plaas-Link A (1992) Crystallization of two bacterial enzymes on an unmanned space mission. Journal of Crystal Growth 122 (1):330-336

Hodgkin DC (1949) The X-ray analysis of the structure of penicillin. Advancement of science. 6(22): 85-89

Inaka K, Takahashi S, Aritake K, Tsurumura T, Furubayashi N, Yan B, Hirota E, Sano S, Sato M, Kobayashi T, Yoshimura Y, Tanaka H, Urade Y (2011) High-Quality Protein Crystal Growth of Mouse Lipocalin-Type Prostaglandin D Synthase in Microgravity. Crystal Growth & Design 11 (6):2107-2111

Kabsch W (2010) Xds. Acta Crystallographica Section D: Biological Crystallography 66(2): 125-132

Kademani B, Kalyane V, & Jange S (1999) Scientometric portrait of nobel laureate Dorothy Crowfoot Hodgkin. Scientometrics 45(2): 233-250

Kinoshita T, Maruki R, Warizaya M, Nakajima H, Nishimura S (2005) Structure of a high-resolution crystal form of human triosephosphate isomerase: improvement of crystals using the gel-tube method. Acta Crystallographica Section F: Structural Biology and Crystallization Communications 61 (4):346-349

Kitano K, Sasaki R, Nogi T, Fukami TA, Nakagawa A, Miki K, Tanaka I (2000) Utilization of microgravity to improve the crystal quality of biologically important proteins: chaperonin-60, GrpE, B-subunit of V-type ATPase, and MIF. Journal of Crystal Growth 210 (4):819-823

Klukas O, Schubert WD, Jordan P, Krauss N, Fromme P, Witt HT, Saenger W (1999) Photosystem I, an improved model of the stromal subunits PsaC, PsaD, and PsaE. The Journal of biological chemistry 274 (11):7351-7360

Ko TP, Day J, Malkin AJ, McPherson A (1999) Structure of orthorhombic crystals of beef liver catalase. Acta crystallographica Section D, Biological crystallography 55 (Pt 8):1383-1394

Ko TP, Kuznetsov YG, Malkin AJ, Day J, McPherson A (2001) X-ray diffraction and atomic force microscopy analysis of twinned crystals: rhombohedral canavalin. Acta crystallographica Section D, Biological crystallography 57 (Pt 6):829-839

Koszelak S, Day J, Leja C, Cudney R, McPherson A (1995) Protein and virus crystal growth on international microgravity laboratory-2. Biophysical Journal 69 (1):13-19

Krauspenhaar R, Rypniewski W, Kalkura N, Moore K, DeLucas L, Stoeva S, Mikhailov A, Voelter W, Betzel C (2002) Crystallisation under microgravity of mistletoe lectin I from Viscum album with adenine monophosphate and the crystal structure at 1.9 A resolution. Acta crystallographica Section D, Biological crystallography 58 (Pt 10 Pt 1):1704-1707

Kundrot CE, Judge RA, Pusey ML, Snell EH (2001) Microgravity and macromolecular crystallography. Crystal Growth & Design 1(1): 87-99

Kuranova IP, Smirnova EA, Abramchik YA, Chupova LA, Esipov RS, Akparov VK, Kovalchuk MV (2011) Crystal growth of phosphopantetheine adenylyltransferase, carboxypeptidase t, and

thymidine phosphorylase on the international space station by the capillary counter-diffusion method. Crystallography reports. 56(5): 884

Labeit S, Gautel M Lakey A, & Trinick J (1992) Towards a molecular understanding of titin. The EMBO journal 11(5): 1711-1716

Laemmli UK (1970) Cleavage of structural proteins during the assembly of the head of bacteriophage T4. Nature (227): 680–685

Larson SB, Day J, Greenwood A, McPherson A (1998) Refined structure of satellite tobacco mosaic virus at 1.8 Å resolution1. Journal of Molecular Biology 277 (1):37-59

Lee CP, Chernov AA (2002) Solutal convection around growing protein crystals and diffusional purification in space. Journal of crystal growth 240(3): 531-544

Liebau E, Bergmann B, Campbell AM, Teesdale-Spittle P, Brophy PM, Lüersen K, Walter RD (2002) The glutathione S-transferase from Plasmodium falciparum. Molecular and biochemical parasitology 124(1): 85-90

Linderstrom-Lang, KU (1953) How is a protein made?. Scientific American 189(3) 100-107

Littke W, John C (1984) Materials. Protein Single Crystal Growth Under Microgravity 225 (4658):203-204. doi:10.1126/science.225.4658.203

Littke W, John C (1986) Protein single crystal growth under microgravity. Journal of Crystal Growth 76 (3):663-672

Long MM, Bishop JB, DeLucas LJ, Nagabhushan TL, Reichert P, Smith GD (1997) Protein crystal growth in microgravity review of large scale temperature induction method: Bovine insulin, human insulin and human α-interferon. AIP Conference Proceedings 387 (1):671-678

Lorber B (2002) The crystallization of biological macromolecules under microgravity: a way to more accurate three-dimensional structures? Biochimica et Biophysica Acta (BBA) - Proteins and Proteomics 1599 (1–2):1-8

Lorber B, Sauter C, Ng J, Giegé R (1999a) Characterization of protein crystals grown in microgravity during STS-95 mission: I. Comparison of high resolution data sets of thaumatin crystals grown in gel on earth or in space. Space 41212 (P41212):P41212

Lorber B, Sauter C, Robert MC, Capelle B, Giege R (1999b) Crystallization within agarose gel in microgravity improves the quality of thaumatin crystals. Acta Crystallographica Section D 55 (9):1491-1494

Lorenz S, Perbandt M, Lippmann C, Moore K, DeLucas LJ, Betzel C, Erdmann VA (2000) Crystallization of engineered Thermus flavus 5S rRNA under earth and microgravity conditions. Acta Crystallographica Section D 56 (4):498-500

Małecki PH, Rypniewski W, Szymański M, Barciszewski J, Meyer A (2012) Binding of the plant hormone kinetin in the active site of Mistletoe Lectin I from Viscum album. Biochimica et Biophysica Acta (BBA)-Proteins and Proteomics 1824 (2):334-338

Mapelli M, Tucker PA (1999) Crystallization and Preliminary X-Ray Crystallographic Studies on the Herpes Simplex Virus 1 Single-Stranded DNA Binding Protein. Journal of Structural Biology 128 (2):219-222

Martirosyan A, DeLucas LJ, Schmidt C, Perbandt M, McCombs D, Cox M, Radka C and Betzel C (2019) Effect of macromolecular mass transport in microgravity protein crystallization. Gravitational and Space Research. To be published

McPherson A, Malkin AJ, Kuznetsov YG, Koszelak S, Wells M, Jenkins G, Howard J, Lawson G (1999) The effects of microgravity on protein crystallization: evidence for concentration gradients around growing crystals. Journal of crystal growth 196: 572-586

Meyer A, Rypniewski W, Szymański M, Voelter W, Barciszewski J, Betzel C (2008) Structure of mistletoe lectin I from Viscum album in complex with the phytohormone zeatin. Biochimica et Biophysica Acta (BBA)-Proteins and Proteomics 1784 (11):1590-1595

Miele AE, Federici L, Sciara G, Draghi F, Brunori M, Vallone B (2003) Analysis of the effect of microgravity on protein crystal quality: the case of a myoglobin triple mutant. Acta crystallographica Section D, Biological crystallography 59 (Pt 6):982-988

Mohamad Aris SNA, Thean Chor AL, Mohamad Ali MS, Basri M, Salleh AB, Raja Abd. Rahman RNZ (2014) Crystallographic Analysis of Ground and Space Thermostable T1 Lipase Crystal Obtained via Counter Diffusion Method Approach. BioMed Research International 2014:8

Moore KM, Long MM, DeLucas LJ (1999) Protein crystal growth in microgravity: Status and commercial implications. AIP Conference Proceedings 458 (1):217-224

Mulder GJ (1839) On the composition of some animal substances. Journal für praktische Chemie 16(129): 15

Murshudov GN, Skubák P, Lebedev AA, Pannu NS, Steiner RA, Nicholls R a, Winn MD, Long F, Vagin AA (2011): REFMAC5 for the refinement of macromolecular crystal structures. Acta Crystallogr D Biol Crystallogr (67):(Pt 4):355–67

Ng JD, Lorber B, Giege R, Koszelak S, Day J, Greenwood A, McPherson A (1997) Comparative Analysis of Thaumatin Crystals Grown on Earth and in Microgravity. Acta Crystallographica Section D 53 (6):724-733

Ng JD, Sauter C, Lorber B, Kirkland N, Arnez J, Giege R (2002) Comparative analysis of space-grown and earth-grown crystals of an aminoacyl-tRNA synthetase: space-grown crystals are more useful for structural determination. Acta Crystallographica Section D 58 (4):645-652

Ng JD, Gavira JA & García-Ruíz JM (2003) Protein crystallization by capillary counterdiffusion for applied crystallographic structure determination. Journal of structural biology 142(1): 218-231

Nichesola D, Perduca M, Capaldi S, Carrizo ME, Righetti PG, Monaco HL (2004) Crystal Structure of Chicken Liver Basic Fatty Acid-Binding Protein Complexed with Cholic Acid†. Biochemistry 43 (44):14072-14079

Oberthuer D, Melero-García E, Dierks K, Meyer A, Betzel C, Garcia-Caballero A, & Gavira JA (2012) Monitoring and scoring counter-diffusion protein crystallization experiments in capillaries by in situ dynamic light scattering. PLoS One 7(6): e33545

Otálora Fn, Luisa Novella M, Rondón D, García-Ruiz J-M (1999) Growth of lysozyme crystals under microgravity conditions in the LMS (STS-78) mission. Journal of Crystal Growth 196 (2–4):649-664

Otálora F, Novella ML, Gavira JA, Thomas BR, García-Ruiz JM (2001) Experimental evidence for the stability of the depletion zone around a growing protein crystal under microgravity. Acta Crystallographica Section D: Biological Crystallography 57(3): 412-417

Otálora F, Gavira JA, Ng JD, García-Ruiz JM (2009) Counterdiffusion methods applied to protein crystallization. Progress in biophysics and molecular biology 101(1-3): 26-37

Owens GE, New DM, Olvera AI, Manzella JA, Macon BL, Dunn JC, Cooper DA, Rouleau RL, Connor DS and Bjorkman PJ (2016) Comparative analysis of anti-polyglutamine Fab crystals grown on Earth and in microgravity. Acta Crystallographica Section F: Structural Biology Communications 72(10): 762-771

Pan J-S, Niu X-T, Gui L-L, Zhou Y-C, Bi R-C (1996) Crystallization of Biological MacromoleculesCrystallization under microgravity of acidic phospholipase A2 from venom of Agkistrodon halys Pallas. Journal of Crystal Growth 168 (1):227-232

Perbandt M, Burmeister C, Walter RD, Betzel C, & Liebau E (2004) Native and inhibited structure of a Mu class-related glutathione S-transferase from Plasmodium falciparum. Journal of Biological Chemistry 279(2): 1336-1342

Perbandt M, Eberle R, Fischer-Riepe L, Cang H, Liebau E, & Betzel C (2015) High resolution structures of Plasmodium falciparum GST complexes provide novel insights into the dimer–tetramer transition and a novel ligand-binding site. Journal of structural biology 191(3): 365-375

Plaas-Link A, Cornier J (1988) Concepts for crystallization of organic material under microgravity. Appl. Microgravity Tech 3: 123

Ponassi M, Felli L, Parodi S, Valbusa U, Rosano C (2011) Crystals of the hydrogenase maturation factor HypF N-terminal domain grown in microgravity, display improved internal order. Journal of Crystal Growth 314 (1):246-251

Riès-Kautt M, Broutin I, Ducruix A, Shepard W, Kahn R, Chayen N, Blow D, Paal K, Littke W, Lorber B, Thèobald-Dietrich A, Giegé R (1997) Crystallogenesis studies in microgravity with the Advanced Protein Crystallization Facility on SpaceHab-01. Journal of Crystal Growth 181 (1):79-96

Safonova TN, Mordkovich NN, Polyakov KM, Manuvera VA, Veiko VP, Popov VO (2012) Crystallization of uridine phosphorylase from Shewanella oneidensis MR-1 in the laboratory and under microgravity and preliminary X-ray diffraction analysis. Acta Crystallographica Section F: Structural Biology and Crystallization Communications 68 (Pt 11):1387-1389

Sauter C, Lorber B, Giegé R (2002) Towards atomic resolution with crystals grown in gel: the case of thaumatin seen at room temperature. Proteins: Structure, Function, and Bioinformatics 48 (2):146-150

Sauter C, Otalora F, Gavira J-A, Vidal O, Giege R, Garcia-Ruiz JM (2001) Structure of tetragonal hen egg-white lysozyme at 0.94 A from crystals grown by the counter-diffusion method. Acta Crystallographica Section D 57 (8):1119-1126

Shabalin IG, Serov AE, Skirgello OE, Timofeev VI, Samygina VR, Popov VO, Tishkov VI, Kuranova IP (2010) Recombinant formate dehydrogenase from Arabidopsis thaliana: Preparation, crystal growth in microgravity, and preliminary X-ray diffraction study. Crystallography Reports 55 (5):806-810

Sjölin L, Wlodawer A, Bergqvist G, Holm P, Loth K, Malmström H, Zaar J, Svensson LA, Gilliland GL (1991) Protein crystal growth of Ribonuclease A and Pancreatic Trypsin Inhibitor aboard the MASER 3 rocket. Journal of Crystal Growth 110 (1):322-332

Skinner R, Abrahams J-P, Whisstock JC, Lesk AM, Carrell RW, Wardell MR (1997) The 2.6 Å structure of antithrombin indicates a conformational change at the heparin binding site1. Journal of Molecular Biology 266 (3):601-609

Smirnova EA, Kislitsyn YA, Sosfenov NI, Lyashenko AV, Popov AN, Baĭdus' AN, Timofeev VI, Kuranova IP (2009) Protein crystal growth on the Russian segment of the International Space Station. Crystallography Reports 54 (5):901-911

Smith GD, Ciszak E, Pangborn W (1996) A novel complex of a phenolic derivative with insulin: structural features related to the T-->R transition. Protein Science : A Publication of the Protein Society 5 (8):1502-1511

Smith LM, Kelleher NL, Linial M, Goodlett D, Langridge-Smith P, Goo YA, Safford G, Bonilla L, Kruppa G, Zubarev R and Rontree J (2013) Proteoform: a single term describing protein complexity. Nature methods 10(3): 186

Snell EH, Weisgerber S, Helliwell JR, Weckert E, Holzer K, Schroer K (1995) Improvements in lysozyme protein crystal perfection through microgravity growth. Acta Crystallographica Section D 51 (6):1099-1102

Snell EH, Cassetta A, Helliwell JR, Boggon TJ, Chayen NE, Weckert E, Holzer K, Schroer K, Gordon EJ, Zagalsky PF (1997) Partial Improvement of Crystal Quality for Microgravity-Grown Apocrustacyanin C1. Acta Crystallographica Section D 53 (3):231-239

Snell EH, Judge RA, Crawford L, Forsythe EL, Pusey ML, Sportiello M, Todd P, Bellamy H, Lovelace J, Cassanto JM (2001) Investigating the effect of impurities on macromolecule crystal growth in microgravity. Crystal Growth & Design 1: 151-158

Snell, EH, & Helliwell, JR (2005) Macromolecular crystallization in microgravity. Reports on Progress in Physics 68(4): 799

Stadtman TC (1996) Selenocysteine. Annual review of biochemistry 65(1): 83-100

Stoddard BL, Strong RK, Arrott A, Farber GK (1992) Mir for the crystallographers' money. Nature 360 (6402):293-294

Strelov VI, Kuranova IP, Zakharov BG, Voloshin AE (2014) Crystallization in space: Results and prospects. Crystallography Reports 59 (6):781-806

Strong RK, Stoddard BL, Arrott A, Farber GK (1992) Long duration growth of protein crystals in microgravity aboard the MIR space station. Journal of Crystal Growth 119 (3):200-214

Stura EA & Wilson IA (1991) Applications of the streak seeding technique in protein crystallization. Journal of Crystal Growth 110(1-2): 270-282

Symersky J, Devedjiev Y, Moore K, Brouillette C, DeLucas L (2002) NH3-dependent NAD+ synthetase from Bacillus subtilis at 1 A resolution. Acta crystallographica Section D, Biological crystallography 58 (Pt 7):1138-1146

Tanaka H, Tsurumura T, Aritake K, Furubayashi N, Takahashi S, Yamanaka M, Hirota E, Sano S, Sato M, Kobayashi T, Tanaka T, Inaka K, Urade Y (2011) Improvement in the quality of hematopoietic prostaglandin D synthase crystals in a microgravity environment. Journal of synchrotron radiation 18 (1):88-91

Tanaka H, Umehara T, Inaka K, Takahashi S, Shibata R, Bessho Y, Sato M, Sugiyama S, Fusatomi E, Terada T, Shirouzu M, Sano S, Motohara M, Kobayashi T, Tanaka T, Tanaka A, Yokoyama S

(2007) Crystallization of the archaeal transcription termination factor NusA: a significant decrease in twinning under microgravity conditions. Acta Crystallographica Section F: Structural Biology and Crystallization Communications 63 (Pt 2):69-73

Terzyan SS, Bourne CR, Ramsland PA, Bourne PC, Edmundson AB (2003) Comparison of the three-dimensional structures of a human Bence-Jones dimer crystallized on Earth and aboard US Space Shuttle Mission STS-95. Journal of molecular recognition : JMR 16 (2):83-90

Thomas DH, Rob A, & Rice DW (1989) A novel dialysis procedure for the crystallization of proteins. Protein Engineering, Design and Selection 2(6): 489-491

Thomas BR, Vekilov PG, & Rosenberger F (1998) Effects of microheterogeneity in hen egg-white lysozyme crystallization. Acta Crystallographica Section D: Biological Crystallography, 54(2): 226-236

Timofeev V, Smirnova E, Chupova L, Esipov R, Kuranova I (2012a) X-ray study of the conformational changes in the molecule of phosphopantetheine adenylyltransferase from Mycobacterium tuberculosis during the catalyzed reaction. Acta crystallographica Section D, Biological crystallography 68 (Pt 12):1660-1670

Timofeev VI, Abramchik YA, Fateev IV, Zhukhlistova NE, Murav'eva TI, Kuranova IP, Esipov RS (2013a) Three-dimensional structure of thymidine phosphorylase from E. coli in complex with 3′-azido-2′-fluoro-2′,3′-dideoxyuridine. Crystallography Reports 58 (6):842-853

Timofeev VI, Abramchik YA, Zhukhlistova NE, Muravieva TI, Esipov RS, Kuranova IP (2016) Three-dimensional structure of phosphoribosyl pyrophosphate synthetase from E. coli at 2.71 Å resolution. Crystallography Reports 61 (1):44-54

Timofeev VI, Kuznetsov SA, Akparov VK, Chestukhina GG, Kuranova IP (2013b) Three-dimensional structure of carboxypeptidase T from Thermoactinomyces vulgaris in complex with N-BOC-L-leucine. Biochemistry (Moscow) 78 (3):252-259

Timofeev VI, Smirnova EA, Chupova LA, Esipov RS, Kuranova IP (2010) Preparation of the Crystal Complex of Phosphopantetheine Adenylyltransferase from Mycobacterium tuberculosis with Coenzyme A and Investigation of Its Three-Dimensional Structure at 2.1-Å Resolution. Crystallography Reports 55 (6):1050-1059

Timofeev VI, Smirnova EA, Chupova LA, Esipov RS, Kuranova IP (2012b) Three-dimensional structure of phosphopantetheine adenylyltransferase from Mycobacterium tuberculosis in the apo form and in complexes with coenzyme A and dephosphocoenzyme A. Crystallography Reports 57 (1):96-104

Travis Gallagher D, Stover C, Charlton D, Arnowitz L, Black DR (2003) X-ray topography of microgravity-grown ribonuclease S crystals. Journal of Crystal Growth 255 (3–4):403-413

Tyn MT, Gusek TW (1990) Prediction of diffusion coefficients of proteins. Biotechnology and bioengineering 35(4): 327-338

Vagin A, Teplyakov A (1997) MOLREP: an Automated Program for Molecular Replacement. J Appl Crystallogr (30):1022–1025

Vahedi-Faridi A, Lovelace J, Bellamy HD, Snell EH, Borgstahl GE (2003a) Physical and structural studies on the cryocooling of insulin crystals. Acta crystallographica Section D, Biological crystallography 59 (Pt 12):2169-2182

Vahedi-Faridi A, Porta J, Borgstahl GE (2003b) Improved three-dimensional growth of manganese superoxide dismutase crystals on the International Space Station. Acta crystallographica Section D, Biological crystallography 59 (Pt 2):385-388

Vallazza M, Banumathi S, Perbandt M, Moore K, DeLucas L, Betzel C, Erdmann VA (2002) Crystallization and structure analysis of Thermus flavus 5S rRNA helix B. Acta crystallographica Section D, Biological crystallography 58 (Pt 10 Pt 1):1700-1703

Vaney MC, Broutin I, Retailleau P, Douangamath A, Lafont S, Hamiaux C, Prange T, Ducruix A, Ries-Kautt M (2001) Structural effects of monovalent anions on polymorphic lysozyme crystals. Acta crystallographica Section D, Biological crystallography 57 (Pt 7):929-940

Vaney MC, Maignan S, Ries-Kautt M, Ducruix A (1996) High-Resolution Structure (1.33 A) of a HEW Lysozyme Tetragonal Crystal Grown in the APCF Apparatus. Data and Structural Comparison with a Crystal Grown under Microgravity from SpaceHab-01 Mission. Acta Crystallographica Section D 52 (3):505-517

Vekilov PG., & Rosenberger F (1996) Dependence of lysozyme growth kinetics on step sources and impurities. Journal of crystal growth, 158(4), 540-551

Vekilov PG (1999) Protein crystal growth—Microgravity aspects. Advances in Space Research 24: 1231-1240

Vergara A, Corvino E, Sorrentino G, Piccolo C, Tortora A, Carotenuto L, Mazzarella L and Zagari A (2002) Crystallization of the collagen-like polypeptide (PPG) 10 aboard the International Space Station. 1. Video observation. Acta Crystallographica Section D: Biological Crystallography 58(10): 1690-1694

Vergara A, Lorber B, Zagari A, & Giegé R (2003) Physical aspects of protein crystal growth investigated with the Advanced Protein Crystallization Facility in reduced-gravity environments. Acta Crystallographica Section D: Biological Crystallography, 59(1): 2-15

Vince R, Daluge S, Wadd WB (1971) Studies on the inhibition of glyoxalase I by S-substituted glutathiones. J Med Chem (14): 402-04

Vitagliano L, Berisio R, Mazzarella L, Zagari A (2001) Structural bases of collagen stabilization induced by proline hydroxylation. Biopolymers 58 (5):459-464

von Laue M (1915) Concerning the detection of X-ray interferences. Nobel lecture 13

Wang K, McClure J, & Tu ANN (1979) Titin: major myofibrillar components of striated muscle. Proceedings of the National Academy of Sciences 76(8): 3698-3702

Wardell MR, Skinner R, Carter DC, Twigg PD, Abrahams JP (1997) Improved diffraction of antithrombin crystals grown in microgravity. Acta crystallographica Section D, Biological crystallography 53 (Pt 5):622-625

Wilcox WR (1983) Influence of convection on the growth of crystals from solution. Journal of Crystal Growth 65(1-3): 133-142

Winn MD, Ballard CC, Cowtan KD, Dodson EJ, Emsley P, Evans PR, Keegan RM, Krissinel EB, Leslie AG, McCoy A. and McNicholas SJ (2011) Overview of the CCP4 suite and current developments. Acta Crystallographica Section D: Biological Crystallography, 67(4): 235-242

Yoshida H, Yoshihara A, Ishii T, Izumori K, Kamitori S (2016) X-ray structures of the Pseudomonas cichorii D-tagatose 3-epimerase mutant form C66S recognizing deoxy sugars as substrates. Applied Microbiology and Biotechnology 100 (24):10403-10415

Yoshikawa S, Kukimoto-Niino M, Parker L, Handa N, Terada T, Fujimoto T, Terazawa Y, Wakiyama M, Sato M, Sano S (2013) Structural basis for the altered drug sensitivities of non-small cell lung cancer-associated mutants of human epidermal growth factor receptor. Oncogene 32 (1):27-38

Zagalsky PF, Wright CE, Parsons M (1995) EURECA Scientific ResultsCrystallisation of α-crustacyanin, the lobster capapace astaxanthin-protein: Results from EURECA. Advances in Space Research 16 (8):91-94

Zegers I, Carotenuto L, Evrard C, Garcia-Ruiz J, De Gieter P, Gonzales-Ramires L, Istasse E, Legros JC, Martial J, Minetti C and Otalora F (2006) Counterdiffusion protein crystallisation in microgravity and its observation with PromISS (Protein Microscope for the International Space Station). Microgravity-Science and Technology 18(3-4): 165

Zhu D-W, Zhou M, Mao Y, Labrie F, Lin S-X (1995) Crystallization of human estrogenic 17β-hydroxysteroid dehydrogenase under microgravity. Journal of Crystal Growth 156 (1):108-111

IX Appendix

LMM Biophysics to Principle Investigator Integration Agreement

September, 2015

AUTHORIZED by CM when under FORMAL Configuration Control	
Date	**Signature**

Availability:

[X] Public (No Restriction) [ ] Export Controlled

National Aeronautics and Space Administration
John H. Glenn Research Center
Space Operations Project Office
Cleveland, Ohio 44135

SIGNATURE PAGE
LMM BIOPHYSICS TO PRINCIPLE INVESTIGATOR
INTEGRATION AGREEMENT

Prepared By: _____ **Date:** _____

Tibor Lorik
LMMBIO Systems Engineer ZIN
Technologies, Inc.

Date: _____

Approved By: _____

Ray Pavlik
LMMBIO Project Lead
ZIN Technologies, Inc.

Date: _____

Approved By: _____

Dr. Larry DeLucas
LMM Biophysics-1 Principle Investigator
University of Alabama-Birmingham (UAB)

Date: _____

Approved By: _____

Dr. Edward Snell
LMM Biophysics-3 Principle Investigator
Hauptman Woodward Institute (HWI)

Date: _____

Concurred By: _____

Laurel Karr
Project Scientist
Marshall Space Flight Center (MSFC)

Concurred By: _____ **Date:** _____

Ronald Sicker
LMM Science Manager

NASA Glenn Research Center (GRC)

REVISION PAGE

LMM BIOPHYSICS TO PRINCIPLE INVESTIGATOR INTEGRATION AGREEMENT

Revision	Date	Description of Change	Contractor Verification and Date	NASA Verification and Date*

TABLE OF CONTENTS

1.0 INTRODUCTION

1.1 Purpose and Scope

The Integration Agreement (IA) documents the agreements between the LMM Biophysics engineering team and their representatives and the Principle Investigator

(PI).

2.0 DOCUMENTS

2.1 Applicable Documents

The following documents require reference and/or action by the users of this IA. The list below includes specifications, models, standards, guidelines, handbooks, and other special publications. The documents listed in this section are applicable to the extent specified herein. Inclusion of applicable documents herein does not in any way supersede the order of precedence identified in Section **Error! Reference source not found.**of this document.

2.1.1 Government Documents

LMMBIO-CONOPS-001	LMM Biophysics Concept of Operations
FCF-PLN-0031	Ground Processing Plan Fluids and Combustion Facility
FCF-PLN-0788	FCF User Training/Certification Plan
FCF-PLN-0875	FCF Utilization Process
NASA-STD-3000/T	ISS Crew Integration Standard
SSP 30599 Appendix J	Payload Safety Review and Data Submittal Requirements for Payload Using the: Space Shuttle, International Space Station
SSP 50004	ISS Ground Support Equipment Design Requirements
SSP 50005	International Space Station Flight Crew Integration Standard (NASA-STD-3000/T)
SSP 50223	International Space Station Export Control Plan
SSP 50257	Program Controlled Document Index
SSP 50431	Space Station Program Requirements For Payloads
SSP 50502	ISS Hardware Pre-Flight Imagery Requirements
SSP 51700	Payload Safety Policy and Requirements for the International Space Station
SSP 52005	Payload Flight Equipment Requirements and Guidelines for Safety-Critical Structures
SSP 52000-PAH-KSC	International Space Station Payload Accommodations Handbook – Payload Processing Accommodations at KSC
SSP 52054	ISS Program Payloads Certification of Flight Readiness Implementation Plan, Generic
SSP 57000	Pressurized Payload Interface Requirements Document

SSP 57008	Unique Pressurized Payload Non–Rack Interface Control Document
SSP 57117	Payload Integration Agreement for the Fluids and Combustion Facility
SSP 57218	Fluid and Combustion Facility (FCF) Fluids Integrated Rack (FIR) ICD
SSP 58002	Multilateral Payload Regulations
SSP 58309	Payload Training Implementation Plan (NPTIP)
SSP 58313	NASA Payload Regulations
FCF-IDD-FIR	FIR Payload IDD
LMM-DOC-1679	LMM User's Manual

2.2 Reference Documents

The following documents contain supplemental information to guide the user in the application of this document. These reference documents are not specifically cited within the text of this document.

DoD STD 100	Engineering, Drawing Practices
MSFC-PLAN-2846	NASA Payload Training Implementation Plan (NPTIP)
SSP 52000-PAH-PRP	ISS Payload Accommodations Handbook - Pressurized Payloads
TSC-DOC-006	GRC Telescience Support Center User Guide

3.0 PAYLOAD OVERVIEW

3.1 General Payload Description

LMM Biophysics is a Glenn Research Center (GRC) and Center for the Advancement of Science in Space (CASIS) sponsored biological protein crystal growth experiment utilizing the Fluids Integrated Rack (FIR)/Light Microscopy Module (LMM) on the International Space Station (ISS). The LMM Biophysics experiments that have been identified are LMM Biophysics-1 and LMM Biophysics-3. The experiments expand an ongoing program into the complex realm of membrane proteins that move signals or molecules to and from a cell's interior or help cells identify each other for immune responses. Proteins in the microgravity environment are exposed to conditions that concentrate them so they form crystals that would be too fragile to form on Earth, but which can be returned to Earth for X-ray analysis.

The investigation entails the launch of 3 Biophysics Plates (cassettes) for each of the two PIs containing capillaries with various protein samples, 2 dataloggers to monitor the temperature of the cassette once removed from cold stowage and during descent, and the LMM Base Adapter to replace the XY-Stage Cold Plate to utilize the full range of travel for the XY-Stage. The cassettes will be a late turnover and launched aboard SpaceX in cold stowage at -80 °C. The dataloggers will be a late turnover in ambient storage. The LMM Base Adapter will have a nominal turnover and be launched in ambient storage. Each cassette will be contained within a Bitran Zip-Lock bag that includes desiccant to preclude condensation from forming on the cassette. The Bitran Bag will then be placed into a Bubble Bag and installed in a POLAR or similar cold stowage for launch. Upon reaching ISS the cassettes will be transferred to ISS cold stowage while awaiting science operations. The FIR/LMM will require the XY-Stage Cold Plate to be removed and replaced with the LMM Base Adapter prior to installation of a

cassette. With the FIR/LMM properly configured the cassette will be removed from cold stowage, thawed, and installed onto the LMM Petri Plate using Velcro. The datalogger will also be installed onto the LMM Petri Plate using Velcro. The LMM Petri Plate will then be installed onto the LMM Base Adapter and the FIR/LMM prepared for powered science operations.

LMM Biophysics will compare the crystal growth rates for macromolecules covering a wide molecular weight in microgravity versus gravity. LMM Biophysics-1 will also evaluate the percentage incorporation of different molecular aggregates (protein impurities) into the crystalline lattice of growing crystals. Based on the percentage incorporation of larger aggregates within the crystals, the effect of molecular filtering based on differences in diffusion rates will be indirectly assessed. This will be accomplished by fluorescently tagging the aggregates. Once the crystals are returned to Earth they will be subjected to X-ray crystallography to determine the structure and hence understand the biology of the system.

3.2 Pre-Flight Operations

The LMM Biophysics payload will utilize the FIR GIU located in the High Bay of building 333 at the NASA Glenn Research Center to perform physical integration fit checks of the flight hardware and conduct science characterization testing. The physical integration fit check will include generating a PlatenRegistry Map. The science characterization testing will educate the PI as to the capabilities of the FIR/LMM thereby aiding them in the development of their samples and experiment operations.

The LMM Biophysics PI has requested testing be performed on the ground as a comparison with the flight results. In order to evaluate orientation effects the LMM Biophysics-1 PI requests testing be done with gravity oriented through the depth of the capillary and with gravity through the width of the capillary. The latter orientation requires the use of the LMM GSE to rotate the microscope. The details of what runs are to be performed is TBD.

3.3 On-Orbit Operations Preparation

The LMM Petri Base and MICRORHTEMP datalogger will be gathered from Stowage and temporarily stowed at the FIR. The crew will install a piece of loop Velcro to the LMM Petri Base per crew procedure as shown below. The datalogger will be removed from its ziplock bag and mounted to the added piece of Velcro.

Prior to operating the LMM Biophysics payload the FIR/LMM will be configured with the LMM Base Adapter (which replaces the LMM Cold Plate) and 2.5X, 10X, 20X, and 50X objectives. With the FIR rack doors open and the AFC Front Door removed the selected Biophysics Plate will be removed from Cold Stowage and allowed to thaw while contained in its Bubble/Bitran Zip-lock bags. Once thawed the crew will remove the Bitran Bag from the Bubble Bag, inspect the Biophysics Plate for condensation and damage and assuming no condensation or damage the crew will remove the Biophysics Plate from the Bitran bag, place the Biophysics Plate on the LMM Petri Base taking care to align the edge of the Biophysics Plate with the edge of the LMM Petri Base. Attachment of the Biophysics Plate to the LMM Petri Base will be with Velcro. The

Bubble Bag, Bitran Bag and datalogger ziplock bag will be stowed in the AFC. The LMM Petri Base will then be installed onto the LMM Base Adapter, the crew will install the AFC Front Door, rotate LMM to the Operate position and close the rack doors.

The first and second run for each PI will start with a cassette being removed from Cold Stowage, thawed, installed in the FIR/LMM as described above, and the science observations performed. Once these runs have successfully completed the third cassette from each PI will be removed from Cold Stowage, thawed, and placed into nominal stowage with the other two cassettes to allow crystal growth to occur unmonitored. All three cassettes will be returned to the ground for further observation.

3.4 On-Orbit Science Operations

Powered operations will begin as soon as practical after installation is complete with initiation of the crystal search phase occurring within 4 hours of the cassette being installed. The start of the crystal search phase is defined here as the point when 2.5X images of the first capillary are acquired in support of generating a composite of each capillary. In order to initiate the crystal search phase the PD must locate the index marks and set the offsets and alignment corrections to allow use of the pre-flight generated PlatenRegistry map. The crystal search phase will be conducted via a script that will

acquire up to 24 images of each capillary. A custom LMM Biophysics application located on the PD TREK will generate a composite image of each capillary using the images acquired during the crystal search script. For LMM Biophysics-1 the search may be performed using the 50/50 and/or Texas Red filters. It is estimated that it will take 3 hours to acquire the 24 images of each capillary for each filter. For LMMBIO-1 the 2.5X composite will be generated by acquiring an image array that is 23 images long x 1 image wide for each of the 8 capillaries. For LMMBIO-3 the 2.5X composite will be generated by acquiring an image array of 12 images long x 2 images wide for each of the 18 capillaries. It should be noted that the crystal growth rate will generally be different for each capillary. It is possible that there will be no evidence of crystal growth initially in which case the PD will repeat the 2.5X crystal search.

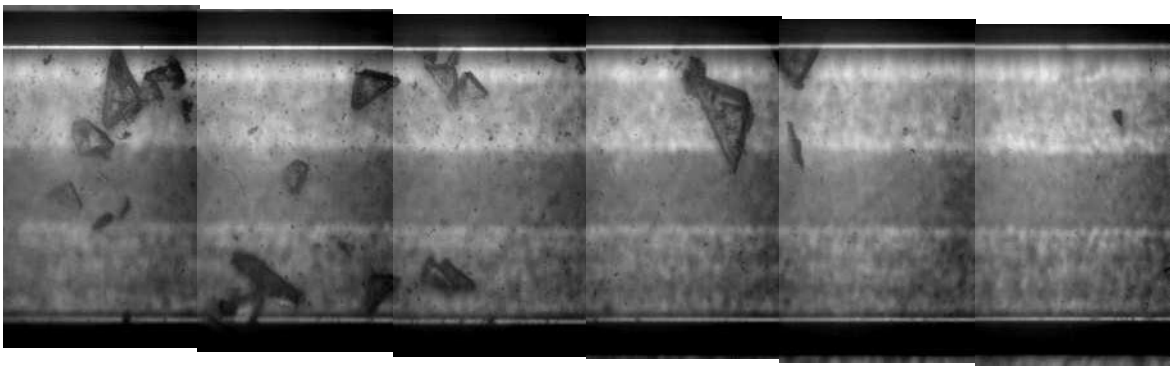

Example of a 1 x 6 image composite at 2.5X (100 mm Capillary)

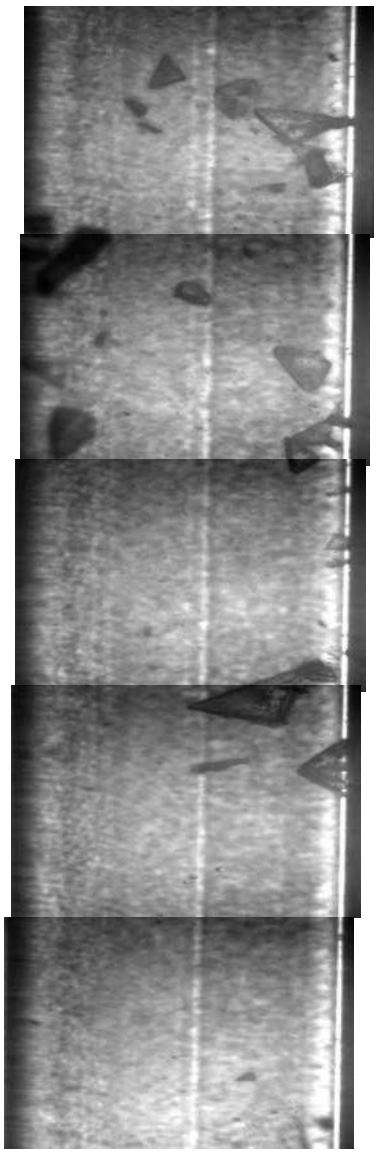

Example of a 1 x 5 image composite at 2.5X (50 mm Capillary)

Upon completion of the 2.5X crystal search the PI will identify up to 10 locations per capillary to investigate further with the 10X objective. The PD will initiate “Live Imaging”, move to each location, and attempt to focus on the feature to ascertain if it is the nucleation position of a crystal. The PD may be need to search several fields of view around the selected area with the 10X objective to locate the feature that was observed with the 2.5X objective to account for the smaller field of view and the parcentricity of the objectives. The PD TREK may acquire images with the 10X objective to generate a 4x3 composite. The composite will have a FOV that is (660 microns x 4 = 2640 microns) in the X-stage direction by (820 microns x 3 = 2460 microns) in the Y-stage direction. Thus for the 50 mm capillary a 10X composite will be 2460 microns (3 images) along the capillary length and 2640 along its width (4 images), and for the 100 mm capillary it will be 2640 microns along its length (4 images) and 2460 microns (3 images) along the width. If the feature is a crystal, log the position to a table, and acquire a Z-stack of either a single XY position or the 4x3 composite per PI direction. The number of Z-positions and the step size is TBD. This process will be repeated for each location. It is possible that the Z-stack will be performed using the 20X objective instead of or in addition to the 10X objective. With the 20X objective only a single XY position Z-stack is supported.

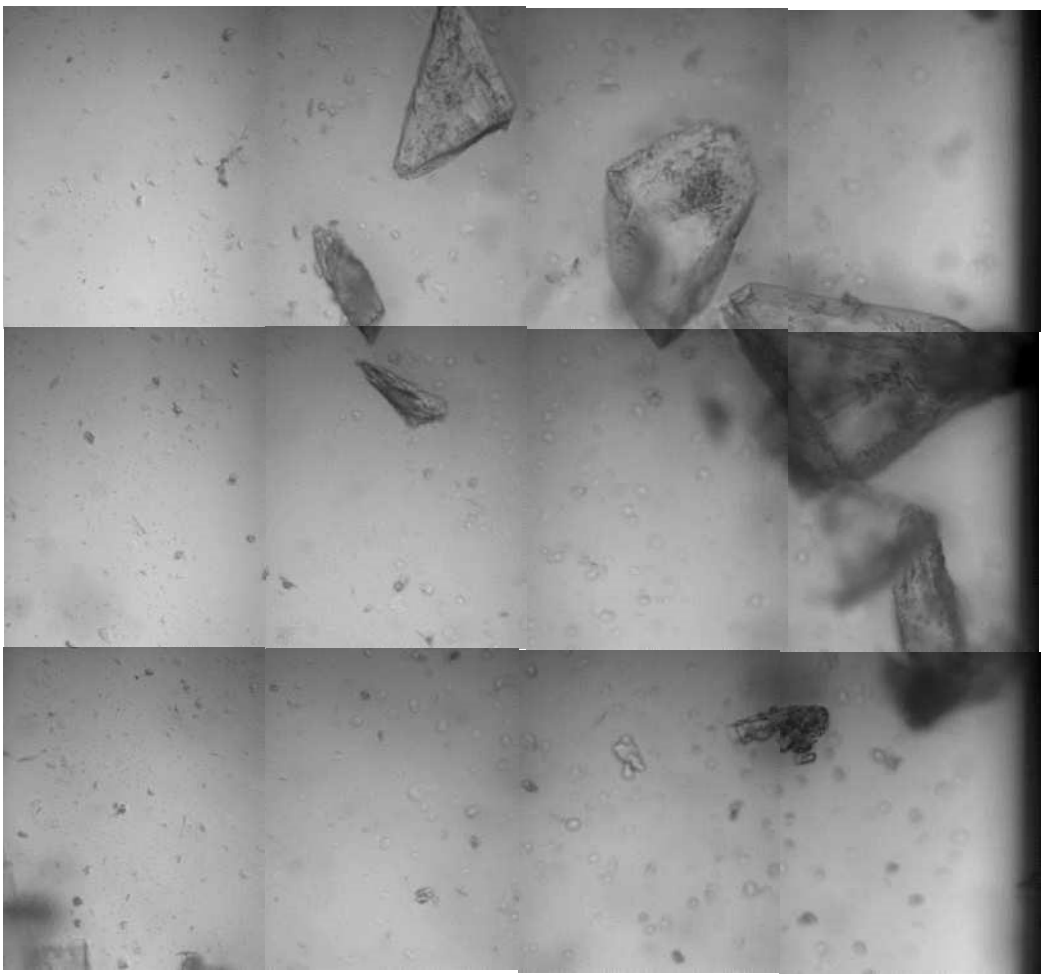

Example of a 3 long x 4 wide image composite at 10X (50 mm Capillary)

Once all identified positions have been observed with the 10X and/or 20X objectives the PD will repeat the 2.5X crystal search on capillaries that do not have 10 locations identified. After the crystal search is complete imaging will be conducted with the 10X and/or 20X objectives at all of the locations previously identified as well as new locations found during subsequent crystal searches. Once 10 locations are identified on a capillary that capillary no longer needs to have crystal search performed. Once the PI has determined that a crystal has completed its growth no further observations of that crystal is required and once all crystals have completed their growth the experiment is complete. The experiment duration requested by the PIs may be up to 30 days per cassette.

During the science operations described above the FIR Rack Officer will monitor the temperature within the AFC. If the temperature exceeds 24 C the Rack Officer will need to take TBD action such as powering down ORU's. During LOS no monitoring or action is expected.

During the conduct of the experiment during image acquisition the microscope settings will be recorded in MIC file and the camera setting will be recorded in the IRG file. The telemetry being recorded is documented in the LMM User's Manual, LMM-DOC-1679.

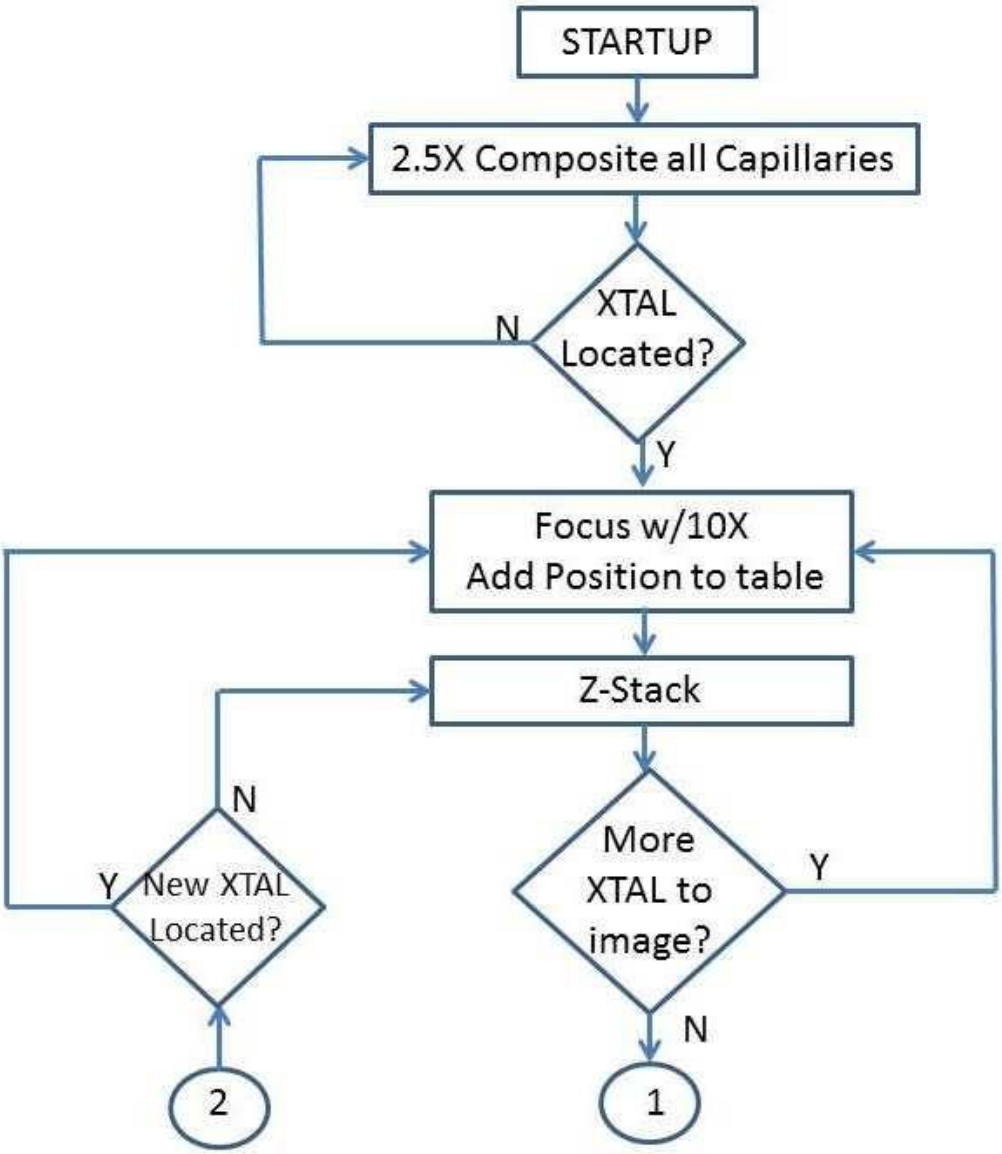
STARTUP
2.5X Composite all Capillaries
XTAL Located?
N
Y
Focus w/10X
Add Position to table
Z-Stack
More XTAL to image?
Y
N
N
Y
New XTAL Located?
2
1

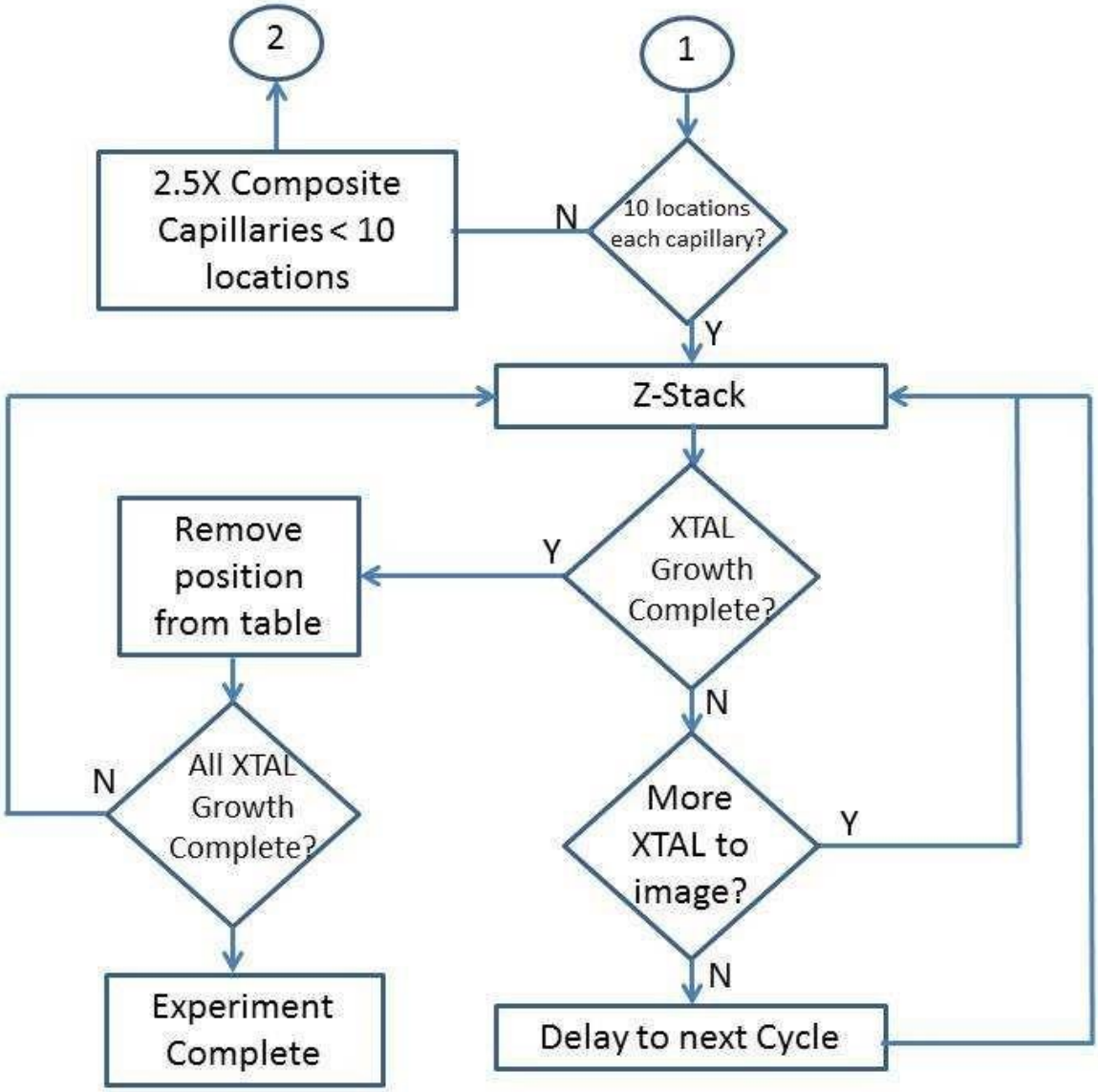

3.5 On-Orbit Operations – Hardware Stow

Upon completion of the science run the datalogger and cassette will be removed from the LMM Petri Base, placed in the ziplock bag and Bitran/Bubble Bag, respectively, and co-located in stowage.

3.6 Hardware Return

The LMM Biophysics PIs do not want the crystals that formed on-orbit to become jammed into one end of the capillary during descent. To prevent this, the cassettes must be oriented in Dragon so that the main descent vector X is not parallel with the long axis of the capillaries as shown below. The LMM Biophysics PIs will retrieve the samples at Long Beach Airport after splashdown.

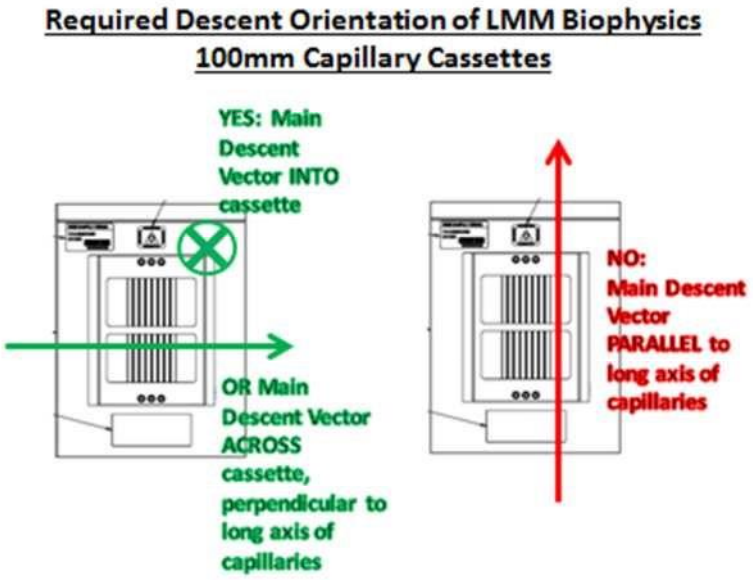

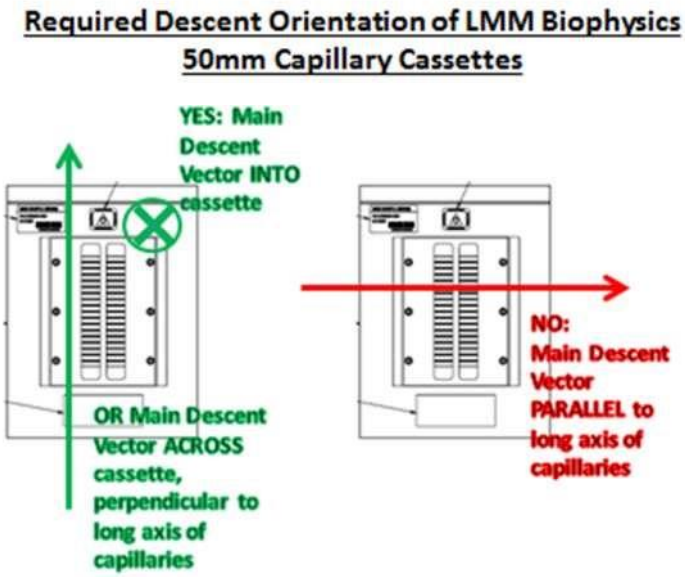

4.0 REQUIREMENTS

4.1 Capillary Filling & Assembly Requirements

The flight hardware will consist of Biophysics Plates (cassettes) that will hold capillaries filled by the PI. Each PI has their choice of either of 2 designs; one that will hold 8 capillaries that are 100 mm long each or one that will hold 18 capillaries that are 50 mm long each. Each PI will be allocated 3 cassettes for launch.

- The PI shall use fused silica capillaries available from Vitrocom. Part number 3530S-50 will be used with the 50 mm capillary cassette (P/N S2196MFA1050) and part number 3530S-100 will be used with the 100 mm capillary cassette (P/N S2196MFA1000).

- The cassette assembly design provides the PI with a ±18 mm field of view from the center of the capillary for the 50 mm cassette and a ± 30 mm field of view from the center of the capillary for the 100 mm cassette. The PI should fill each end of the 50 mm capillary with a minimum of 7 mm of Apezion N grease or similar and a minimum of 20 mm of Apezion N grease or similar to each end of the 100 mm capillary in order to preclude crystals from growing in an area outside the available fled of view.

- Each PI shall develop a procedure for filling and sealing their capillaries and submit for archiving by January 15, 2016 or 1 month after the dry run whichever is later.

- The filling of each capillary shall be conducted at the PI site or other appropriate location with no oversight required.

- The PI shall identify the composition and quantity of each component inserted into the capillary. The PI shall only use components listed in the HMST submitted to the Toxicologist. The HMST is provided in Appendix A.

- The capillaries shall be sealed with Hardman 2-part extra fast setting epoxy from Royal Adhesives, P/N 04001.

- Once sealed the capillary shall be dimensionally compatible with the cassette as shown below:

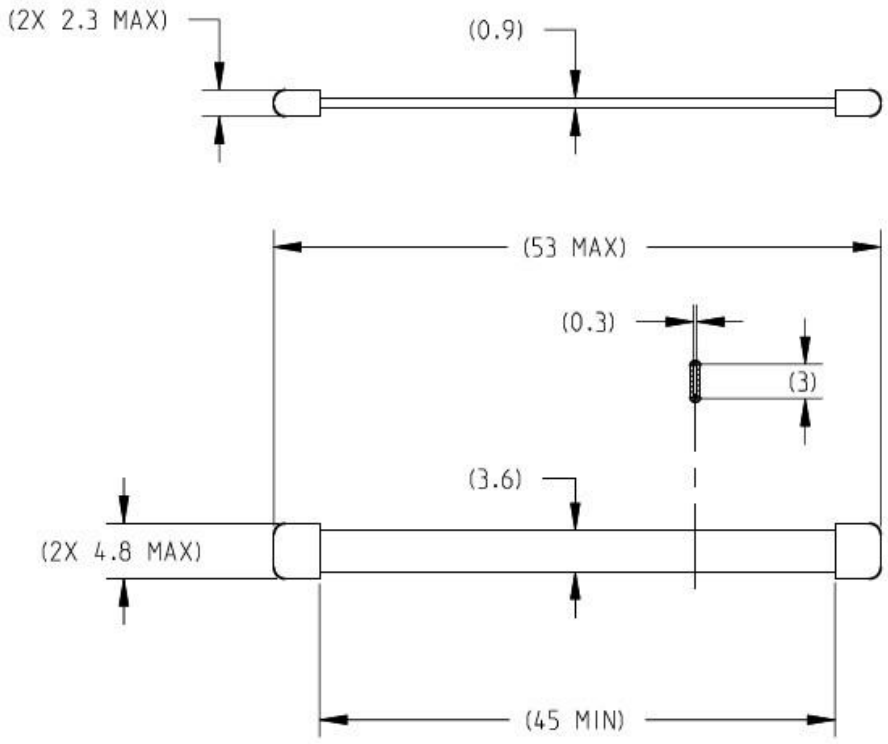

Figure 1: 50 mm Sealed Capillary dimensions

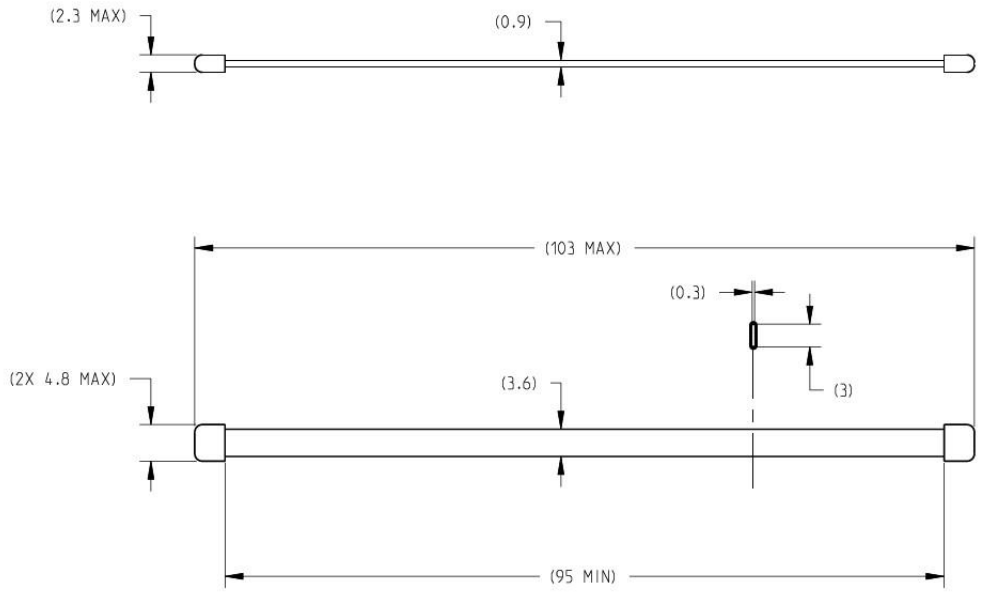

Figure 2: 100 mm Sealed Capillary dimensions

4.2 Cassette Assembly Requirements

- The PI shall deliver their filled capillaries to Kennedy Space Center (KSC) where they will meet the LMMBIO team to complete the assembly and turn over the hardware to ISS Cold Stowage.
- Turn over shall be made no later than 7 days before launch therefore arrival at KSC should be at least 8 days prior to launch.
- LMMBIO shall provide all of the items listed on assembly drawings except for the capillaries, its contents or sealing components. See Appendix B for the assembly drawings.

4.3 Pre-flight Operations Requirements

- The PI shall provide a set of flight-like capillaries of sufficient quantity to fill a cassette to LMMBIO by November 15, 2015. The PI and LMMBIO can use this as a dry run for the development of the fill and seal and cassette assembly procedures. This assembly will then be installed in the GIU to perform a ground test to finalize the operations and provide an opportunity for ground personnel training. The PI should provide support at the GRC TSC during this dry run.
- LMMBIO shall arrange for the PI to have access to the real-time ISS video downlink at their site of preference.

- Each PI shall provide the operations timeline for conducting their experiment by January 15, 2016 or 1 month after the dry run whichever is later.

    - In lieu of operations timeline from the PI LMMBIO-1 will operate one cassette while SpaceX-10 is docked with the second cassette being operated at TBD. The operations for each cassette will be 24/7 for a twoweek run.

    - In lieu of operations timeline from the PI LMMBIO-3 will operate two cassettes at TBD time after SpaceX-10 undocks. The operations for each cassette will be 24/7 for the first week, a 24 hour run every other day for the next 2 weeks (6 runs), and a 24 hour run twice the final week.

- Each PI shall provide the operations matrix defining the data to acquire for each crystal located on each capillary by February 1, 2016 or 2 months after the dry run whichever is later. This includes identifying what magnification to acquire images, which filter, and how many depths per crystal. During the dry run the capabilities and constraints should become evident.

4.4 On-Orbit Science Operations Requirements

- The PI shall support on-orbit operations. It would certainly be advantageous if the PI were present at the TSC during the entire run however this is sometimes unrealistic.

- The PI shall support daily operations meetings by telephone when not present at the TSC.

- The PI shall monitor the real-time ISS video as well as inspect a subset of the high resolution images in order to provide real-time instructions.

- The LMMBIO operator shall provide suggestions for making data acquisition most efficient.

- The LMMBIO operator shall provide high resolution images to the PI in near realtime via a website that will be made accessible to the PI. It should be noted that there may be trade-offs between seeing the data in near real-time and the rate at which data can be acquired.

4.5 Hardware Return

 The PI shall provide for the transport and maintenance of the samples upon receiving them at the Long Beach Airport. LMMBIO shall coordinate and support the operations at the Long Beach Airport.

4.6 Milestone Schedule

The following provides a summary of the milestones and delivery dates identified in this document.

Milestone	Date
Flight Cassettes Assembly Complete	11/1/15
Flight-like Capillaries for Ground Test	11/15/15
Ground Test in GIU complete	12/15/15
Operations Timeline	1/15/16
Fill & Seal Procedure	1/15/16
Operations Matrix	2/1/16

APPENDIX AHMST

HAZARDOUS MATERIALS SUMMARY TABLE
SpX-10 ASCENT to ISS Increment 46

Verification Status
V-1: *Preliminary Data*
V-2:

Expt /Hdwr/Item: **LMM Bio-Physics (LMMBIO)-1**
Expt/HW Acronym: LMM-B-M1

OpNom: TBD

Record # SX10.LMM.01 **PAYLOAD CHEMICAL or BIOLOGICAL INFORMATION**

Last Modified 8/3/15

Part #	Sub-System	Label	Chemicals or Biological Materials	Maximum Concentration	Maximum Volume or Amount	Tox Lvl	BioSafety Lvl	Flammability Haz Lvl
TBD	Capillary cassette- capillaries	TBD	Candidate Proteins/Viruses:		0.090 ml	0	NA	0
			P-glycoprotein	TBD	per capillary	0		
			Cytochrome-c (~12 kDa)	TBD	x24 capillaries	0		
			Alpha-chymotrypsinogen (25 kDa)	TBD		0		
			Equine or bovine serum albumin (~66 kDa)	TBD		0		
			Xenorhabdus-A, XptA1 (1,250 kDa)	TBD		0		
			Tobacco Mosaic Virus (18.0 mm dia x ~300	TBD		0		
			Plasmodium flaciparum glutathione-S-transferase (PFGST) 26 kDa	TBD		0		
			Thioredoxin / Wucheria Bancrofti/ 16.1 kDa	TBD		0		

HAZARD RESPONSE LEVEL (HRL) = 0

HAZARD LEVELS

Toxicity (THL) **0** BioSafety (BSL) **NA** Flammability **0**

Target Organ(s): None

Principal Adverse Effect(s)

Mild, transient eye irritation.

Contacts and Comments

Contact: Wayne Borelli, borrelliw@zin-tech.com, 440-625-1974

Comments: This experiment seeks to investigate the underlying reason for the improved quality of microgravity-grown protein crystals and how microgravity protein transport influences the crystal growth rate and crystal quality. Four aqueous proteins, one membrane protein (P-glycoprotein) and one virus (tobacco mosaic virus, TMV) will be selected with the proteins covering a broad range of molecular weights (i.e. ~10kDa to as high as 1,250kDa) and tobacco mosaic virus (TMV) which exhibits a particle diameter of 18.0 nm and a length of ~300 nm. Purified batches of protein and virus particles will be produced and isolated in different aggregate populations. Glass capillaries will be filled with protein and precipitant solutions and frozen to -80 deg C. The capillaries will be secured within a capillary cassette/holder and placed into a cold stowage container such as GLACIER. On orbit, the capillaries will be thawed to 20 deg C, then mixed to initiate crystal growth. Each capillary cassette will be placed under the FIR/LMM microscope to image the developing phases of crystal growth. Once imaging is completed, the protein crystal samples will be stowed at 20 deg C for return. Upon return, the crystal samples will undergo additional processing such as X-ray analysis.

As of August 10, 2015 1:53:14 PM Page 1 **Record # SX10.LMM.01** Mission Toxicologist: Dr. Garcia

HAZARDOUS MATERIALS SUMMARY TABLE
SpX-10 ASCENT to ISS Increment 46

Verification Status
V-1: *Preliminary Data*
V-2:

Expt /Hdwr/Item: **LMM Bio-Physics (LMMBIO)-1**
Expt/HW Acronym: **LMM-B-M1**
OpNom: **TBD**

Record # SX10.LMM.02 — **PAYLOAD CHEMICAL or BIOLOGICAL INFORMATION**

Last Modified 7/24/15

Part #	Sub-System	Label	Chemicals or Biological Materials	Maximum Concentration	Maximum Volume or Amount	Tox Lvl	BioSafety Lvl	Flammability Haz Lvl
TBD	Capillary cassette- capillaries	TBD	Salts:		0.090 ml	1	NA	0
			K2HPO4	3M	per capillary	1		
			Na2HPO4	3M	x24 capillaries	1		
			(NH4)2SO4	4M		1		
			Sodium malonate	3M		1		
			Lithium sulfate	3M		1		
			Sodium succinate	1.5M		1		
			Sodium formate	4M		1		
			Sodium acetate	4M		1		
			Sodium isocitrate	1.5M		1		
			Na-K Tartarate	1.6M		1		
			Sodium citrate	3M		1		
			NaCl	4M		1		
			NH4Cl	4M		1		
			CaCl2	0.05M		0		
			MgSO4	2M		1		
			MgCl2	0.05M		0		
			NaNO3	0.2M		1		
			ZnCl2	0.05M		0		

HAZARD RESPONSE LEVEL (HRL) = 1

HAZARD LEVELS

Toxicity (THL)	1	BioSafety (BSL)	NA	Flammability	0

Target Organ(s): None

Principal Adverse Effect(s)

Mild to moderate eye irritation.

Contacts and Comments

Contact: Wayne Borelli, borrelliw@zin-tech.com, 440-625-1974

Comments: This experiment seeks to investigate the underlying reason for the improved quality of microgravity-grown protein crystals and how microgravity protein transport influences the crystal growth rate and crystal quality. Four aqueous proteins, one membrane protein (P-glycoprotein) and one virus (tobacco mosaic virus, TMV) will be selected with the proteins covering a broad range of molecular weights (i.e. ~10kDa to as high as 1,250kDa) and tobacco mosaic virus (TMV) which exhibits a particle diameter of 18.0 nm and a length of ~300 nm. Purified batches of protein and virus particles will be produced and isolated in different aggregate populations. Glass capillaries will be filled with protein and precipitant solutions and frozen to -80 deg C. The capillaries will be secured within a capillary cassette/holder and placed into a cold stowage container such as GLACIER. On orbit, the capillaries will be thawed to 20 deg C, then mixed to initiate crystal growth. Each capillary cassette will be placed under the FIR/LMM microscope to image the developing phases of crystal growth. Once imaging is completed, the protein crystal samples will be stowed at 20 deg C for return. Upon return, the crystal samples will undergo additional processing such as X-ray analysis.

HAZARDOUS MATERIALS SUMMARY TABLE
SpX-10 ASCENT to ISS Increment 46

Verification Status
V-1: *Preliminary Data*
V-2:

Expt /Hdwr/Item: **LMM Bio-Physics (LMMBIO)-1**
Expt/HW Acronym: **LMM-B-M1**
OpNom: **TBD**

Record # SX10.LMM.03 **PAYLOAD CHEMICAL or BIOLOGICAL INFORMATION**

Last Modified 7/24/15

Part #	Sub-System	Label	Chemicals or Biological Materials	Maximum Concentration	Maximum Volume or Amount	Tox Lvl	BioSafety Lvl	Flammability Haz Lvl
TBD	Capillary cassette- capillaries	TBD	Buffers:		0.090 ml	1	NA	0
			Trizma base (TRIS buffer)	0.2M	per capillary	1		
			MES	0.2M	x24 capillaries	1		
			HEPES	0.2M		1		
			Sodium borate	0.2M		0		
			Glycine	0.2M		1		
			Sodium cacodylate	0.2M		1		
			Bis Tris propane	0.2M		0		
			Sodium acetate	0.2M		0		

HAZARD RESPONSE LEVEL (HRL) = 1

HAZARD LEVELS

Toxicity (THL) 1 | BioSafety (BSL) NA | Flammability 0

Target Organ(s): None

Principal Adverse Effect(s)

Mild to moderate eye irritation.

Contacts and Comments

Contact: Wayne Borelli, borrelliw@zin-tech.com, 440-625-1974

Comments: This experiment seeks to investigate the underlying reason for the improved quality of microgravity-grown protein crystals and how microgravity protein transport influences the crystal growth rate and crystal quality. Four aqueous proteins, one membrane protein (P-glycoprotein) and one virus (tobacco mosaic virus, TMV) will be selected with the proteins covering a broad range of molecular weights (i.e. ~10kDa to as high as 1,250kDa) and tobacco mosaic virus (TMV) which exhibits a particle diameter of 18.0 nm and a length of ~300 nm. Purified batches of protein and virus particles will be produced and isolated in different aggregate populations. Glass capillaries will be filled with protein and precipitant solutions and frozen to -80 deg C. The capillaries will be secured within a capillary cassette/holder and placed into a cold stowage container such as GLACIER. On orbit, the capillaries will be thawed to 20 deg C, then mixed to initiate crystal growth. Each capillary cassette will be placed under the FIR/LMM microscope to image the developing phases of crystal growth. Once imaging is completed, the protein crystal samples will be stowed at 20 deg C for return. Upon return, the crystal samples will undergo additional processing such as X-ray analysis.

HAZARDOUS MATERIALS SUMMARY TABLE
SpX-10 ASCENT to ISS Increment 46

Verification Status
V-1: *Preliminary Data*
V-2:

Expt /Hdwr/Item: **LMM Bio-Physics (LMMBIO)-1**
Expt/HW Acronym: **LMM-B-M1**
OpNom: TBD

Record # SX10.LMM.04 **PAYLOAD CHEMICAL or BIOLOGICAL INFORMATION**

Last Modified 7/24/15

Part #	Sub-System	Label	Chemicals or Biological Materials	Maximum Concentration	Maximum Volume or Amount	Tox Lvl	BioSafety Lvl	Flammability Haz Lvl
TBD	Capillary cassette- capillaries	TBD	Precipitants & Other Additives:		0.090 ml	1	NA	0
			3,5-Methylpentanediol	60% v/v	per capillary	1		
			PEG 200	60% v/v	x24 capillaries	0		
			PEG 400	60% v/v		0		
			PEG 1000	40% w/v		0		
			PEG 3350	35% w/v		0		
			PEG 8000	25% w/v		0		
			Jeffamine ED-4000	25% w/v		0		
			Hexanediol	50% v/v		1		
			Propanol	10% v/v		0		
			Ethanol	20% v/v		0		
			Glycerol	25% v/v		0		
			Butanol	10% v/v		0		
			2-methyl-2,4-pentanediol	60% v/v		1		

HAZARD RESPONSE LEVEL (HRL) = 1

HAZARD LEVELS

Toxicity (THL) 1 | BioSafety (BSL) NA | Flammability 0

Target Organ(s): None

Principal Adverse Effect(s)

Mild to moderate eye irritation.

Contacts and Comments

Contact: Wayne Borelli, borrelliw@zin-tech.com, 440-625-1974

Comments: This experiment seeks to investigate the underlying reason for the improved quality of microgravity-grown protein crystals and how microgravity protein transport influences the crystal growth rate and crystal quality. Four aqueous proteins, one membrane protein (P-glycoprotein) and one virus (tobacco mosaic virus, TMV) will be selected with the proteins covering a broad range of molecular weights (i.e. ~10kDa to as high as 1,250kDa) and tobacco mosaic virus (TMV) which exhibits a particle diameter of 18.0 nm and a length of ~300 nm. Purified batches of protein and virus particles will be produced and isolated in different aggregate populations. Glass capillaries will be filled with protein and precipitant solutions and frozen to -80 deg C. The capillaries will be secured within a capillary cassette/holder and placed into a cold stowage container such as GLACIER. On orbit, the capillaries will be thawed to 20 deg C, then mixed to initiate crystal growth. Each capillary cassette will be placed under the FIR/LMM microscope to image the developing phases of crystal growth. Once imaging is completed, the protein crystal samples will be stowed at 20 deg C for return. Upon return, the crystal samples will undergo additional processing such as X-ray analysis.

HAZARDOUS MATERIALS SUMMARY TABLE
SpX-10 ASCENT to ISS Increment 46

Verification Status
V-1: *Preliminary Data*
V-2:

Expt /Hdwr/Item: **LMM Bio-Physics (LMMBIO)-1**
Expt/HW Acronym: **LMM-B-M1**
OpNom: TBD

Record # SX10.LMM.05 **PAYLOAD CHEMICAL or BIOLOGICAL INFORMATION**

Last Modified 7/24/15

Part #	Sub-System	Label	Chemicals or Biological Materials	Maximum Concentration	Maximum Volume or Amount	Tox Lvl	BioSafety Lvl	Flammability Haz Lvl
TBD	Capillary cassette- capillaries	TBD	Other Additives:		0.090 ml	0	NA	0
			n-Octyl-beta-D-glucoside	0.05 M	per capillary	0		
			1,2,3-Hexanetriol	10% w/v	x24 capillaries	0		
			EDTA	0.05 M		0		
			1,4-Dithiothreitol	0.05 M		0		
			n-Dodecyl-beta-D-maltoside	0.05 M		0		
			n-Decyl-bet-D-maltoside	0.05 M		0		
			Octyl-beta-D-thiornaltoside	0.05 M		0		
			Beta-Mercaptoethanol	0.010 M		0		
			Meletic acid	0.10 M		0		
			Trimesic acid	0.10 M		0		

HAZARD RESPONSE LEVEL (HRL) = 1

HAZARD LEVELS

Toxicity (THL)	0	BioSafety (BSL)	NA	Flammability	0

Target Organ(s): None

Principal Adverse Effect(s)

Mild, transient eye irritation.

Contacts and Comments

Contact: Wayne Borelli, borrelliw@zin-tech.com, 440-625-1974

Comments: This experiment seeks to investigate the underlying reason for the improved quality of microgravity-grown protein crystals and how microgravity protein transport influences the crystal growth rate and crystal quality. Four aqueous proteins, one membrane protein (P-glycoprotein) and one virus (tobacco mosaic virus, TMV) will be selected with the proteins covering a broad range of molecular weights (i.e. ~10kDa to as high as 1,250kDa) and tobacco mosaic virus (TMV) which exhibits a particle diameter of 18.0 nm and a length of ~300 nm. Purified batches of protein and virus particles will be produced and isolated in different aggregate populations. Glass capillaries will be filled with protein and precipitant solutions and frozen to -80 deg C. The capillaries will be secured within a capillary cassette/holder and placed into a cold stowage container such as GLACIER. On orbit, the capillaries will be thawed to 20 deg C, then mixed to initiate crystal growth. Each capillary cassette will be placed under the FIR/LMM microscope to image the developing phases of crystal growth. Once imaging is completed, the protein crystal samples will be stowed at 20 deg C for return. Upon return, the crystal samples will undergo additional processing such as X-ray analysis.

As of August 10, 2015 1:53:14 PM Page 5 **Record # SX10.LMM.05** Mission Toxicologist: Dr. Garcia

HAZARDOUS MATERIALS SUMMARY TABLE
SpX-10 ASCENT to ISS Increment 46

Verification Status
V-1: *Preliminary Data*
V-2:

Expt /Hdwr/Item: **LMM Bio-Physics (LMMBIO)-3**
Expt/HW Acronym: **LMM-B-M3** *OpNom:* TBD

Record # SX10.LMM.06 **PAYLOAD CHEMICAL or BIOLOGICAL INFORMATION**

Last Modified 7/24/15

Part #	Sub-System	Label	Chemicals or Biological Materials	Maximum Concentration	Maximum Volume or Amount	Tox Lvl	BioSafety Lvl	Flammability Haz Lvl
TBD	Capillary cassette- M61 capillary	TBD	Ammonium chloride	1M	0.045 ml	1	NA	0
			Bis Tris Propane, pH=TBD	1M	per capillary			
			Polyethyleneglycol 20,000	30% v/v	x48 capillaries			

HAZARD RESPONSE LEVEL (HRL) = 1

HAZARD LEVELS

Toxicity (THL) 1 | BioSafety (BSL) NA | Flammability 0

Target Organ(s): None

Principal Adverse Effect(s)

Mild to moderate eye irritation.

Contacts and Comments

Contact: Wayne Borelli, borrelliw@zin-tech.com, 440-625-1974

Comments: The experiment is a protein crystal growth rate dispersion experiment. The protein will be variations on T4 lysozyme with single amino acid mutations. Glass capillaries will be filled with protein and precipitant solutions and frozen to -80 deg C. The capillaries will be secured within a capillary cassette/holder and placed into a cold stowage container such as GLACIER. On orbit, the capillaries will be thawed to 20 deg C, then mixed to initiate crystal growth. Each capillary cassette will be placed under the FIR/LMM microscope to image the developing phases of crystal growth. Once imaging is completed, the protein crystal samples will be stowed at 20 deg C for return. Upon return, the crystal samples will undergo additional processing such as X-ray analysis.
There are 8 different crystallization conditions which will be in Max of 50 mm x 3.0 x 0.3 mm capillaries having a maximum volume of 0.045 ml each. Actual fluid volumes and pH levels of each sample is unknown at this time. Assume worst case fluid volumes of 0.045 ml per capillary x 48 capillaries = 2.16 ml.

As of August 10, 2015 1:53:14 PM Page 6 **Record # SX10.LMM.06** Mission Toxicologist: Dr. Garcia

HAZARDOUS MATERIALS SUMMARY TABLE
SpX-10 ASCENT to ISS Increment 46

Verification Status
V-1: *Preliminary Data*
V-2:

Expt /Hdwr/Item: **LMM Bio-Physics (LMMBIO)-3**
Expt/HW Acronym: **LMM-B-M3**
OpNom: TBD

Record # SX10.LMM.07 **PAYLOAD CHEMICAL or BIOLOGICAL INFORMATION**

Last Modified 4/30/15

Part #	Sub-System	Label	Chemicals or Biological Materials	Maximum Concentration	Maximum Volume or Amount	Tox Lvl	BioSafety Lvl	Flammability Haz Lvl
TBD	Capillary cassette- S44F capillary	TBD	Zinc acetate	1M	0.045 ml	1	NA	0
			Sodium acetate, pH=TBD	1M	per capillary			
			Polyethyleneglycol 20,000	30% v/v	x48 capillaries			

HAZARD RESPONSE LEVEL (HRL) = 1

HAZARD LEVELS

Toxicity (THL) **1** BioSafety (BSL) **NA** Flammability **0**

Target Organ(s): None

Principal Adverse Effect(s)

Mild to moderate eye irritation.

Contacts and Comments

Contact: Wayne Borelli, borrelliw@zin-tech.com, 440-625-1974

Comments: The experiment is a protein crystal growth rate dispersion experiment. The protein will be variations on T4 lysozyme with single amino acid mutations. Glass capillaries will be filled with protein and precipitant solutions and frozen to -80 deg C. The capillaries will be secured within a capillary cassette/holder and placed into a cold stowage container such as GLACIER. On orbit, the capillaries will be thawed to 20 deg C, then mixed to initiate crystal growth. Each capillary cassette will be placed under the FIR/LMM microscope to image the developing phases of crystal growth. Once imaging is completed, the protein crystal samples will be stowed at 20 deg C for return. Upon return, the crystal samples will undergo additional processing such as X-ray analysis. There are 8 different crystallization conditions which will be in Max of 50 mm x 3.0 x 0.3 mm capillaries having a maximum volume of 0.045 ml each. Actual fluid volumes and pH levels of each sample is unknown at this time. Assume worst case fluid volumes of 0.045 ml per capillary x 48 capillaries = 2.16 ml.

HAZARDOUS MATERIALS SUMMARY TABLE
SpX-10 ASCENT to ISS Increment 46

Verification Status
V-1: *Preliminary Data*
V-2:

Expt /Hdwr/Item: **LMM Bio-Physics (LMMBIO)-3**
Expt/HW Acronym: **LMM-B-M3**
OpNom: TBD

Record # SX10.LMM.08 **PAYLOAD CHEMICAL or BIOLOGICAL INFORMATION**

Last Modified 4/30/15

Part #	Sub-System	Label	Chemicals or Biological Materials	Maximum Concentration	Maximum Volume or Amount	Tox Lvl	BioSafety Lvl	Flammability Haz Lvl
TBD	Capillary cassette- E45A capillary	TBD	Magnesium chloride	1M	0.045 ml per capillary x48 capillaries	1	NA	0
			(4-(2-hydroxyethyl)-1-piperazineethane-sulfonic acid), pH=7.5	1M				
			Polyethyleneglycol 20,000	30% v/v				

HAZARD RESPONSE LEVEL (HRL) = 1

HAZARD LEVELS

Toxicity (THL)	1	BioSafety (BSL)	NA	Flammability	0

Target Organ(s): None

Principal Adverse Effect(s)

Mild to moderate eye irritation.

Contacts and Comments

Contact: Wayne Borelli, borrelliw@zin-tech.com, 440-625-1974

Comments: The experiment is a protein crystal growth rate dispersion experiment. The protein will be variations on T4 lysozyme with single amino acid mutations. Glass capillaries will be filled with protein and precipitant solutions and frozen to -80 deg C. The capillaries will be secured within a capillary cassette/holder and placed into a cold stowage container such as GLACIER. On orbit, the capillaries will be thawed to 20 deg C, then mixed to initiate crystal growth. Each capillary cassette will be placed under the FIR/LMM microscope to image the developing phases of crystal growth. Once imaging is completed, the protein crystal samples will be stowed at 20 deg C for return. Upon return, the crystal samples will undergo additional processing such as X-ray analysis. There are 8 different crystallization conditions which will be in Max of 50 mm x 3.0 x 0.3 mm capillaries having a maximum volume of 0.045 ml each. Actual fluid volumes and pH levels of each sample is unknown at this time. Assume worst case fluid volumes of 0.045 ml per capillary x 48 capillaries = 2.16 ml.

As of August 10, 2015 1:53:14 PM Page 8 **Record # SX10.LMM.08** Mission Toxicologist: Dr. Garcia

HAZARDOUS MATERIALS SUMMARY TABLE
SpX-10 ASCENT to ISS Increment 46

Verification Status
V-1: *Preliminary Data*
V-2:

Expt /Hdwr/Item: **LMM Bio-Physics (LMMBIO)-3**
Expt/HW Acronym: **LMM-B-M3**
OpNom: **TBD**

Record # SX10.LMM.09 **PAYLOAD CHEMICAL or BIOLOGICAL INFORMATION**

Last Modified 4/30/15

Part #	Sub-System	Label	Chemicals or Biological Materials	Maximum Concentration	Maximum Volume or Amount	Tox Lvl	BioSafety Lvl	Flammability Haz Lvl
TBD	Capillary cassette- S44E (a) capillary	TBD	Sodium acetate, pH=TBD Tris(hydroxymethyl)aminomethane) Glycerol	1M 1M 75% v/v	0.045 ml per capillary x48 capillaries	1	NA	0

HAZARD RESPONSE LEVEL (HRL) = 1

HAZARD LEVELS

Toxicity (THL) **1** | BioSafety (BSL) **NA** | Flammability **0**

Target Organ(s): None

Principal Adverse Effect(s)

Mild to moderate eye irritation.

Contacts and Comments

Contact: Wayne Borelli, borrelliw@zin-tech.com, 440-625-1974

Comments: The experiment is a protein crystal growth rate dispersion experiment. The protein will be variations on T4 lysozyme with single amino acid mutations. Glass capillaries will be filled with protein and precipitant solutions and frozen to -80 deg C. The capillaries will be secured within a capillary cassette/holder and placed into a cold stowage container such as GLACIER. On orbit, the capillaries will be thawed to 20 deg C, then mixed to initiate crystal growth. Each capillary cassette will be placed under the FIR/LMM microscope to image the developing phases of crystal growth. Once imaging is completed, the protein crystal samples will be stowed at 20 deg C for return. Upon return, the crystal samples will undergo additional processing such as X-ray analysis. There are 8 different crystallization conditions which will be in Max of 50 mm x 3.0 x 0.3 mm capillaries having a maximum volume of 0.045 ml each. Actual fluid volumes and pH levels of each sample is unknown at this time. Assume worst case fluid volumes of 0.045 ml per capillary x 48 capillaries = 2.16 ml.

HAZARDOUS MATERIALS SUMMARY TABLE
SpX-10 ASCENT to ISS Increment 46

Verification Status
V-1: *Preliminary Data*
V-2:

Expt /Hdwr/Item: **LMM Bio-Physics (LMMBIO)-3**
Expt/HW Acronym: **LMM-B-M3**
OpNom: TBD

Record # SX10.LMM.10 **PAYLOAD CHEMICAL or BIOLOGICAL INFORMATION**

Last Modified 4/30/15 Part #	Sub-System	Label	Chemicals or Biological Materials	Maximum Concentration	Maximum Volume or Amount	Tox Lvl	BioSafety Lvl	Flammability Haz Lvl
TBD	Capillary cassette- S44E (b) capillary	TBD	Sodium nitrate	1M	0.045 ml per capillary x48 capillaries	1	NA	0
			(4-(2-hydroxyethyl)-1-piperazineethane-sulfonic acid), pH=7.5	1M				
			Polyethylene glycol 20,000	30% v/v				

HAZARD RESPONSE LEVEL (HRL) = 1

HAZARD LEVELS

Toxicity (THL) 1 | BioSafety (BSL) NA | Flammability 0

Target Organ(s): None

Principal Adverse Effect(s)

Mild to moderate eye irritation.

Contacts and Comments

Contact: Wayne Borelli, borrelliw@zin-tech.com, 440-625-1974

Comments: The experiment is a protein crystal growth rate dispersion experiment. The protein will be variations on T4 lysozyme with single amino acid mutations. Glass capillaries will be filled with protein and precipitant solutions and frozen to -80 deg C. The capillaries will be secured within a capillary cassette/holder and placed into a cold stowage container such as GLACIER. On orbit, the capillaries will be thawed to 20 deg C, then mixed to initiate crystal growth. Each capillary cassette will be placed under the FIR/LMM microscope to image the developing phases of crystal growth. Once imaging is completed, the protein crystal samples will be stowed at 20 deg C for return. Upon return, the crystal samples will undergo additional processing such as X-ray analysis. There are 8 different crystallization conditions which will be in Max of 50 mm x 3.0 x 0.3 mm capillaries having a maximum volume of 0.045 ml each. Actual fluid volumes and pH levels of each sample is unknown at this time. Assume worst case fluid volumes of 0.045 ml per capillary x 48 capillaries = 2.16 ml.

HAZARDOUS MATERIALS SUMMARY TABLE
SpX-10 ASCENT to ISS Increment 46

Verification Status
V-1: *Preliminary Data*
V-2:

Expt /Hdwr/Item: **LMM Bio-Physics (LMMBIO)-3**
Expt/HW Acronym: **LMM-B-M3**
OpNom: **TBD**

Record # SX10.LMM.11 **PAYLOAD CHEMICAL or BIOLOGICAL INFORMATION**

Last Modified 4/30/15 Part #	Sub-System	Label	Chemicals or Biological Materials	Maximum Concentration	Maximum Volume or Amount	Tox Lvl	BioSafety Lvl	Flammability Haz Lvl
TBD	Capillary cassette- WT (a) capillary	TBD	Ammonium sulfate	4M	0.045 ml per capillary x48 capillaries	1	NA	0
			(4-(2-hydroxyethyl)-1-piperazineethane-sulfonic acid), pH=7.5	1M				
			Methyl-2,4-pentanediol	75% v/v				

HAZARD RESPONSE LEVEL (HRL) = 1

HAZARD LEVELS

Toxicity (THL) **1** BioSafety (BSL) **NA** Flammability **0**

Target Organ(s): None

Principal Adverse Effect(s)

Mild to moderate eye irritation.

Contacts and Comments

Contact: Wayne Borelli, borrelliw@zin-tech.com, 440-625-1974

Comments: The experiment is a protein crystal growth rate dispersion experiment. The protein will be variations on T4 lysozyme with single amino acid mutations. Glass capillaries will be filled with protein and precipitant solutions and frozen to -80 deg C. The capillaries will be secured within a capillary cassette/holder and placed into a cold stowage container such as GLACIER. On orbit, the capillaries will be thawed to 20 deg C, then mixed to initiate crystal growth. Each capillary cassette will be placed under the FIR/LMM microscope to image the developing phases of crystal growth. Once imaging is completed, the protein crystal samples will be stowed at 20 deg C for return. Upon return, the crystal samples will undergo additional processing such as X-ray analysis. There are 8 different crystallization conditions which will be in Max of 50 mm x 3.0 x 0.3 mm capillaries having a maximum volume of 0.045 ml each. Actual fluid volumes and pH levels of each sample is unknown at this time. Assume worst case fluid volumes of 0.045 ml per capillary x 48 capillaries = 2.16 ml.

HAZARDOUS MATERIALS SUMMARY TABLE
SpX-10 ASCENT to ISS Increment 46

Verification Status
V-1: *Preliminary Data*
V-2:

Expt /Hdwr/Item: **LMM Bio-Physics (LMMBIO)-3**
Expt/HW Acronym: LMM-B-M3

OpNom: TBD

Record # SX10.LMM.12 **PAYLOAD CHEMICAL or BIOLOGICAL INFORMATION**

Last Modified 4/30/15 Part #	Sub-System	Label	Chemicals or Biological Materials	Maximum Concentration	Maximum Volume or Amount	Tox Lvl	BioSafety Lvl	Flammability Haz Lvl
TBD	Capillary cassette- WT (b) capillary	TBD	Manganese sulfate	1M	0.045 ml per capillary x48 capillaries	1	NA	0
			Sodium acetate	1M				
			Polyethylene glycol, 1,000	50% v/v				

HAZARD RESPONSE LEVEL (HRL) = 1

HAZARD LEVELS

Toxicity (THL) 1 | BioSafety (BSL) NA | Flammability 0

Target Organ(s): None

Principal Adverse Effect(s)

Mild to moderate eye irritation.

Contacts and Comments

Contact: Wayne Borelli, borrelliw@zin-tech.com, 440-625-1974

Comments: The experiment is a protein crystal growth rate dispersion experiment. The protein will be variations on T4 lysozyme with single amino acid mutations. Glass capillaries will be filled with protein and precipitant solutions and frozen to -80 deg C. The capillaries will be secured within a capillary cassette/holder and placed into a cold stowage container such as GLACIER. On orbit, the capillaries will be thawed to 20 deg C, then mixed to initiate crystal growth. Each capillary cassette will be placed under the FIR/LMM microscope to image the developing phases of crystal growth. Once imaging is completed, the protein crystal samples will be stowed at 20 deg C for return. Upon return, the crystal samples will undergo additional processing such as X-ray analysis. There are 8 different crystallization conditions which will be in Max of 50 mm x 3.0 x 0.3 mm capillaries having a maximum volume of 0.045 ml each. Actual fluid volumes and pH levels of each sample is unknown at this time. Assume worst case fluid volumes of 0.045 ml per capillary x 48 capillaries = 2.16 ml.

HAZARDOUS MATERIALS SUMMARY TABLE
SpX-10 ASCENT to ISS Increment 46

Verification Status
V-1: *Preliminary Data*
V-2:

Expt /Hdwr/Item: **LMM Bio-Physics (LMMBIO)-3**
Expt/HW Acronym: **LMM-B-M3**
OpNom: **TBD**

Record # SX10.LMM.13 **PAYLOAD CHEMICAL or BIOLOGICAL INFORMATION**

Last Modified 4/30/15

Part #	Sub-System	Label	Chemicals or Biological Materials	Maximum Concentration	Maximum Volume or Amount	Tox Lvl	BioSafety Lvl	Flammability Haz Lvl
TBD	Capillary cassette- WT (cys) capillary	TBD	Zinc acetate	1M	0.045 ml	1	NA	0
			Tris(hydroxymethyl)aminomethane)	1M	per capillary			
			Polyethylene glycol, 8,000	50% v/v	x48 capillaries			

HAZARD RESPONSE LEVEL (HRL) = 1

HAZARD LEVELS

Toxicity (THL) 1 | BioSafety (BSL) NA | Flammability 0

Target Organ(s): None

Principal Adverse Effect(s)

Mild to moderate eye irritation.

Contacts and Comments

Contact: Wayne Borelli, borrelliw@zin-tech.com, 440-625-1974

Comments: The experiment is a protein crystal growth rate dispersion experiment. The protein will be variations on T4 lysozyme with single amino acid mutations. Glass capillaries will be filled with protein and precipitant solutions and frozen to -80 deg C. The capillaries will be secured within a capillary cassette/holder and placed into a cold stowage container such as GLACIER. On orbit, the capillaries will be thawed to 20 deg C, then mixed to initiate crystal growth. Each capillary cassette will be placed under the FIR/LMM microscope to image the developing phases of crystal growth. Once imaging is completed, the protein crystal samples will be stowed at 20 deg C for return. Upon return, the crystal samples will undergo additional processing such as X-ray analysis. There are 8 different crystallization conditions which will be in Max of 50 mm x 3.0 x 0.3 mm capillaries having a maximum volume of 0.045 ml each. Actual fluid volumes and pH levels of each sample is unknown at this time. Assume worst case fluid volumes of 0.045 ml per capillary x 48 capillaries = 2.16 ml.

HAZARDOUS MATERIALS SUMMARY TABLE
SpX-10 ASCENT to ISS Increment 46

Verification Status
V-1: *Preliminary Data*
V-2:

Expt /Hdwr/Item: **LMM Bio-Physics (LMMBIO)-3**
Expt/HW Acronym: **LMM-B-M3**
OpNom: **TBD**

Record # SX10.LMM.14 **PAYLOAD CHEMICAL or BIOLOGICAL INFORMATION**

Last Modified 8/10/15

Part #	Sub-System	Label	Chemicals or Biological Materials	Maximum Concentration	Maximum Volume or Amount	Tox Lvl	BioSafety Lvl	Flammability Haz Lvl
TBD	Capillary cassette- WT*(cys) capillary	TBD	Other chemicals that may be used:		0.045 ml	0	NA	0
			PEG 8K	50% v/v	per capillary	0		
			PEG 3350	50% v/v	x48 capillaries	0		
			PEG 4K	50% v/v		0		
			Apiezon N Grease (cryogenic high vacuum)	100%	0.070 ml/cap x45 capillaries			

HAZARD RESPONSE LEVEL (HRL) = 0

HAZARD LEVELS

Toxicity (THL) 0 | BioSafety (BSL) NA | Flammability 0

Target Organ(s): None

Principal Adverse Effect(s)

Mild, transient eye irritation.

Contacts and Comments

Contact: Wayne Borelli, borrelliw@zin-tech.com, 440-625-1974

Comments: The experiment is a protein crystal growth rate dispersion experiment. The protein will be variations on T4 lysozyme with single amino acid mutations. Glass capillaries will be filled with protein and precipitant solutions and frozen to -80 deg C. The capillaries will be secured within a capillary cassette/holder and placed into a cold stowage container such as GLACIER. On orbit, the capillaries will be thawed to 20 deg C, then mixed to initiate crystal growth. Each capillary cassette will be placed under the FIR/LMM microscope to image the developing phases of crystal growth. Once imaging is completed, the protein crystal samples will be stowed at 20 deg C for return. Upon return, the crystal samples will undergo additional processing such as X-ray analysis. There are 8 different crystallization conditions which will be in Max of 50 mm x 3.0 x 0.3 mm capillaries having a maximum volume of 0.045 ml each. Actual fluid volumes and pH levels of each sample is unknown at this time. Assume worst case fluid volumes of 0.045 ml per capillary x 48 capillaries = 2.16 ml.

As of August 10, 2015 1:53:14 PM Page 14 **Record # SX10.LMM.14** Mission Toxicologist: Dr. Garcia

HAZARDOUS MATERIALS SUMMARY TABLE
SpX-10 ASCENT to ISS Increment 46

Verification Status
V-1: *Preliminary Data*
V-2:

Expt /Hdwr/Item: **LMM Bio-Physics (LMMBIO)-1**
Expt/HW Acronym: **LMM-B-M1**
OpNom: TBD

Record # SX10.LMM.15 — **PAYLOAD CHEMICAL or BIOLOGICAL INFORMATION**

Last Modified 8/10/15 Part #	Sub-System	Label	Chemicals or Biological Materials	Maximum Concentration	Maximum Volume or Amount	Tox Lvl	BioSafety Lvl	Flammability Haz Lvl
TBD	Kit-- vials	TBD	**Alexa Fluor 488 Protein Labelling Kit:**			1	NA	0
			Component A: Alexa Fluor 488 dye	N/A	3x 6.1 microg			
			Component B: Sodium bicarbonate	N/A	3 x 84 mg			
			Component C: Purification resin: Bio-Rad	N/A				
			BioGel P-30 Fine size		25 ml			
			Component D: 10x elution buffer:	N/A	25 ml			
			Potassium phosphate	0.1M				
			NaCl	1.5 M				
			Sodium azide	2 mM				

HAZARD RESPONSE LEVEL (HRL) = 1

HAZARD LEVELS

Toxicity (THL)	1	BioSafety (BSL)	NA	Flammability	0

Target Organ(s): Eye

Principal Adverse Effect(s)

Moderate eye irritation.

Contacts and Comments

Contact: Wayne Borelli, borrelliw@zin-tech.com, 440-625-1974

Comments:

HAZARDOUS MATERIALS SUMMARY TABLE
SpX-10 ASCENT to ISS Increment 46

Verification Status
V-1: *Preliminary Data*
V-2:

Expt /Hdwr/Item: **LMM Bio-Physics (LMMBIO)-1**
Expt/HW Acronym: LMM-B-M1 *OpNom:* TBD

Record # SX10.LMM.16 **PAYLOAD CHEMICAL or BIOLOGICAL INFORMATION**

Last Modified 8/10/15 Part #	Sub-System	Label	Chemicals or Biological Materials	Maximum Concentration	Maximum Volume or Amount	Tox Lvl	BioSafety Lvl	Flammability Haz Lvl
TBD	Kit-- vials	TBD	**Alexa Fluor 594 Protein Labelling Kit:**			1	NA	0
			Component A: Alexa Fluor 488 dye	N/A	3x 5.7 microg			
			Component B: Sodium bicarbonate	N/A	3x 84 mg			
			Component C: Purification resin: Bio-Rad	N/A				
			BioGel P-30 Fine size		25 ml			
			Component D: 10x elution buffer:	N/A	25 ml			
			Potassium phosphate	0.1M				
			NaCl	1.5 M				
			Sodium azide	2 mM				

HAZARD RESPONSE LEVEL (HRL) = 1

HAZARD LEVELS

Toxicity (THL) **1** BioSafety (BSL) **NA** Flammability **0**

Target Organ(s): Eye

Principal Adverse Effect(s)

Moderate eye irritation.

Contacts and Comments

Contact: Wayne Borelli, borrelliw@zin-tech.com, 440-625-1974

Comments:

APPENDIX B Assembly Drawings

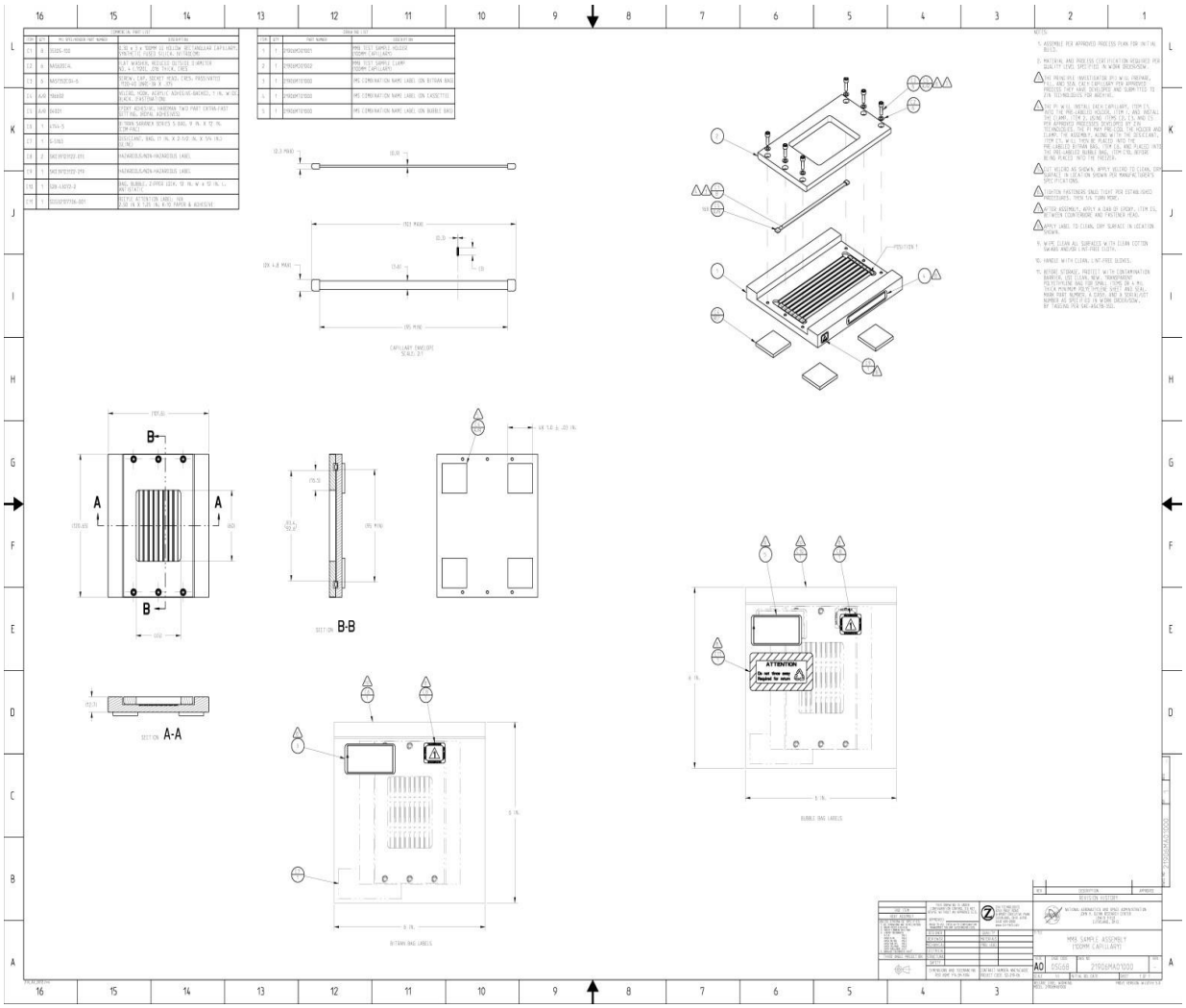

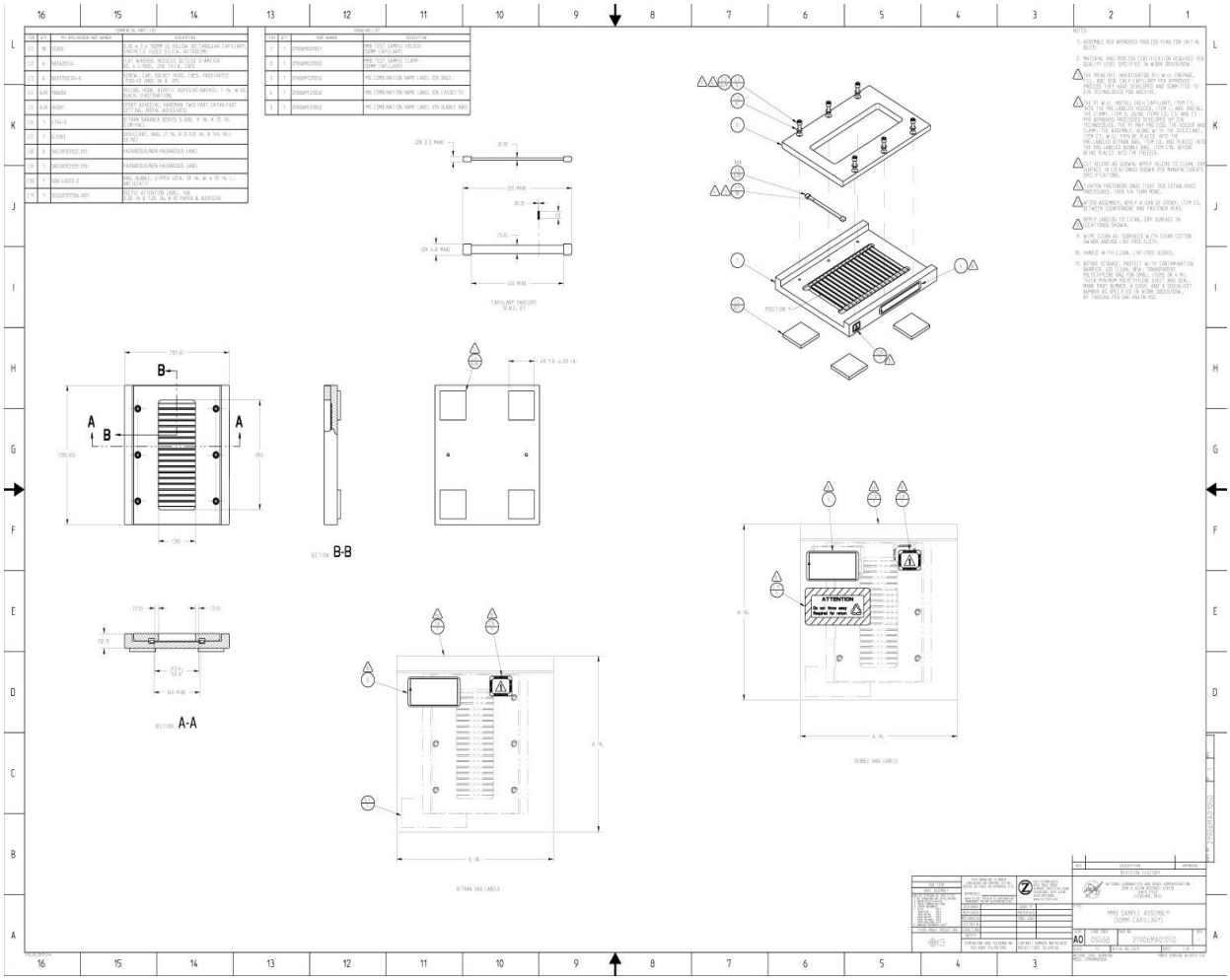

X Risk and safety statements

Table 35. Chemicals used, GHS classification.

Compound	CAS-No.	Supplier	GHS hazard	Hazard Statements	Precautionary Statements
Acetic acid	64-19-7	Chem-solute	GHS02 GHS05	H226, H314	P280, P305+351+338, P310
Acrylamide 37%	79-06-1	Carl Roth	GHS06 GHS08	H301, H312, H315, H317, H319, H332, H340, H350, H361f, H372	P201,P280, P301+310, P305+351+338, P308+313
Agarose	9012-36-6	Serva	-	-	-
$(NH_4)_2SO_4$	7283-20-2	Carl Roth	-	-	-
Ampicillin	69-52-3	Carl Roth	GHS08	H334, H317	P280, P261, P302+352, P342+311
APS	7727-54-0	Carl Roth	GHS03 GHS07 GHS08	H272, H302, H315, H317, H319, H334, H335	P280, P305+351+338, P302+352, P304+341, P342+311
Bromphenol blue	115-39-9	Applichem	-	-	-
4-Bromobenzyl bromide	589-15-1	Sigma	GHS05 GHS08	H314, H315, H316, H317, H318, H319, H320, H321, H322, H323, H324, H325, H326, H327, H328, H329, H330, H331, H332, H333, H334	P261-P280-P305 + P351 + P338-P310
$CaCl_2$	10043-52-4	Merck	GHS07	H319	P305+351+338
Citric acid	77-92-9	Sigma	GHS05	H318	P305+351+338, P311
Coomassie Brilliant Blue R250	6104-59-2	Serva	-	-	-
Dimethyl sulfoxide (DMSO)	67-68-5	Merck	GHS02	H227	P210-P280-P370 + P378-P403 + P235-P501
DTT	578517	Applichem	GHS07	H302, H315, H319, H335	P302+352, P305+351+338
EDTA	60-00-4	Sigma	GHS07	H319	P305+351+338

Ethanol	64-17-5	Carl Roth	GHS02	H225	P210
Glycerol	56-81-5	Sigma	-	-	-
Guanidinhydrochlorid	50-01-1	Applichem	GHS07	H302, H315, H319	P305+351+388, P302+352
Hepes	7365-45-9	Sigma Aldrich	-	-	-
Hydrochloric acid >25 %	7647-01-0	Merck	GHS05 GHS07	H314, H335	P261, P280, P310, P305+351+338
Imidazole	288-32-4	Carl Roth	GHS05 GHS06 GHS08	H301, H314, H361	P260, P281, P303+361+353, P301+330+3 31, P305+351+3 38, P308+313
Isopropanol	67-63-0	Carl Roth	GHS02 GHS07	H225, H319, H336.	P210, P233, P305+351+338
KCl	7447-40-7	Carl Roth	-	-	-
$MgCl_2$	7786-30-3	Carl Roth	-	-	-
2-Mercaptoethanol	60-24-2	Fisher Scientific	GHS06 GHS09	H302, H411, H315, H335, H311, H319	P280, P312, P302+350, P261, P273, P301+312, P305+351+338
NaOAc	127-09-3	Applichem	-	-	-
$(CH_3)_2AsO_2Na$)	124-65-2	Sigma	GHS06 GHS09	H301, H331, H410	P261, P273, P301+310, P311, P501
NaCl	7647-14-5	Carl Roth	-	-	-
NaH_2PO_4	10049-21-5	Applichem	-	-	-
NaOH	1310-73-2	Merck	GHS05	H314	P280, P310, P305+351+338
Paraffin	8002-74-2	Applichem	-	-	-
PEG 4000	25322-68-3	Merck	-	-	-
PEG 6000	25322-68-3	Merck	-	-	-
PEG 8000	25322-68-3	Sigma	-	-	-
PMSF	329-98-6	Applichem	GHS06 GHS05	H301, H314	P280, P305+351+3 38, P310
SDS	151-21-3	Sigma	GHS02 GHS06	H228, H302, H311, H315, H319, H335	P210, P261, P280, P312, P305+351+338

TEMED	110-18-9	Merck	GHS02 GHS05 GHS07	H225, H302, H314, H332	P261, P280, P305+351+338
Tris	1185-53-1	Fluka	GHS07	H315, H319, H335	P261, P305+351+338
Tween 20	9005-64-5	Carl Roth	-	-	-

GHS pictograms

Figure 74: GHS pictograms (source: https://www.sigmaaldrich.com/help-welcome/hazard-and-precautionary-statements.html#precautionary

Table 36. GHS Hazard Statements.

H225	Highly flammable liquid and vapor
H226	Flammable liquid and vapor
H227	Combustible liquid
H228	Flammable solid
H272	May intensify fire; oxidizer
H301	Toxic if swallowed
H302	Harmful if swallowed
H311	Toxic in contact with skin
H312	Harmful in contact with skin
H314	Causes severe skin burns and eye damage
H315	Causes skin irritation
H317	May cause an allergic skin reaction
H318	Causes serious eye damage
H319	Causes serious eye irritation
H320	Serious eye damage/eye irritation
H330	Fatal if inhaled
H331	Toxic if inhaled
H332	Harmful if inhaled
H334	May cause allergy or asthma symptoms or breathing difficulties if inhaled
H335	May cause respiratory irritation
H336	May cause drowsiness or dizziness
H340	May cause genetic defects
H341	Suspected of causing genetic defects
H350	May cause cancer

H350i	May cause cancer by inhalation
H360	May damage fertility or the unborn child
H360D	May damage the unborn child
H360Fd	May damage fertility. Suspected of damaging the unborn child
H360FD	May damage fertility. May damage the unborn child
H361	Suspected of damaging fertility or the unborn child
H361d	Suspected of damaging the unborn child.
H361f	Suspected of damaging fertility
H370	Cause damage to organs
H372	Causes damage to organs through prolonged or repeated exposure
H373	May cause damage to organs through prolonged or repeated exposure.
H410	Very toxic to aquatic life with long lasting effects
H411	Toxic to aquatic life with long lasting effects
H412	Harmful to aquatic life with long lasting effects.

Table 37. GHS Precautionary Statements.

P101	If medical advice is needed, have product container or label at hand
P201	Obtain special instructions before use
P210	Keep away from heat/sparks/open flames/hot surfaces – No smoking
P233	Keep container tightly closed
P260	Do not breathe dust/fume/gas/mist/vapors/spray
P261	Avoid breathing dust/fume/gas/mist/vapors/spray
P264	Wash thoroughly after handling
P270	Do not eat, drink or smoke when using this product
P273	Avoid release to the environment
P281	Use personal protective equipment as required
P280	Wear protective gloves/protective clothing/eye protection/face protection
P284	Wear respiratory protection
P309	IF exposed or you feel unwell
P310	Immediately call a POISON CENTER or doctor/physician
P311	Call a POISON CENTER or doctor/physician
P312	Call a POISON CENTER or doctor/physician if you feel unwell
P321	Specific treatment (see respective MSDS)
P330	Rinse mouth
P362	Take off contaminated clothing and wash before reuse
P405	Store locked up
P501	Dispose of contents/container in accordance with local/regional/national/international regulations
P301+310	IF SWALLOWED: Immediately call a POISON CENTER or doctor/physician
P301+312	IF SWALLOWED: Call a POISON CENTER or doctor/physician if you feel unwell
P301+330+ 331	IF SWALLOWED: Rinse mouth. Do NOT induce vomiting
P302+352	IF ON SKIN: Wash with soap and water
P303+361+ 353	IF ON SKIN (or hair): Remove/Take off immediately all contaminated clothing. Rinse skin with water/shower

P304+341	IF INHALED: lf breathing is difficult, remove victim to fresh air and keep at rest in a position comfortable for breathing
P305+351+338	IF IN EYES: Rinse cautiously with water for several minutes. Remove contact lenses if present and easy to do - continue rinsing
P308+313	IF exposed or concerned: Get medical advice/attention
P309+311	IF exposed or you feel unwell: Call a POISON CENTER or doctor/physician
P332+313	lf skin irritation occurs: Get medical advice/attention
P342+311	Call a POISON CENTER or doctor/physician
P403+233	Store in a well-ventilated place. Keep container tightly closed

XI Acknowledgments

First of all, I would like to thank my supervisor, Prof. Dr. Christian Betzel, for giving me the opportunity to work on this project in his laboratory. I am grateful for the scientific guidance and assessment for my work and final thesis. I would also like to thank my co-supervisor PD Dr. Markus Perbandt for the scientific conversations and guidance he contributed to my work during my thesis. Further I would like to thank Prof. Dr. Andrew Torda for the evaluation of my thesis and to the examiners committee of my defense presentation. Thank you, Petra Belda, for guidance in the lab and for always helping to order necessary materials, chemicals etc. for this project.
I would like to thank all the members of our lab, especially Christina, Robin, Sven, Sabine for great cooperation.

A very special thank you to Dr. Lawrence DeLucas (Ex astronaut who flew aboard NASA Space Shuttle mission STS-50) from University of Alabama, Aerospace corporation for providing this NASA biophysics project and giving the opportunity to work on this project in his lab.

I would like to thank all the people that have been involved in the SpaceX Spx-10 and SpaceX Spx-15 missions. I would like to thank all the crew members of ISS expedition 50 and 52. Also I would like to thank all the participants (i.a. Zin Technologies) of Biophysics – 1 and Biophysics – 4 projects. I also acknowledge UAB-High Resolution Imaging Service Center, Shelby 135c, Confocal/Light Microscopy Core at the University of Alabama at Birmingham.

Furthermore, I would like to thank Jan, from the lab Dr. Stefan Hoth, for great help to perform confocal microscopic imaging experiments. I also would like to thank Suki, from the lab Dr. Ignatova, for helping to perform fluorescence intensity measurement experiments using a microplate reader. I would like to thank all the members of the Institute Organic Chemistry , University Hamburg for great cooperation.

Further I would like to thank all of the beamline P11 and P13 staff for providing such a fabulous beamline where the majority of my data was collected.

Finally, I would like to thank my family and all my friends for all they support.

This research has been supported by the NASA (Grant No. 80NSSC18K0013) and Deutsche Luft und Raumfahrt Agentur (DLR) supporting the project via grant 50WB1423.

XII Publications

Publications associated with this thesis

Arayik Martirosyan, Lawrence J. DeLucas, Christina Schmidt, Markus Perbandt, Deborah McCombs, Martin Cox, Christopher Radka and Christian Betzel. Effect of macromolecular mass transport in microgravity protein crystallization. *Gravitational and Space Research*. (Accepted 05.06.2019) .

Sven Falke, Hevila Brognaro, **Arayik Martirosyan,** Karsten Dierks, Christian Betzel. Monitoring protein oligomerisation and liquid dense cluster formation applying a unique multi-channel in situ light scattering instrument (Manuscript in progress).

Book chapters:

1. Betzel, Christian, **Arayik Martirosyan**, and Günter Ruyters. Protein Crystallization on the International Space Station ISS. *Biotechnology in Space*. Springer, Cham, 2017. 27-39.

2. Betzel, Christian, and **Arayik Martirosyan**. Drug Design. *Biotechnology in Space*. Springer, Cham, 2017. 41-58.

XIII Curriculum vitae

- entfällt aus datenschutzrechtlichen Gründen –

XIV Eidesstattliche Erklärung

Hiermit versichere ich an Eides statt, die vorliegende Dissertation selbst verfasst und keine anderen als die angegebenen Hilfsmittel benutzt zu haben. Ich versichere, dass diese Dissertation nicht in einem früheren Promotionsverfahren eingereicht wurde.
Ferner versichere ich, dass ich noch keine Promotionsversuche an anderen Universitäten unternommen habe.

Hamburg, Datum

_____

(Arayik Martirosyan)